



# **Positioning and Timing Calibration of SNO+**

**James R. Sinclair**

Submitted for the degree of Doctor of Philosophy  
University of Sussex  
March 2015

# **Declaration**

I hereby declare that this thesis has not been and will not be submitted in whole or in part to another University for the award of any other degree.

Signature:

James R. Sinclair

UNIVERSITY OF SUSSEX

JAMES R. SINCLAIR, DOCTOR OF PHILOSOPHY

POSITIONING AND TIMING CALIBRATION OF SNO+ABSTRACT

The Sudbury Neutrino Observatory solved the solar neutrino problem, confirming neutrinos have non-zero masses. Massive neutrinos raise questions about the nature of neutrinos, implying physics beyond the standard model and potentially a solution to the observed matter-antimatter asymmetry in the universe. The Sudbury Neutrino Observatory is being upgraded, with the goal of probing the nature of neutrino masses. The experiment will also study reactor, geo, supernovae and solar neutrinos. The upgrade is characterised by changing the target mass from heavy water to scintillator. Using scintillator allows for the lowering of the energy threshold, but this increases sensitivity to backgrounds. To meet the requirements of the physics on detector performance, a detailed optical calibration is needed. Due to increased background sensitivity, a new external LED-based calibration system has been developed and the existing laser calibration system has been modified to meet radiopurity requirements. This thesis describes the development and implementation of both of these calibration systems. With a study of the potential use of the LED system to monitor the detector's structure, enabling a better definition of the fiducial volume by reducing the effects of external backgrounds. An assessment of the impact of these systems on the detector performance will be presented.

# Acknowledgements

Firstly I would like to thank my supervisor, Simon Peeters, from whom I've learnt a great deal during the past four and half years. His patience, enthusiasm, advice and continual support have been invaluable.

A big thank you to Ken Clark for welcoming me into the world of research. Equally, to Gwen Lefevre for filling Ken's boots and continuing my lab training with slightly less Blu-tack.

Thanks also to Phil Jones and Matthew Mottram for their help with SNO+ software throughout the past few years and the various evenings with fine beer. Ian Coulter should be thanked for his time spent as a sounding board, explaining the fitters and a most interesting road trip to the INSS with Cristovao Vilela.

Within SNO+, Jose Maneira's continual guidance on all things optics has been extremely valuable. Gabriel Orebi Gann for her patient explanations of the trigger and the PMT calibration, along with Freija Descamps. Joachim Rose for taking the time to share some of his expertise on LED drivers.

Michael Baker has continually provided impartial words of wisdom and guidance from the other realms of physics.

Thanks also to my fellow Sussex EPP students: Stewart Martin-Haugh, James Waterfield, Mark Stringer, Ed Leming, Yusufu Shehu, Nicky Santoyo, Zara Grout and the student who never grew up Steve Churchwell for their help, answers to many stupid questions and a good deal of fond memories in Brighton.

Technical staff at Sussex also deserve gratitude, Alan Mayers who spent a great deal of time teaching me how to work in the machine shop and the effect beer and biscuits have on workshop efficiency. Richard White, who has been instrumental to the LED driver development.

Everyone at SNOLAB who made a pleasant environment of both the lab and Sudbury.

Particularly, Anna Millington and Ben Davis-Purcell for teaching me the Canadian way of life and making for a very enjoyable summer in the Queens house. Allan Barr for his help understanding more of the engineering aspects of SNO+, and bringing me into the fold of Sudbury life.

Lastly, my family. Without the support of my parents, this would not have been possible.

# Preface

The general subject of this thesis was suggested by my supervisor, Simon Peeters.

Chapter 1 is an introduction to the thesis putting the working into context.

Chapter 2 provides an overview of the relevant neutrino theory and summary of current experimental status. It is an amalgamation of various sources.

Chapter 3 introduces the SNO+ detector, which forms the subject of this thesis. It is also an amalgamation of various sources as well as descriptions based upon my own experience.

Chapter 4 describes the new rope system. Throughout my attachment to SNOLAB I was involved with the installation of the new rope system, writing the code that was used to extract load cell data and providing initial analysis, as well as orchestrating the tensioning procedures. That work is described here, along with the results of a more detailed analysis by the Alberta group.

Chapter 5 describes the LED selection and LED driver boards. I have been extensively involved in the LED selection, writing the analysis of wavelength transmission probability and the testing LEDs. I was involved with the characterisation of the IXLD02 driver, although most of its development took place at Leeds. The Sussex Kapustinsky drive builds on work carried out by the Sussex technician, Richard White, for the Double Chooz experiment. I have been closely involved with the iterative improvements of the Sussex Kapustinsky driver, for SNO+ and beyond. All measurements presented here are my own work. However, Gwen Lefeuvre of Sussex, helped extensively in setting up these measurements.

Chapter 6 describes the entirety of the TELLIE calibration system. I have been involved in the characterisation measurements of all components, and installation of the system. The analysis of expected performance is the work of Freija Descamps at Berkley.

Chapter 7 describes the Laserball. The discussion of the original SNO laserball is based on the work of Nuno de Barros of Lisbon. The designs of the SNO+ laserball are my own, drawings were produced by the Sussex technician Allan Myers. The analysis is based on the work of Mark Stringer at Sussex, who is taking over responsibility for the project.

Chapter 8 describes the use of the Calibration system to monitor the ropes system performance. I developed the initial analysis code, however the results presented here use an updated version of the code, for which Mark Stringer is also responsible.

Chapter 9 presents sensitivity studies of SNO+. I generated the relevant background spectra for the analysis. The analysis software was written by James Waterfield of Sussex and Ashley Back of Queen Mary.

Chapter 10 contains the conclusions. These are my own.

# Contents

<b>List of Tables</b>	<b>xiii</b>
<b>List of Figures</b>	<b>xxiii</b>
<b>1 Introduction</b>	<b>1</b>
<b>2 Theory and Experimental Background</b>	<b>4</b>
2.1 Short History of the Physics of Neutrinos . . . . .	4
2.2 Neutrino Theory . . . . .	6
2.2.1 Neutrino Oscillations . . . . .	6
2.3 Neutrino Masses . . . . .	8
2.3.1 Oscillation Limits . . . . .	10
2.3.2 Beta Decay Limits . . . . .	10
2.3.3 Cosmological Limits . . . . .	11
2.4 Majorana Neutrinos . . . . .	11
2.5 Neutrinoless Double-Beta Decay . . . . .	13
2.5.1 Double-Beta Decay and Oscillations . . . . .	18
2.6 Experimental Status . . . . .	20
<b>3 The SNO+ Detector</b>	<b>22</b>
3.1 The Sudbury Neutrino Observatory . . . . .	22
3.2 Changing SNO into the SNO+ experiment . . . . .	23
3.3 Coordinate System . . . . .	28
3.4 SNO+ Electronics Overview . . . . .	31
3.5 The Rope System . . . . .	33
3.5.1 SNO Ropes . . . . .	34
3.5.2 SNO+ Ropes and Net . . . . .	36
3.6 Scintillator System . . . . .	39

3.7	Calibration System . . . . .	42
3.7.1	Reconstruction Resolution . . . . .	47
3.8	Monte Carlo Simulation and Data Handling . . . . .	47
<b>4</b>	<b>Acrylic Vessel Positioning</b>	<b>49</b>
4.1	Installing the New Rope System . . . . .	50
4.1.1	Replacing Hold-Up Ropes . . . . .	50
4.1.2	Centring the AV . . . . .	51
4.1.3	Net Installation . . . . .	52
4.2	Pretensioning and performance of the Rope System . . . . .	53
4.2.1	Monitoring Creep . . . . .	53
4.2.2	Results . . . . .	56
4.3	Conclusion . . . . .	59
<b>5</b>	<b>The TELLIE LED and Driver Circuits</b>	<b>60</b>
5.1	The TELLIE LED . . . . .	60
5.1.1	LED Timing Properties . . . . .	61
5.1.2	Spectral Constraints . . . . .	61
5.1.3	LED Availability . . . . .	63
5.1.4	LED Selection . . . . .	63
5.2	Driver Development . . . . .	64
5.2.1	Requirements . . . . .	64
5.2.2	Characterisation set-ups . . . . .	70
5.2.3	Kapustinsky Driver Circuit . . . . .	74
5.2.4	IXYS Laser Diode Driver . . . . .	79
5.2.5	Observations and Conclusions . . . . .	85
<b>6</b>	<b>Realisation of the TELLIE System</b>	<b>87</b>
6.1	Requirements . . . . .	87
6.2	LED and Driver . . . . .	88
6.2.1	LED Coupling . . . . .	89
6.2.2	The TELLIE Driver Box . . . . .	89
6.2.3	LED Quality Assurance . . . . .	91
6.2.4	LED and Driver (Channel) Quality Assurance . . . . .	91
6.3	Fibre Selection . . . . .	93
6.3.1	Fibre Characterisation and Quality Assurance . . . . .	94

6.4	Mechanical Structure . . . . .	100
6.4.1	Fibre Termination Points at the Detector . . . . .	101
6.5	Radioactivity . . . . .	102
6.5.1	Radon Emanation . . . . .	103
6.6	Water Compatibility . . . . .	104
6.7	SNO+ Trigger Interface . . . . .	105
6.8	Performance . . . . .	107
6.8.1	Simulation of TELLIE Pulses . . . . .	107
6.8.2	Expected Performance of Complete System . . . . .	108
6.8.3	Commissioning with Partial System . . . . .	110
<b>7</b>	<b>The Laserball</b>	<b>114</b>
7.1	Requirements . . . . .	114
7.2	The SNO Laserball . . . . .	115
7.3	The SNO+ Scintillator Phase Laserball . . . . .	118
7.3.1	Design . . . . .	118
7.3.2	Mechanical Design . . . . .	119
7.3.3	Radioactivity and Scintillator Compatibility . . . . .	122
7.4	Expected Performance . . . . .	123
7.4.1	The Mask Function . . . . .	123
7.4.2	Obtaining the Mask Functions . . . . .	124
7.4.3	PMT Angular Response . . . . .	125
7.5	Conclusions . . . . .	126
<b>8</b>	<b>Acrylic Vessel Monitoring with TELLIE</b>	<b>128</b>
8.1	Principals of Fitting the AV Position . . . . .	129
8.2	Refractive Indices and Group Velocities . . . . .	129
8.3	Time of Flight Calculations . . . . .	130
8.4	Data Selection . . . . .	132
8.4.1	Trigger Delays . . . . .	134
8.5	Uncertainties . . . . .	135
8.5.1	PMT Geometry . . . . .	135
8.5.2	Time . . . . .	137
8.5.3	Minimising Uncertainties . . . . .	138
8.6	Fitting The AV Position . . . . .	138

8.7 Conclusions . . . . .	142
<b>9 Influence of TELLIE on the Neutrinoless Double-Beta Decay Sensitivity of SNO+ . . . . .</b>	<b>144</b>
9.1 Expected Sensitivity . . . . .	144
9.2 AV Location . . . . .	146
9.2.1 Shift in AV Position . . . . .	146
9.2.2 Uncertainty in AV Position . . . . .	150
9.3 Timing Calibration . . . . .	151
9.4 Sensitivity to Neutrinoless Double-Beta Decay . . . . .	152
9.5 Conclusions . . . . .	154
<b>10 Discussion and Conclusions . . . . .</b>	<b>156</b>
10.1 SNO+ . . . . .	156
10.2 Optical Calibration Systems . . . . .	157
10.2.1 Scintillator Phase Laserball . . . . .	157
10.2.2 TELLIE . . . . .	157
10.2.3 AV Location . . . . .	159
<b>Bibliography . . . . .</b>	<b>160</b>
<b>A Laserball Construction Instructions . . . . .</b>	<b>172</b>
<b>B Laserball Technical Drawings . . . . .</b>	<b>174</b>

# List of Tables

2.1	<i>Results of global three neutrino oscillation analysis [27], for normal and inverted hierarchies.</i>	10
3.1	<i>Table of counting results for Vectran ropes used in SNO and Tensylon ropes of SNO+, with Kevlar ropes shown for comparison. Vectran and Kevlar results are from germanium counting at Laurentian University [78], Tensylon results are from the Borexino calibration [76]. SNO+ goal is the criteria used ropes had to meet to be suitable for SNO+. These values were defined in the initial external backgrounds document [77].</i>	39
5.1	<i>Hit probability from [105] and subsequent TELLIE running times for different phases of SNO+. Assuming a 504 nm LED pulse width of 6 ns and a desired accuracy of 0.5 ns running at 10 Hz.</i>	69
5.2	<i>Summary of time profile measurements for the Sussex LED driver at intensities of <math>10^3</math> and <math>10^6</math> photons per pulse. All measurements made with the driver running at 10 kHz. The measurement of the number of photons is performed after 0.5 m of optical fibre coupling the driver and LED combinations to the PMT. The results are the mean of three different driver-LED combinations.</i>	78
5.3	<i>Summary of time profile measurements for a single LED and driver at varying intensities. All measurements made with the driver running at 1 kHz. The measurement of the number of photons is performed after 45.75 m of optical fibre, i.e., not including the 2 m patch cord. The measurements of time profile of a single channel reported in this table are smaller, and more accurate, than the FWHM reported in Figure 6.3 due to systematic errors from the response time of the PMT and readout of the oscilloscope used in those measurements, that refer to all 96 channels.</i>	85

6.1	<i>Fibre quality checking and selection was based on three parameters connected to transmission, numerical aperture and timing profile. The LED driver used was a prototype of the final version.</i>	100
6.2	<i>Full installation values for the amount of each isotope included in the calibration systems. The amount shown corresponds to 110 fibre cables and 9500 PMTs and PMT cables.</i>	103
6.3	<i>Radon emanation budget for the PMT calibration system. The fibre results come from measurements of <math>^{222}\text{Rn}</math> emanation. The values for the other parts of the system come from a worst-case scenario estimate based on the bulk radioactivity results (Table 6.2). The total mass considered for the plates and additional materials was 16.0 kg and 6.0 kg, respectively, corresponding to 110 units.</i>	104
8.1	<i>Group velocity and refractive indices as stored in RAT, for a wavelength of 507 nm. The refractive indices for ultra-pure water and scintillator agree with [138, 139] respectively.</i>	129

# List of Figures

2.1	<i>Known particle masses and neutrino mass limits, assuming normal hierarchy [24].</i>	8
2.2	<i>Possible neutrino mass orderings for the normal and inverted hierarchies. The electron, muon and tau flavour fraction of each mass state are shown in the colours green, red and blue respectively.</i>	9
2.3	<i>Values of the nuclear matrix element, <math>M^{0\nu}</math>, for several double-beta decaying isotopes of experimental interest calculated with different methods: Nuclear Shell Model (NSM); Quasi-particle Random Phase Approximation (QRPA); Interacting Boson Model (IBM); Energy Density Functional (EDF); Projected Hartree-Fock-Bogoliubov model (PHFB). The error bars have no statistical meaning, but represent the range of values of <math>M^{0\nu}</math> in the corresponding model under variations of model parameters and treatment of interactions [26].</i>	14
2.4	<i>Generic energy spectrum showing the energy spectrum for two neutrino and neutrinoless double-beta decay [39].</i>	14
2.5	<i>Nuclear level structure decays for isotopes of atomic number 130 [44].</i>	17
2.6	<i>The effective Majorana neutrino mass <math>\langle m_{\beta\beta} \rangle</math> as a function of the lightest mass eigenstate, in the cases of normal and inverted hierarchy and the quasi-degenerate spectra. Taken from [26].</i>	18
2.7	<i>Left: The effective Majorana neutrino mass <math>\langle m_{\beta\beta} \rangle</math> as a function of the effective electron neutrino mass <math>m_\beta</math>, in the cases of normal and inverted hierarchy and the quasi-degenerate spectra. Right: The effective Majorana neutrino mass <math>\langle m_{\beta\beta} \rangle</math> as a function of the sum of neutrino masses, in the cases of normal and inverted hierarchy and the quasi-degenerate spectra. Both taken from [26].</i>	19
2.8	<i>The expected sensitivity as a function of live-time for 0.3% loading of Te [56].</i>	21

3.1	<i>Artist impression of the Sudbury Neutrino Observatory (National Geographic). The acrylic vessel is the centre volume in yellow, containing the target medium, and is surrounded by the (partially omitted to allow a view of the acrylic vessel) PMT support structure.</i>	23
3.2	<i>Stylised schematic of the SNO+ detector, roughly to scale. The Geodesic PSUP is shown in dark green, only the stainless steel struts are shown with PMTs removed for visibility. The hold-up and down ropes are shown in pink and red respectively. The AV is shown in bold blue. The thickness of all lines does not represent anything. The cavity, deck (with person) are shown in black [41].</i>	25
3.3	<i>The decay chain of <math>^{238}\text{U}</math>. All half-lives are shown, with the Q-values of beta and alpha decays in MeV, and gamma rays in keV [63].</i>	26
3.4	<i>Drawing showing the orientation of construction, PSUP, and true north. True North lies <math>49.58^\circ</math> east of PSUP north and <math>40.42^\circ</math> north of the electronics corridor [68].</i>	29
3.5	<i>A map of the PMT support structure with PSUP north and east marked, each of the numbered nodes are being used as injection points for the TELLIE system.</i>	30
3.6	<i>Flow diagram showing the SNO+ trigger system. PMT outputs are sent to the PMT interface card then the daughterboard, where the time and charge are calculated and read out by the front end card. The crate trigger card sums the triggers for individual crates and passes these to the analogue master trigger card, to sum hits for all crates. The digital master trigger card generates a global trigger, either because the sum crossed threshold, or an external trigger fired. Numbers in red are propagation delays and those in brackets are the values used in simulations, understanding these delays are important for any precision measurement or simulation. Details are provided in the text.</i>	32
3.7	<i>Left: Photograph of a whippetree used to support the AV hold-up ropes, the load cell is concealed within the centre of the base. Right: Photograph showing how the rope connects to the whippetree.</i>	34
3.8	<i>Left: The Acrylic Vessel as in SNO, showing the suspension ropes and belly plates. Right: A photograph of a belly plate on display in SNOLAB. A small length of rope can be seen looping through the u-shaped section, as the hold-up ropes do in SNO+.</i>	35
3.9	<i>Flow diagram showing how the loadcells connect to the DeltaV.</i>	36
3.10	<i>The installed rope net, as viewed from the base of the AV (with the author being lowered into the AV).</i>	37

3.11	<i>View from the base of the cavity, showing the rope net anchored to the cavity floor.</i>	38
3.12	<i>An overview of the SNO+ scintillator system, showing the continuous recirculation and filtration of the scintillator. Adapted from [79].</i>	41
3.13	<i><sup>222</sup>Rn activity as a function of time, in Kamland following the deployment of calibration sources [80]. Red and blue lines are the start of calibration runs.</i>	42
3.14	<i>Small pulses take longer to cross the discriminator threshold than large pulses, with respect to the centre of the peak. Adapted from [83].</i>	43
3.15	<i>Schematics of the SNO source manipulator system [87].</i>	45
3.16	<i>Sketch of the SNO+ detector showing the ELLIE calibration hardware on the top deck as well as an example of the light injection points around the PSUP.</i>	46
3.17	<i>Diagram of showing the basic function of the SNO+ Monte Carlo and data acquisition.</i>	48
4.1	<i>Total load of hold-up load cells (uncalibrated), during tensioning and rope net deployment on the 19-02-2012. The steps at 07:00 and 17:00 are due to tensioning. The slow rise a little after 15:00 is the rope net being lowered into place. Some fluctuation in total load is also evident prior to 15:00, as the legs of the hold-down net were lowered onto the vessel. The increase in load following tensioning is largely due to the response time of the load cells (of order an hour). Taken from [91].</i>	51
4.2	<i>Photograph showing corrosion to one of the pulleys of the equator-monitoring system.</i>	54
4.3	<i>The data extraction process from the DeltaV system.</i>	56
4.4	<i>Left: A typical data set for a period of tensioning, used to determine Hooke's constant through a straight line fit. The fit produced a gradient of <math>1.16 \times 10^5</math> in/lbs. Taken from [93]. Right: The variation in Hooke's constant over a five month period.</i>	57
4.5	<i>The FEA simulation of the maximum strain in the acrylic caused by the hold-down rope net during the normal working conditions. Maximum stresses predicted by FEA are localised inside the AV under the knots of the net. The units shown are relevant only to the FEA software used, the maximum corresponds to a value of 1.9 MPa. Taken from [97]</i>	58
5.1	<i>The absorption probability spectrum of <sup>130</sup>Te doped LAB and PPO (black), the average spectrum for all 96 LEDs (green), in arbitrary units, and the SNO+ PMT quantum efficiency (red)[101].</i>	62
5.2	<i>The absorption probability spectrum of <sup>150</sup>Nd doped LAB and PPO (black), the average spectrum for all 96 LEDs (purple), in arbitrary units, and the SNO+ PMT quantum efficiency (red)[101].</i>	63

5.3	<i>Approximation of a timing pulse as produced by TELLIE. The fit is a combination of two Gaussians with different sigmas for rising and falling edges . . . . .</i>	65
5.4	<i>A diagram showing how the injection angle is defined, based on [107]. . . . .</i>	66
5.5	<i>Total hit probabilities (both single and multiple photon hits) as a function of injected angle at 0.3% <math>^{130}\text{Te}</math> loading for pulse intensities of <math>10^3</math>, <math>10^4</math>, and <math>10^5</math> photons. The increased hit probability above <math>60^\circ</math> is due to scattering around the injection point and light reflected back from the near surface of the AV . . . . .</i>	67
5.6	<i>The Sussex single photon counting set-up used to measure the time profile of LED pulses. The TDC has a resolution of 25 ps. Adapted from [112]. . . . .</i>	72
5.7	<i>An ADC spectrum confirming the PMT is operating in single photon mode; the peak shows the trigger firing without a PMT signal, the shoulder to the right of the peak is the charge emitted upon detection of a single photon [112]. The units of the x axis is the ADC channel, proportional to integrated charge. . . . .</i>	73
5.8	<i>The original Kapustinsky LED driver, developed as a calibration source for scintillator detectors [98]. . . . .</i>	74
5.9	<i>A Kapustinsky LED driver modified for faster single pulses. . . . .</i>	76
5.10	<i>The time profile (TDC spectrum) for the Sussex driver with (red) and without (black) the clamping diode. The area of the pulses have been normalised, both pulses are of the same intensity: <math>10^3</math> photons. . . . .</i>	76
5.11	<i>The time profile for the Sussex driver at a pulse intensity of <math>10^3</math> photons per pulse, running at 10 kHz. For the measurement, the driver and LED were connected to the PMT via 0.5 m of optical fibre. . . . .</i>	77
5.12	<i>The time profile for the Sussex driver at a pulse intensity of <math>10^6</math> photons per pulse, running at 10 kHz. For the measurement, the driver and LED were connected to the PMT via 0.5 m of optical fibre. . . . .</i>	78
5.13	<i>The driver circuit based on the IXLDO2SI chip. Details of function are described in the text; here only the main components of the chip are shown, with the rest of the integrated circuit represented as grey boxes. . . . .</i>	80
5.14	<i>The voltages as measured at the anode (blue) and cathode (yellow) of the LED, the ringing is due to impedance miss matches at the probes. <math>I_{OP}</math> sets the maximum bias applied to LED (1); The Bias current <math>I_{BI}</math> sets the maximum length of time that the voltages at the anode and cathode of the LED can be inverted (2); <math>I_{PW}</math> sets the time that the voltages are inverted(3). . . . .</i>	81

5.15 <i>The time profile for the IXLD02SI driver at a pulse intensity of <math>10^3</math> photons per pulse, running at 10 kHz. For the measurement, the driver and LED were connected to the PMT via 45.75 m of optical fibre.</i>	84
5.16 <i>The time profile for the IXLD02SI driver at a pulse intensity of <math>10^6</math> photons per pulse, running at 10 kHz. For the measurement, the driver and LED were connected to the PMT via 45.75 m of optical fibre.</i>	84
6.1 <i>Left: Drilled LED with mounted optical fibre (ruler in cm). Right: Coupler containing LED and photodiode to monitor the number of photons at injection.</i>	89
6.2 <i>A schematic of the TELLIE driver box showing the basic connections to the control box and the position of the PIN diode boards monitoring LED output.</i>	90
6.3 <i>FWHM of the measured light pulses from all the 96 LED and driver combinations as a function of their photon output. The light pulses are measures after going through 45.75 m of optical fibre. The FWHM reported in this figure is larger than the true FWHM reported in Table 5.3 due to systematic errors from the response time of the PMT and readout of the oscilloscope. The true FWHM is lower due to systematic errors from the response time of the PMT and readout of the oscilloscope. The LED driver was operated at maximum current while varying the electrical pulse width to control the number of photons per pulse. The observed increase in optical pulse width as the intensity reaches <math>10^6</math> photons per pulse is due to the electrical pulse width for high intensities starts to exceed the modal time dispersion in the optical fibre.</i>	93
6.4 <i>Diagram of the scan setup used to perform timing and aperture profiles. The PMT is fixed on an automated arm with three-dimensional movement, and its window covered by a plate with a 1 mm diameter hole limiting the effective detecting area. The duplex fibre is fixed on a stand facing the PMT. A neutral density filter reduces its intensity so that the measurement can be operated in single photoelectron mode. In order to reduce backgrounds, the data acquisition requires a coincidence between the LED driver signal and the PMT output signal within a 50 ns window [122].</i>	95
6.5 <i>Time distribution of a light pulse emitted by the LED driver after going through the full length optical fibre, and a pulse measured from the driver box (without additional fibre). Both pulses are at the same driver setting (<math>10^3</math> photons after the fibre), with the pulses normalised to amplitudes. Despite the broadening of the pulse, it remains low enough to meet the SNO+ requirements.</i>	96

6.6	<i>Time distribution of the light pulses emitted by the LED driver after going through the full length optical fibre, at the central position (filled area) and at an angle corresponding to 11° in water (solid line). The time offset is common to both histograms, and both are normalised to their integrals.</i>	97
6.7	<i>Two dimensional angular emission profile of a fibre. The white area corresponds to zero intensity. The steps in x and y are fixed during the measurement, hence the variable angular resolution, ranging from 0.6° at the centre to 0.26° at the edges.</i>	98
6.8	<i>The interior of the dark box, showing the mounting of three 45 m fibres in front of the PMT and light guide with associated slit.</i>	99
6.9	<i>Comparison of independent measurements of the intensity profile of the fibre with respect to the angle in water: the black histogram is the profile of the detailed measurement with one fibre, from Figure 6.7; the coloured bands summarise the measurements of the full set of fibre cables. The yellow band shows the full spread and the green band represents the RMS, both over the total 220 fibres.</i>	100
6.10	<i>Illustration of a SNO+ PMT casing (hex cell) with a mount fitted for TELLIE fibres. The face hex cell is a little over 30 cm across.</i>	101
6.11	<i>Delays in a light calibration run. The control board must send out a light pulse and a trigger signal delayed by a predetermined time, to account for both the light propagation time in the fibre and in the detector on one hand, and in the PMTs and electronics on the other. The total light and signal time, from the emission to the acquisition of the data, is about 620 ns.</i>	106
6.12	<i>Left: 3D viewer display for a simulated high intensity light injection event inside the SNO+ detector. Each dot represents a PMT, and open circles represent PMTs on the far side of the detector as viewed. Right: The colour indicates the time at which the PMT triggered, according to the time histogram.</i>	108
6.13	<i>Left: An example of the discriminator walk effect in simulated light injection data. The data points with error bars correspond to an average evaluated in a given charge bin and used to interpolate the time-charge dependence. Right: simulated light injection data after applying the extracted time corrections. For a comparison with SNO data, see Fig. 3.2 of reference [83].</i>	111

6.14 Number of hits per event versus the cosine of the angle between PMT and fibre position for commissioning data (black, thick solid). The light grey band represents the region between minimum (simulation with $11^\circ$ opening angle and $9 \times 10^4$ photons per pulse) and maximum ( $13^\circ$ opening angle and $1.1 \times 10^5$ photons per pulse) hit probability. The direct and reflected light are detected around $\cos\theta = -1$ and 1 respectively. . . . .	112
6.15 An example of the PMT charge calibration constant extraction using low-intensity light injection data. The dashed (solid) lines show the position of the threshold, peak and high-half point from left to right for SNO (SNO+) data. . . . .	113
7.1 The SNO laserball and umbilical connection [87]. . . . .	116
7.2 Schematic of the SNO laserball system [129]. . . . .	117
7.3 Spectra of $N_2$ laser and dyes used in SNO [129]. . . . .	118
7.4 A prototype of the scintillator phase laserball, showing the main components without seals or shrouds. . . . .	120
7.5 A drawing of the scintillator phase laserball connection, showing how the main components of the connection fit together. . . . .	120
7.6 Left: A prototype LB illuminated with a laser diode, using an acrylic light guide. Right: A filled LB, for the DEAP-3600 dark matter experiment. . . . .	121
7.7 The fitted mask functions for the Monte Carlo generated SNO (green) and scintillator phase (blue) laserball designs, experimental data from SNO is also shown (red). . . . .	125
7.8 Monte Carlo simulation of the angular distribution of photons incident on the PMT photocathode that cause a successful hit [136]. . . . .	126
7.9 Angular distribution of photons incident on the PMT photocathode that cause a successful hit, showing only PMTs at least 6.5m above the equator [135]. The Monte Carlo generated mask functions for the scintillator phase (black) and SNO (blue) laserball designed were used [135]. This is for all LB positions. The peaks at $10^\circ$ and $35^\circ$ are due to the limits of range of motion in $z$ . The peak at $4^\circ$ is due to the laserball being positioned at the centre of the detector, it is non-zero because the PSUP is geodesic rather than a perfect sphere, which means that only a very small number of PMTs are actually inline with and perpendicular to the LB position. . . . .	127

8.1	<i>The refractive indices for water (black), acrylic (red) and scintillator (green) as stored in RAT. Adapted from [137].</i>	130
8.2	<i>Vector diagram used to calculate the light path between the injection and detection points, and subsequently, the time of flight.</i>	131
8.3	<i>The types of reflection for light injected from the PSUP: 1 - reflection from near AV surface, 2 - direct transmission, 3 - reflection from far AV surface, 4 - reflection around AV from PSUP, 5 - reflection of direct transmission, 6 - 35° reflection from PMT concentrator.</i>	133
8.4	<i>Time of detection for light injected at node 79, as a function of distance from the injection point. The types of reflection are highlighted with reference to the numbering system used in Figure 8.3. The earlier diagonal band between 5000 and 13000 mm is due to scattering from the AV. Prepulseing can be seen just before the direct transmission (2).</i>	134
8.5	<i>Dimensions (in cm) of the PMT and light concentrator housing. The PMT location as stored in RAT is marked in red: the centre of the front of the concentrator. Adapted from [57]</i>	136
8.6	<i>The hit times for a single PMT within the cut of distance from the injection point and the time window surrounding the expected time of flight. The spread is due to uncertainties described in Section 8.5.</i>	139
8.7	<i>Hit times for all PMTs within the 2.5 m distance cut from the injection point, The grouping of data is due to the structure of the PMT panels within the PSUP.</i>	140
8.8	<i>The residual of hit times (<math>t_{\text{measured}} - t_{\text{calculated}}</math>) for all PMTs within the 2.5 m.</i>	141
8.9	<i>The spread in residuals for the times of flight, centred at -0.03 ns with the AV at (0,0,0).</i>	141
8.10	<i>The spread in residuals for the times of flight, centred at 0.24 ns with the AV at (0,0,50) (mm).</i>	142
9.1	<i>The expected signal and BG for neutrinoless double-beta decay in SNO+ assuming 0.3% loading of tellurium, after five years of data taking. Taken from [56].</i>	145
9.2	<i>The reduced radial (defined as <math>R_{\text{reduced}} = (R/R_{AV})^3</math>) distributions for the external BG in the signal range for neutrinoless double beta decay from <math>^{130}\text{Te}</math>. The energy range is defined from 2.4 to 2.64 MeV. The distributions for <math>^{208}\text{Tl}</math> (left) and <math>^{214}\text{Bi}</math> (Right). The <math>^8\text{B}</math> solar flux is also shown for comparison. Taken from [146].</i>	146

9.3	<i>The number of <math>^{208}\text{Tl}</math> events from the hold-down ropes reconstructed within the FV as a function of AV position along the z-axis. The linear fit produced a gradient of <math>-0.16</math> events/mm . . . . .</i>	147
9.4	<i>The number BG events reconstructed in the FV, caused by <math>^{208}\text{Tl}</math> and <math>^{214}\text{Bi}</math> from the AV, as a function of AV position along the z-axis. The linear fit produced a gradient of <math>-7.9 \times 10^{-2}</math> events/mm. . . . .</i>	148
9.5	<i>The number BG events reconstructed in the FV, caused by <math>^{208}\text{Tl}</math> and <math>^{214}\text{Bi}</math> from the UPW, as a function of AV position along the z-axis. The linear fit produced a gradient of <math>-7.8 \times 10^{-3}</math> events/mm. . . . .</i>	148
9.6	<i>The number BG events reconstructed in the FV, caused by <math>^{208}\text{Tl}</math> from the hold-down ropes, UPW and AV as well as the <math>^{214}\text{Bi}</math> from the AV and the UPW, as a function of AV position along the z-axis. The linear fit produced a gradient of <math>-0.25</math> events/mm. . . . .</i>	149
9.7	<i>The number BG events reconstructed in the FV, caused by <math>^{208}\text{Tl}</math> from the hold-down ropes, UPW shielding and AV and the <math>^{214}\text{Bi}</math> from the AV and the UPW, as a function of the smearing of the reconstructed event radius. The plot has been fitted with a second order polynomial; the parameters were minimised to: <math>P_0 = 829.1</math>, <math>P_1 = 6.4 \times 10^{-5}</math> and <math>P_2 = 4.2 \times 10^{-4}</math>. . . . .</i>	150
9.8	<i>The reconstructed radius for 3 MeV electrons generated at the radius of the FV (3500 mm), with the PMT hit time spread by 0.5 ns. The mean of the fit is taken to be the reconstructed radius with <math>\sigma</math> describing the uncertainty. . . . .</i>	151
9.9	<i>The reconstructed radius of 3 MeV electrons simulated at the radius of the FV as function of the magnitude of an offset applied to PMT hit time, demonstrating the effect of an inaccurate timing calibration. . . . .</i>	152
9.10	<i>The limit on the neutrinoless double-beta decay life time as a function of the AV displacement along the z-axis. The linear fit produced a gradient of <math>2.7 \times 10^{23}</math> years/mm. . . . .</i>	153
9.11	<i>The limit on the neutrinoless double-beta decay life time as a function of the uncertainty in radius. The linear fit produced a gradient of <math>-7.4 \times 10^{22}</math> years/mm. . . . .</i>	154
B.1	<i>The dimensions of the SNO+ scintillator phase laserball flask. . . . .</i>	174
B.2	<i>Technical drawing of shroud for SNO+ scintillator phase laserball. . . . .</i>	175
B.3	<i>Technical drawing of clamps for SNO+ scintillator phase laserball. . . . .</i>	176
B.4	<i>Technical drawing of plug for SNO+ scintillator phase laserball. . . . .</i>	177
B.5	<i>Technical drawing of light guide shaft for SNO+ scintillator phase laserball. . . . .</i>	178
B.6	<i>Technical drawing of driver housing base for DEAP-3600 laserball. . . . .</i>	179

B.7	<i>Technical drawing of driver housing for DEAP-3600 laserball.</i>	180
B.8	<i>Technical drawing of driver housing cap for DEAP-3600 laserball.</i>	181
B.9	<i>Technical drawing of DEAP-3600 laserball assembly.</i>	182

# Chapter 1

## Introduction

Neutrinos provide a probe for physics beyond the standard model, and could explain the matter-antimatter asymmetry of the Universe and the problem of the undetermined fermion masses and mixing angles. They are also a powerful tool for investigating a broad range of physics topics such as: nuclear physics, the early Universe, supernovae explosions, and the interior of the Earth.

The Sudbury Neutrino Observatory (SNO) solved the solar neutrino problem in 2002 [1], implying neutrinos change flavour. This neutrino flavour change intrinsically confirmed that neutrinos have non-zero masses. The neutrino masses have yet to be directly measured, but upper limits have been set. Surprisingly, the upper limit of the heaviest neutrino mass is at least five orders of magnitude lower than the next lightest fermion; based on the third family quark and lepton masses, one might expect the third family neutrino mass to be in a similar mass range. In the Standard Model massive fermions are described by a Dirac mass term, however, this cannot explain the relative lightness of neutrinos. That is not to say the model is wrong, it was constructed around what was known and has proved extremely successful, parts are simply missing.

This suppression can be explained if a Majorana mass term is used with the Dirac term to describe neutrinos: the right-handed neutrinos are given a much larger mass, which has the effect of highly suppressing the left-handed neutrinos' mass.

Majorana particles have the interesting property of coinciding with their own antiparticle. Therefore, any interaction involving a Majorana particle has the potential to violate lepton number conservation, a symmetry unbroken within the Standard Model. Some cosmological models require violation of lepton number as a mechanism to create the observed

matter-antimatter asymmetry in the universe.

Currently the only known way to prove neutrinos are Majorana particles is through the observation of neutrinoless double-beta decay. Double-beta decay occurs in a few nuclei for which single beta decay is energetically forbidden. By violating lepton number conservation, the electron neutrino or anti-electron neutrino emitted in one of the two elementary beta decays forming the double-beta decay can be absorbed by the other, thus causing neutrinoless double-beta decay. The summed electron energy spectrum should be monochromatic since the recoil energy of a daughter nucleus is negligible and the sum of the energies of the two final state electrons should be equal to the total energy release.

SNO is being transformed into SNO+, with the main physics goal of addressing the question of whether neutrinos are Majorana particles, through the search for neutrinoless double-beta decay. The experiment will also be studying reactor, geo, supernovae and solar neutrinos. The transformation is characterised by the change in target mass: from heavy water to a novel scintillator mixture. The use of liquid scintillator generates more light per event and allows for more extensive filtration of soluble backgrounds, this lowers the threshold energy to the MeV range of rare nuclear decays.

To meet the requirements imposed by the physics on detector performance, a detailed optical calibration is needed. Due to the increased sensitivity to backgrounds introduced by deployed calibration sources, a new LED-based external calibration system has been developed, significantly reducing the need to deploy sources within the scintillator. The existing deployed laser-based calibration system has been modified to further reduce the possibility of introducing backgrounds.

This thesis describes the development and implementation of the LED and laser calibration systems and the use of the LED system to better define the fiducial volume and study how this affects the sensitivity to neutrinoless double-beta decay.

A more detailed motivation for the search for neutrinoless double-beta decay and the current status of measurements are described in Chapter 2.

The SNO+ detector will be described in-depth in Chapter 3, as well as introducing the requirements and constraints on the calibration system.

The additional detector support system required by the use of liquid scintillator will be presented along with its expected performance in Chapter 4. A motivation for the use of the timing calibration system, as a method of monitoring the support system's perform-

ance, will also be provided.

The selection of LEDs, based on the absorption spectrum of the scintillator and the wavelength dependent sensitivity of the detector will be described alongside the two candidate LED drivers developed for the calibration system in Chapter 5. The LED driver presented in this chapter is the first of its kind to be optimised for the new generation of low-resistance LEDs.

The LED-based calibration system will be introduced in its entirety in Chapter 6, with the selection criteria and performance of individual components summarised alongside the performance of the system during commissioning phases of the experiment.

The motivation for and development of a new laser-based calibration source will be discussed in Chapter 7; the manufacturing procedure for the source will be described in detail along with simulations of its expected improvement in performance.

The use of the LED-based calibration system, to measure the performance of the support system and its importance in accurately defining the fiducial volume will be described in Chapter 8.

The sensitivity to neutrinoless double-beta decay will be adversely effected by an uncertainty in the detector position due to uncertainties in the performance of the support system, as well as a reduction of the accuracy of the timing calibration. A study of these affects will be presented in Chapter 9.

## Chapter 2

# Theory and Experimental Background

This chapter provides a detailed motivation for the search for neutrinoless double-beta decay and gives the current status of measurements.

### 2.1 Short History of the Physics of Neutrinos

The neutrino was first proposed in 1930 by Pauli, in his letter to the Radioactive Ladies and Gentlemen of the Tubingen conference [2], as an explanation for the non-discrete spectrum of the beta decay. Pauli described an electronically neutral “neutron” emitted with the electron. Chadwick’s 1932 discovery of the neutron [3] and Perrin’s 1933 observations that Pauli’s “neutron” must be significantly less massive than the electron [4], led to Fermi’s description of the neutrino (little neutral one) in his 1934 theory of beta decay [5].

The neutrino was first detected by Reines and Cowan in 1956, through the observation of inverse beta decay caused by reactor antineutrinos,  $\bar{\nu} + p \rightarrow n + e^+$ . The antineutrinos interacted with protons in water, producing positrons, which annihilate quickly with electrons producing gammas and a neutron which is captured by cadmium nuclei, dissolved in the water, producing more gammas after a delay of 5  $\mu\text{s}$ . This allowed the use of the delayed coincidence to distinguish events from backgrounds [6].

In 1957 Goldhaber et al. used the inverse beta decays of samarium atoms via electron capture to measure the neutrino helicity, where the helicity is the projection of the spin on its momentum. It was found to be negative i.e. spin anti-parallel to the momentum [7].

The weak interaction only couples to left handed (LH) neutrinos and right handed (RH) antineutrinos so only LH neutrinos have been observed in nature. In the limit of a massless neutrino, LH neutrinos are equivalent to negative helicity neutrinos.

Lederman et al. discovered the muon neutrino in 1962 [8], demonstrating the doublet structure of the leptons.

Davis et al. measured the solar electron neutrino flux for the first time in 1968 [9]. The flux was found to be significantly less than that predicted by the solar models, giving rise to the solar neutrino problem.

In 1976 Perl et al. discovered the tau lepton through electron-positron annihilation, suggesting the existence of a third neutrino [10].

An atmospheric neutrino anomaly, similarly to the solar neutrino problem, was observed in 1988 by the IMB [11] and Kamiokande [12] experiments.

The total number of neutrino flavours, coupling to the weak force and with mass below half that of the Z boson, was measured experimentally from the width of the  $Z^0$  mass at LEP in 1989, and found to be consistent with three [13].

The atmospheric neutrino anomaly was solved by Super-Kamiokande in 1998, finding an energy and zenith angle dependent deficit of muon neutrinos, providing evidence for neutrino oscillations and implying a neutrino mass [14, 15].

Confirmation of the LEP prediction came in 2000, when the tau neutrino was observed at DONUT [16].

SNO solved the solar neutrino problem in 2002, measuring a deficit in the electron neutrino flux and no deficit in the total neutrino flux, implying flavour change of the electron neutrinos into muon or tau neutrinos [1]. This neutrino flavour change intrinsically confirmed that neutrinos have non-zero masses.

Recently, observations from T2K [17] and MINOS [18] as well as first direct measurements from the reactor experiments Double Chooz, Daya Bay and RENO [19, 20, 21, 22] have set a relatively large value for the mixing angle  $\theta_{13}$ , a non-zero value for which is required for CP violation in neutrino oscillations.

## 2.2 Neutrino Theory

Neutrinos are a fundamental Standard Model (SM) particle with neutral charge and one half spin. They exist as doublets with the charged leptons, in three distinct neutrino flavours,  $\nu_e$ ,  $\nu_\mu$ , and  $\nu_\tau$  along with their corresponding anti-neutrinos. Neutrinos interact only with the weak force and gravity, coupling the  $W^\pm$  and  $Z$  bosons to negative chirality neutrinos and positive chirality anti-neutrinos. In the SM neutrinos are massless, implying RH chiral neutrinos and left handed chiral anti-neutrons to be sterile if they exist.

### 2.2.1 Neutrino Oscillations

As a result of the SNO, Super-Kamiokande and other subsequent experiments' results, neutrinos are known to oscillate, change flavour and therefore have non-zero mass. The basic observation is that if neutrino are massive, their weak eigenstates do not coincide with their mass eigenstates. The mixing of weak and mass eigenstates can be described by [23]:

$$\nu_\alpha = \sum_{i=1}^3 U_{\alpha i} \nu_i, \quad \alpha \in \{e, \mu, \tau\}, \quad (2.1)$$

where the mass eigenstates are denoted  $\nu_i$  and  $U$  is a  $3 \times 3$  unitary Pontecorvo Maki Nakagawa Sakata (PMNS) leptonic mixing matrix. The PMNS matrix can be parameterised in terms of 6 parameters: 3 mixing angles  $\theta_{12}, \theta_{13}, \theta_{23}$  and 3 phases  $\delta, \phi_1, \phi_2$ . A standard parametrisation is then given by:

$$U = \begin{pmatrix} c_{12}c_{13} & s_{12}c_{13} & s_{13}e^{-i\delta} \\ -s_{12}c_{23} - c_{12}s_{23}s_{13}e^{i\delta} & c_{12}c_{23} - s_{12}s_{23}s_{13}e^{i\delta} & s_{23}c_{13} \\ s_{12}s_{23} - c_{12}c_{23}s_{13}e^{i\delta} & -c_{12}s_{23} - s_{12}c_{23}s_{13}e^{i\delta} & c_{23}c_{13} \end{pmatrix} \cdot \text{diag}(e^{i\phi_1}, e^{i\phi_2}, 1), \quad (2.2)$$

where  $s_{ij} = \sin \theta_{ij}$  and  $c_{ij} = \cos \theta_{ij}$ . This parameterisation is basically the same as the CKM matrix, except for the additional Majorana phases  $\phi_1$  and  $\phi_2$ , whose inclusion will be explained below. These phases signal that neutrino masses can be described in a different manner than other massive fermions.

Consider an ultra-relativistic neutrino state produced at time  $t = 0$  in the flavour  $\alpha$ . At time  $t$  it will have evolved as:

$$|\nu_\alpha(t)\rangle = \sum_{i=1}^3 U_{\alpha i}^* |\nu_i(t)\rangle, \quad (2.3)$$

with the probability of oscillating into a  $\beta$  neutrino given by

$$P_{\alpha\beta} = |\langle \nu_\beta | \nu_\alpha(t) \rangle|^2 = \left| \sum_{i,j} U_{\alpha i}^* U_{\beta j} \langle \nu_j | \nu_i(t) \rangle \right|^2. \quad (2.4)$$

Using the standard plane wave approximation

$$|\nu_i(t)\rangle = e^{-iE_i t} |\nu_i(0)\rangle, \quad (2.5)$$

the ultra-relativistic approximation

$$E_i = \sqrt{p^2 + m_i^2} \approx p + \frac{m_i^2}{2E}, \quad (2.6)$$

and the orthonormality condition  $\langle \nu_i | \nu_j \rangle = \delta_{i,j}$ , the probability of neutrino oscillation in a vacuum is given by:

$$\begin{aligned} P_{\alpha\beta} &= \delta_{\alpha\beta} - 4 \sum_{i < j}^{1,3} \Re [U_{\alpha i} U_{\beta i}^* U_{\alpha j}^* U_{\beta j}] \sin^2 \left( \pi \frac{L}{L_{ij}^0} \right) \\ &\quad + 2 \sum_{i < j}^{1,3} \Im [U_{\alpha i} U_{\beta i}^* U_{\alpha j}^* U_{\beta j}] \sin \left( \pi \frac{L}{L_{ij}^0} \right), \end{aligned} \quad (2.7)$$

where

$$L_{ij}^0 = \frac{4\pi}{\Delta m_{ij}^2} \approx 2.48 \text{ km} \frac{E(\text{GeV})}{\Delta m_{ij}^2 (\text{eV}^2)}, \quad \Delta m_{ij}^2 = m_j^2 - m_i^2, \quad (2.8)$$

are the oscillation lengths in vacuum. If  $L \ll L_{ij}^0$  for any  $i, j$  then oscillations do not have enough time to develop and  $P_{\alpha\beta} \approx \delta_{\alpha\beta}$ . Conversely, if  $L \gg L_{ij}^0$  then so many oscillations occur that only an averaged oscillation probability can be measured. The maximum sensitivity to  $\Delta m_{ij}^2$  occurs when  $L \approx L_{ij}^0$ , i.e. when  $E/L \approx \Delta m_{ij}^2$ .

Equation 2.7 shows that neutrinos oscillate only if they are massive and  $\Delta m_{ij}^2 \neq 0$ . It also shows that neutrino oscillations are not sensitive to Majorana phases, as they cancel. This cancellation has to happen since the Majorana phases arise when a Majorana mass term

that violates lepton number conservation is included, while neutrino oscillations conserve lepton number. It should also be noted that the sum of the imaginary components is CP violating, since it has opposite sign for neutrinos and anti-neutrinos.

The PMNS matrix can be rewritten as:

$$U = \begin{pmatrix} 1 & 0 & 0 \\ 0 & c_{23} & s_{23} \\ 0 & -s_{23} & c_{23} \end{pmatrix} \cdot \begin{pmatrix} c_{13} & 0 & s_{13}e^{-i\delta} \\ 0 & 1 & 0 \\ -s_{13}e^{i\delta} & 0 & c_{13} \end{pmatrix} \cdot \begin{pmatrix} c_{12} & s_{12} & 0 \\ -s_{12} & c_{12} & 0 \\ 0 & 0 & 1 \end{pmatrix} \cdot \text{diag}(e^{i\phi_1}, e^{i\phi_2}, 1), \quad (2.9)$$

where the first matrix can be tested by atmospheric and long baseline neutrino oscillations. The second matrix can be tested by reactor and long baseline neutrino oscillations. The third matrix can be tested in solar and reactor neutrino oscillations. The Majorana phases cannot be tested by neutrino oscillations, the only known test is through neutrinoless double-beta decays.

## 2.3 Neutrino Masses

As mentioned, neutrino oscillations are only possible if they are massive and  $\Delta m_{ij}^2 \neq 0$ . The neutrino masses have yet to be directly measured, but upper limits have been set. Surprisingly, the upper limit of the heaviest neutrino mass is five orders of magnitude lower than the next lightest fermion, see Figure 2.1.

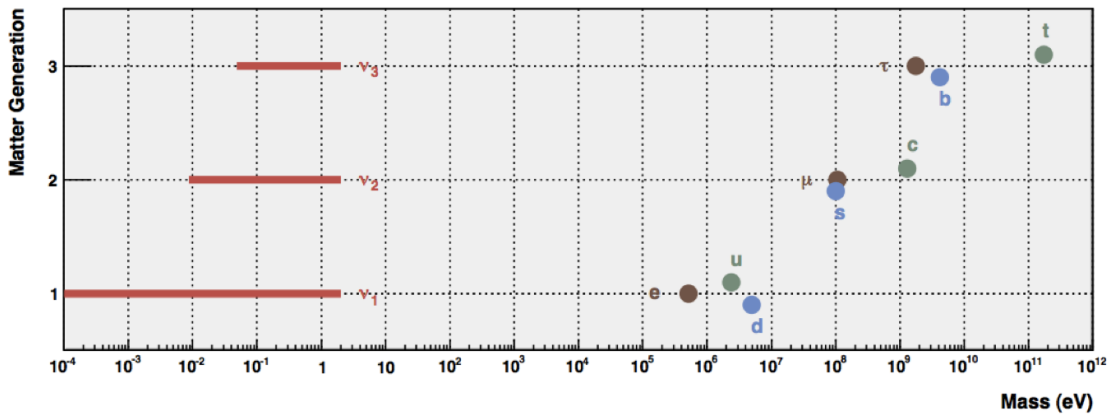


Figure 2.1: Known particle masses and neutrino mass limits, assuming normal hierarchy [24].

Neutrino phenomenology implies that the neutrino mass spectrum is formed by a doublet of relatively close states and by a third lone neutrino state, which may be either heavier than

the doublet - normal hierarchy (NH), or lighter - inverted hierarchy (IH), see Figure 2.2. The lightest neutrino in the doublet is labeled  $\nu_1$  and the heaviest  $\nu_2$ , their squared mass difference is:

$$\delta m^2 = m_2^2 - m_1^2 > 0. \quad (2.10)$$

The lone state is labeled  $\nu_3$ , and the sign of  $m_3^2 - m_{1,2}^2$  distinguishes NH from IH. Defining the second independent squared mass difference  $\Delta m^2$  as:

$$\Delta m^2 = \left| m_3^2 - \frac{m_1^2 + m_2^2}{2} \right|, \quad (2.11)$$

avoids complication arising from changes in hierarchies if  $\Delta m^2$  was given as  $m_3^2 - m_1^2$  or  $m_3^2 - m_2^2$ . Using Equation 2.11, the hierarchies are simply related by the transformation  $+\Delta m^2 \rightarrow -\Delta m^2$  [25].

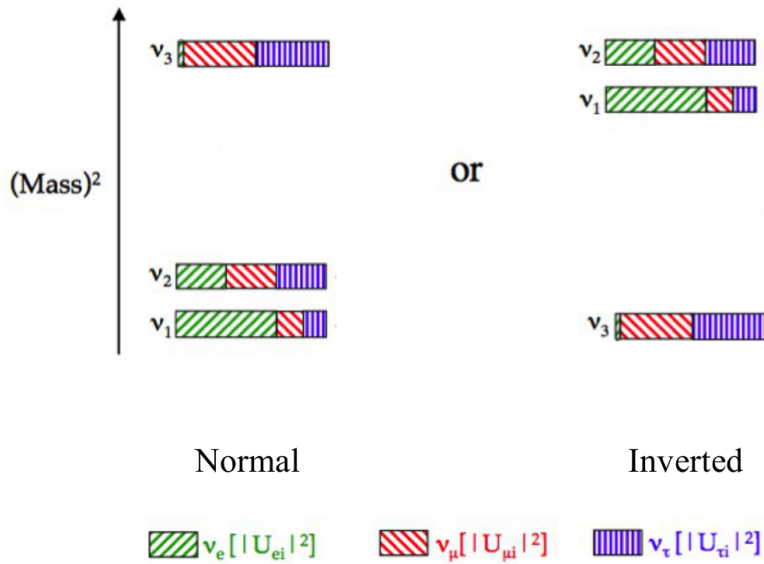


Figure 2.2: Possible neutrino mass orderings for the normal and inverted hierarchies. The electron, muon and tau flavour fraction of each mass state are shown in the colours green, red and blue respectively.

There is the possibility of a quasi-degenerate (QD) for both NH and IH where [26]:

$$(NH) \quad m_1 \lesssim m_2 \lesssim m_3 \simeq m_\nu^{\text{QD}} \quad (2.12)$$

$$(IH) \quad m_3 \lesssim m_1 \lesssim m_2 \simeq m_\nu^{\text{QD}} \quad (2.13)$$

### 2.3.1 Oscillation Limits

Oscillations measurements cannot probe neutrino masses directly, but as has been shown they are sensitive to differences in the squared masses. Observed oscillation frequencies are governed by the two aforementioned differences in the squared masses  $\delta m^2$  and  $\Delta m^2$ . The current best values for the neutrino mass differences, based on a global fit of available data taken from [27], are shown along with the other oscillation parameters in Table 2.1.

Parameter	Best Fit	$1\sigma$ Range	$2\sigma$ Range	$3\sigma$ Range
$\delta m^2/10^{-5} \text{ eV}^2$ (NH or IH)	7.54	7.32-7.80	7.15-8.00	6.99-8.18
$\sin^2\theta_{12}/10^{-1}$ (NH or IH)	3.08	2.91-3.25	2.75-3.42	2.59-3.59
$\Delta m^2/10^{-3} \text{ eV}^2$ (NH)	2.43	2.37-2.49	2.30-2.55	2.23-2.61
$\Delta m^2/10^{-3} \text{ eV}^2$ (IH)	2.38	2.32-2.44	2.25-2.50	2.19-2.56
$\sin^2\theta_{13}/10^{-2}$ (NH)	2.34	2.15-2.54	1.95-2.74	1.76-2.95
$\sin^2\theta_{13}/10^{-2}$ (IH)	2.40	2.18-2.59	1.98-2.79	1.78-2.98
$\sin^2\theta_{23}/10^{-1}$ (NH)	4.37	4.14-4.70	3.93-5.52	3.74-6.26
$\sin^2\theta_{23}/10^{-1}$ (IH)	4.55	4.24-5.94	4.00-6.20	3.80-6.41

Table 2.1: *Results of global three neutrino oscillation analysis [27], for normal and inverted hierarchies.*

Due to the uncertainties on the mass differences, it is not possible to determine the hierarchy of the neutrino masses.

### 2.3.2 Beta Decay Limits

The most direct way to probe neutrino mass is the measurement of beta decay spectrum endpoints. The shape of the spectrum at the endpoint is dependent upon the neutrino mass. The measurements' spectroscopic resolving power is  $E/\Delta E$ , making a low end point decay energy desirable. Tritium is the isotope of choice, with an endpoint of 18.6 keV, and relatively simple structure that further reduces uncertainties due to nuclear and atomic effects.

The current best limit of  $\nu_e$  mass is  $< 2$  eV, from the Mainz [28] and Troitsk [29] experiments. The KATRIN experiment is nearing completion, and expects to set a limit of  $< 0.2$  eV [30].

### 2.3.3 Cosmological Limits

Neutrinos are the second most numerous particle in the universe after photons. A massive neutrino would therefore have a noticeable effect on the large-scale structure of the universe, detectable through observations of the Cosmic Microwave Background (CMB) and Baryon Acoustic Oscillations (BAO).

Planck has placed further constraints on the number of neutrino flavours and the sum of neutrino masses using BAO and CMB data. They found no evidence for additional neutrino-like relativistic particles beyond the three families of neutrinos in the SM, with  $N_{\text{eff}} = 3.30 \pm 0.27$  for the effective number of relativistic degrees of freedom, and an upper limit of 0.23 eV for the sum of neutrino masses [31].

## 2.4 Majorana Neutrinos

It has been demonstrated that neutrinos are massive and their masses are surprisingly suppressed relative to other fermions.

In the SM, charged massive fermions are described by a Dirac mass term to preserve quantum numbers like charge through particle antiparticle interactions. The SM could be extended to describe neutrinos by introducing RH neutrinos and a Yukawa interaction term for them; after electroweak symmetry breaking a Dirac mass term is generated. However, this does not explain the suppression of neutrino masses.

The introduction of RH neutrinos does allow of an additional mass term for neutrinos, the Majorana mass term. The suppression of neutrino masses can be explained if a Majorana mass term is used with the Dirac term to describe neutrinos.

Adding one RH neutrino per fermion generation restores the quark-lepton symmetry. RH neutrinos can have the usual Yukawa couplings to lepton doublets plus a bare Majorana mass. After electroweak symmetry breaking, the neutrino mass term addition to the SM Lagrangian can be written as:

$$-\mathcal{L}_m^\nu = \frac{1}{2} \left[ \begin{pmatrix} \bar{\nu}_L^c & \bar{\nu}_R \end{pmatrix} \begin{pmatrix} 0 & m_D^T \\ m_D & M \end{pmatrix} \begin{pmatrix} \nu_L \\ \nu_R^c \end{pmatrix} \right] + h.c., \quad (2.14)$$

where  $m_D$  is the Dirac matrix and  $M$  the Majorana matrix. Masses and mass eigenstates are found by diagonalising the matrix:

$$\mathcal{M}_\nu = \begin{pmatrix} 0 & m_D^T \\ m_D & M \end{pmatrix}, \quad (2.15)$$

for  $m_D = 0$  the Majorana case is recovered, while for  $M = 0$  the Dirac case is recovered. The most interesting situation is  $M \gg m_D$ , the seesaw limit: consider the 1 generation case. In this case  $m_D$  and  $M$  are just numbers and  $\mathcal{M}$  is a  $(2 \times 2)$  matrix with eigenvalues  $\lambda$  given as:

$$\lambda_\pm = \frac{M}{2} \pm \frac{M}{2} \sqrt{1 + 4 \frac{m_D^2}{M^2}} \approx \frac{M}{2} \pm \frac{M}{2} \left( 1 + 2 \frac{m_D^2}{M^2} \right), \quad (2.16)$$

giving:

$$\lambda_+ = M_{heavy} \approx M \quad \text{and} \quad \lambda_- = -m_\nu \approx -\frac{m_D^2}{M}. \quad (2.17)$$

The positive eigenvalue corresponds to the mass of a new very heavy neutrino predicted by the seesaw mechanism while the negative eigenvalue would correspond to (minus) the mass of the ordinary light neutrino that is in this way suppressed of a factor  $m_D/M$  compared to the Dirac neutrino mass. RH neutrinos are given a much larger mass, which has the effect of highly suppressing the LH neutrinos' mass.

Furthermore, Majorana particles have the interesting property that the charge conjugate of a Majorana field coincides with itself up to a phase factor:

$$\psi^c = e^{-i\phi} \psi, \quad (2.18)$$

and are therefore genuinely neutral, since they coincide with their own antiparticle. That is to say, any interaction involving a Majorana particle has the potential to violate lepton number conservation, a symmetry unbroken within the SM. Some cosmological models require violation of lepton number as a mechanism to meet the Sakharov conditions [32] and create the observed matter-antimatter asymmetry in the universe.

## 2.5 Neutrinoless Double-Beta Decay

Currently the only way to prove neutrinos are Majorana particles is through the observation of neutrinoless double-beta decay. Double-beta decay occurs in a few nuclei for which single beta decay is energetically forbidden or strongly suppressed due to too large a change in spin. By violating lepton number conservation by two units, the  $\nu_e$  or  $\bar{\nu}_e$  emitted in one of the two elementary beta decays forming the double-beta decay can be absorbed by the other, thus causing neutrinoless double-beta decay. Neutrinoless double-beta decays violate not only lepton number but there also has to be a helicity flip since the absorbed  $\nu_e$  or  $\bar{\nu}_e$  has a wrong helicity, this is only possible if neutrinos have a non-vanishing Majorana mass. The decay rate of the process is therefore proportional to neutrino masses [33], the half-life can be expressed as:

$$(T_{1/2}^{0\nu})^{-1} = G^{0\nu} |M^{0\nu}|^2 \left( \frac{\langle m_{\beta\beta} \rangle}{m_e} \right)^2, \quad \langle m_{\beta\beta} \rangle = \left| \sum_{i=1}^3 U_{ei}^2 m_i \right|, \quad (2.19)$$

where  $G^{0\nu}$  is the decay phase space factor dependent of the Q-value of the transition and the atomic number,  $M^{0\nu}$  is the nuclear matrix element of the selected isotope,  $m_e$  the electron mass,  $U_{ei}^2$  as the PMNS matrix elements containing the electron neutrino,  $m_i$  the mass of the neutrino eigenstate and  $m_{\beta\beta}$  is the effective Majorana neutrino mass.

$M^{0\nu}$  gives the transition rate of the interaction within the nucleus.  $M^{0\nu}$  cannot be directly measured, it has to be calculated from a complicated many-body nuclear problem [26]. Its value depends upon the model used and assumptions made to calculate it. Five different methods have been used for the calculation: Nuclear Shell Model (NSM) [34], Quasi-particle Random Phase Approximation (QRPA) [35], Interacting Boson Model (IBM) [36], Energy Density Functional (EDF) [37] and Projected Hartree-Fock-Bogoliubov approach (PHFB) [38]. Figure 2.3 shows recent values of  $M^{0\nu}$  calculated with these methods, the error bars do not have a statistical meaning as theoretical calculations are not random events, but rather they represent the range of  $M^{0\nu}$  in the corresponding model under variations of parameters and treatment of interactions. The range of values of  $M^{0\nu}$  for each isotope have large theoretical uncertainties, which are problematic for any neutrinoless double-beta decay measurement. Therefore, the search for neutrinoless double-beta decay must use a variety of isotopes, as multiple isotopes are required in order to factor out the theoretical uncertainty on  $M^{0\nu}$ .

The summed electron energy spectrum should be monochromatic since the recoil energy of

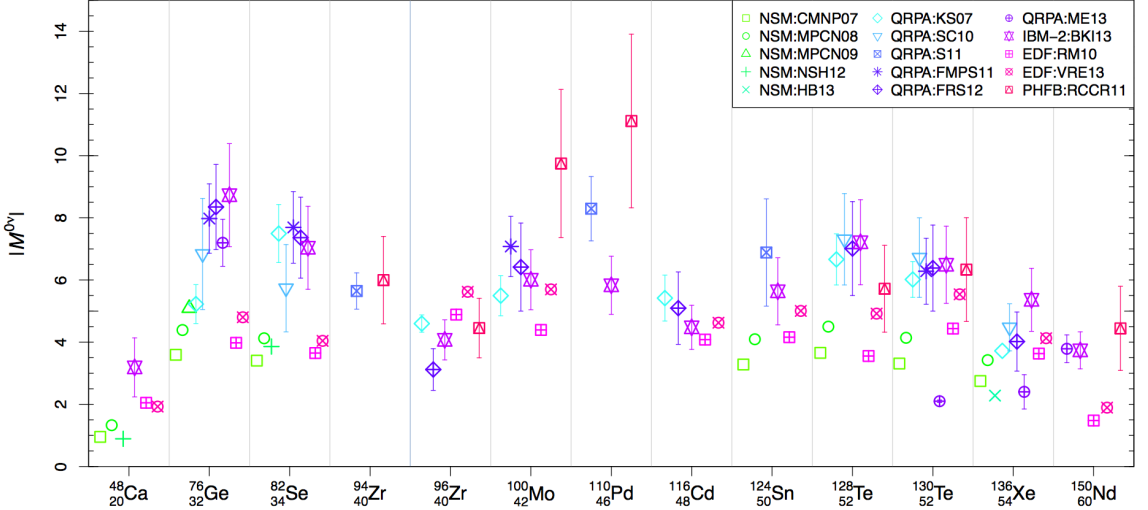


Figure 2.3: Values of the nuclear matrix element,  $M^{0\nu}$ , for several double-beta decaying isotopes of experimental interest calculated with different methods: Nuclear Shell Model (NSM); Quasi-particle Random Phase Approximation (QRPA); Interacting Boson Model (IBM); Energy Density Functional (EDF); Projected Hartree-Fock-Bogoliubov model (PHFB). The error bars have no statistical meaning, but represent the range of values of  $M^{0\nu}$  in the corresponding model under variations of model parameters and treatment of interactions [26].

a daughter nucleus is negligible and, the sum of the energies of the two final state electrons should be equal to the total energy release. Figure 2.4 shows the idealised spectrum.

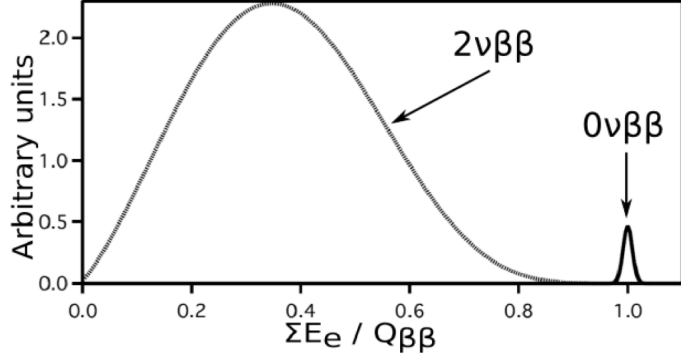


Figure 2.4: Generic energy spectrum showing the energy spectrum for two neutrino and neutrinoless double-beta decay [39].

The half-life in case of no background is given by the radioactive decay law [40], assuming the live time  $t$  to be much less than the half-life. The half-life is given by:

$$T_{1/2}^{0\nu} = \frac{Mt \ln 2}{N_{\beta\beta} A}, \quad (2.20)$$

where  $M$  is the isotope mass,  $N_{\beta\beta}$  is the number of neutrinoless double-beta decay events and  $A$  is the atomic mass number. In the background limiting case  $N_{\beta\beta} \approx \sqrt{B}$ , where  $B$  is the background index. The half-life becomes:

$$T_{1/2}^{0\nu} \propto \frac{Mt \ln 2}{\sqrt{BA}}, \quad (2.21)$$

There are two possible background limiting cases, in the one case  $B$  is dominated by a single background, such as  ${}^8\text{B}$  for SNO+, and is therefore proportional only to the live-time and energy resolution; assuming  $B = t\Delta E$  then the half-life can be expressed as:

$$T_{1/2}^{0\nu} \propto \frac{M\sqrt{t}}{\sqrt{\Delta E}}. \quad (2.22)$$

In the other case,  $B$  is proportional to the energy resolution, live time and isotope mass; assuming  $B = Mt\Delta E$ , where  $\Delta E$  is the energy resolution, the half-life can be expressed as [41]:

$$T_{1/2}^{0\nu} \propto \sqrt{\frac{Mt}{\Delta E}}. \quad (2.23)$$

This case is true for most experiments, where the number of background events is proportional to the isotope mass. For this case, the sensitivity to  $m_{\beta\beta}$  scales with isotope mass as:

$$m_{\beta\beta} \propto M^{-\frac{1}{4}}. \quad (2.24)$$

However, for experiments like SNO+, where the dominant background is independent of isotope mass, the second case is true and the sensitivity to  $m_{\beta\beta}$  scales with isotope mass as:

$$m_{\beta\beta} \propto M^{-\frac{1}{2}}. \quad (2.25)$$

Hence, the most crucial parameters are a high isotope abundance, and the energy resolution should be as good as possible to concentrate the few expected events in a small region. Ideally any experiment should be background free.

There are 35 naturally occurring isotopes for which double-beta decay is observable. However, as the decay rate of neutrinoless double-beta decay scales with  $Q^5$  only the eleven

isotopes with Q-values beyond 2 MeV are considered for experimental searches.  $^{130}\text{Te}$  is one of these eleven, and has been selected for SNO+.  $^{130}\text{Te}$  has a recommended double-beta decay lifetime of  $6.9 \pm 1.3 \times 10^{20}$  yr [42], based on measurements from NEMO-3 [43] and others. The nuclear level structure diagram of the double-beta decay of  $^{130}\text{Te}$  to  $^{130}\text{Xe}$  is shown in Figure 2.5.

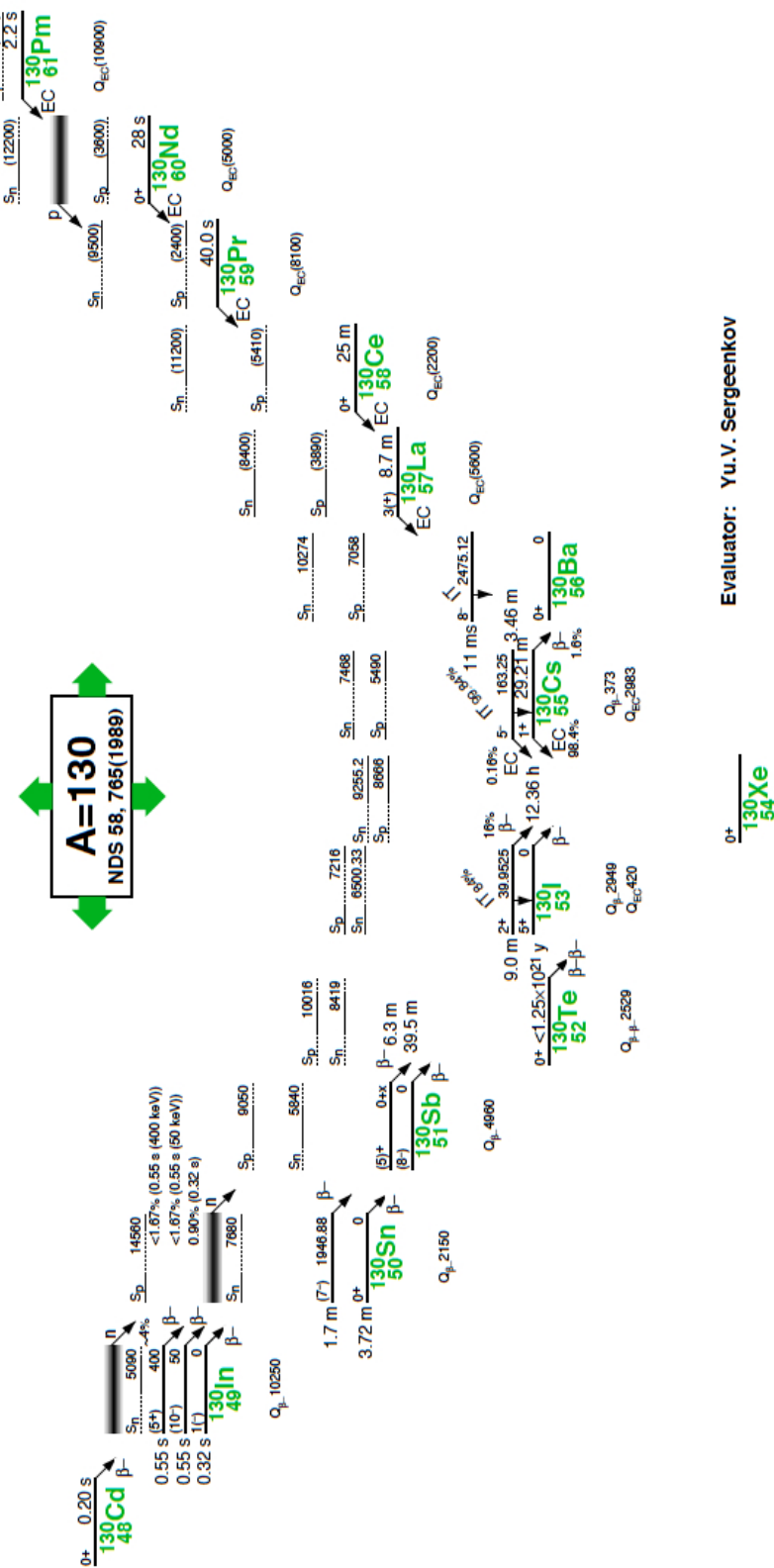


Figure 2.5: Nuclear level structure decays for isotopes of atomic number 130 [44].

### 2.5.1 Double-Beta Decay and Oscillations

Equation 2.19 shows that the effective Majorana neutrino mass  $\langle m_{\beta\beta} \rangle$  depends on the neutrino oscillation parameters, and can therefore be expressed as [26]:

$$\langle m_{\beta\beta} \rangle = |c_{13}^2 c_{12}^2 e^{2i\phi_1} m_1 + c_{13}^2 s_{12}^2 e^{2i\phi_2} m_2 + s_{13}^2 m_3|. \quad (2.26)$$

Using the values shown in Table 2.1,  $\langle m_{\beta\beta} \rangle$  can now be plotted as a function of the lightest neutrino mass  $m_{min} = m_1$  in the NH and  $m_{min} = m_3$  in the IH, as shown in Figure 2.6, using Equations 2.10 and 2.11.

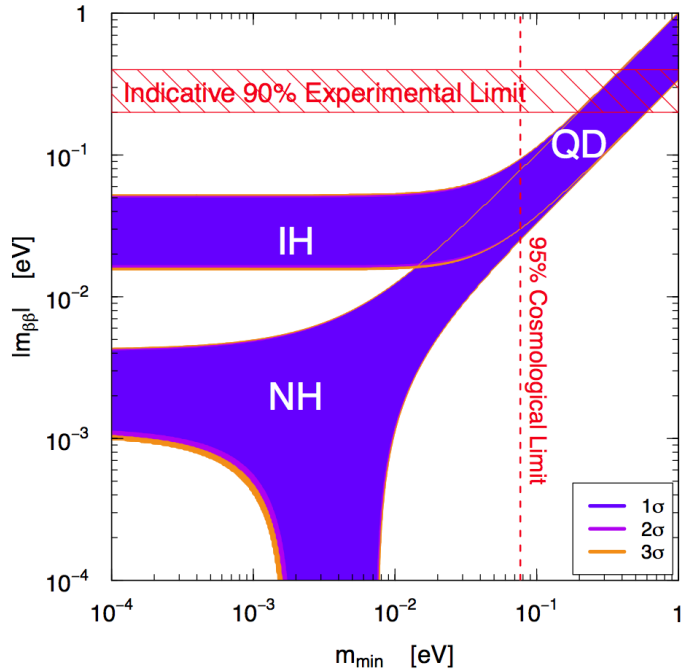


Figure 2.6: The effective Majorana neutrino mass  $\langle m_{\beta\beta} \rangle$  as a function of the lightest mass eigenstate, in the cases of normal and inverted hierarchy and the quasi-degenerate spectra. Taken from [26].

The largeness of the allowed bands are mainly due to the unknown values of the Majorana phases  $\phi_1$  and  $\phi_2$ , which can cause significant cancellations between the contributions to  $\langle m_{\beta\beta} \rangle$  [26]. Figure 2.6 shows that a complete cancellation is not possible in the case of an IH, where  $\langle m_{\beta\beta} \rangle$  is bounded to be larger than about  $2 \times 10^{-2}$  eV. In the NH a complete cancellation is not possible in the QD region, but it is possible in the NH region for  $m_{min} = m_1$  between  $2 \times 10^{-3}$  and  $7 \times 10^{-3}$  eV. The lower bound on  $\langle m_{\beta\beta} \rangle$  of about  $2 \times 10^{-2}$  eV in the IH is encouraging for neutrinoless double-beta decay searches aiming to measure if neutrino masses are IH, or, excluding the IH if no signal is observed. However,

IH can only be determined if it is independently established that  $m_{min} \lesssim 10^{-2}$  eV. If not, the neutrino mass spectrum can be either NH or IH, with nearly QD masses.

$m_{min}$  is difficult to measure directly and as mentioned the current measurements of neutrino masses are those of the effective electron neutrino mass  $m_\beta$  in beta decay experiments and through the measurements of the sum of neutrino masses  $\sum_{k=1}^3 m_k$  in cosmological experiments. Hence, it is useful to plot  $\langle m_{\beta\beta} \rangle$  as a function  $m_\beta$  and  $\sum_{k=1}^3 m_k$ , as shown in Figures 2.7(a) and 2.7(b) respectively.

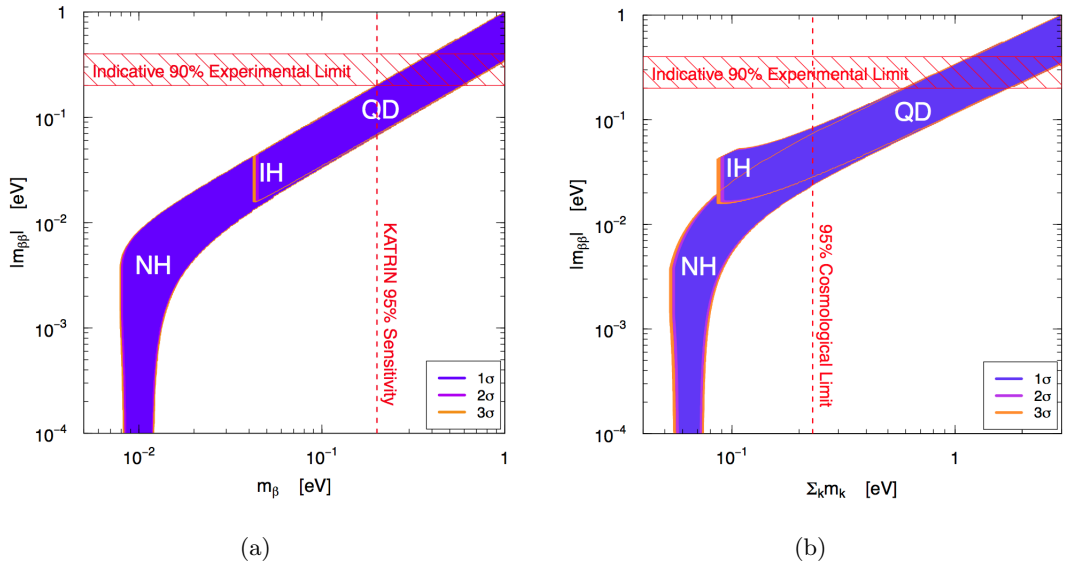


Figure 2.7: Left: The effective Majorana neutrino mass  $\langle m_{\beta\beta} \rangle$  as a function of the effective electron neutrino mass  $m_\beta$ , in the cases of normal and inverted hierarchy and the quasi-degenerate spectra. Right: The effective Majorana neutrino mass  $\langle m_{\beta\beta} \rangle$  as a function of the sum of neutrino masses, in the cases of normal and inverted hierarchy and the quasi-degenerate spectra. Both taken from [26].

The allowed regions in the NH and IH spectra have large overlaps. Therefore, if  $\langle m_{\beta\beta} \rangle$  is found to be larger than about  $2 \times 10^{-2}$  eV it may be difficult to distinguish the normal and inverted spectra with absolute neutrino mass measurements.

To summarise, in units normally used to describe the sensitivity of neutrinoless double-beta decay experiments: the IH covers a range between about 20 to 50 meV and the NH is in the region below 10 meV. Half-lives for the IH are in the region beyond  $10^{26}$  years while half-lives in the NH go up to well beyond  $10^{28}$  years [40].

## 2.6 Experimental Status

Measurements of these extremely long half-lives are non-trivial. There are currently no direct measurements of  $\langle m_{\beta\beta} \rangle$ . However, upper limits on  $\langle m_{\beta\beta} \rangle$  have been set. The scaling of signal with isotope mass in Equation 2.22 and 2.23 is the reason why almost all next generation experiments are using enriched materials.

There was a claimed observation of neutrinoless double-beta decay in  $^{76}\text{Ge}$  by some members of the Heidelberg-Moscow collaboration [45]. However, this has been directly ruled out by GERDA [46]. GERDA is based on Ge-semiconductors consisting of Ge-crystals enriched in  $^{76}\text{Ge}$ . The crystals are submerged in liquid Ar, for shielding and cooling. In a first phase, the enriched detectors from the Heidelberg-Moscow experiment and others (IGEX) were used, with a total mass of 17.7 kg. Data taking started November of 2011, no signal was found to support the claim [47].

Due to the relatively low enrichment costs for noble gases, there are two large scale experiments based on enriched  $^{136}\text{Xe}$ . EXO-200 is using about 175 kg liquid Xe in form of a Time Projection Chamber (TPC). EXO-200 provided a limit of  $1.1 \times 10^{25}$  years at a 90% CL [48]. KamLAND-Zen is reusing the KamLAND infrastructure, with a specially designed balloon of Xe-loaded liquid scintillator deployed within the detector. The balloon is filled with roughly 330 kg of enriched Xe. Data taking started in September of 2011, and a lower limit of  $1.9 \times 10^{25}$  years at a 90% CL has been set [49].

NEMO3 used thin foils of enriched  $^{100}\text{Mo}$  and  $^{82}\text{Se}$  within a cylindrical tracking detector, achieving limits of  $1.1 \times 10^{24}$  [50] and  $3.2 \times 10^{23}$  [51] years respectively. NEMO is being replaced by SuperNEMO, using the same technique with 20 modular planar trackers, with the aim of achieving a lifetime limit of  $10^{26}$  years and a mass sensitivity in the range of 50 meV. Each module houses 5 kg of  $^{82}\text{Se}$  and has a fiducial area of  $15 \text{ m}^2$  [52]. The first model is currently under construction and is due to start taking data as demonstrator in 2016.

CUORE is a 741 kg array of  $\text{TeO}_2$  bolometers. The detector is nearing completion, and will start taking data in 2015. If target backgrounds are reached, a  $1\sigma$  half life sensitivity of  $10^{26}$  years is expected after five years of data taking [53]. CUORE-0 is a demonstrator module for CUORE, with 52 750 g bolometers, corresponding to roughly 11 kg of  $^{130}\text{Te}$ , using the CUORICINO infrastructure [54]. CUORE-0 started taking data in spring 2013, with results published in spring 2015, a median lower-limit sensitivity of  $2.9 \times 10^{24}$  years at

90% CL surpassed the sensitivity of Cuoricino. No evidence for neutrinoless double-beta decay of  $^{130}\text{Te}$  was found, a Bayesian lower bound on the decay half-life,  $T_{1/2}^{0\nu} > 2.7 \times 10^{24}$  years at 90% CL was set. By combining CUORE-0 data with Cuoricino data the most stringent lower-limit to date was obtained as  $T_{1/2}^{0\nu} > 4.0 \times 10^{24}$  years at 90% CL [55].

SNO+ is reusing the SNO infrastructure, filling the detector with Te-doped liquid scintillator. The expected sensitivity for the initial phase of 0.3% Te loaded scintillator is shown in Figure 2.8, this assumes that cosmogenically induced backgrounds can be reduced to negligible levels and that external backgrounds can be reduced through a conservative fiducial volume (FV) cut and  $\alpha$  coincidence tagging, which relies on 100% efficiency in reconstruction. The definition of the FV and the dominate external backgrounds will be discussed in Chapter 9.

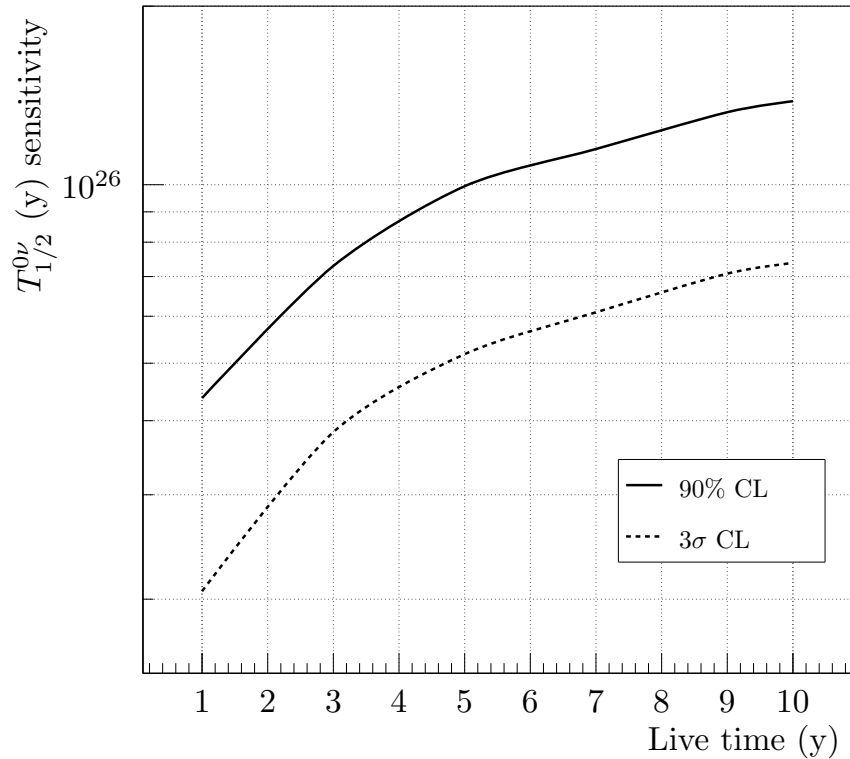


Figure 2.8: *The expected sensitivity as a function of live-time for 0.3% loading of Te [56].*

In later phases the Te loading will be increased to the multi-tonne scale, pushing the sensitivity further into the IH. The SNO+ detector will be discussed in greater detail in the following chapter.

## Chapter 3

# The SNO+ Detector

This chapter gives an overview of the SNO+ detector. This detector is an upgrade of the Sudbury Neutrino Observatory (SNO), hence it starts with an overview of the original SNO detector, focussing on its overall structure and the timing calibration sources used. After this, the upgrades that define the transition from SNO to SNO+ will be discussed, in particular the elements relevant for this thesis: the rope system, the data-acquisition system and the calibration system.

### 3.1 The Sudbury Neutrino Observatory

The Sudbury Neutrino Observatory (SNO) detector, shown in Figure 3.1, was built between 1990 and 1999. It is located near the city of Sudbury, Ontario. In this section, an overview of this detector is given, details can be found in [57]. The centre of the detector is at  $46^{\circ}28'30''$  N latitude ( $56^{\circ}33'$  magnetic north),  $81^{\circ}12'4''$  W longitude, at a depth of  $2092 \pm 5$  m ( $5890 \pm 94$  meter-water-equivalent) underground [58], Northern Ontario. This overburden provides effective shielding from cosmic muons: on average, only about 3 muons pass through the detector per hour. The detector consists of a 600.5 cm radius acrylic vessel (AV) of 5 cm thick acrylic, containing the target mass. The AV is mounted within a stainless steel geodesic sphere, 17.8 m in diameter. The geodesic sphere, known as the PMT support structure (PSUP), holds approximately 9500 20-cm photo-multiplier tubes (PMTs). A non-imaging light concentrator is mounted on each PMT to increase the total effective photocathode coverage to 54%. The PSUP and AV are suspended inside a 34 m deep barrel-shaped cavity. The cavity is lined with Urylon as a Rn barrier and filled with a little over 7000 tonnes of ultra pure water (UPW), providing further shielding to the

inner detector from the intrinsic radioactivity of the PMTs and surrounding rocks.

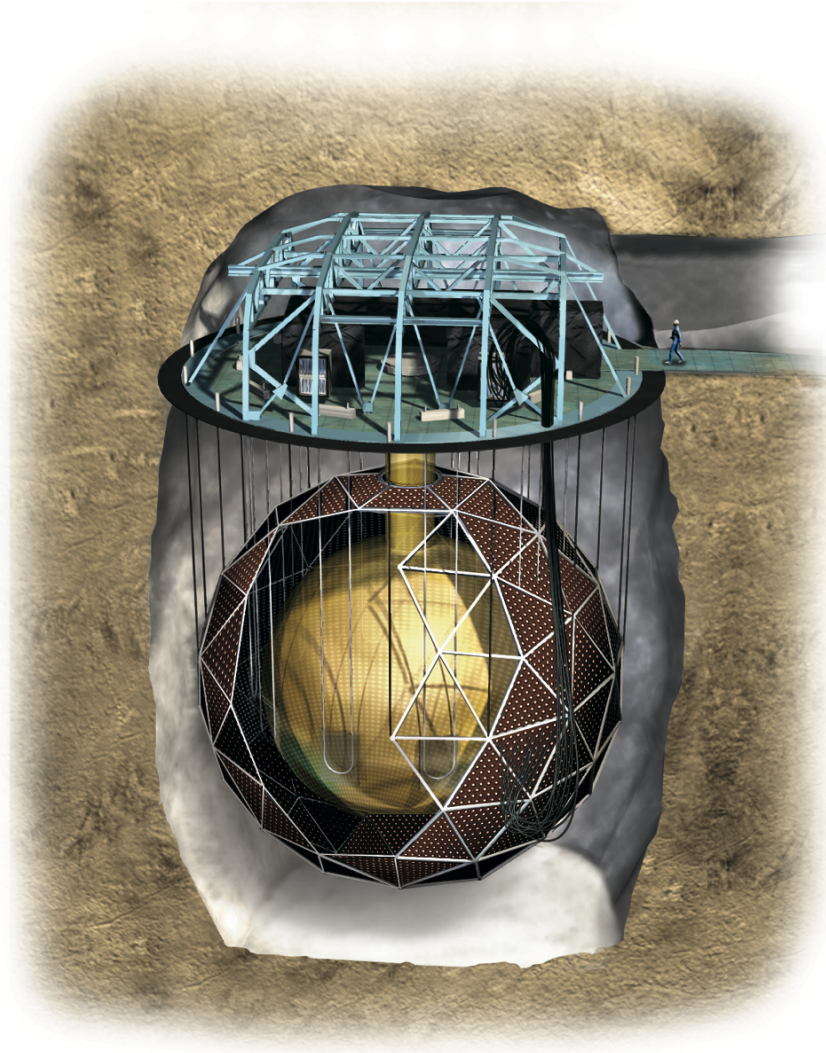


Figure 3.1: *Artist impression of the Sudbury Neutrino Observatory (National Geographic). The acrylic vessel is the centre volume in yellow, containing the target medium, and is surrounded by the (partially omitted to allow a view of the acrylic vessel) PMT support structure.*

The target medium for the SNO experiment was approximately one kilotonne of heavy water. It took data between 1999 and 2006, before passing the detector over to the SNO+ experiment.

### 3.2 Changing SNO into the SNO+ experiment

Upgrade work required for SNO+ started in 2011 and is expected to finish in 2016 allowing the detector to be turned back on in early 2017; when filled with liquid scintillator. SNO+

is a graded-shield type detector: the centre of the detector inside the Acrylic Vessel (AV) has the least background, with rates increasing as the distance outwards increases. The upgrade is characterised by the change in central mass to a novel scintillator mixture.

Using liquid scintillator enables the experiment to lower the energy threshold to approximately 200 keV, making SNO+ a multifaceted experiment. SNO+'s main physics goal is addressing the question of whether neutrinos are Dirac or Majorana particles, through the search for neutrinoless double-beta decay of  $^{130}\text{Te}$ . SNO+ will also be studying reactor, geo, supernovae and solar neutrinos; the experiment will be sensitive to  $^7\text{Be}$  neutrinos during the initial commissioning phase.

SNO+ is expected to detect at least 200 and possibly up to 350 photo-electrons per MeV from scintillation, depending on whether the scintillator is loaded with double-beta decay isotope and at what concentration. At energies of 10 MeV, above the range of the main physics goals, the expected average number of photoelectrons per PMT is such that the majority of PMT hits in an events will be Single Photon Electron (SPE), with a significant fraction of Multi-Photon Electron (MPE) [59].

With the new target mass, several changes to the detector were needed, including new scintillator processing and purification systems, new trigger and DAQ electronics and new calibration systems, as well as structural improvements.

To minimise cosmogenic backgrounds, the scintillator and isotope are to be purified underground in a purpose built plant.

As well as refurbishing the existing electronics, the higher data rates intrinsic to lower energy thresholds have necessitated the replacement of significant parts of the trigger and front-end DAQ electronics, to provide additional functionality and improved stability. PMTs, known from SNO to be faulty, have also been repaired or replaced.

Due to the nature of the norite rocks surrounding SNOLAB, radon levels are relatively high within the facility, at  $120 \text{ Bq m}^{-3}$  [60].  $^{222}\text{Rn}$  is part of the decay chain of  $^{238}\text{U}$ , shown in Figure 3.3, it is daughter nuclei  $^{214}\text{Bi}$  that are a direct background for neutrinoless double beta decay. The longer lived daughter nuclei  $^{210}\text{Pb}$  decays to  $^{210}\text{Bi}$ , which has a similar energy spectrum to the CNO neutrino spectrum [61]. As yet SNO+ has no direct measurement of the levels of  $^{222}\text{Rn}$  present in LAB, though it is expected that Borexino levels will be achieved. Borexino measured  $^{238}\text{U}$  at  $1.6 \times 10^{-17} \text{ g/g}$  [62] which at a decay rate of  $1.55 \times 10^{-4} \text{ Hz}$  corresponds to 6278 events/year/ktonne. So for 780 tonnes of LAB

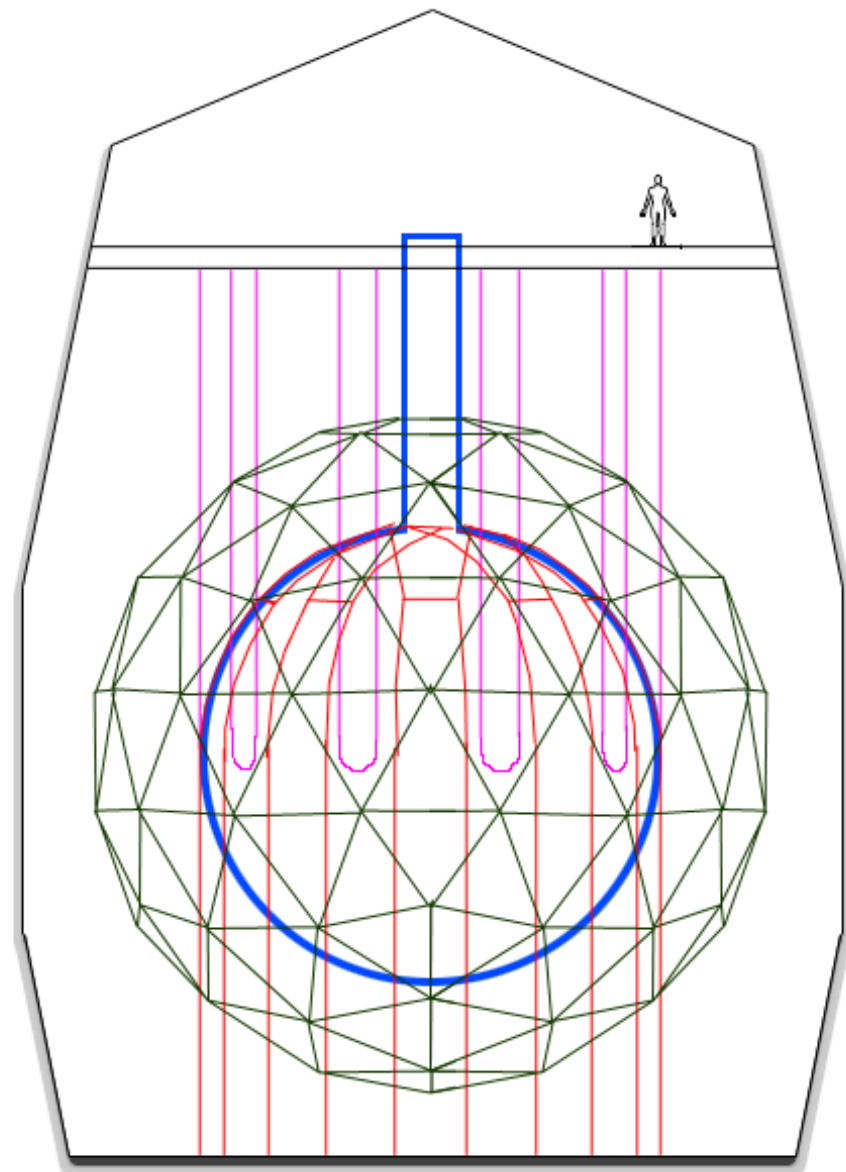


Figure 3.2: *Stylised schematic of the SNO+ detector, roughly to scale. The Geodesic PSUP is shown in dark green, only the stainless steel struts are shown with PMTs removed for visibility. The hold-up and down ropes are shown in pink and red respectively. The AV is shown in bold blue. The thickness of all lines does not represent anything. The cavity, deck (with person) are shown in black [41].*

at this level of  $^{238}\text{U}$ , 4897  $^{222}\text{Rn}$  events/year are expected, this corresponds to 13.4 counts per day, which defines the upper limit of  $^{222}\text{Rn}$  emanation for deployed sources.

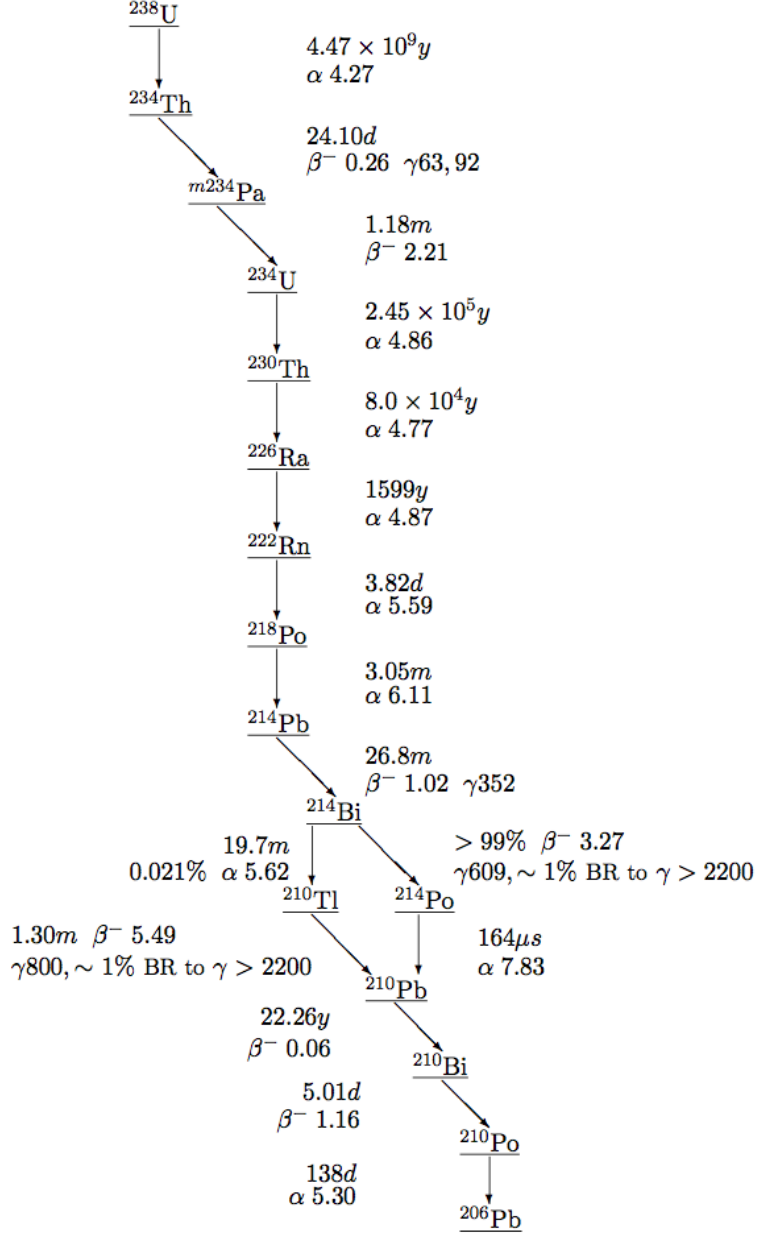


Figure 3.3: The decay chain of  $^{238}\text{U}$ . All half-lives are shown, with the Q-values of beta and alpha decays in MeV, and gamma rays in keV [63].

$^{222}\text{Rn}$  has a half-life of 3.82 days, whereas the half-life of  $^{210}\text{Pb}$  is several thousand times longer, 22.6 years.  $^{210}\text{Pb}$  decays by beta emission to  $^{210}\text{Bi}$ , which decays by beta emission to  $^{210}\text{Po}$ . These isotopes are particularly important for the solar neutrino phase, as they are a direct background. Due to its similarity with the CNO neutrino spectrum, any uncertainty in the amount of  $^{210}\text{Bi}$  will affect the precision of a CNO flux measurement [64].

The main ways  $^{210}\text{Pb}$  can enter the detector are: intrinsic contamination of the scintillator, ingress during transportation, and leaching from the AV. The intrinsic  $^{238}\text{U}$  contamination in the scintillator will be minimised by the purification process, which will be discussed in detail later. As mentioned, mine air is rich in Rn, which is particularly soluble in LAB, so ingress of  $^{222}\text{Rn}$  during transportation, handling and filling of the scintillator remains a problem. Therefore, care must be taken to minimise exposure of scintillator to mine air. Leaching of  $^{210}\text{Pb}$  from the surface of the AV is caused by Rn plating out from mine air onto the AV. The flow of air past the AV led to a build up of net charge, of sufficient magnitude to generate sparks when workers within the AV touched the cleaning ladder. The net charge was a particular concern due to the way  $^{222}\text{Rn}$  decays, any daughter of  $^{222}\text{Rn}$  on the surface is embedded deeper into the surface as it decays via alphas. It is hoped that cleaning the inner AV surface will reduce the amount of radon progeny plated out. To prevent  $^{222}\text{Rn}$  plating out after the surface had been cleaned, a radon tent [65] was erected above the aperture of the AV, the tent walls have a low Rn-permeability and airlocks prevented mine air entering the tent, the tent and AV being filled with filtered and humidified radon-free air.

The only realistic method of measuring these concentrations is to look at the 5.30 MeV alphas from  $^{210}\text{Po}$  decay. As the anticipated amount of  $^{210}\text{Po}$  is very low, it may prove difficult to extract from the other background signals. Conversely, an obvious  $^{210}\text{Po}$  peak would indicate a serious contamination problem. Measurement of the  $^{210}\text{Po}$  peak in the scintillator volume relies upon the assumption of equilibrium between  $^{210}\text{Bi}$  and  $^{210}\text{Po}$ , which may not be true if Po leaches from the AV at a significant rate [66].

The increased sensitivity to backgrounds, in particular the daughters of  $^{222}\text{Rn}$ , imposes tight constraints on the calibration system. A number of self-contained radioactive sources will be used to calibrate absolute light yield, energy linearity, geometric uniformity and alpha-beta discrimination. Two complimentary systems, a deployed diffuse light source referred to as the laserball (LB), and the External LED/Laser Light Injection Entity (ELLIE) will be used to calibrate the PMT timing and gain, scintillator properties and PMT response as function of event position. Source deployment must be kept to a minimum and eliminated if possible to meet the stringent radio-purity requirements. The ELLIE system, the subject of this thesis, is external and does not come into contact with the scintillator.

The density of LAB is  $0.86 \text{ gcm}^{-3}$ , so there is now a significant buoyant force on the

scintillator-filled AV, which is dealt with by means of a rope net that is anchored to the floor of the detector cavity (see Figure 3.2). A consequence to the addition of the rope net is the removal of a number of PMTs, to allow the ropes to pass through the PSUP, this, along with the decision not to replace some PMTs, has lead to the coverage reducing to 51%.

All of these updates will be described in greater detail below.

### 3.3 Coordinate System

The coordinate system of SNO+ can be confusing, due to a number of definitions sometimes used. Therefore, this section will explain the nuances of the coordinate system in detail.

The global SNO+ coordinate system is a right-handed Cartesian system centred on the centre of the PSUP (the geometric centre). (0,0,0) is defined at the centre of the PSUP, from which distances are measured using PMT timing. The z-axis is pointing directly upwards, the x-axis toward detector east along the electronics corridor, and the y-axis toward PSUP north, identified as the side of the AV where the pipes are located. True north is  $49.58^\circ$  to the east of PSUP north, as illustrated in Figure 3.4, PSUP north and east are shown in relation to a map of the PSUP nodes in Figure 3.5. A detailed discussion of the geometry in the context of simulations is provided here [67]. As events are measured using charge and time with the PMTs, the coordinate system is always relative to the PSUP in SNO+, and the AV must be positioned as accurately as possible within this system. Work to accurately understand the position of the AV after filling is ongoing at the moment, and will be discussed later.

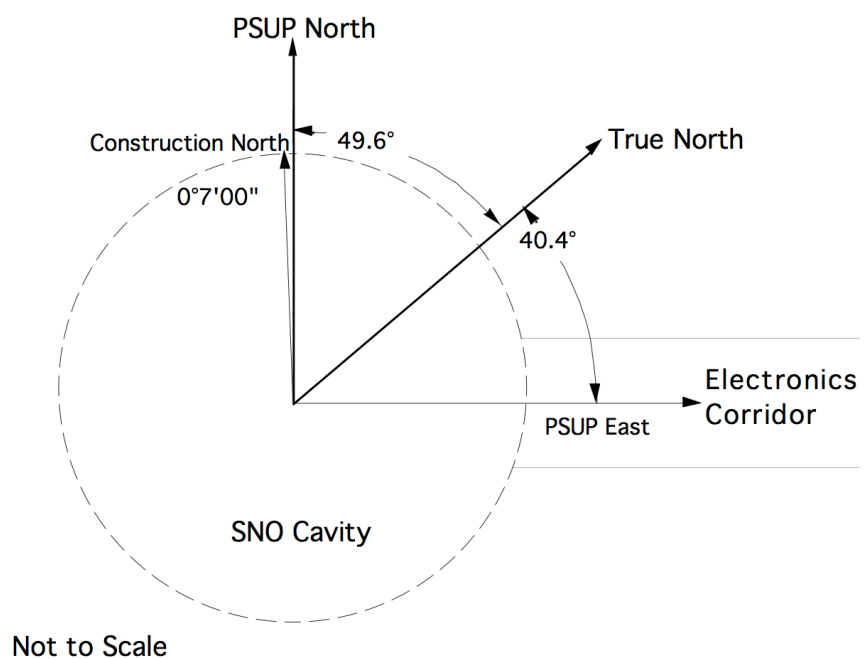


Figure 3.4: Drawing showing the orientation of construction, PSUP, and true north. True North lies  $49.58^\circ$  east of PSUP north and  $40.42^\circ$  north of the electronics corridor [68].

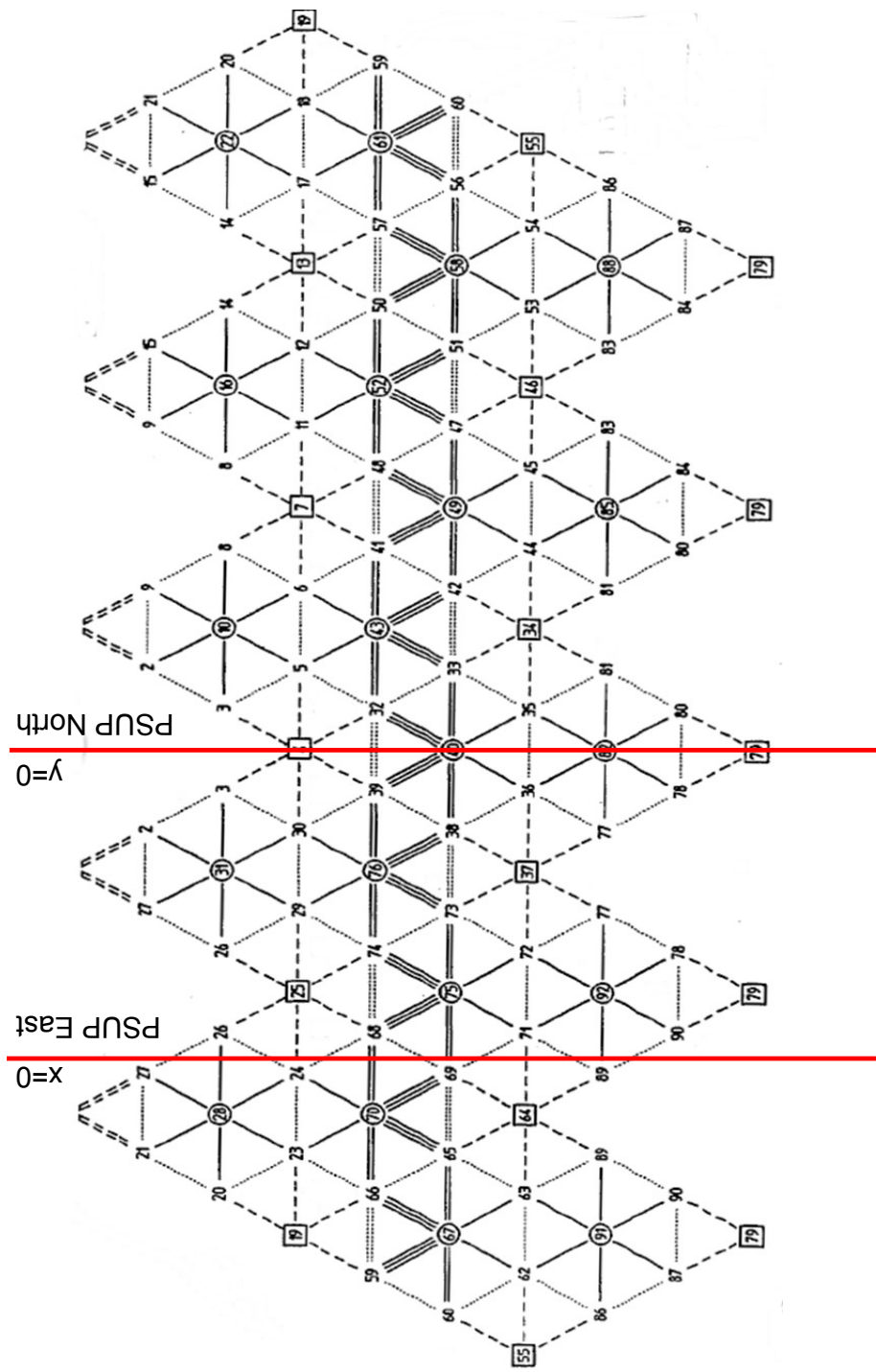


Figure 3.5: A map of the PMT support structure with PSUP north and east marked, each of the numbered nodes are being used as injection points for the TELLIE system.

### 3.4 SNO+ Electronics Overview

This section describes the SNO+ electronics, beginning by defining the observables, then describing how the trigger system works and the most common trigger modes, closing with a short summary of the upgraded components. It is important that these are understood for the timing calibration and reconstruction.

The SNO+ observables are the charge and timing information of each PMT hit. Time is stored as a single value by the Time to Amplitude Converter (TAC). The charge is separated into three values: High-gain Short integration (QHS), High-gain Long integration (QHL) and Low-gain Long integration (QLL). QHS describes the size of the pulse that caused the PMT to trigger, QHL also includes the late and scattered light, QLL is used to monitor in-window pileup.

The trigger systems functionality and associated delays are shown in Figure 3.6. On detecting the light, an analogue pulse from a PMT travels 35 m along a coaxial cable to a PMT Interface Card (PMTIC). Each PMTIC has 32 channels<sup>1</sup>, each channel potentially connecting to a PMT. The pulse is sent from PMTIC to a Front End Card (FEC) which determines if the channel crosses the discriminator threshold of approximately 0.25 photo-electrons. When the discriminator fires, a TAC starts to ramp, increasing in voltage from zero. Every PMT that crosses the discriminator threshold generates a trigger signal. Trigger signals from all channels are sent to the Crate Trigger Card (CTC) in each crate, the CTC then sends its sums onto the Master Trigger Card Analog (MTCA+) to be summed. There is a propagation delay of between 60 and 120 ns, for triggers sent from the Front End Card (FEC) to the MTCA+. The MTCA+ informs the Master Trigger Card Digital (MTCD) whether the sum has crossed a threshold for the number of hits within a given integration time (NHITs), another 2 to 3 ns propagates here. The MTCD generates a Global Trigger (GT), either because the NHITs sum crossed threshold, or an external trigger gets fired. The GT is latched to the 50 MHz clock, i.e. the GT is the next clock tick, occurring every 20 ns. The GT is sent to the FEC to collect data from the PMTs, with another signal propagation delay of between 60 and 150 ns. Receipt of the GT stops the TACs from ramping. The voltage read from the TAC corresponds to when the hit occurred, a large voltage meaning the hit occurred early in time. All of the components mentioned are described in detail here [69].

The FEC produces several signals that can be used to form a trigger sum and generate a

---

<sup>1</sup>There are twenty crates, each containing sixteen PMTICs [69].

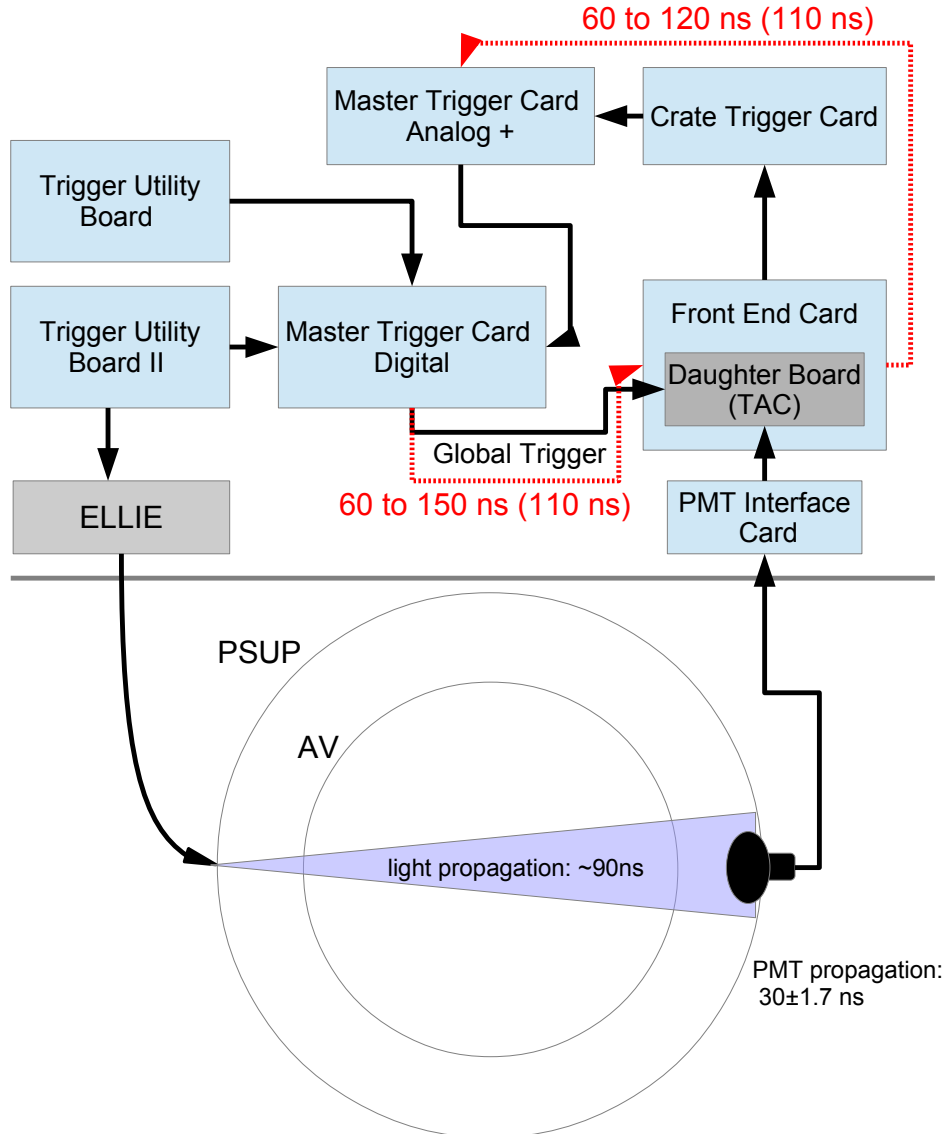


Figure 3.6: Flow diagram showing the SNO+ trigger system. PMT outputs are sent to the PMT interface card then the daughterboard, where the time and charge are calculated and read out by the front end card. The crate trigger card sums the triggers for individual crates and passes these to the analogue master trigger card, to sum hits for all crates. The digital master trigger card generates a global trigger, either because the sum crossed threshold, or an external trigger fired. Numbers in red are propagation delays and those in brackets are the values used in simulations, understanding these delays are important for any precision measurement or simulation. Details are provided in the text.

GT, the most commonly used are NHIT100, NHIT20, and ESUMHI/LO. NHIT100 is a discrete pulse of uniform height for each hit PMT, normally of 100 ns width. NHIT20 is also a discrete pulse, normally 20 ns wide; these pulses can be delayed between channels to change the position of in-time coincidence around the detector. Both NHIT100 and NHIT20 can be set to high, low, and medium thresholds. ESUMHI/LO is a copy of the PMT pulse at high gain or low gain. NHIT100 is the most commonly used trigger in SNO+, NHIT20 is useful for the study of backgrounds within the centre of the detector, and ESUMHI/LO provides a diagnostic tool or a means of constructing more complex triggers. There are also a number of other triggers for OutWard Looking (OWL) PMTs, and external triggers linked to GPS.

Due to the synchronisation of the GT, the time between the raw trigger firing and the beginning of the GT depends on the phase of the 50 MHz clock, which can vary from 0 to 20 ns between events [69]. For a single event, or back-to-back triggers this is seen as a systematic. It can potentially cause some uncertainty between the time of separate events, however the trigger rate is expected to be high enough (kHz) to prevent this. There remains some jitter on the trigger due to time walk, which will be calibrated out and is expected to be of order 0.1 ns.

As in SNO, the Trigger Utility Board (TUB) provides the master clock for the trigger systems and utilities and diagnostics to interface with the MTCD. For SNO+ there is an additional Trigger Utility Board (TUBII) alongside the TUB, providing an additional clock and more external triggers, connecting to the MTCD via a dedicated external trigger port. The CTCs have been modified to cope with larger currents for longer periods. New control boards (XL3) for the CTCs have been developed to set trigger masks and charge pedestals. The MTCA was upgraded to increase the upper limit to the number of channels that could fire simultaneously.

The readout in the event of a trigger is the timing information from the TAC and energy in the form of charge at each channel.

### 3.5 The Rope System

A consequence of the change in target mass is a buoyant force experienced by the AV. This has lead to the development of an entirely new rope system to support the AV for SNO+, shown in Figure 3.2, which has been perhaps the most challenging of upgrades, due

to the magnitudes of the forces involved and subsequent risk of deforming and damaging the AV. Radiopurity constraints limit the choice of suitable materials for such a system. These complexities will be summarised along with the system itself in the following sections.

### 3.5.1 SNO Ropes

For SNO, the AV was filled with a target mass of 1 tonne of heavy water and suspended within UPW. The AV was supported by a set of 10 loops of rope (see Figure 3.8(a)) providing an upward force of 980 kN (49 kN/rope).



Figure 3.7: *Left: Photograph of a whippletree used to support the AV hold-up ropes, the load cell is concealed within the centre of the base. Right: Photograph showing how the rope connects to the whippletree.*

The 10 loops of rope are 30.48 m long, and were made of Vectran, a liquid crystal polymer produced by Kuraray Co. Ltd [70]. Each of the 10 loops are connected to the AV via belly-plates, slabs of acrylic bonded to the AV at equidistant intervals around the equator, with a U-shaped section machined into them to hold the rope, as in Figure 3.8(a) and 3.8(b).

The ends of the loops are supported by whippletrees, mounted on the deck above the cavity. Whippletrees, pictured in Figure 3.7(a), are used to distribute evenly the load from each end of one rope. A whippletree is effectively a bar balanced on a pivot, the bar is loaded at each end and the pivot serves to balance the load. The ends of the ropes are braided into eyelets that are connected to the ends of the whippletree beam via a clevis anchor, see Figure 3.7(b). In turn, the clevis anchor is attached to a section of threaded bar which passes through the end of the beam, held in place by two locknuts that rest upon a thrust-bearing. The bearing allows the ropes to rotate freely, preventing additional tension caused by the ropes twisting. By adjusting the position of the locknuts on the threaded bar, the tension on the ropes can be altered. Thus, through careful adjustment at each of the ten whippletrees the exact position of the AV can be manipulated.

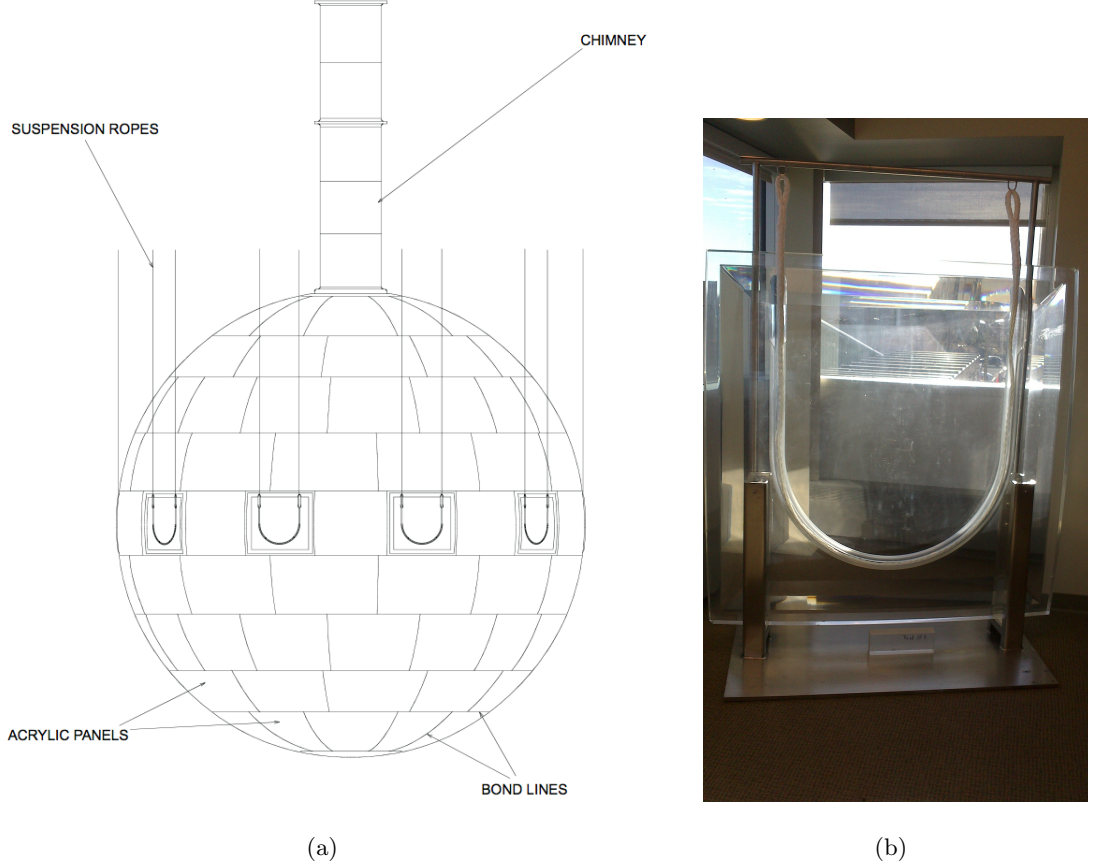


Figure 3.8: *Left:* The Acrylic Vessel as in SNO, showing the suspension ropes and belly plates. *Right:* A photograph of a belly plate on display in SNOLAB. A small length of rope can be seen looping through the u-shaped section, as the hold-up ropes do in SNO+.

If the AV is to be positioned correctly, knowing the tension the ropes are under and how it is changing is vital. This is why the whippetrees are mounted on load cells. The load cells used for the hold-up ropes are Omega's LCWD-50K [71], with a rated capacity of 22.68 tonnes. They make use of a full Wheatstone bridge run on a 10 V bias with a 20 mV output. Each load cell connects to a DIN mounted Omega DRC-4720 bridge input signal conditioner, see Figure 3.9, which provides an output for the monitoring system, DeltaV [72], of between 4 and 20 mA, with a temperature coefficient of  $0.05\%^{\circ}\text{C}^{-1}$ . Omega stipulate their load cells be re-calibrated every 13 months, this was not possible in SNO and will not be in SNO+. Hence, a combination of the rope tension and predicted creep [73] are not sufficient to determine the AV position over a prolonged period.

Equator monitors are used to determine the AV's position relative to the deck. Consisting of four Vectran strings mounted to the AV at  $90^{\circ}$  intervals around its equator, the other end of these strings are attached to extension meters on the deck, allowing vertical movements

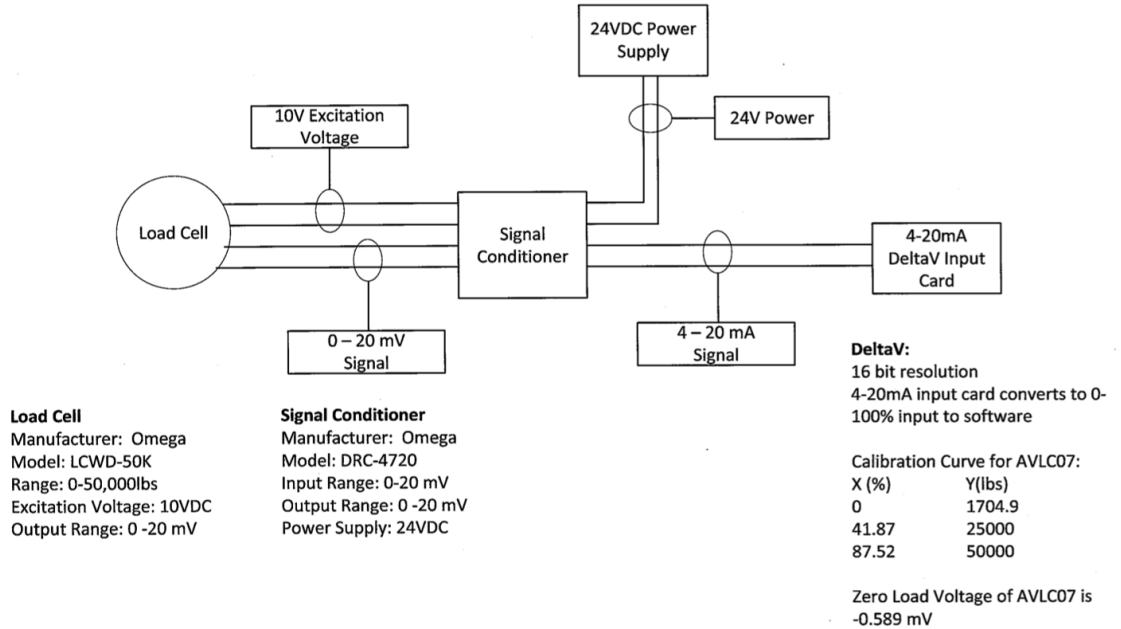


Figure 3.9: *Flow diagram showing how the loadcells connect to the DeltaV.*

of the AV relative to the deck to be measured. Combining these measurements with those taken manually at the AV neck flange, this allows for a crude interpretation of deformation of the AV, as well as a measurement of the creep in the ropes.

### 3.5.2 SNO+ Ropes and Net

SNO+'s liquid scintillator has a density of  $860.0 \text{ kgm}^{-3}$ , in comparison to  $999.7 \text{ kgm}^{-3}$  of the UPW providing the shielding within the cavity. This leads to the AV experiencing a buoyant force of 1.25 MN. To counteract this very large buoyancy force, a hold-down system has been developed; a hold-down rope net designed using finite element analysis to spread the load evenly, minimising stress to and thus the possibility of deformation of the AV.

The installed hold-down rope net is shown in Figure 3.10. The net consists of five sub-nets, each composed of two 3.8 cm diameter ropes passing on either side of the neck and connected by a pair of slings. Each of the rope ends are anchored to the cavity floor, as in Figure 3.11. The anchors are mounted into the concrete lining of the cavity and sealed with Urylon, completing the cavity seal. Load cells are then employed again to provide data on the tension of the individual ropes, the submersible load cells used are supplied by Sensing-Systems and have a capacity of 89 kN. A single load cell is attached to each end of the twenty ropes, mounted directly to the anchor on the cavity floor and connected

via turnbuckles to the eyelets braided into the ends of the ropes. A number of PMTs were removed to allow space for the ropes to pass through the PSUP to their respective anchor points.

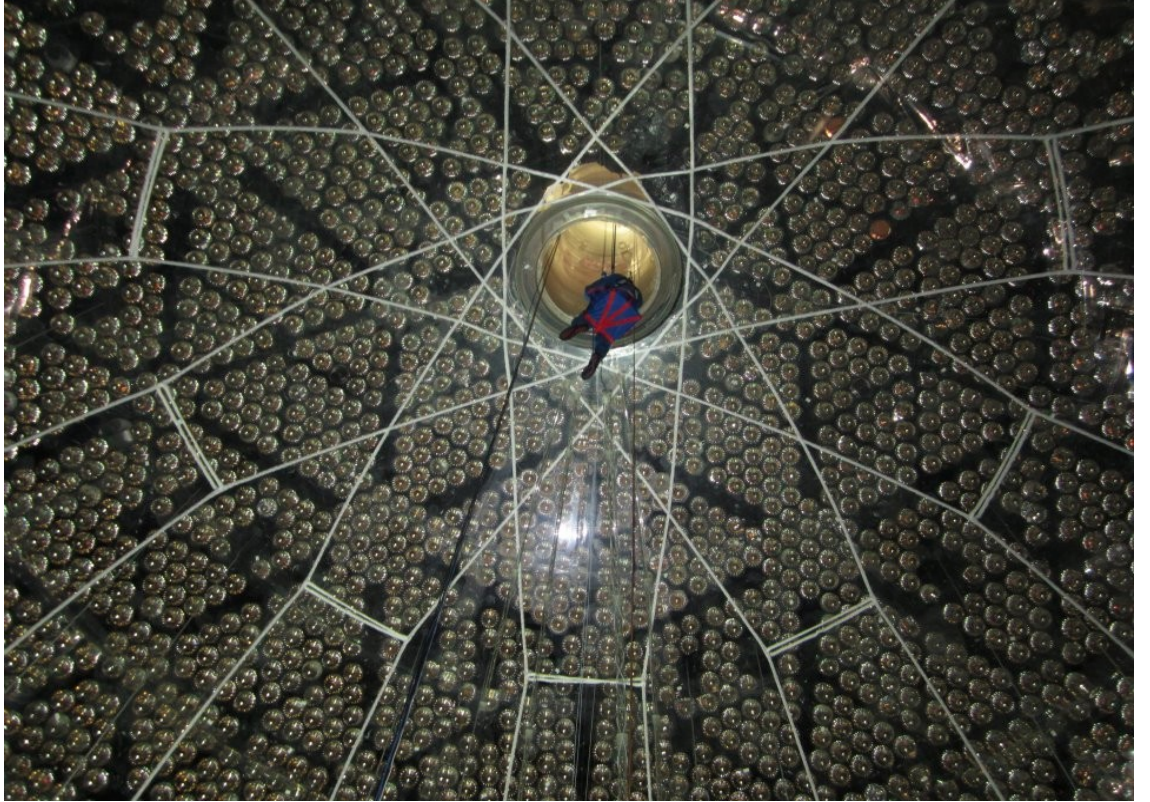


Figure 3.10: *The installed rope net, as viewed from the base of the AV (with the author being lowered into the AV).*

Potassium is a background of particular concern for the pep solar neutrino analysis, due to the relatively high natural abundance 0.0117%, of  $^{40}\text{K}$ .  $^{40}\text{K}$  has a 10.72% probability of decaying via electron capture to  $^{40}\text{Ar}$ , emitting a neutrino, and a 1.46 MeV photon [74]. If energy resolution of the detector is insufficiently accurate, this is an issue as at large mixing angles pep neutrinos are mono-energetic at 1.44 MeV [75]. Like most other nylon based ropes, Vectran ropes are coated with potassium salts [76]. The concentration of  $^{40}\text{K}$  in the rope net must be kept below 1 ppm, for it to not be a dominant background [77].

Although the Vectran ropes used in SNO performed well, given the area of the rope net on the AV, it was even more important to select a radioactively pure material for the net. The same argument follows for the hold-up ropes, which are still necessary to support the AV during commissioning and water fill, despite their contact area being approximately only a twelfth of the net's. Tensylon was selected for this purpose, an ultrahigh molecular weight polyethylene developed by BAE Systems as ballistic armour. Prior to SNO+ it



Figure 3.11: *View from the base of the cavity, showing the rope net anchored to the cavity floor.*

was used in Borexino to support the inner and outer nylon vessels, after extensive testing [76]. Like Vectran it is resistant to UPW, but more importantly potassium salts are not used in its production. The results of germanium counting for Tensylon and Vectran are shown in Table 3.5.2; Tensylon is comparable to Vectran in both in  $^{232}\text{Th}$  and  $^{238}\text{U}$ , but an order of magnitude lower in  $^{40}\text{K}$ .

In this system, extension under load, creep, is expected. There are two types of creep: construction stretch, where the fibres of the rope settle into position as the initial load is applied to the ropes, and extension of the bulk material, where the fibres themselves extend under load. This latter type has been shown to be temperature dependent. According to Yale Cordage<sup>1</sup>, the designers and manufacturers of the original SNO hold-up ropes and the new SNO+ rope system, the Tensylon ropes should experience a 3% extension in overall length as the initial construction stretch has been removed, under sufficient load this will be removed within hours. Work done by the collaboration demonstrated creep in Dyneema [78], a similar ultrahigh molecular weight polyethylene to Tensylon, at 10°C, presenting a measurement that shows an expected creep of about 1% creep for a 10 year

---

<sup>1</sup><http://www.yalecordage.com/>

Source	$^{232}\text{Th}$	$^{238}\text{U}$	<i>natural</i> K
SNO+ Goal	< 200 ppt	< 200 ppt	1 ppm
Vectran	< 271 ppt	$116 \pm 159$ ppt	$68.2 \pm 4.2$ ppm
Tensylon	$< 160 \rightarrow 180$ ppt	$< 70 \rightarrow 95$ ppt	$0.2 \rightarrow 0.5$ ppm
Kevlar	$255 \pm 189$ ppt	$26 \pm 49$ ppt	$9.4 \pm 0.9$ ppm

Table 3.1: *Table of counting results for Vectran ropes used in SNO and Tensylon ropes of SNO+, with Kevlar ropes shown for comparison. Vectran and Kevlar results are from germanium counting at Laurentian University [78], Tensylon results are from the Borexino calibration [76]. SNO+ goal is the criteria used ropes had to meet to be suitable for SNO+. These values were defined in the initial external backgrounds document [77].*

run. This is more than Vectran, yet less than other high modulus ropes.

### 3.6 Scintillator System

The scintillator selected for the use in SNO+ is Linear Alkyl-Benzene (LAB), which has an intrinsic light yield of approximately  $10^4$  optical photons per MeV energy deposited by charged particles, with low scattering and a fast decay. It is these properties that allow for discrimination between alphas and betas. Most importantly, it is chemically compatible with the AV and its low toxicity and relatively high flash and boiling points, 140°C and 278 to 314°C respectively, make it a safe option for use underground.

As mentioned, to reduce the effect of cosmogenically induced backgrounds, the scintillator and isotope are to be purified underground in a purpose built plant, in close proximity to the detector. A flow diagram of the scintillator system is shown in Figure 3.12. The plant uses multistage distillation to remove heavy metals, improving UV transparency with dual-stream distillation of the PPO wave length shifter. N<sub>2</sub> and steam stripping are used to remove Rn, Kr, Ar, and O<sub>2</sub>. Water extraction removes Ra, K, and Bi. Metal scavengers are used to remove remaining Bi, and Pb. Dust and other particulates are removed by micro-filtration.

To add the Te to the scintillator, Te acid is dissolved in water and then a surfactant is used to mix it in to the scintillator. The isotope purification is done in two stages, above ground and below ground. Above ground Te(OH)<sub>6</sub> is dissolved in UPW and re-crystallised using nitric acid, then it is rinsed with ethanol. Below ground the crystals are dissolved

in water at 80 °C, then thermally re-crystallised.

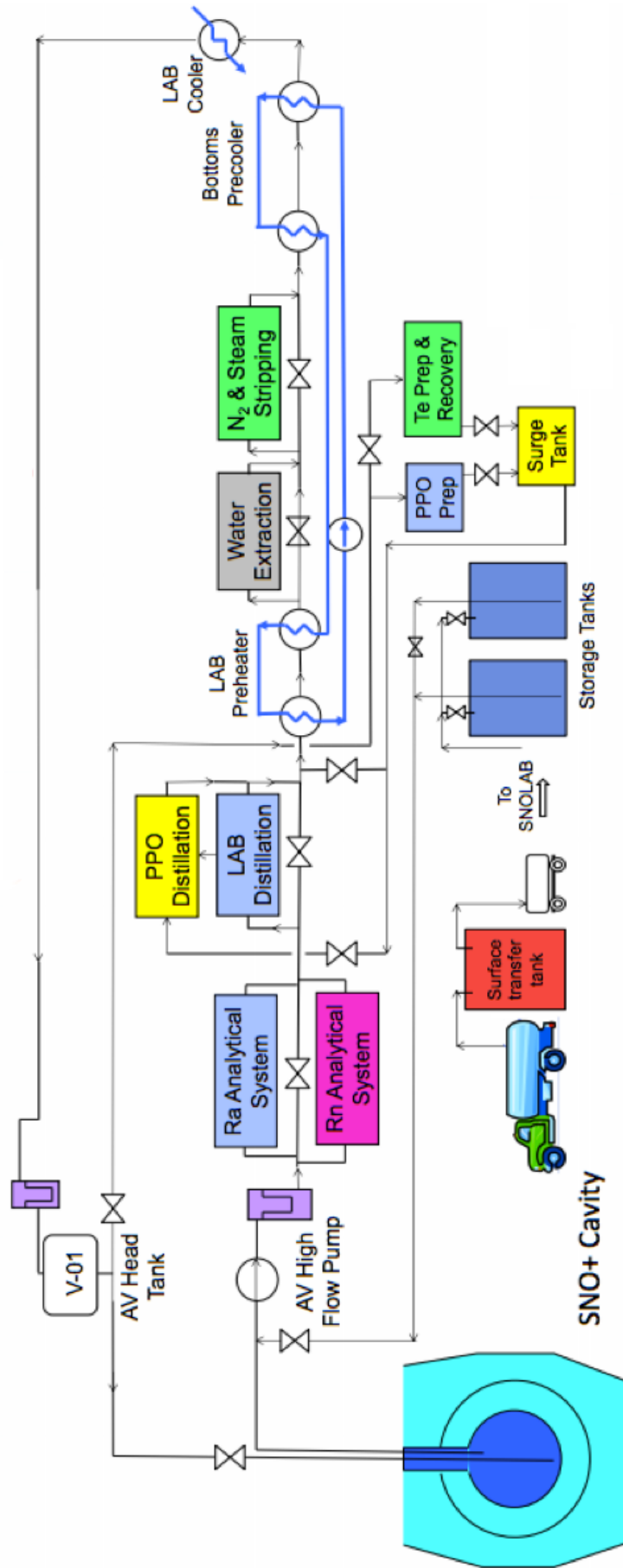


Figure 3.12: An overview of the SNO+ scintillator system, showing the continuous recirculation and filtration of the scintillator. Adapted from [79].

### 3.7 Calibration System

The use of liquid scintillator generates more light per event, lowering the threshold energy to the MeV. This increases sensitivity to backgrounds, in particular the daughters of  $^{228}\text{Ra}$  and  $^{222}\text{Rn}$ , which imposes tight constraints on the calibration system. Figure 3.13 illustrates the background effect of  $^{222}\text{Rn}$  from deployed calibration sources in Kamland [80]. Source deployment must be kept to a minimum and eliminated if possible to meet radio purity requirements.

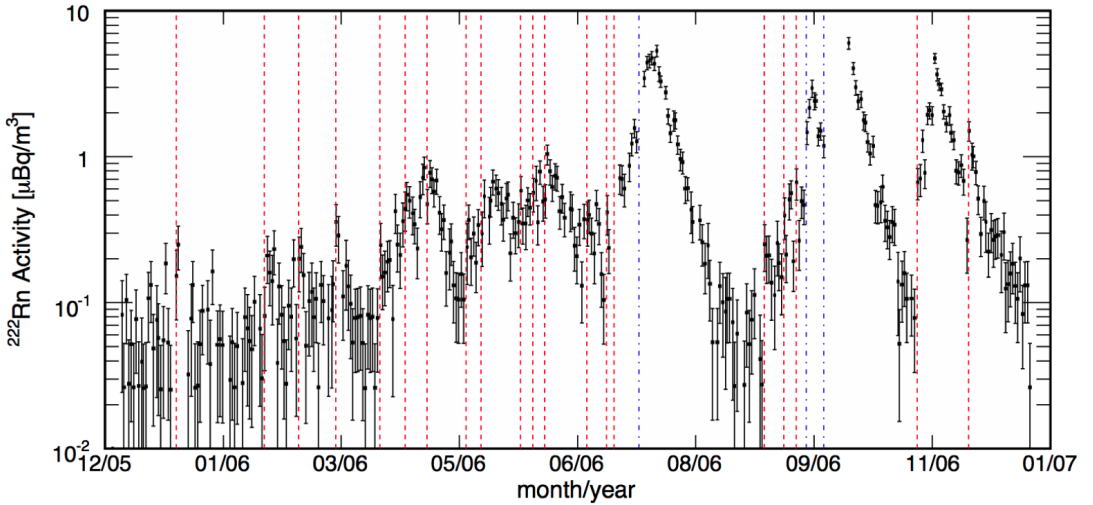


Figure 3.13:  $^{222}\text{Rn}$  activity as a function of time, in Kamland following the deployment of calibration sources [80]. Red and blue lines are the start of calibration runs.

The calibration is a delicate task, that must provide a comprehensive understanding of the detector over a wide energy range, 0.1 to 10 MeV. Among the most important parameters to determine are the scattering and absorption in scintillator, acrylic, water, and the timing and charge response of the PMTs, as well as PMT response as a function of event position. PMT angular response is a measure of how well a PMT can detect a photon entering it at a certain angle: a photon entering the PMT in a direction normal to its surface has a higher probability of detection than a photon entering at an angle relative to the normal. Part of the PMT's structure is a concentrator - a series of aluminium coated petals that focus light onto the PMT surface, since their installation in SNO these have been degrading [81], reducing the angular response of the PMT.

To reconstruct position from the time measurement, any channel dependent offsets must be corrected and the discriminator time walk effect for each PMT must be understood, see Figure 3.14. Time walk is a systematic effect caused by low amplitude pulses taking

longer to cross the discriminator threshold than larger pulses, with respect to the centre of the peak [82]. These two effects can be measured by analysing the time-versus-charge distributions with SPE pulses, as the spread in charge is large enough to populate all the relevant charge regions. The SPE resolution of the PMTs is dominated by the spread (root mean squared) on the time taken for a SPE to propagate from the photo-cathode to anode of the PMTs, known as Transit Time Spread (TTS) and is 1.7 ns [57]. Alternatively, MPE pulses, which are unaffected by time-walk due to increased charge, can be used to measure the channel-dependent offsets. Then SPE pulses can be used to constrain the time-versus-charge dependence independently of the individual channel delays.

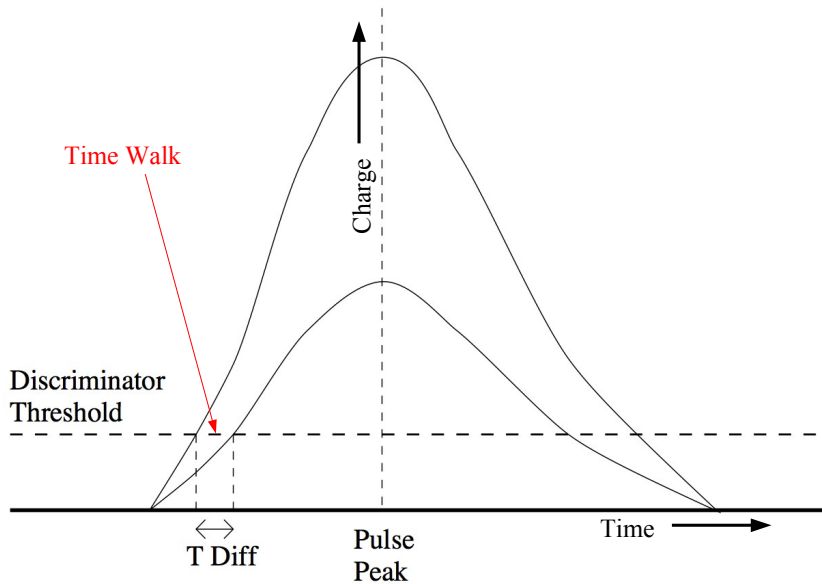


Figure 3.14: *Small pulses take longer to cross the discriminator threshold than large pulses, with respect to the centre of the peak. Adapted from [83].*

The ability to operate in SPE is also important as single photon sampling provides the most accurate measurement of the time profile of a pulse, whereas MPE always skews the time profile in the favour of the first photon detected.

To reconstruct energy from the charge measurement, it must be corrected for any gain variations of the PMTs, and also for the dependence of the light collection efficiency as a function of the event position. The measurement and monitoring of these three quantities - PMT time offset, discriminator time walk, and gain - is the main goal of the PMT calibration system.

A number of self-contained radioactive sources will be used to calibrate absolute light yield,

energy linearity, geometric uniformity and alpha-beta discrimination. Some of the sources have been reused from SNO and modified for use in the scintillator, new sources have also been developed to probe the lower energy scale of SNO+. Some of the new sources are tagged, using either a self-contained PMT or coincident decays of the isotope. The new sources include a  $^{60}\text{Co}$  source, producing a 2.5 MeV  $\gamma$ , a  $^{48}\text{Sc}$  source with a 3.3 MeV  $\gamma$ , a  $^{24}\text{Na}$  with a 4.1 MeV  $\gamma$  and, refurbished from SNO, a  $^{16}\text{N}$  source producing a tagged 6.1 MeV  $\gamma$ . Other sources under development are an AmBe neutron source as well as  $^{90}\text{Y}$  and  $^8\text{Li}$  beta sources [84]. These sources will be deployed within the AV, suspended from an umbilical cable and positioned in three dimensions using a combination of the umbilical and a set of Tensylon calibration side ropes, as shown in Figure 3.15. As in Borexino [85], six cameras have been installed on the PSUP, looking inwards, and will be used to triangulate deployed sources to an accuracy of less than 1 cm [86], using an LED mounted on the source or umbilical. When not in use, the sources are sealed within a nitrogen filled “glove box” in the Deck Clean Room.

In SNO, the PMT calibration was accomplished through the use of a deployed source, the LB, a diffuse light source composed of a dye laser giving selectable wavelengths and transmitting the light via optical fibres to a spherical diffuser [87]. A modified version of the LB will be used in SNO+, and a more detailed discussion will be presented in Chapter 7. However, radiopurity requirements forbid the regular immersion of external sources into the AV. This has lead to the development of a system complementary to the LB: The External LED/Laser Light Injection Entity (ELLIE). Installed outside the active volume of the detector, ELLIE is designed to provide continual calibration of the PMT timing and gain, and scintillator properties.

ELLIE has three sub systems: attenuation monitoring (AMELLIE), measuring scattering (SMELLIE) and timing (TELLIE). Each of ELLIE’s sub systems use electronics mounted on the deck to generate optical pulses, which are then transmitted into the AV via optical fibres terminating at the nodes of the PSUP, see Figure 3.16.

AMELLIE uses LEDs at multiple wavelengths, injecting light at four different locations, in two different directions. Wide-angle quartz fibres are used to ensure reasonable coverage, allowing in-situ monitoring of the stability of attenuation of the scintillator.

SMELLIE uses four lasers at 375, 405, 440 and 500 nm wavelengths, connected via a optical fibre switch to twelve quartz fibres terminating at four different locations. At the injection points the fibres are each connected to a collimator, pointing in three different

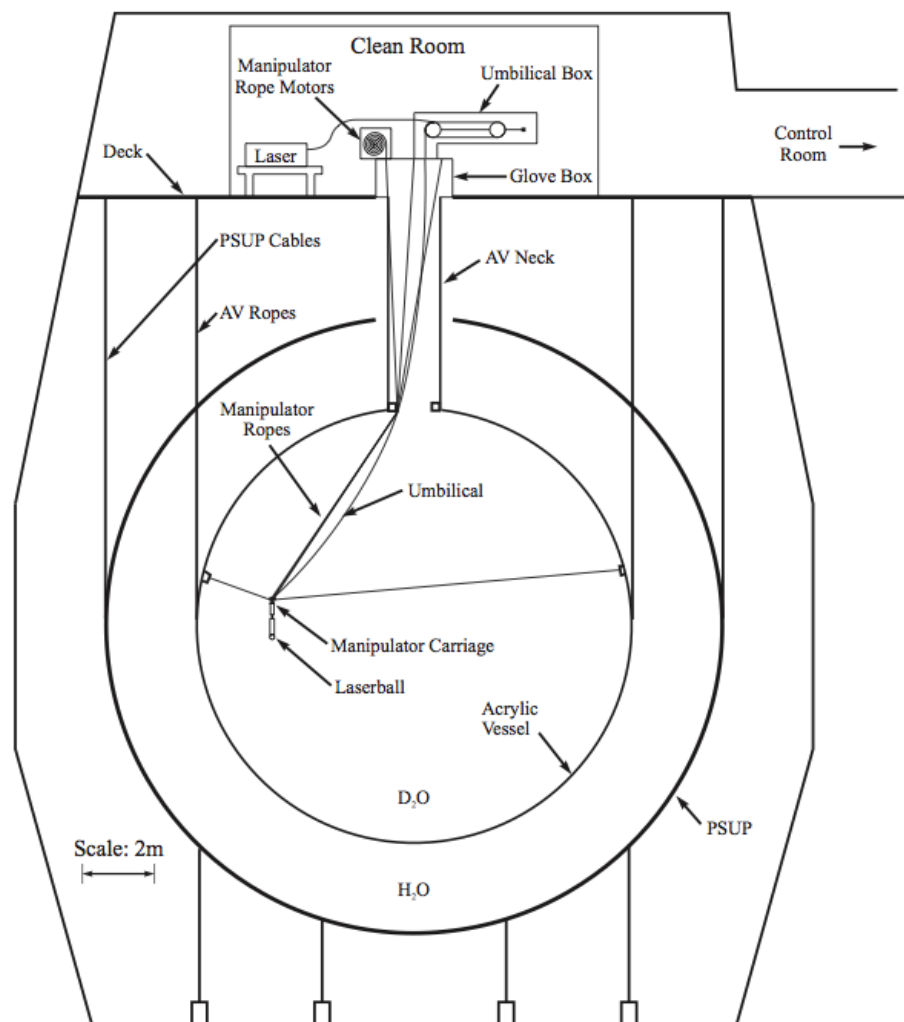


Figure 3.15: *Schematics of the SNO source manipulator system [87].*

directions:  $0^\circ$ ,  $10^\circ$  and  $20^\circ$  reactive to the centre of detector. Analysing the position and time of PMT hits relative to the initial beam direction, provides a measure of the scattering of the scintillator. The multiple injection points and directions provide a check against systematics.

TELLIE uses LEDs at a single wavelength, injecting light via PMMA fibres into each of the 91 PSUP nodes and one at the neck of the AV. Wide-angled fibres ensure complete coverage of the PMTs, providing a continuous calibration of timing and charge response for each PMT. The development of the TELLIE hardware, initial results and another possible use for the system will be presented in the following chapters.

TELLIE and AMELLIE share the same control hardware. LEDs were selected for both systems, as the cost of 91 plus laser channels would have been prohibitive. SMELLIE requires a tightly collimated beam, therefore a coherent light source is necessary.

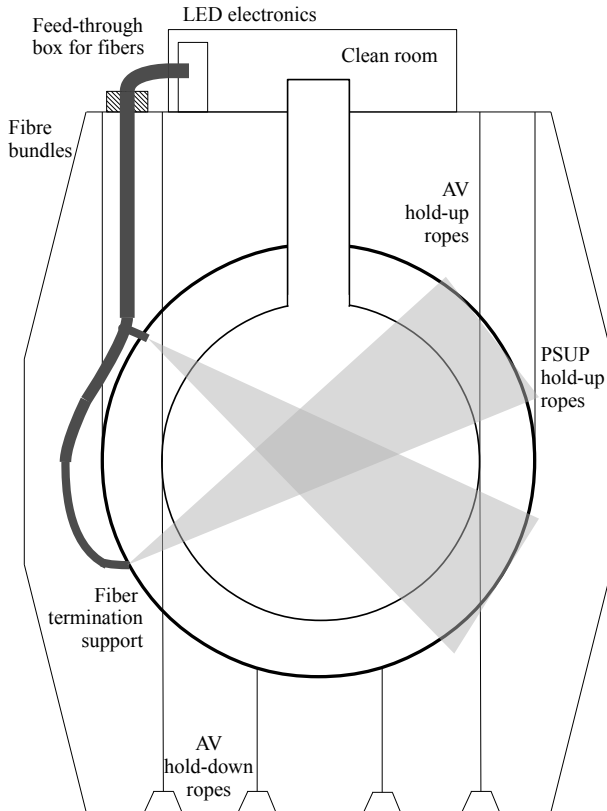


Figure 3.16: Sketch of the SNO+ detector showing the ELLIE calibration hardware on the top deck as well as an example of the light injection points around the PSUP.

### 3.7.1 Reconstruction Resolution

Assuming the calibration to be successful, making the uncertainty in PMT time delays and walk corrections insignificant with respect to the other effects in the reconstruction of the vertex position of events, the detector is expected to achieve position resolutions of approximately 10 cm in scintillator and 25 cm in water [88]. Although the directional information of the ionising particle is partially conserved in water, it is almost completely lost in scintillator<sup>1</sup>. For scintillator the increased statistics lead to the improved resolution.

## 3.8 Monte Carlo Simulation and Data Handling

The Monte Carlo (MC) and DAQ of SNO+ are shown in Figure 3.17. The database contains all relevant details of the detector and its status necessary for MC and data analysis. The SNO+ MC was originally developed for the Braidwood collaboration, called Reactor Analysis Tools (RAT), based on software which simulated a generic liquid scintillator experiment with a KamLAND like geometry. It is written primarily in C++, with some python, using Geant4 [89] libraries to simulate physical processes and ROOT [90] libraries to store data. ORCA is an Object-Oriented DAQ, written in Obj-C using the Cocoa framework and the Apple developer tools. The data from ORCA can be used to update the database and is processed, and sometimes reprocessed, by RAT before being sent to the Grid for analysis.

---

<sup>1</sup>A Cherenkov component is present but hard, if not impossible, to detect

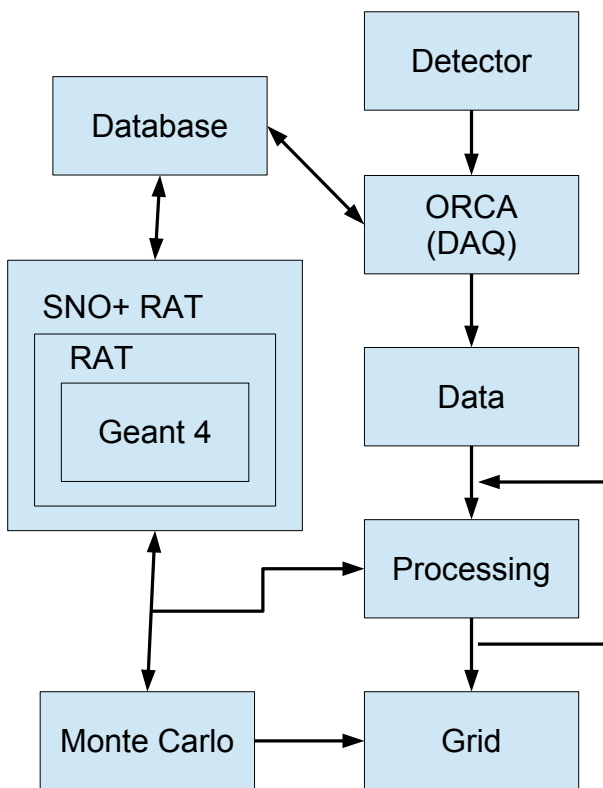


Figure 3.17: Diagram of showing the basic function of the SNO+ Monte Carlo and data acquisition.

## Chapter 4

# Acrylic Vessel Positioning

As mentioned in Chapter 3, the upgrades to SNO+ have made it necessary to develop a new rope system for supporting and positioning the AV. When the AV is filled with scintillator, it becomes buoyant and requires holding to the cavity floor. However, during air-filled commissioning and water-filled phase the AV is denser than the surrounding mediums, and needs to be held up. While transitioning between phases, the cavity will be filled with UPW and there will be no opportunities to directly adjust the tension of the rope net. As a result, the AV will be held in tension throughout. The expected extension of the ropes and net have to be well understood in order ensure their integrity and to accurately position the AV prior to the water fill. Despite the rope net being designed to spread load evenly across the AV, holding the AV in tension means that it will deform. Knowing the position of the AV is vital in defining the Fiducial Volume (FV), and there are drawbacks to the current monitoring system.

This chapter will explain the complications of replacing the hold-up ropes and installing the hold-down rope net and drawbacks of the current system used to monitor the position and shape of the AV. Results of the system performance so far will be summarised, and the expected long-term performance discussed. The goal of this chapter is to provide a motivation for the need of an additional system to monitor the AV's position and shape.

Since the company contracted to manufacture the rope system are American and the institute leading the project are Canadian, imperial units are commonplace. To save unnecessarily accurate numbers as the result of unit conversion, imperial units will be used throughout out this chapter, with conversion only applied in comparison to other

parts of this thesis<sup>1</sup>.

## 4.1 Installing the New Rope System

Before describing the tensioning and performance of the ropes, the process of installing the new rope system should be summarised in order to make the complexities of the system clear.

### 4.1.1 Replacing Hold-Up Ropes

Since the rope net weighs 600 lbs, the hold-up ropes had to be replaced before it was installed, in order to minimise the load on the existing Vectran ropes as they were changed out. To replace the hold-up ropes, a single Vectran rope has to be slackened, with the remaining 9 ropes taking the load of the AV (81500 lbs). Once the rope is slack, one end of the Tensylon rope is attached to one end of the Vectran rope. The same end of the Vectran rope is then removed from the whippetree and the free end of the Tensylon rope attached in its place. The other end of the Vectran rope is then detached from the whippetree and the rope drawn from the cavity, pulling the Tensylon rope into place. The two ropes are then separated and the free end of the Tensylon is attached to the whippetree.

The new rope can then be brought up to tension. During air-fill, the total load measured for the hold-up ropes is given by the sum of masses acting on the load cells: the AV mass and the mass of the whippetrees,  $m_{AV} + m_{whippetree} = 81500 + 10 \times 500 = 86500$  lbs, so the load on each rope should be 8650 lbs. As mentioned in Chapter 3, there is a small amount of construction stretch that will need to be removed from the ropes, this is done by increasing the initial load to between 10000 and 14000 lbs. In normal operation the buoyant force would be spread across the surface of the AV, however during pre-tensioning the upward force is provided by the ropes at the belly plates. The safe engineering limit for sheering forces at the belly plates is what sets the upper limit of 14000 lbs. The load is increased by adjusting the whippetree so as to lift the AV from the belly plate only, this reduces the load for the neighbouring ropes and increases it for the rope at said whippetree. As the new rope extends the load on the neighbouring ropes increase and the load of the new rope reduces toward the normal operating load. Figure 4.1 shows tensioning of the hold-up ropes at 07:00 and 17:00 on the 19<sup>th</sup> of February 2012, a sharp

---

<sup>1</sup>1 lbs = 0.45 kg and 1" = 2.54 cm

increase in load as the rope is brought up to tension on individual ropes, for the removal of construction stretch. Figure 4.1 was made using the uncalibrated readouts of the load cells, hence the total load is not equal to 86500 lbs. The increase in load following tensioning is mainly due to the response time of the load cells (of order an hour), although there are additional components which will be discussed later.

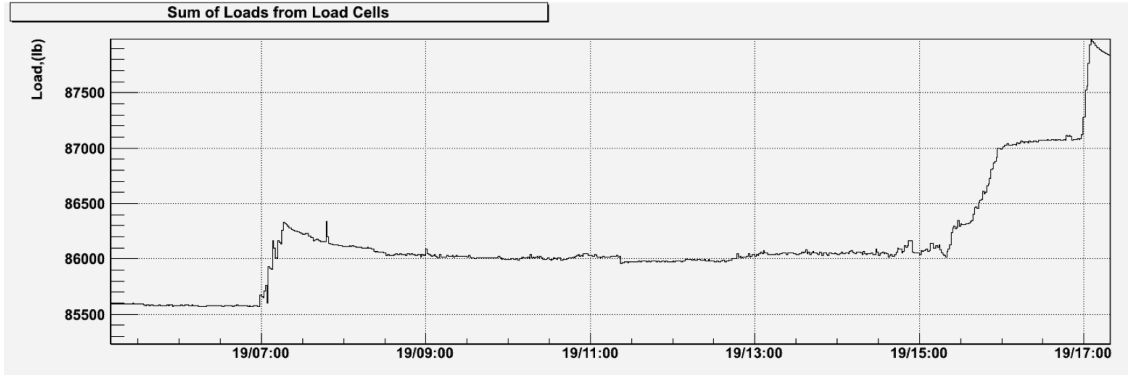


Figure 4.1: *Total load of hold-up load cells (uncalibrated), during tensioning and rope net deployment on the 19-02-2012. The steps at 07:00 and 17:00 are due to tensioning. The slow rise a little after 15:00 is the rope net being lowered into place. Some fluctuation in total load is also evident prior to 15:00, as the legs of the hold-down net were lowered onto the vessel. The increase in load following tensioning is largely due to the response time of the load cells (of order an hour). Taken from [91].*

As soon as one rope was replaced and its construction stretch removed, it was safe to replace the next rope. The rope on the opposite side of the AV was the next to be swapped, and so on. Following the same techniques as in the construction of a spoked wheel [92].

#### 4.1.2 Centring the AV

The process of replacing the hold-up ropes results in the AV being misaligned within the PSUP, due mainly to the ropes remaining too high in the whippetrees after their artificial tensioning. Before the hold-down rope net could be installed, the AV had to be centred with respect to the deck.

Normally, the equator monitors would be used to provide the AV's position relative to the deck. However, they had to be disconnected in order to replace the ropes, and as a consequence, their zero positions were not calibrated when they were reconnected. Other problems also became apparent, which will be discussed later. In short, the equator

monitors were not sufficient for locating the AV relative to the deck.

The AV had tilted about its equator; the goal was to get the AV level and centred, with the loads at each whippletree equal. The solution was to have two teams of workers, one group harnessed to the support structure above the neck of the AV, providing direct measurements of the distance between the AV neck flange and the aperture in the deck. A second group were on deck to adjust the rope tension at the whippletrees, with one person in the control room monitoring loads at each rope with the DeltaV system (see Chapter3), co-ordinating the operation by radio. The procedure was to slacken the ropes at the highest side of the AV's equator (opposite the point where the AV's neck was closest to the aperture edge) and increase tension for those at the lowest point on the equator. This had to be done in small increments to make sure the load remained balanced between ropes, and to accommodate the response time of the load cells. The procedure worked and the AV was centred to within 5 mm, more precisely than the expected reconstruction resolution.

There were complications caused by two of the ropes being too long, meaning there was very little adjustment left at the whippletrees once the AV was centred. These ropes were replaced at a later date, using the procedure described above.

#### **4.1.3 Net Installation**

With the AV centred and new hold-up ropes in place, the rope net could now be installed. The rope net came bundled in such a way that it could simply be positioned above the AV, and lowered into the cavity around the AV neck. Guide lines routed through openings in PSUP to the cavity floor, were attached to eyelets at the end off the rope net, and the net was carefully lowered into position. The turnbuckles, which are used to apply tension to the ropes at each anchor point, were then attached to the ends of the net to hold it in position. Before the turnbuckles could be attached to the anchor points, the net had to be centred around the neck of the AV. Figure 4.1 shows an increase in total load at 15:00 as the net was lowered onto the AV.

Once centred the turnbuckles could be anchored and tensioning begun; initially they were anchored via strips of 60 cm long steel. Again, the construction stretch needed removing, one sub-net was tensioned at a time. For this task there were two teams: one at either end of the sub-net and one person monitoring the tensions of each rope making up the sub-net via DeltaV, using the load cells at each leg of the net while making sure the hold-up

load did not pass the safe limit. The person monitoring DeltaV would coordinate the tensioning, making sure each side of the net was kept at approximately the same tension, to avoid it shifting off centre. This was done in relatively small increments to allow for the friction of the rope moving across the AV. As soon as one sub-net was up to tension, the sub-net at 90° to it could be brought up to tension, and so on. When all sub-nets had been tensioned, the strips of steel anchoring the turnbuckles were replaced for strips of half the original length, and the tensioning process repeated, until the strips could be removed altogether. To remove the last of the construction stretch , the final stage of tensioning brought the sub-nets up to 14000 lbs at each load cell. To achieve the higher tension, the turnbuckles had to be removed, and hydraulic jacks had to be used in their place

## 4.2 Pretensioning and performance of the Rope System

A detailed summary of the expected performance of the SNO+ rope system is provided in [93]. While this paper's content goes beyond the scope of this thesis, it provides a good presentation of the pretensioning results and serves well to motivate the need for an additional system to monitor the AV's shape and position. Thus, much of what follows will be a summary of the main results of this paper.

The purpose of pretensioning the ropes was to remove as much construction stretch as possible, minimising the extension of the ropes during operation and gaining a better understanding of the ropes' behaviour at near operational load. By monitoring the extension of the ropes during tensioning, it is possible to determine Hooke's constant. Knowing Hooke's constant for the ropes should allow for an accurate prediction of the ropes' behaviour during operation. During tensioning the load at each hold-down rope was individually increased to 14000 lbs, just below the operating load during scintillator-fill of 14100 lbs. This load is spread between the hold-up ropes, keeping them below their safe limit.

### 4.2.1 Monitoring Creep

Here, the system currently used to monitor the AV's position and shape will be discussed, along with any drawbacks. The monitoring system has two subsystems, load cells that monitor the load on each rope, and the equator monitors which use the extension of four strings looped over pulleys on the deck and attached at equidistance around the AV

equator to provide a measurement of the movement of the AV relative to the deck.

For the centring procedure it was possible to directly measure the position of the AV's neck within the aperture in the deck, this will not be possible when the detector is running as the aperture will be sealed, though throughout commissioning it provides the most accurate measurement of the AV's location.

As in SNO, the equator monitors provide a continuous measurement of the the AV's equator position relative to the deck. Without a zero point calibrated, they can provide only a measurement of any shift in position. During the hold-up rope replacement, the equator monitors had to be detached. It became apparent that since their installation, they had suffered from corrosion, see Figure 4.2. The corrosion prevents the pulleys from moving freely, this presents itself as what looks like a digitisation error on the readout of the equator monitors, stepping instead of a smooth curve. Another problem that became apparent, was that a cord from an equator-monitor, which should run parallel with the hold-up rope had been coiled around it. Thus this equator-monitor can no longer provide a direct measurement of the shift, since the cord it uses is now looped around a rope prior to its connection at the equator. Finally the equator monitors cannot be used to provide exact measurements of the ropes' length, without knowing the position of the turnbuckles on the rope net or the length of the threaded bar at the whippertrees. Since neither the whippertree or turnbuckles are instrumented, there is an additional error at these adjustment points which should be included in any calculation of length.



Figure 4.2: *Photograph showing corrosion to one of the pulleys of the equator-monitoring system.*

Load cells are used to monitor the load at each of the hold-up ropes and every leg of the rope net. A measure of the load each rope is under can be used as an indicator of deformation in the AV, rope performance, and to help determine Hooke's constant for the ropes.

The range of the hold-up load cells is 50000 lbs, however the hold-up load at each rope should not exceed 14000 lbs, so not even half of the full range is used, limiting the resolution. The hold-down load cells have a range of 20000 lbs, which is better suited to their operational range of up to 14100 lbs.

As mentioned in Chapter 3, the bridge input conditioners have a temperature coefficient of  $0.05\% \text{ }^{\circ}\text{C}^{-1}$ . While in normal operation this should not be an issue as the temperature on deck will remain constant. Shortly after the installation of the rope net the air-conditioning for the cavity and deck failed, causing the temperature to increase by more than  $15^{\circ}\text{C}$  for the period of April to May of 2012.

According to the manufacturer, the load cells should be returned to them and re-calibrated every 13 months; this is not possible when the detector is running. A crude calibration took place. With the load cells in-situ shortly after the hold-up ropes had been replaced, a hydraulic jack was used to raise the whippertrees from the load cells, in order to find its zero reading. During this calibration it became apparent that the load cell had a non-zero response time, taking a few minutes to fall to its minimum value.

There is some friction in the balancing of the whippertrees, this friction is a combination of the pivot at the whippertree and the rope moving through the belly plate. As mentioned the thrust bearings at the whippertree should reduce the torsion in the ropes, but as with all bearings they are not 100% efficient. Friction is also present for the rope net as it moves across the surface of the AV.

## Software

The outputs from the load cells and equator monitors are stored in the DeltaV control system. For security reasons, it is vital the DeltaV system has no link to an external network, since as well as monitoring, it can be used to control various systems. This made extracting the data for analysis non-trivial. DeltaV has built in tools that allow for parameters to be extracted to a Microsoft Excel spreadsheet at intervals down to one second, though to save memory one minute intervals were used. Once a spreadsheet had

been setup with all the relevant parameters and a given time window set, the data could be saved to a text file and transferred to a machine with network access, the data was then converted to a series of histograms and saved in a root file for analysis, as shown in Figure 4.3.

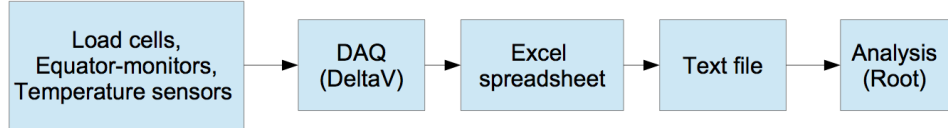


Figure 4.3: *The data extraction process from the DeltaV system.*

#### 4.2.2 Results

##### Hooke's Constant

Tests by Yale Cordage on samples of the 0.75 inch (1.9 cm) diameter hold-up and 1.5 inch (3.8 cm) net ropes, found Hooke's constant to be  $4490 \pm 702$  lbs/inch and  $14200 \pm 1200$  lbs/inch respectively. The ratio between these two values,  $3.08 \pm 0.36$ , agrees well with the ratio of the ropes' weights, 3.28.

To determine this value for the hold-up ropes in situ, all ropes are treated as a single spring. With Hooke's law given as:

$$T = k(x - x_0), \quad (4.1)$$

where  $T$  is the tension on the hold-up ropes,  $x$  the length of the ropes, and  $x_0$  the original rope length. The load cells provide a measure of the tension and the equator monitors give the rope length, so data from pretensioning can be analysed to find Hooke's constant,  $k$ .

To minimise the effects of creep, data was selected from periods of tensioning, lasting a few hours at a time, where the tension of the ropes changed relatively quickly and the total hold-up load was greater than 105000 lbs. For such data sets, with a sufficient number of points,  $k$  was determined through fitting a straight line, as shown in Figure 4.4(a).

Plotting the various values of  $k$  against time showed no significant change over a five month period, see Figure 4.4(b). Hooke's constant for the hold-up ropes was found to be

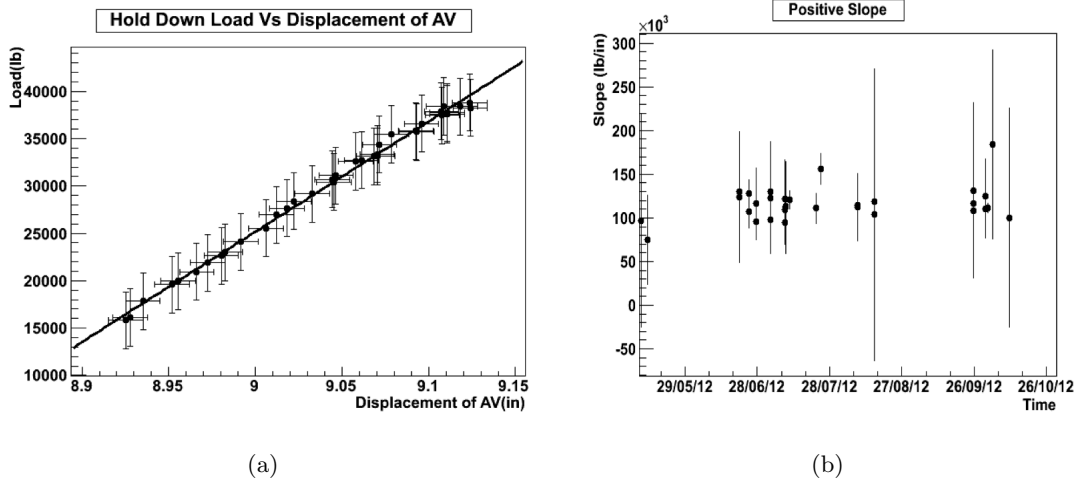


Figure 4.4: Left: A typical data set for a period of tensioning, used to determine Hooke’s constant through a straight line fit. The fit produced a gradient of  $1.16 \times 10^5$  in/lbs. Taken from [93]. Right: The variation in Hooke’s constant over a five month period.

$116000 \pm 19000$  lbs/inch, which is in agreement with twenty times the expected value for 0.75 inch rope,  $89800 \pm 14400$  lbs/inch.

### Construction Stretch

From the results of tests carried out by Yale Cordage on samples of Tensylon to find the limits of the rope [94], it was predicted that the AV would sink during pretensioning by only  $3.6 \pm 1$  cm. However for the period May through November 2012 the AV sank by  $7.1$  cm [93], and while the AV was stationary with both hold-up and hold-down ropes under tension, the ropes were seen to stretch through an observed reduction in tension. The large difference is likely due to Yale’s test only running for a comparably short time period, and the temperature of the cavity and deck during this period.

### Temperature Dependence

For a period of roughly one month of the pretensioning process, the air-conditioning for the deck and cavity failed, the temperature fluctuated between  $20^\circ\text{C}$  and  $40^\circ\text{C}$  depending on the work taking place in the vicinity. For this period the correlation between cavity temperature and the total load was found to be  $416 \text{ lbs } ^\circ\text{C}^{-1}$  [93].

For fibres similar to Tensylon tests have shown that at  $10^\circ\text{C}$ , 1% creep for a ten year run is expected [78]. If temperature increases by a factor of two the rate of creep is increased

by a factor of ten [93]. The temperature of the cavity and deck during the pretensioning process would have contributed to the observed stretch.

## Deformation of AV

The rope net was designed to spread the load evenly across the surface of the AV. Figure 4.5 shows the finite element analysis of the design. In normal operation, when the AV is filled with scintillator, the upward force is from the whole upper hemisphere of the AV, though during the tensioning process the upward force is provided by the hold-up ropes at the belly plates. So any deformation of the AV would have shown up as variation in the distribution of load between the hold-up load cells, as different sub-nets were tensioned.

In normal operating conditions the maximum tension stresses predicted by the FEA are localised inside the AV under the knots of the net with a maximum value of 1.9 MPa whereas the allowable long term tension stresses are 4.1 MPa. According to [95] damage is expected to appear after 12 years if stressed to 4.1 MPa. In normal operation, the AV is expected to deform by no more than 1 cm [96].

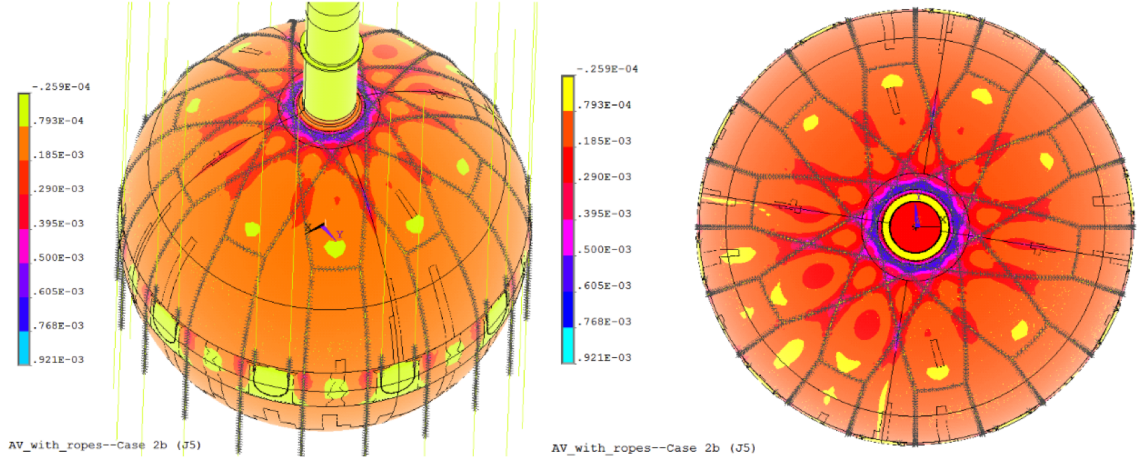


Figure 4.5: *The FEA simulation of the maximum strain in the acrylic caused by the hold-down rope net during the normal working conditions. Maximum stresses predicted by FEA are localised inside the AV under the knots of the net. The units shown are relevant only to the FEA software used, the maximum corresponds to a value of 1.9 MPa. Taken from [97]*

The distribution of load between the hold-up load cells remained the same, regardless of which sub-net was tensioned. This showed the AV behaved as a rigid body, as, since the hold-down net was centred and load always applied symmetrically, a change in the distribution would have signified a deformation AV.

### 4.3 Conclusion

Based on the performance of the ropes during pretensioning, it was decided that the AV position should be set 5 cm below centre. Pretensioning should have removed the construction stretch, and some of the early creep. The vessel will creep up due to the buoyant force, but it should not do so by more than about 5 cm over a ten years period, provided the temperature of the water is maintained at 10°C.

In the worst case scenario, construction stretch continues and the vessel will rise by no more than an additional 9 cm. However, the long term relaxation has been consistent with what was expected for creep in the ropes.

These predictions will be tested during the “Float the Boat”, when the cavity is filled with UPW causing a buoyant force to be applied to the AV. If large movements are observed, the UPW will have to be drained and the ropes shortened.

As mentioned, knowing the AV’s position and shape is vital in defining the FV. There remain large uncertainties in the measurement of both the load on the ropes and the position of the equator, and only limited techniques in place to monitor the deformation of the AV.

A system such as TELLIE should be used to continually monitor the position and shape of the AV, by measuring the time of flight for light pulses injected at the PSUP and reflected from the surface of the AV. TELLIE has injection points at every node of the PSUP, providing ample coverage to precisely locate the AV within the PSUP, any shift in position or deformation would be detected as a change in the time of flight for reflected photons. As will be shown in Chapter 8, using the reflections the AV can be located with an accuracy of a few cm, less than the expected reconstruction resolution.

## Chapter 5

# The TELLIE LED and Driver Circuits

This chapter will describe the selection and characterisation of the TELLIE LED, and the development of the TELLIE LED driver. Beginning with LED properties that affect the time profile of their optical pulse, the spectral limitations imposed by the scintillator will be discussed. The criteria for the drivers will be introduced and the development of two different LED drivers will be discussed and their performance presented.

### 5.1 The TELLIE LED

LEDs have been used as a timing calibration source for scintillator detectors since the 1980's [98]. The development of high intensity blue LEDs in the mid 1990s made them an appealing option for many detectors, such as MINOS [99]. Indeed, the idea to use LEDs in SNO+ is not a new one, it was attempted in SNO although the LED and electronics were mounted on the PSUP, failing quickly. It is speculated that the failure was due to corrosion in UPW. Recent developments in LED manufacture have led to them becoming faster, brighter, and more efficient, making them comparable with lasers as calibration sources.

For the purposes of TELLIE, or any timing calibration system, it is vital that the time profile of the LED pulse be as short as possible, ideally of the same order as the lower limit on the resolution of whatever is being calibrated. In the case of SNO+ the lower limit on the time resolution of the PMTs is the intrinsic jitter on the time it takes for an electron

to propagate from the photocathode to the first dynode, or as it is known in SNO+: the Transit Time Spread (TTS), which has been shown to be 1.7 ns [57].

Another criterion for selecting an LED is set by the absorption spectrum of the medium the LEDs have to illuminate. For a timing calibration it is also important that an appropriate amount of prompt light makes it to the PMTs, and that the PMT is sensitive to the light reaching it.

### 5.1.1 LED Timing Properties

Here, a commonly used approximation for the LED modulation characteristics [100] is used. In this approximation, the LED is described as an active region of volume  $V_a$  driven by a constant forward current  $I_f$  switched on at  $t = 0$ . Electrons are injected into  $V_a$  increasing the carrier concentration  $n_a$ . The emitted rate of photons per volume is  $dn_\gamma/dt = n_a/\tau_e$  where  $\tau_e$  is the average time for a charge carrier to recombine and generate a photon. For a constant  $I$ , which switches on instantaneously once the voltage across the LED reaches a threshold, thus neglecting the large stationary charge densities either side of the LED's active region and their inherent capacitance, the emitted rate of photons is:

$$\frac{dn_\gamma}{dt}(t) = I_f \cdot \frac{1}{e V_a} \cdot \frac{\tau_l}{\tau_e} \cdot \left(1 - e^{-\frac{t}{\tau_l}}\right). \quad (5.1)$$

Here  $\tau_l$  is the average time for a charge carrier to be lost from the active volume and  $e$  is the charge of the electron.  $\tau_l$  and  $\tau_e$  are intrinsic to the pn-junction and not variable. Therefore, Equation 5.1 implies that the current through the pn-junction is critical for the time to reach a desired photon emission rate, i.e., a increasing the current will reduce the rise time. A similar argument applies for the fall time on application of a reverse current  $I_r$ : applying a current in reverse bias, sweeps charge carries from  $V_a$ , reducing the fall time of the LED light pulse. The limiting factor to the amount of current that can be applied to an LED is its resistance. The resistance is therefore the most important parameter to consider when seeking an optimal time profile [59].

### 5.1.2 Spectral Constraints

As the Rayleigh scattering of a medium quickly drops with increasing wavelength, the LEDs should have the highest possible peak wavelength in order to achieve the optimal

direct transmission. The limiting factor is the quantum efficiency of the PMTs, which drops quickly at higher wavelengths [101]. Given the expected absorption spectrum of the Te doped LAB-based scintillator and the quantum efficiency of the SNO+ PMTs, the optimal peak wavelength is close to 500 nm. These spectra, together with the measured wavelength distribution of the selected LEDs, are shown in Figure 5.1.

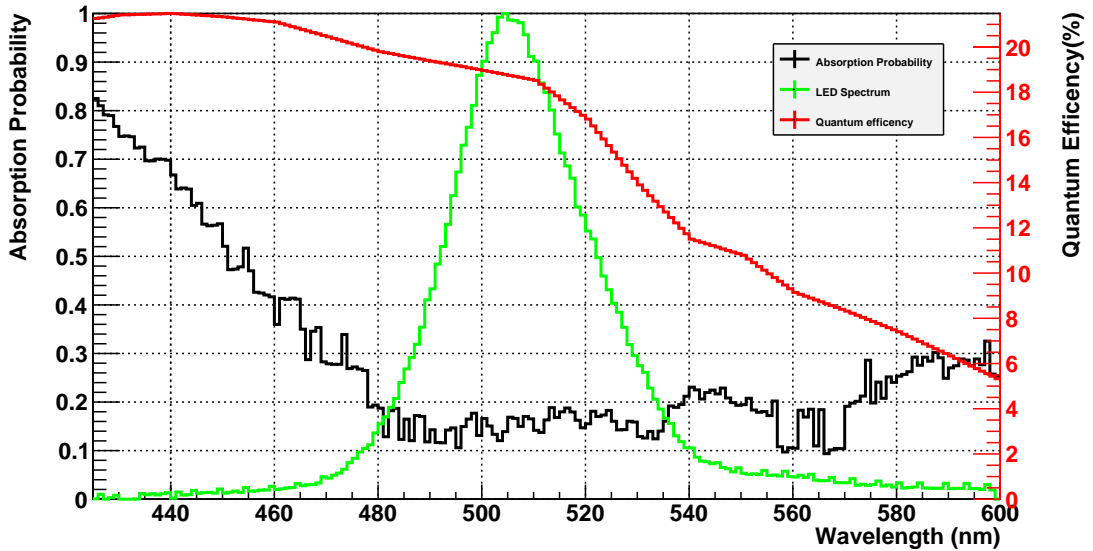


Figure 5.1: The absorption probability spectrum of  $^{130}\text{Te}$  doped LAB and PPO (black), the average spectrum for all 96 LEDs (green), in arbitrary units, and the SNO+ PMT quantum efficiency (red)[101].

One of the deciding factors in selecting  $^{130}\text{Te}$  over the  $^{150}\text{Nd}$ , was its optical purity. This is illustrated nicely by comparing the absorption probability spectrum for Nd-doped scintillator, Figure 5.2, with Figure 5.1. The peak wavelength selected for a Nd-doped scintillator was 435 nm. There would have been substantially more adsorption and a slight increase in scattering, though the calibration would still have been possible with a longer running time.

It should be noted that the final scintillator mix has yet to be decided upon. Any additional components in the scintillator, such as wavelength shifters, are likely to alter its absorption probability spectrum and care will have to be taken to ensure a sufficient amount of prompt light can still reach the PMTs.

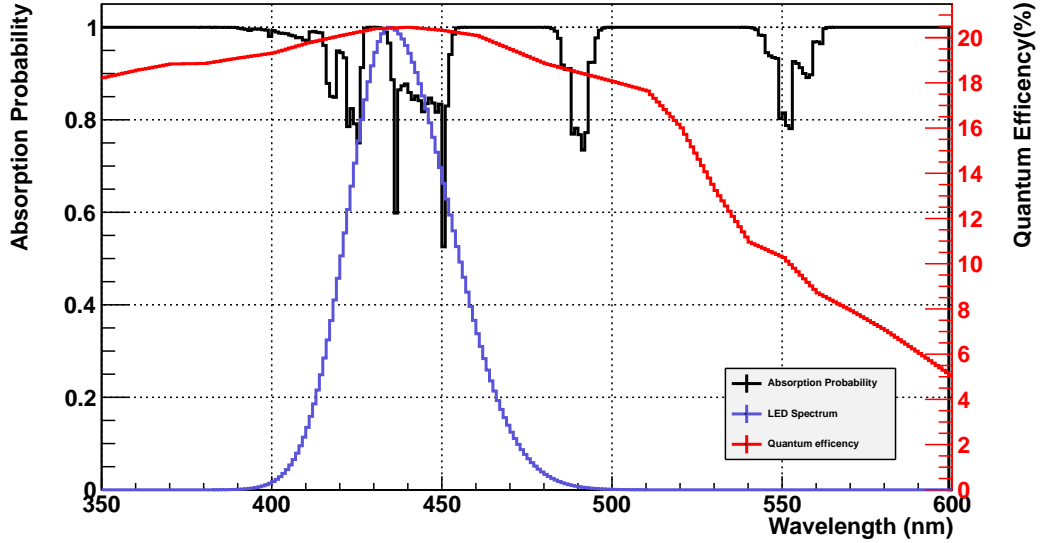


Figure 5.2: The absorption probability spectrum of  $^{150}\text{Nd}$  doped LAB and PPO (black), the average spectrum for all 96 LEDs (purple), in arbitrary units, and the SNO+ PMT quantum efficiency (red)[101].

### 5.1.3 LED Availability

Initially, an LED had been selected from a distributor in Europe (Roithner Lasertechnik), however after testing a sample batch of LEDs the distributor was unable to supply LEDs of the same specification. It was decided that we should approach a manufacturer directly. Brite LED of Florida<sup>1</sup> produce a large number of LEDs from ultraviolet to infrared, with relatively low resistances. They were happy to deal with us directly and guarantee that we would receive LEDs from the same production runs as those we tested. They also pre-screened the LEDs removing any outliers, assuring minimal variation in peak wavelength and intensity.

### 5.1.4 LED Selection

A number of Brite LED's visible light LEDs were tested at Sussex using an Ocean Optics USB2000 spectrometer, with data analysed in ROOT [102]. The selected LED [103] has a peak wavelength of 505 nm and a differential resistance of only  $10\ \Omega$  in the near linear region of forward current against forward voltage above the LED threshold voltage. Typically, the resistance of a standard LED is between 40 and  $100\ \Omega$ .

---

<sup>1</sup><http://www.briteled.com/contact.htm>

Figure 5.1 also shows the average spectrum for all 96 LEDs selected for TELLIE. The circuit used to drive the LED for these measurements was simply a resistor in series with the LED, supplied with a constant voltage. Ocean Optics Maya 2000 Pro was used with their SpectraSuite to record each spectrum, for analysis as above. The spectra were found to be identical regardless of whether the LED was pulsed or at constant voltage. These measurements will be described in greater detail in Chapter 6.

## 5.2 Driver Development

### 5.2.1 Requirements

To understand the requirements of the TELLIE driver, constraints on the dynamic range of three driver properties need to be defined; the pulse intensity, pulse time profile, and operating frequency. The constraints are ultimately set by the desired precision and running time of the timing calibration. The TELLIE system has to be capable of providing a measurement of the time offset of all PMTs to a precision of 0.5 ns within one day of low rate data taking [59]. The running time of the calibration is dependent upon these three driver properties; what follows is an approximation serving to demonstrate the relationship between them; although the time distribution of an LED pulse is not exactly Gaussian, for simplicity it is assumed so here. For a Gaussian, the precision on the mean,  $\Delta\mu$ , is given by:

$$\Delta\mu = \frac{\sigma}{\sqrt{N}},$$

where  $N$  is the number of PMT hits and  $\sigma$  the standard deviation of the distribution. The number of hits is simply the PMT hit probability,  $P_{hit}$ , multiplied by the number of LED pulses,  $N_{pulse}$ . So it is possible to calculate  $N_{pulse}$  needed to achieve a desired  $\Delta\mu$ , in turn dictating the duration of calibration, from:

$$N_{pulse} = \frac{\sigma^2}{P_{hit} \times \Delta\mu^2}.$$

So to minimise  $N_{pulse}$  the distribution's  $\sigma$  must be minimised. Since  $\sigma$  is described by the FWHM of the pulse, it is important that this time is minimised. As mentioned in Chapter 3 the time resolution of the PMTs is limited by the Transit Time Spread (TTS),

1.7 ns, therefore pulse widths of this order are desirable.

As mentioned the time distribution of the LED pulse is not exactly Gaussian, in fact it is better modelled as a combination of two half-Gaussians sharing the same mean with differing  $\sigma$ , see Figure 5.3.

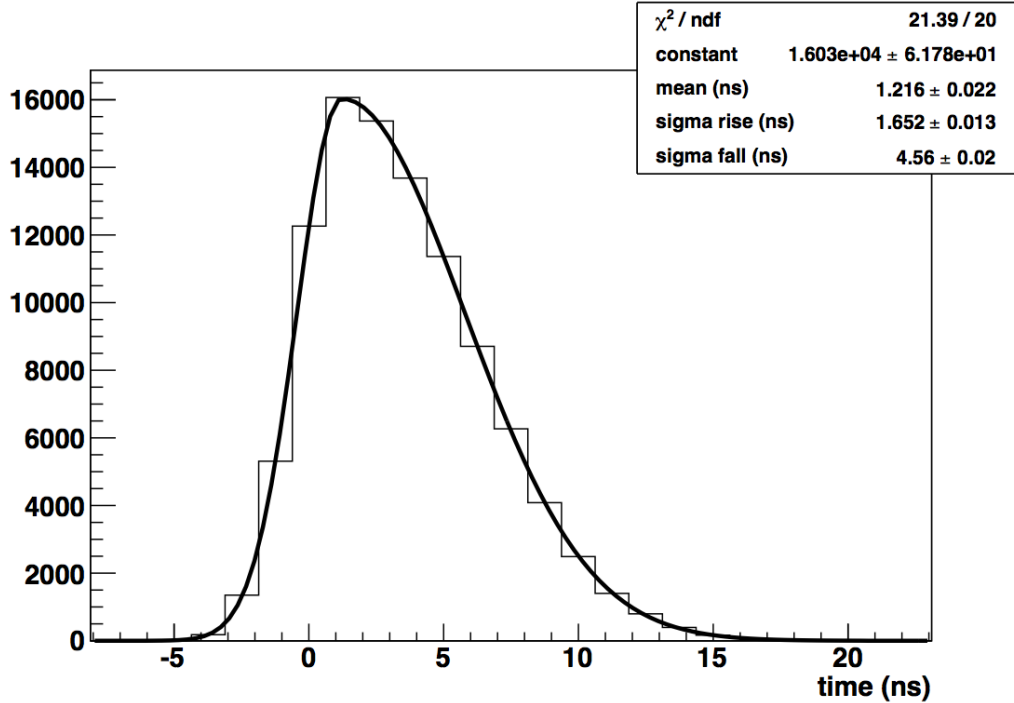


Figure 5.3: *Approximation of a timing pulse as produced by TELLIE. The fit is a combination of two Gaussians with different sigmas for rising and falling edges*

Combining two Gaussians complicates the precision on mean slightly, but it has been empirically shown to be described by [104]:

$$\Delta\mu = \frac{\text{FWHM}}{\sqrt{N}},$$

so the argument that FWHM should be minimised in order to minimise the running time holds, and we now have a more precise expression for calculating the necessary running time of the TELLIE system. Yet, we still need to define  $P_{hit}$ , which is in turn dependent upon both the intensity of the injected pulse and the angle of the hit PMT with respect to the direction of the injected pulse.  $P_{hit}$  can be determined using Monte Carlo [105], by simulating the injection of pulses of varying intensity. As mentioned in Chapter 3, the intensity range of the injected pulses needs to allow for both SPE and MPE hits across all

PMTs. The angular profile of the injected pulse is an important factor; a PMT inline with the injecting fibre's direction will have a higher probability of being hit than a PMT at an angle to it. Considering an injection point we define two regions among the hit PMTs, a central spot and a fringe. The angle defining the limit of the central spot is the angle at which the injected pulse is at 20% of its maximal intensity; this has been measured to be  $14.5^\circ$  [106], this measurement will be discussed in the following chapter. So, the central spot contains hit PMTs at angles less than  $14.5^\circ$  and the fringe is between  $14.5$  and  $29^\circ$  for the angle from the fibre direction. Figure 5.4 shows how the angle is defined.

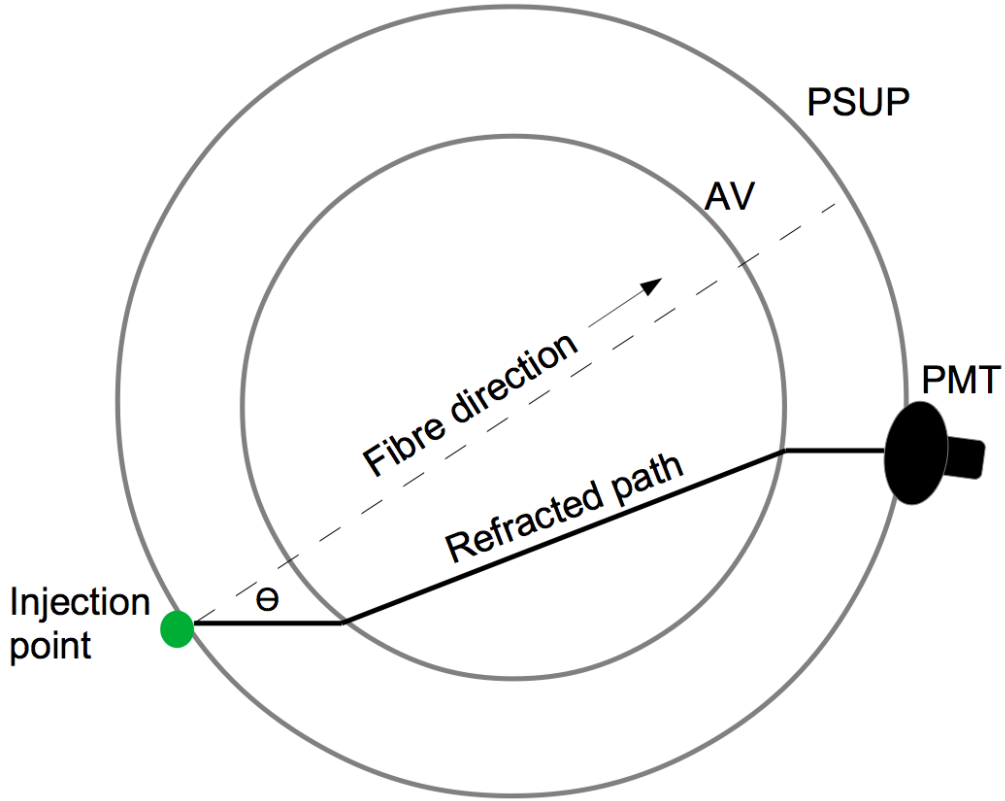


Figure 5.4: A diagram showing how the injection angle is defined, based on [107].

The Monte Carlo provides  $P_{hit}$  as a function of injected angle, which is shown for 0.3%  $^{130}\text{Te}$  loading at pulse intensities of  $10^3$ ,  $10^4$ , and  $10^5$  photons in Figure 5.5.

Given the mean total hit probability (single + multiple photon), as in Figure 5.5, it is possible to calculate the probability of single and multiple photons striking a PMT at a given angle relative to the fibre direction using Poisson statistics:

$$P_k = \frac{\mu^k}{k!} e^{-\mu},$$

where in this case  $k$  is the number of photons and  $\mu$  the mean probability at a given angle.

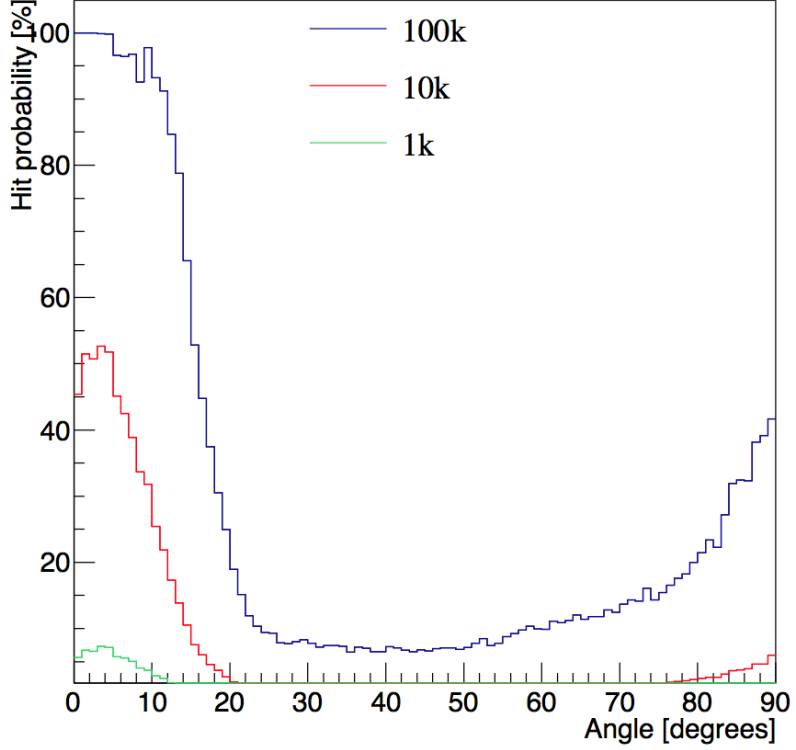


Figure 5.5: Total hit probabilities (both single and multiple photon hits) as a function of injected angle at 0.3%  $^{130}\text{Te}$  loading for pulse intensities of  $10^3$ ,  $10^4$ , and  $10^5$  photons. The increased hit probability above  $60^\circ$  is due to scattering around the injection point and light reflected back from the near surface of the AV

Thus the probability of single photon hit is:

$$P_1 = \mu e^{-\mu},$$

and the probability of multi photon:

$$P_{2+} = 1 - P_0 - P_1 = 1 - (1 - \mu)e^{-\mu}$$

With these probabilities we can now calculate  $N_{pulse}$  needed to achieve the desired accuracy, using:

$$N_{pulse} = \frac{FWHM^2}{P_{hit} \times \Delta\mu^2}. \quad (5.2)$$

The operating frequency is the last factor limiting the running time of the calibration. The upper limit is set by the capability of SNO+ DAQ, as described in Chapter 3, which

is about 10 kHz. Constant monitoring requires a lower frequency of roughly 10 Hz. The predicted running times are shown with the hit probabilities for central and fringe PMTs in Table 5.2.1. To get the running time for the entire PMT array from that of a single injection, it is simply multiplied by the number of injection points, 92 (91 PSUP nodes and 1 at the neck aperture of the PSUP), as it is not possible to operate different injection points simultaneously.

Phase:	Photons per pulse:	Total Hit Probability			Single Photon Hit Probability			Run Time Single Fibre			Total Run Time		
		Centre:	Fringe:	Centre:	Centre:	Fringe:	Centre (s):	Fringe (s):	Centre (hr):	Fringe (hr):	Centre (hr):	Fringe (hr):	Centre (hr):
UPW	1000	$2.73 \times 10^{-2}$	$2.65 \times 10^{-3}$	$2.69 \times 10^{-2}$	$2.58 \times 10^{-3}$	$5.35 \times 10^2$	$5.58 \times 10^3$	$1.37 \times 10^1$	$1.43 \times 10^2$				
	10000	$2.37 \times 10^{-1}$	$2.56 \times 10^{-2}$	$2.06 \times 10^{-1}$	$1.98 \times 10^{-2}$	$6.98 \times 10^1$	$7.28 \times 10^2$	$1.78$	$1.86 \times 10^1$				
	100000	$8.84 \times 10^{-1}$	$2.01 \times 10^{-1}$	$2.50 \times 10^{-1}$	$2.60 \times 10^{-1}$	$5.76 \times 10^1$	$5.53 \times 10^2$	$1.47$	$1.41 \times 10^1$				
LABPPO	1000	$3.87 \times 10^{-2}$	$2.66 \times 10^{-3}$	$3.79 \times 10^{-2}$	$2.56 \times 10^{-3}$	$3.80 \times 10^2$	$5.62 \times 10^3$	$9.70$	$1.44 \times 10^2$				
	10000	$3.13 \times 10^{-1}$	$2.64 \times 10^{-2}$	$2.58 \times 10^{-1}$	$1.84 \times 10^{-2}$	$5.58 \times 10^1$	$7.83 \times 10^2$	$1.43$	$2.00 \times 10^1$				
	100000	$9.14 \times 10^{-1}$	$2.13 \times 10^{-1}$	$2.11 \times 10^{-1}$	$2.06 \times 10^{-2}$	$6.82 \times 10^1$	$6.99 \times 10^2$	$1.74$	$1.79 \times 10^1$				
$\text{LAB+PPO} + (0.3\%) \text{Te}$	1000	$3.62 \times 10^{-2}$	$2.49 \times 10^{-3}$	$3.55 \times 10^{-2}$	$2.40 \times 10^{-3}$	$4.05 \times 10^2$	$5.99 \times 10^3$	$1.04 \times 10^1$	$1.53 \times 10^2$				
	10000	$2.96 \times 10^{-1}$	$2.44 \times 10^{-2}$	$2.47 \times 10^{-1}$	$1.74 \times 10^{-2}$	$5.83 \times 10^1$	$8.28 \times 10^2$	$1.49$	$2.12 \times 10^1$				
	100000	$9.04 \times 10^{-1}$	$1.99 \times 10^{-1}$	$2.25 \times 10^{-1}$	$2.13 \times 10^{-2}$	$6.40 \times 10^1$	$6.76 \times 10^2$	$1.64$	$1.73 \times 10^1$				

Table 5.1: Hit probability from [105] and subsequent TELLIE running times for different phases of SNO+. Assuming a 504 nm LED pulse width of 6 ns and a desired accuracy of 0.5 ns running at 10 Hz.

To reiterate the requirements: the TELLIE system has to be capable of providing a measurement of the time offset of all PMTs to a precision of 0.5 ns within one day of low rate data taking. To do this the FWHM of the time profile should be minimised, pulses of the same order as the TTS, 1.7 ns, are desirable. The upper limit of operating frequency is set at 10 kHz by the SNO+ electronics, with order 10 Hz as a lower limit. The pulse intensities should be adjustable between  $10^3$  and  $10^5$  photons per pulse, to ensure prompt SPE and MPE at PMTs inline with the injected fibre direction and those at a greater angle to it.

Two LED drivers were developed for TELLIE: a driver based around a proprietary laser diode driver was developed between Sussex and Leeds, and a low cost driver made from off-the shelf components was developed at Sussex. Although the proprietary laser diode driver was selected for TELLIE in the end, the development of both drivers are presented below.

### 5.2.2 Characterisation set-ups

Before the drivers are introduced, the method used to characterise the time profiles and intensities of their pulses will be discussed.

For convenience, in both the intensity and time profile measurements the drivers are mounted in the same driver boxes as those of SNO+. The driver box will be discussed in greater detail in the following chapter. The driver box allows drivers and LEDs to be coupled via a 0.75 m length of optical fibre, terminating at a bayonet type (ST) connection at the box's edge. For initial measurements the fibre used to couple the driver and LED to the measuring PMT was only the 0.75 m section. For the final characterisation of the selected driver, the fibre combination used was as it would be in the detector: the 0.75 m, a 2.00 m patch, and a 45.00 m length.

All fibres used are the same specification as those installed in the detector, duplex polymethyl-methacrylate (PMMA) polyethylene jacketed optical fibre [108].

The results of the characterisation have been added to RAT, in order to better model the expected performance of the TELLIE system.

### Intensity Measurement set-up at Sussex

The intensity measurement is relatively simple. A driver and LED are connected to a PMT via an optical fibre, which in turn is connected to an oscilloscope. Given the PMT gain and quantum efficiency, QE, as a function of wavelength, it is possible to calculate the number of photons per pulse from the integration as measured by the oscilloscope.

The PMT [109] was calibrated by Hamamatsu on the 30/10/2010 and at a control voltage (used to set the high voltage [110]) of 1 V the gain was  $1.80 \times 10^6$  electrons per photon. From the cathode radiant sensitivity of  $77.4 \text{ mAW}^{-1}$  the QE was calculated to be 19.2 % at 503 nm. The number of photons  $N_{\text{Photons}}$  per pulse is then given by:

$$N_{\text{Photons}} = \frac{A}{R \cdot e \cdot G \cdot QE}, \quad (5.3)$$

where  $A$  is the area of the pulse (Vs)  $R$  is the resistance of the connection between the PMT and oscilloscope ( $50 \Omega$ ),  $G$  is the PMT gain at a given control voltage and  $e$  is the charge on an electron.

The driver intensity was adjusted until the integrated pulse area matched the predetermined values for  $10^3$ ,  $10^4$ ,  $10^5$ , and  $10^6$  photons per pulse.  $10^6$  photons per pulse is a higher intensity than required; this is due to the expected attenuation of the optical fibre and losses at connections. The attenuation will be discussed along with other fibre properties in the following chapter. Once it had been established that the driver could achieve the desired intensity range, the driver setting were recorded in order to characterise the time profile at these intensities.

### Time Profile Measurement

The time profile measurement uses a single photon counting technique, similar to those previously used for delayed coincidence measurements in scintillator [111]. The DAQ is a simple coincidence set-up between the trigger for the driver and a signal from a low background PMT, allowing the suppression of most of the PMT noise. The signals are fed to NIM, then CAMAC modules to be recorded and displayed by a TDC acquisition routine in LabVIEW. The operation of the set-up is described in detail here [112], a schematic of its various components is shown with corresponding base setting in Figure 5.6.

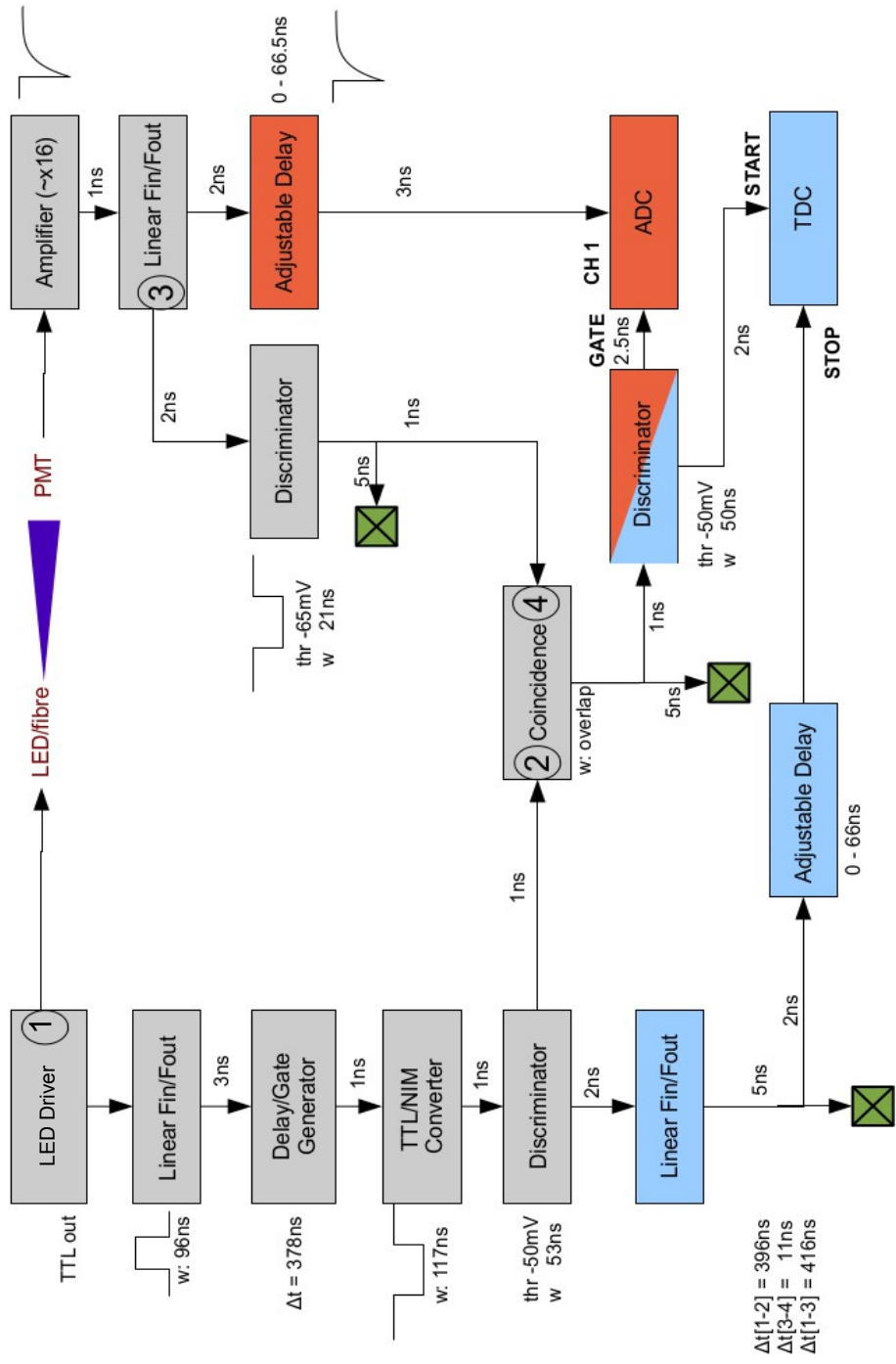


Figure 5.6: The Sussex single photon counting set-up used to measure the time profile of LED pulses. The TDC has a resolution of 25 ps. Adapted from [112].

The PMT used is of the same type as the that of the intensity measurement, though it is certified as having low dark count rate and thus suitable for photon counting [109]. It is important to ensure the set-up is operating in SPE mode prior to taking the time profile measurement, this is done by triggering on the gate generated by the driver trigger as opposed to the PMT signal, the light intensity was then reduced using Neutral Density (ND) filters so that the baseline PMT signal was comparable with the noise, i.e. “zero pulses” were observed more and more often, hence the need to trigger on another signal. To confirm SPE mode, an ADC spectrum was taken, see Figure 5.7 which shows the pulse height distribution in single photoelectron mode. At very low light level photon detection is hit or miss and thus PMTs follow Poisson statistics: the first peak shows the “0 hit”, i.e. a trigger without a PMT signal. The second, “1 hit”, shows the charge emitted after emission of a single photoelectron [112].

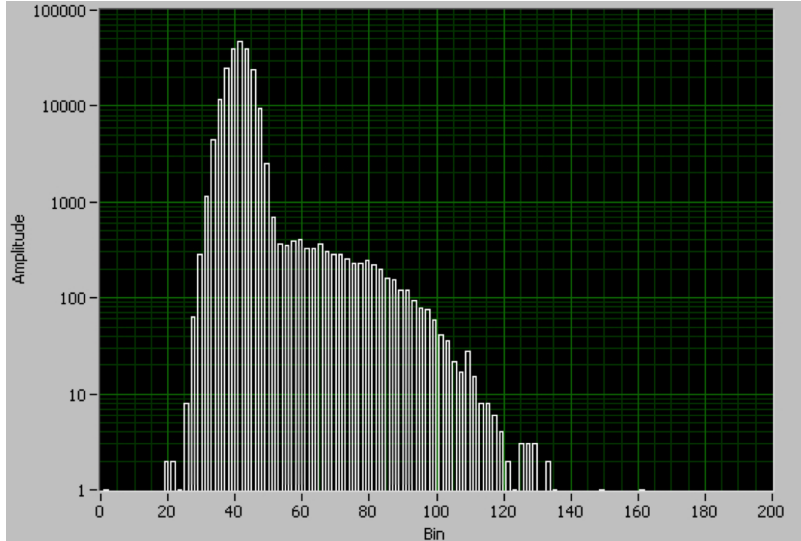


Figure 5.7: An ADC spectrum confirming the PMT is operating in single photon mode; the peak shows the trigger firing without a PMT signal, the shoulder to the right of the peak is the charge emitted upon detection of a single photon [112]. The units of the x axis is the ADC channel, proportional to integrated charge.

With the driver set to pulse intensities of  $10^3$  photons, the set-up had been tuned to SPE using Neutral Density (ND) filters, the settings could be left unchanged with only the addition of extra ND filters to accommodate for the incremental increases in the order of magnitude of pulse intensities. In reality some of the delays had to be adjusted, due the variations in the trigger to pulse time between driver types and channels. After confirming the various gates and signals were correctly set and operating in SPE mode the TDC spectrum could be taken.

Although this technique is the most accurate way to measure the time profile of the LED pulse, it is resource intensive and thus not a feasible method for characterising the entire system (92 drivers).

### 5.2.3 Kapustinsky Driver Circuit

One of the possible TELLIE drivers, developed at Sussex, was based on a design by Kapustinsky *et al*, from 1985 [98]. The original driver, shown in Figure 5.8, functions through a negative 1.5 V trigger pulse superimposed onto a 0 – 24 V DC bias. The DC bias charges the 100 pF capacitor. The trailing edge of the differentiated pulse activates the transistor pair, creating a low impedance path across the LED for the capacitor to dump its charge to ground. The inductor develops a charge opposing the discharging capacitor, that applies a reverse bias to the LED, sweeping out its active region - reducing the fall time of the LEDs pulse.

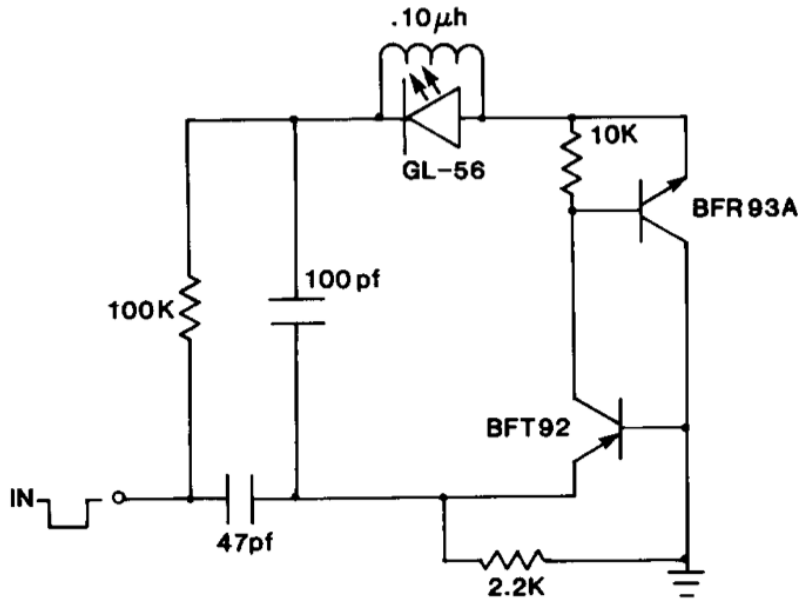


Figure 5.8: *The original Kapustinsky LED driver, developed as a calibration source for scintillator detectors [98].*

### Improvements Made Since the Original Design

Variants of this driver are already widely used in astroparticle physics experiments, such as the TUNKA-133 Cherenkov array [113] and the cosmic ray detectors AUGER and HESS

[114] as well as ANTARES [115] and the reactor neutrino experiment Double Chooz [19], for the purpose of timing and gain calibrations.

Using the circuit shown in Figure 5.8, with 370 nm and 470 nm LEDs, a group from the Institute for Nuclear Research, Moscow, reported achieving pulse widths sub 3 ns [113].

A group working on the calibration system for the upgrades to the Lake Baikal neutrino experiment [116], have achieved pulse widths of just below 2 ns at intensities of  $10^{10}$  photons per pulse [117]. To achieve the intensity, arrays of LEDs were used.

Veledar *et al* [118] have carried out extensive development work on the Kapustinsky driver. By doing away with the inductor and coupling the LED to the driver circuit via a transformer, they report sub-nanosecond pulse widths. They used 472 nm LEDs, with a typical series resistance of  $30\ \Omega$ . The minimum bias voltage, necessary to stimulate light production, was used to ensure the pulses be as short as possible.

### **Optimisation of the Circuit using Low-Resistance LEDs**

The Sussex version of the driver is shown in Figure 5.9. It was developed through iterative empirical improvements, based on the work described in [118]. Unlike all other versions of the Kapustinsky driver discussed above, which display a double pulse in their optical outputs, the addition of the diode next to the differentiating capacitor-resistor pair prevents the negative half pulse from the differentiated trigger, removing the double pulse feature. A separate trigger line is used to reduce the effect of noise on the trigger. Instead of current shaping in the traditional method, with a capacitor-resistor pair in series with the LED [100], a clamping diode was used in parallel with the LED. The clamping diode (1N4148) is a fast switching diode that upon reverse bias, due to the inductor's opposing charge, forces more current through the LED - reducing the fall time. This is the first version of the Kapustinsky driver that has been optimised for the new generation of low resistance LEDs.

Figure 5.10 shows the result of adding the clamping diode in parallel with the LED and inductor. The addition of the diode meant a larger bias voltage was needed to achieve the desired intensities, however the FWHM of the pulse was reduced by more than 50%. The addition of a clamping diode with higher resistance LEDs is a less appealing modification due to the detrimental effect on pulse intensities.

The bias voltage is the only parameter that needs to be altered in order to increase or

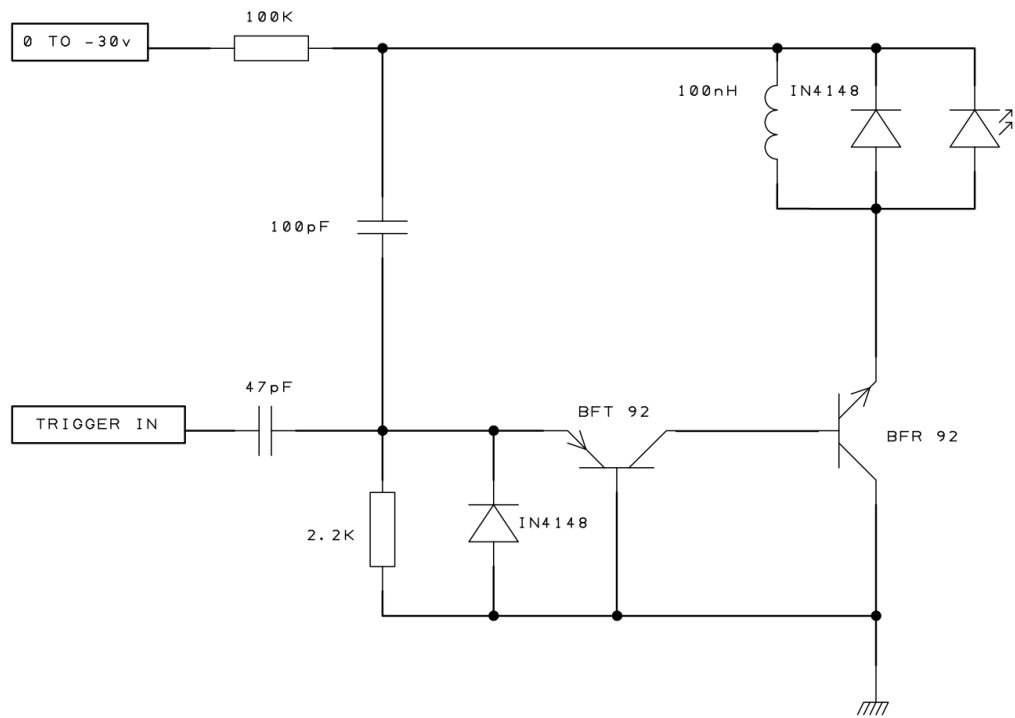


Figure 5.9: A Kapustinsky LED driver modified for faster single pulses.

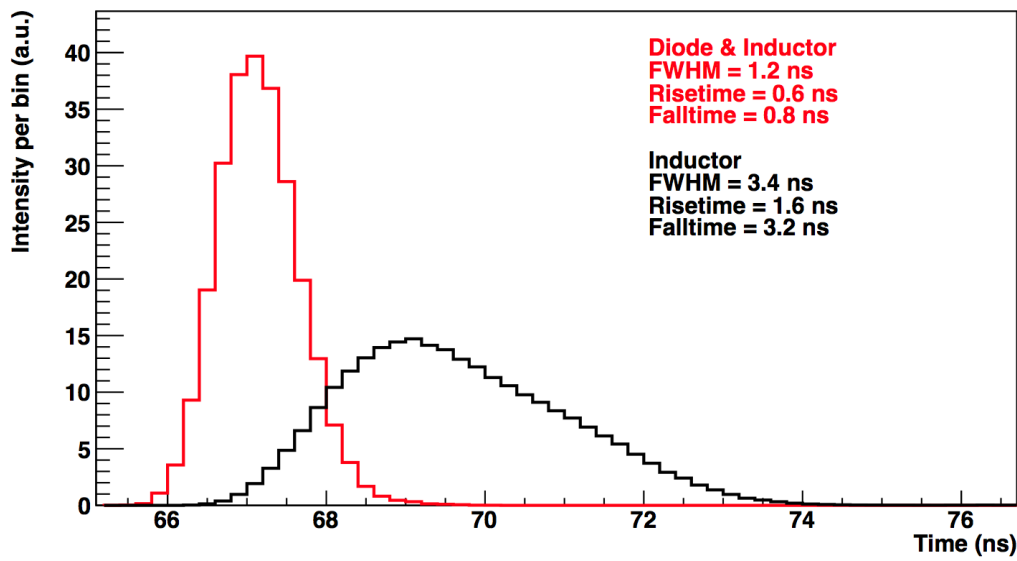


Figure 5.10: The time profile (TDC spectrum) for the Sussex driver with (red) and without (black) the clamping diode. The area of the pulses have been normalised, both pulses are of the same intensity:  $10^3$  photons.

decrease the amplitude of the LED pulse. To accommodate standard power supplies the bias range is set between 0 and 30 V. The lower voltage limit should be set just above threshold voltage  $V_{thr}$  of the LED.

## Results

All measurements were taken with a 435 nm LED<sup>1</sup> with a resistance of  $8\Omega$  and  $V_{thr} = 3.25$  V [119].

The typical time profiles for the Sussex driver operating at 10 kHz at pulse intensities of  $10^3$  and  $10^6$  photons are shown in Figures 5.11 and 5.12 respectively. This measurement was carried out with the 0.75 m length of PMMA fibre within the driver box connecting the driver-LED combination to the PMT. The effect of additional fibre on the time profile of the pulses will be presented in the following chapter.

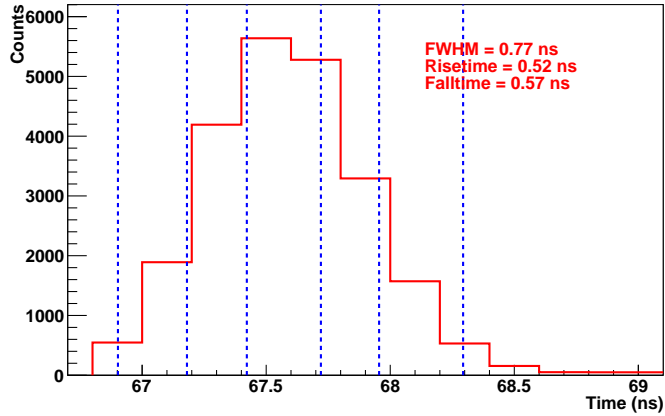


Figure 5.11: The time profile for the Sussex driver at a pulse intensity of  $10^3$  photons per pulse, running at 10 kHz. For the measurement, the driver and LED were connected to the PMT via 0.5 m of optical fibre.

Three Sussex drivers were produced, the combined results can be seen in Table 5.2. The variation, while small at sub-2%, is most likely due to differences in the LED to fibre coupling between driver-LED combinations. The LED coupling will be described in the following chapter.

---

<sup>1</sup>the LED selected prior to the switch from  $^{150}\text{Nd}$  to  $^{130}\text{Te}$

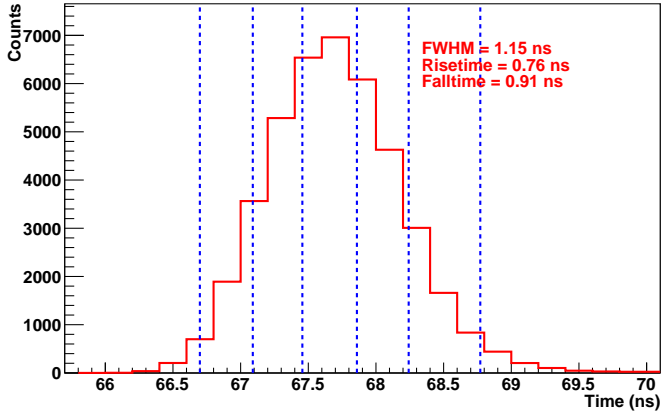


Figure 5.12: *The time profile for the Sussex driver at a pulse intensity of  $10^6$  photons per pulse, running at 10 kHz. For the measurement, the driver and LED were connected to the PMT via 0.5 m of optical fibre.*

Number of Photons	Full Width Half Maximum (ns)	Rise Time (ns)	Fall Time (ns)
$10^3$	$0.78 \pm 0.01$	$0.54 \pm 0.02$	$0.61 \pm 0.03$
$10^6$	$1.18 \pm 0.02$	$0.75 \pm 0.02$	$0.96 \pm 0.05$

Table 5.2: *Summary of time profile measurements for the Sussex LED driver at intensities of  $10^3$  and  $10^6$  photons per pulse. All measurements made with the driver running at 10 kHz. The measurement of the number of photons is performed after 0.5 m of optical fibre coupling the driver and LED combinations to the PMT. The results are the mean of three different driver-LED combinations.*

### Observations and Conclusions

The Sussex version of the Kapustinsky driver met the criteria for a TELLIE driver: it was capable of operating up to 10 kHz, producing intensities between  $10^3$  and  $10^6$  photons per pulse, with  $0.78 \pm 0.01$  and  $1.18 \pm 0.02$  ns pulse widths respectively, see Table 5.2. Less than 2% variation was seen between the drivers tested. This variation is most likely due to the coupling of the fibre to the LED.

Though there are only a few modifications in comparison with the original circuit, the performance of the driver has been significantly improved: the double pulsing has been removed, and the use of low resistance LEDs made it possible to include a clamping side to narrow the pulse time profile, while maintaining a usable intensity range without need to increase the bias voltage beyond 30 V. The use of low-resistance LEDs has made for the largest improvement in performance in comparison with the previous incarnations of

the driver, allowing more current to flow through the LED increases intensity as well as narrowing the time profile of the pulse. Despite its demonstrated performance and prior to the completion of its optimisation, it was decided for political reasons not to use this variant of the Kapustinsky driver for TELLIE. The performance of the driver could be further improved through the optimisation of the inductor.

The Sussex version of the Kapustinsky driver is fast, stable, robust and reliable. Being made from inexpensive readily available components it is both cheap and easy to repair. All of this makes it a viable option for any LED based timing calibration system.

#### 5.2.4 IXYS Laser Diode Driver

This LED driver has been developed solely for the purpose of TELLIE through a collaborative effort between Leeds and Sussex. It is based around a commercially available laser diode driver, the IXLD02SI from IXYS Colorado [120]. The IXLD02 is sold as an ultra high-speed differential laser diode driver designed to drive single junction laser diodes.

The IXLD02 does not provide any voltage or current, rather it sinks current by manipulating output sink MOSFETs in a linear manner. The resistance of the MOSFETs are used with external resistor banks to form two potential dividers, one at the anode and the other at the cathode of the LED. To maintain a nominal reverse and forward bias, the external resistances need to be optimised relative to the resistance of the MOSFETs, setting the maximum current that can be delivered LED [120].

#### Implementation of LED Driver

The driver circuit, shown in Figure 5.13, operates by briefly flipping the voltage across the LED into a forward voltage and then back to a reverse. Initially transistor  $Q_1$  is open and transistor  $Q_2$  closed. To allow a forward voltage across the LED,  $Q_1$  closes and  $Q_2$  opens. In switching the LED off, returning  $Q_1$  and  $Q_2$  to their initial states creates a temporary reverse current, which sweeps charge carriers from the LED's active region - reducing the fall time of the LED pulse. Resistor banks  $R_1$  and  $R_2$  serve to limit the current through  $Q_1$  and  $Q_2$  as well as generating sufficiently large forward and reverse voltages across the LED.  $Q_1$  and  $Q_2$  form part of the integrated circuitry (IC) of the IXLD02SI driver, the driver also contains the MOSFET drivers and the circuits to set the pulse width

and pulse amplitude, using currents Pulse Width current ( $I_{PW}$ ) and Operational current ( $I_{OP}$ ) respectively. LED pulses are triggered via the Trigger (TRIG) input, between each pulse the current through  $Q_1$  or  $Q_2$  can be powered down via the Power Down (PDN) input.

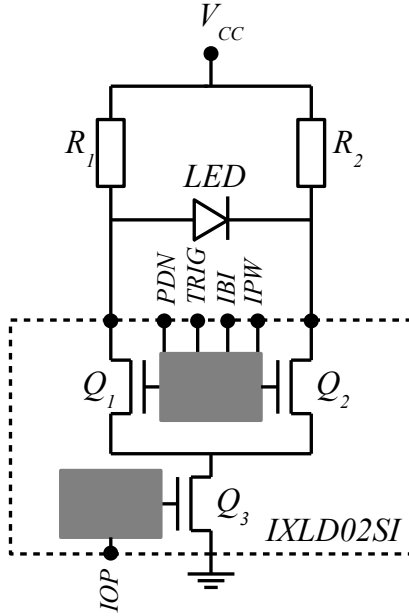


Figure 5.13: *The driver circuit based on the IXLD02SI chip. Details of function are described in the text; here only the main components of the chip are shown, with the rest of the integrated circuit represented as grey boxes.*

The three adjustable parameters are:  $I_{OP}$  activates the chip and sets the maximum bias applied to the LED and in turn the maximum pulse amplitude; the Bias current  $I_{BI}$  sets the maximum length of time that the voltages at the anode and cathode of the LED can be inverted i.e. the maximum possible pulse width;  $I_{PW}$  sets the time that the voltages are inverted, i.e. the pulse width. If  $I_{PW} = I_{BI}$ , the pulse width is 0. As  $I_{PW}$  approaches  $I_{BI}$  but is less than  $I_{BI}$ , the pulse width becomes nonzero [120]. Figure 5.14 shows the voltages measured at the anode and cathode of the LED, with the effect of each current highlighted.

The IC of the IXLD02SI is more complex and fragile than the Kapustinsky driver, operation outside of safe limits has been shown to cause permanent damage to the IC. Thus, safe operating limits have to be defined. The following is a summary of the how the operating limits are set as defined in [121].

The IXLD02SI has no internal protection against over-heating. Two methods are used to



Figure 5.14: The voltages as measured at the anode (blue) and cathode (yellow) of the LED, the ringing is due to impedance miss matches at the probes.  $I_{OP}$  sets the maximum bias applied to LED (1); The Bias current  $I_{BI}$  sets the maximum length of time that the voltages at the anode and cathode of the LED can be inverted (2);  $I_{PW}$  sets the time that the voltages are inverted(3).

protect the driver, a 50 mA fuse and an upper limit of 100 kHz on the trigger rate. Several drivers were damaged by noise on the trigger and the fuse being to slow. To further protect the driver the power supply is limited to a maximum of 7 V and 30 mA. No drivers have been damaged at these settings.

The manufacturers specify 9 V as the upper limit to the supply voltage. However, at this voltage the internal circuitry will no longer reliably switch off the MOSFET current when the PDN signal is asserted. A small remaining quiescent current of order 100 mA, would lead to a large voltage drop of 1 V across the fuse with a resistance of 10  $\Omega$ . The reduced voltage prevents the LED from operating in a reproducible fashion, since the voltage can drop below the threshold needed for light emission. Limiting the supply voltage to 7 V prevents this, as the quiescent MOSFET current reduces to order 1 mA and the voltage drop is minimal provided the fuse resistance is not much larger than 10  $\Omega$ .

Aside from the repetition rate, limiting  $I_{OP}$  will have the greatest effect on reducing the heat generated by the driver.  $I_{OP}$  passes through two sets of resistors  $R_1$  and  $R_2$ , where  $R_1 = R_2 = (20/6)\Omega$ , which then generates either the reverse voltage across the LED ( $R_1$ ) or the forward voltage ( $R_2$ ). A linear approximation for the forward voltage is  $V(I_f) = V_{thr} + R_s I_f$ . For a forward current  $I_f$  through the LED:

$$R_2 \cdot I_{OP} = V_{thr} + R_s I_f.$$

The requirement to achieve a forward current,  $I_f > 0$  is:

$$I_f = \frac{R_2 \cdot I_{OP} - V_{thr}}{R_s} > 0 \Rightarrow I_{OP} > \frac{V_{thr}}{R_2},$$

for an LED threshold voltage of  $V_{thr} = 2.75$  V [103], the minimum  $I_{OP}$  is:

$$I_{OP} > \frac{2.75\text{V}}{(20/6)\Omega} = 0.825\text{ A}.$$

To get a reproducible and fast pulse the LED forward voltage needs to be above the threshold region and as demonstrated in Equation 5.1,  $I_f$  should be as large as possible. The maximum possible operating current is:

$$I_{OP} < \frac{V_{cc}}{R_2},$$

for  $V_{cc} = 7$  V and  $R_1 = (20/6) \Omega$  this gives:

$$I_{OP} < \frac{7\text{V}}{(20/6)\Omega} = 2.1\text{ A},$$

which is below the maximum peak current rating of the IC and safe to operate as the maximum current setting.

To set a maximum repetition rate ( $\Gamma$ ), the power dissipation has to be considered, and no safe upper limit for power dissipation in operation without a heat sink is given. It is advisable to keep power dissipation low, conservatively a maximum of 100 mW. The average power dissipated by the IC is the difference between the total power of dissipated by the circuit and the power lost in resistor bank  $R_1$ .

$$P_{avg} = (V_{cc} \cdot I_{OP} - R_1 \cdot I_{OP}^2) \cdot \Gamma \cdot \Delta t < P_{max},$$

where  $P_{avg}$  is the average power dissipated,  $P_{max}$  is the maximum power dissipated,  $\Delta t$  is the time the circuit is active per pulse, and  $\Gamma$  is the maximum repetition rate. The average power dissipated by the IC reaches a maximum for a current  $I_{OP} = V_{cc}/(2 \cdot R_1)$ . Using this current the maximum repetition rate is:

$$\Gamma < \frac{4 \cdot P_{max} \cdot R_1}{V_{cc}^2 \cdot \Delta t}.$$

For  $V_{cc} = 7\text{ V}$ ,  $R_1 = (20/6)\Omega$ , and  $\Delta t = 200\text{ ns}$  this gives an upper limit for the repetition rate of:

$$\Gamma < 136\text{ kHz}.$$

This is an order of magnitude higher than the limit set by the SNO+ electronics. Hence, in normal operation at the given settings the driver will be operating well within its safe limit.

With the final version of the drivers  $I_{BI}$  was set at its maximum, with  $I_{OP}$  and  $I_{PW}$  remaining as adjustable parameters. Though it was found that any variation in  $I_{OP}$  only affected high intensity pulses (beyond  $10^6$  photons per pulse). As pulses of sufficient time profile and intensity could be achieved without probing the full range of  $I_{OP}$ , in practice it is set to its maximum value and only  $I_{PW}$  is varied. The calibration of the  $I_{PW}$  parameter space will be presented in the following chapter.

## Results

As the IXLD02SI had been selected as the TELLIE driver, all measurements of its time profile were made with 45 m of optical fibre connecting the driver and LED to the PMT, to gain a better understanding of the time profile as it will be when injected into the detector.

The time profiles for the IXLD02SI driver operating a 1 kHz at pulse intensities of  $10^3$  and  $10^6$  photons are shown in Figures 5.15 and 5.16 respectively. This measurement was carried out with the 45 m length of PMMA fibre in addition to the 0.75 m length within the driver box connecting the driver-LED combination to the PMT. As mentioned, Figure 6.5 shows the effect of additional fibre on the time profile of the pulses.

The results of the characterisation of one driver's output is shown in Table 5.3, a summary of the time profiles for four different amplitudes. As expected the broadening of the pulse at higher intensities is observed. The observed pulse widths are considerably larger than those of the Kapustinsky, the post injection increase in optical pulse width due to modal time dispersion in the fibre is larger than the width of the pulse generated by the LED.

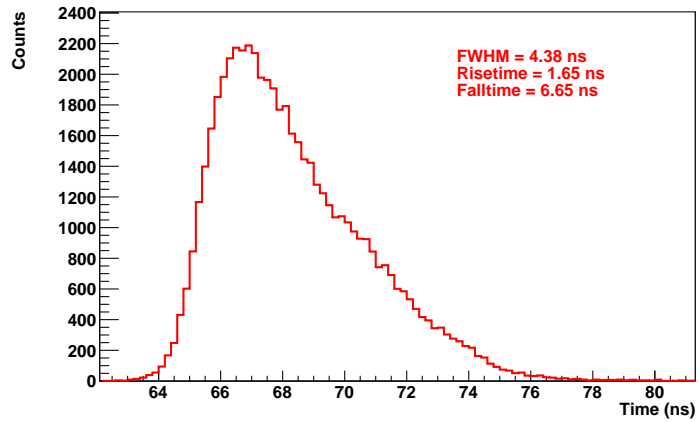


Figure 5.15: *The time profile for the IXLD02SI driver at a pulse intensity of  $10^3$  photons per pulse, running at 10 kHz. For the measurement, the driver and LED were connected to the PMT via 45.75 m of optical fibre.*

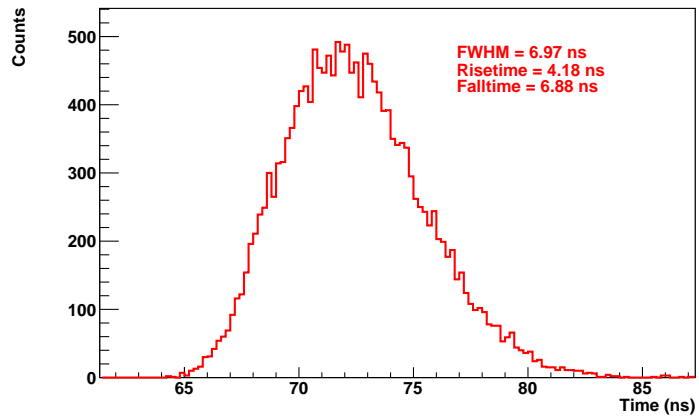


Figure 5.16: *The time profile for the IXLD02SI driver at a pulse intensity of  $10^6$  photons per pulse, running at 10 kHz. For the measurement, the driver and LED were connected to the PMT via 45.75 m of optical fibre.*

Number of Photons	Full Width Half Maximum (ns)	Rise Time (ns)	Fall Time (ns)
$10^3$	4.4	1.6	6.6
$10^4$	4.4	2.0	6.0
$10^5$	5.2	2.0	6.4
$10^6$	7.0	4.2	6.8

Table 5.3: *Summary of time profile measurements for a single LED and driver at varying intensities. All measurements made with the driver running at 1 kHz. The measurement of the number of photons is performed after 45.75 m of optical fibre, i.e., not including the 2 m patch cord. The measurements of time profile of a single channel reported in this table are smaller, and more accurate, than the FWHM reported in Figure 6.3 due to systematic errors from the response time of the PMT and readout of the oscilloscope used in those measurements, that refer to all 96 channels.*

These measurements were made with the long fibre coiled in a bundle, ensuring mode mixing. The results shown here are for only one driver, the variation across the entire system is described in Chapter 6.

### 5.2.5 Observations and Conclusions

The IXLD02SI laser diode driver was successfully modified to be operated as an LED driver, meeting the criteria set out for a TELLIE driver. It is capable of reliably producing pulses with intensities between  $10^3$  and  $10^6$  photons per pulse after 45.75 m of fibre, with pulse widths of between 4.4 and 7.0 ns respectively, see Table 5.3, with an operational frequency range of a few Hz up to 10 kHz. All of which will allow for a timing offset calibration of all PMTs to a precision of 0.5 ns within one day of data taking.

Like the Kapustinsky driver, the IXLD02SI performance has benefitted from the selection of low resistance LEDs. Allowing more current to flow through the LED increases intensity as well as narrowing the time profile of the pulse.

Although the driver met the criteria, there are some concerns inherent to the use of a commercial driver chip, namely the longterm availability and cost of replacement components. The more complicated nature of the driver, relative to the Kapustinsky, will increase the time needed to repair a driver - extending any down time.

It has also been shown that the driver's performance exhibits a temperature dependence [121]. However, since their operating environment is carefully maintained at constant

temperature and humidity it is unlikely to cause an issue.

The driver has now been successfully used during two commissioning runs (both air fill and partial water fill), the results of which will be presented in the following chapter. One observation of note is the apparent warm-up time of the driver, prior to it reaching stable and reproducible operation; this is more evident at sub kHz frequencies. The first few pulses do not match the calibration of the driver, this is believed to be due to the MOSFETs being below optimal temperature. A proposed solution is to run the driver in reverse bias between pulses, this would keep the IC warm with no LED output.

## Chapter 6

# Realisation of the TELLIE System

This chapter will describe the realisation and implementation of the entire TELLIE system. It will begin by reiterating and expanding upon the requirement of the system and then discuss the methodology used to achieve these requirements. The system will then be described, including the performance of various components. It will conclude with a short summary of the results achieved by the system during air and partial water fill phases.

### 6.1 Requirements

The TELLIE system was designed to obtain high quality, frequent timing and gain calibration and monitoring data while avoiding the deployment of a source. Given the decay time of the scintillator signal, which is around 4.6 ns (fast component) for the LAB/PPO mixture, and the SPE PMT resolution (dominated by the transit time spread), which is 1.7 ns (standard deviation) for the SNO PMTs [57], we set the PMT time calibration accuracy goal at 1 ns.

The LED spectrum should be detectable in all operating phases of the detector. In order to monitor the PMT gain, the intensity of the LED light output should be measured with a precision of about 1% [59].

When coupled to the LED and the optical fibre, the driver must be capable of producing pulses fast enough to ensure that the measurement of the time offset of all PMTs can be

done to a precision of 0.5 ns within one day of low rate data taking. In terms of intensity, the driver must provide pulses with a dynamic range in intensity such that the full system can provide SPE pulses in significantly different conditions in terms of optical attenuation of the light in the detector. The driver should also have a wide range of frequencies, allowing a constant monitoring at a low rate of about 10 Hz as well as fast dedicated calibration runs, in which rates up to about 10 kHz are possible.

The modal dispersion in the optical fibres must allow the FWHM of the transmitted LED pulses to be no higher than 5 ns. In addition, the angular emission profile of the optical fibres must allow a sufficient illumination of all the PMTs even if a fibre fails. For the same redundancy reason, there should be two identical fibres per node. Another important aspect of the light emitted from the injection points is to ensure that all of the PMTs have sufficient illumination to allow for their calibration. Further to just illuminating the individual PMTs, timing studies and the PMT calibration require a great deal of overlap between the different injection points to properly determine the respective times of the injections. All of this is dependent on the maximum angle at which light is emitted from the light injection points.

Since most of the SNO detector hardware will not be replaced, the fibre system infrastructure must be adapted to the existing parts. In terms of material compatibility, three criteria were checked for: total radioactivity of bulk material, emanation of Radon atoms, leaching of contaminants when in contact with UPW.

The system control must fit in the main SNO+ trigger and acquisition framework while still retaining its designed flexibility: running quasi-continuous monitoring as well as dedicated calibration runs, monitoring the LED intensity as it flashes, flashing several LEDs in coincidence with different and adjustable intensities.

## 6.2 LED and Driver

As mentioned in Chapter 5, the LED selected for TELLIE has a peak wavelength of 505 nm and a differential resistance of only  $10\Omega$  in the near linear region of forward current against forward voltage above the LED threshold voltage. This wavelength was selected to be as high as possible since Rayleigh scattering decreases with increasing wavelength, while being between the lower limit set by the expected scintillator absorption spectrum and the upper limit defined by the PMTs QE, see Figure 5.1.

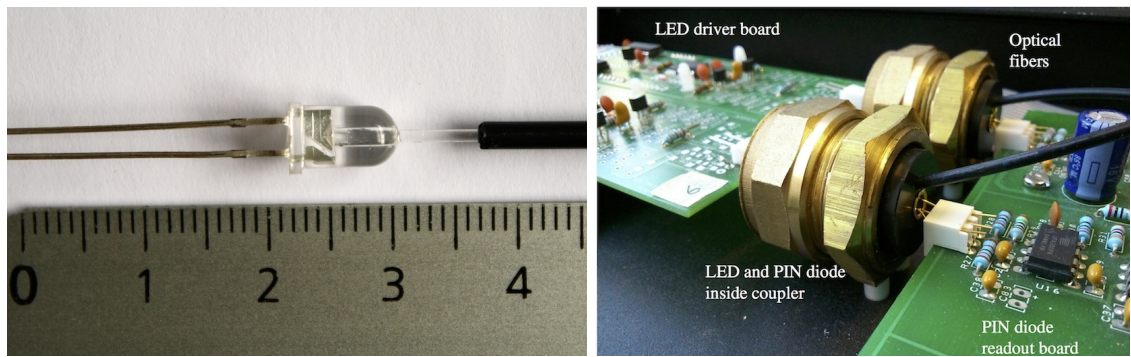


Figure 6.1: *Left: Drilled LED with mounted optical fibre (ruler in cm). Right: Coupler containing LED and photodiode to monitor the number of photons at injection.*

The driver is based around a commercially available laser diode driver. It is capable of producing pulses with intensities between  $10^3$  and  $10^6$  photons per pulse, with pulse widths of 4.4 and 7.0 ns respectively, and has a maximum operating frequency of 136 kHz. The intensity range will allow for measurements in both SPE and MPE modes.

### 6.2.1 LED Coupling

As TELLIE only requires a small number of specifically selected LEDs, the coupling of the LED to the optical fibre was accomplished by drilling into the LED lens to provide a socket into which an optical fibre of 1 mm diameter was fixed, see Figure 6.1. The fibre tip was nominally 1 mm from the diode chip. This method was shown to maximise the number of photons transmitted through the fibre while not altering the time profile of the pulse.

The LED and fibre are contained within a coupler known as a “cone”, which also houses a photodiode mounted opposite the LED to monitor the average level of light injected into the fibre, see Figure 6.1. The digitised output from this photodiode will be included in the data stream, to provide an estimate of the light intensity arriving at each PMT, that is independent from the LED driver settings.

### 6.2.2 The TELLIE Driver Box

Each driver box contains eight channels, a channel is defined by a driver coupled to an LED into which 0.75 m of optical fibre is mounted. The fibre terminates at an ST connector on the box’s edge. The drivers are mounted on a motherboard that is connected to the

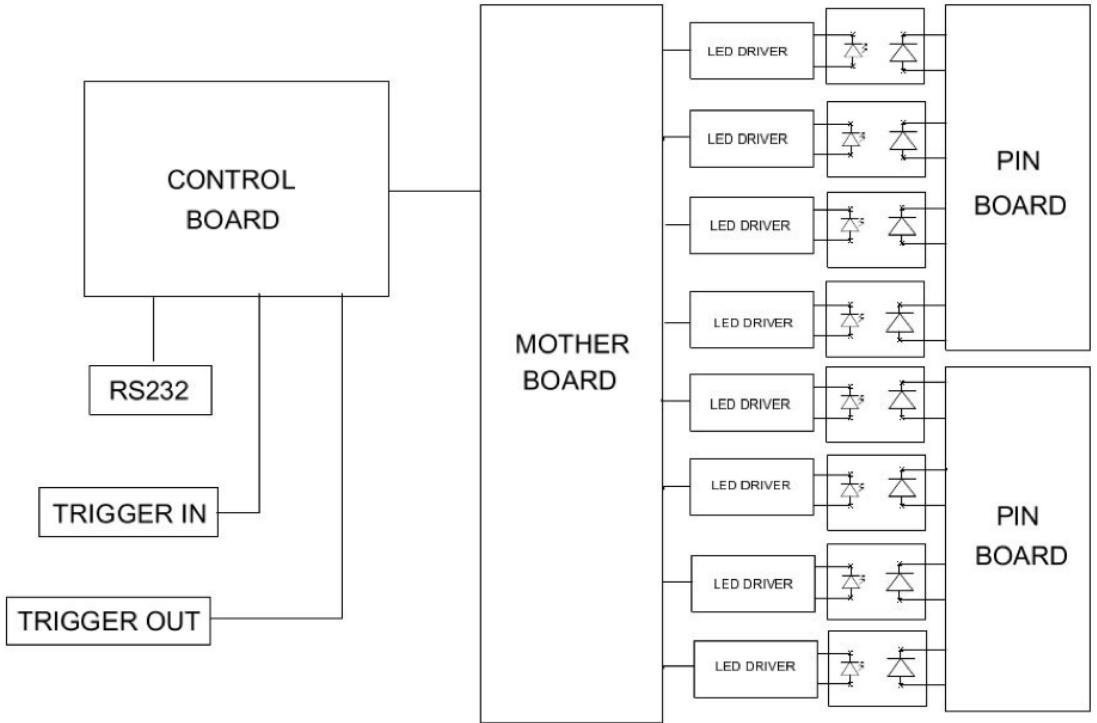


Figure 6.2: A schematic of the TELLIE driver box showing the basic connections to the control box and the position of the PIN diode boards monitoring LED output.

control box. Each LED is contained within a brass “cone”, a PIN diode is mounted at the opposite end of the cone, monitoring the LED’s output at each pulse. The eight PIN diodes are mounted on two PIN boards, four left and four right, see Figure 6.2.

The driver boxes are connected to the control box via a ribbon cable, onto which up to seven can be daisy-chained. As the control box has ports for two ribbon cables, up to fourteen driver boxes can be connected. However, TELLIE will only use twelve boxes and AMELLIE one, leaving one spare connection. On each driver box motherboard there are a set of jumpers next to the control box connection, which identifies the driver box to the control box, as box 1 to 7. Driver box 1 contains channels 1 to 8, box 2 channels 9 to 16 and so on, until channel 112 in box 14. To address a specific channel, only its number is needed.

Each PIN diode has two potentiometers, that allow the PIN’s gain and sample point to be set. Ideally the gain would be set to allow maximal sensitivity to the low light levels without saturating at higher levels, the value varies for each board. However, since TELLIE is normally operating at low intensity, the standard operating procedure is to set

the gain high enough to achieve maximal sensitivity to low intensity pulses. This comes at the cost of saturation at higher intensity pulses and the amplification of noise. To minimise noise additional decoupling has been added to the PIN power supply.

### 6.2.3 LED Quality Assurance

The LED spectrum was measured for all 96 LEDs used in the PMT calibration system. Each LED was connected in series with a  $550\ \Omega$  resistor, supplied with a constant 2.48 V. The LEDs were connected to the spectrometer<sup>1</sup> via 45.75 m of optical fibre, a 0.2 m patch fibre was used to convert to the spectrometer's SMA (threaded type) connection, this 0.2 m fibre is not present in SNO+ and is only required here to interface reproducibly with the spectrometer. Each spectrum was recorded with an integration time of 40 ms and averaged over 20 scans. The spectral output was verified to be identical for pulsed and continuous operation. Figure 5.1 shows the average spectrum for all 96 LEDs, in arbitrary units, showing a good match with both the expected scintillator absorption and PMT quantum efficiency. The mean peak wavelength is  $(505.6 \pm 2.6)$  nm.

The integral of the individual LED spectra provides an estimate of each LED output intensity. The maximum difference between the response of any two LEDs is a factor of 18, and the typical spread (RMS/mean) is 43%. These LED response differences are large, and likely caused by variations in fibre coupling rather than LED itself, but can be compensated for by adjustments on the driver intensity, as will be seen in the following section.

### 6.2.4 LED and Driver (Channel) Quality Assurance

All 96 driver and LED combinations used in the calibration system were characterised using the same 45.75 m long optical fibre used in the SNO+ detector, coupled to the same PMT mentioned earlier [109] with the gain of the photomultiplier set by varying its control voltage between 0.6 V and 0.8 V depending on the pulse intensity. Unfortunately, for this type of PMT there is no way to extract the corresponding high voltage setting [110]. Instead of using the single photon counting technique, the PMT signal was recorded with a Tektronix DPO 3054 oscilloscope. Mismatched impedance and the response times for the PMT and oscilloscope contributed to the broadening of time profile of the pulses; while undesirable, this was a systematic effect for all channels.

---

<sup>1</sup>Ocean Optics Maya2000 Pro

The PMT gain was characterised as a function of the applied voltage using ThorLabs' PM100USB light-meter. The number of photons per LED pulse was obtained for two different LED light intensity settings by taking the average of five light meter readings, each of which was itself taken over two seconds with the LED pulsing at a known rate in the kHz range. This number of photons per pulse was then compared with integrated voltages from the PMT for the same LED and settings. These were taken at seven applied voltages between 0.56 V and 0.85 V, with the integration using the average of 1000 pulses for each reading. The relationships between the applied PMT voltage and the resultant gain were consistent between the two LED intensity settings.

The measured minimum photon output of each board/LED combination averaged at 232 and varied in the range of 20 to 510 photons per pulse. The measured maximum photon output averaged at  $1.13 \times 10^6$  and in the range of  $0.45 \times 10^6$  to  $1.85 \times 10^6$  photons per pulse. These measurements showed that, even with the aforementioned high variations in LED light output, after the LED/driver board pairing the all channels can be tuned to fall within the required operational range of  $10^3$  to  $10^5$  photons per pulse.

Figure 6.3 shows the time pulse FWHM as a function of the number of photons. Due to the lower precision of this method, these widths are higher than those in Chapter 5, which were obtained through single photon counting. Nevertheless, these measurements are useful since they were carried out for all 96 channels and show the response uniformity of the system as a whole.

Before the quality assurance tests, the driver boards were subjected to a basic electronics test, with only 3 out of 99 boards failing. To pass the quality assurance tests the driver boards must be able to produce a minimum photon intensity of  $10^3$  or less and a maximum photon output of  $10^5$  photons or greater, with  $10^6$  photons being desirable. All 96 boards met these requirements with 27 boards having less than the desirable maximum intensity. As mentioned TELLIE must be able to achieve a measurement of the time offset of all PMTs to a precision of 0.5 ns within a day of low rate data taking. Operating at 10 Hz, this corresponds to a FWHM of 6 ns at photon intensity of  $10^3$  for each channel. All channels met this requirement despite systematic errors due to the response time of the PMT and oscilloscope response not taken being into account.

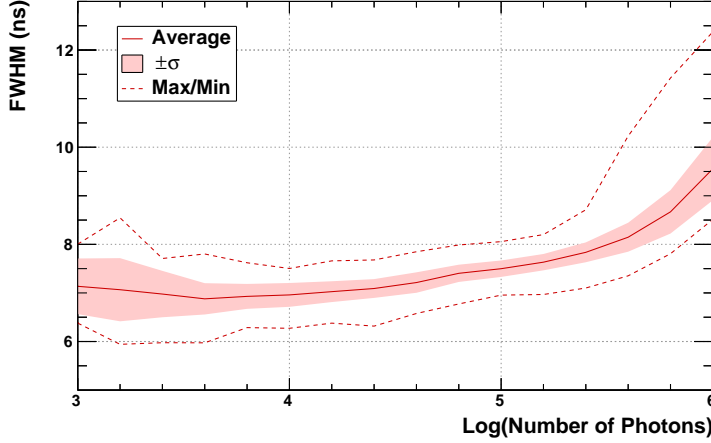


Figure 6.3: *FWHM of the measured light pulses from all the 96 LED and driver combinations as a function of their photon output. The light pulses are measures after going through 45.75 m of optical fibre. The FWHM reported in this figure is larger than the true FWHM reported in Table 5.3 due to systematic errors from the response time of the PMT and readout of the oscilloscope. The true FWHM is lower due to systematic errors from the response time of the PMT and readout of the oscilloscope. The LED driver was operated at maximum current while varying the electrical pulse width to control the number of photons per pulse. The observed increase in optical pulse width as the intensity reaches  $10^6$  photons per pulse is due to the electrical pulse width for high intensities starts to exceed the modal time dispersion in the optical fibre.*

### 6.3 Fibre Selection

The choice of the optical fibre is dictated by constraints of various aspects of this system. For ease of installation, the total number of fibres must be minimised while keeping sufficient overlap of the illuminated areas to allow for the synchronisation of all the PMTs. PMMA step-index fibres from Mitsubishi [108] are used, with a wide aperture which meet the requirements.

For the timing calibration itself it is essential that the fibres do not add significantly to the rise time of the light pulse. The numerical aperture (NA) is defined as:  $NA = \sin \theta_a$ , where  $\theta_a$  is the fibre acceptance angle, NA can be thought of as the light gathering capacity of the fibre [100]. Due to a higher NA, the time dispersion associated with PMMA fibres is higher than that of quartz fibres, so that the aperture and timing requirements conflict. However, as will be shown below, the time dispersion of the chosen fibres is still low enough to meet the SNO+ requirements<sup>1</sup>.

---

<sup>1</sup>According to typical manufacturer's specifications, graded-index fibres could provide a smaller time

Each optical cable has two fibres (duplex), ensuring redundancy at each injection point without multiplying the number of cables to install and with better mechanical robustness than a single fibre cable. Their 1 mm diameter and large numerical aperture (0.5) guarantee a wide illumination area. The LED-side ends are two pre-mounted bayonet type ST connectors, while the detector-side end is a double-fibre connector to be inserted in the mounting plate, shown in Figure 6.10. For convenience all the fibres have the same length, making the propagation delay constant in the entire system.

### 6.3.1 Fibre Characterisation and Quality Assurance

In this section, the characterisation of attenuation, aperture angle and timing distortions of the fibres will be discussed. Key parameters were measured for quality control of 110 double fibre cables, in order to select the best ones and keep track of small variations within the system.

#### Angular and Timing Distributions

A specific setup was built to study the emission properties of the fibres, based on a PMT [109] moving in front of a fixed fibre and shown schematically in Figure 6.4. A prototype of the IXLD02SI driver was used to inject light into a patch cable, then into the full length cable, thus reproducing the connections of the final system. The PMT has its window covered by a plate with a 1 mm diameter hole limiting the effective detecting area. It is fixed onto an automated arm, whose three dimensional motions are independently actuated by a motion controller. The PMT swipes an area in the plane perpendicular to the optical axis with a tuneable increment and records the number of photons at each position using the trigger of the LED driver as a coincidence. In order to measure the true shape of the emitted light pulse it is sampled by a TAC on a single photon basis, as described in Chapter 5.

Using the same setup the effect of the fibres on the time profile of the pulse was measured. Figure 6.5 shows that although the pulse is spread, the fibres do not add significantly to the rise time of the pulse. As expected there is little effect to the rise time with greater spread due to modal mixing in the falling edge of the pulse.

The measurement was done at several positions, corresponding to different angles, in or-  
dispersion than the step-indexed, but their cost is significantly higher.

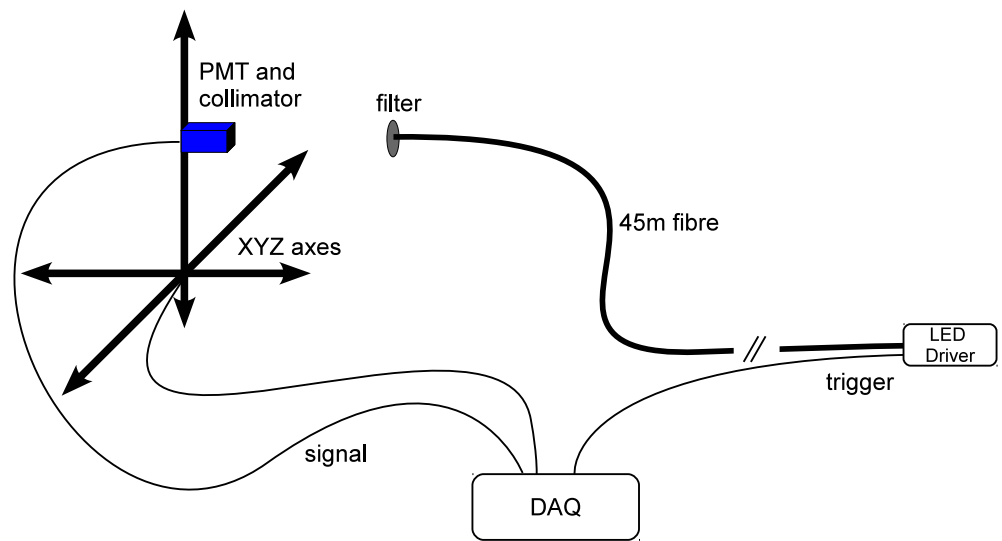


Figure 6.4: *Diagram of the scan setup used to perform timing and aperture profiles. The PMT is fixed on an automated arm with three-dimensional movement, and its window covered by a plate with a 1 mm diameter hole limiting the effective detecting area. The duplex fibre is fixed on a stand facing the PMT. A neutral density filter reduces its intensity so that the measurement can be operated in single photoelectron mode. In order to reduce backgrounds, the data acquisition requires a coincidence between the LED driver signal and the PMT output signal within a 50 ns window [122].*

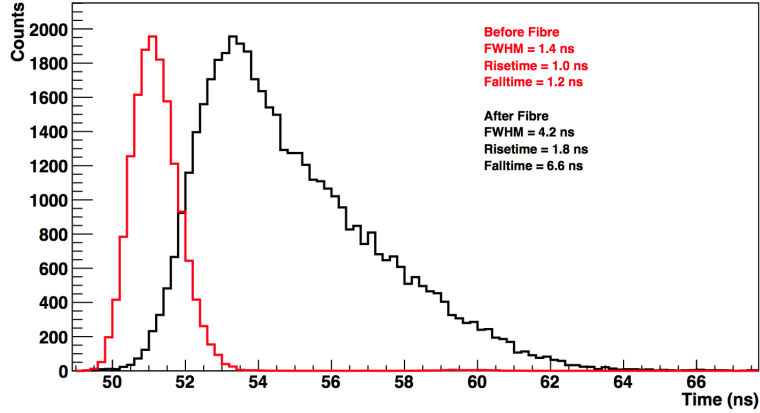


Figure 6.5: *Time distribution of a light pulse emitted by the LED driver after going through the full length optical fibre, and a pulse measured from the driver box (without additional fibre). Both pulses are at the same driver setting ( $10^3$  photons after the fibre), with the pulses normalised to amplitudes. Despite the broadening of the pulse, it remains low enough to meet the SNO+ requirements.*

der to measure the spread of the pulse with respect to both angle and time. Figure 6.6 shows these pulses at the central position and at an angle corresponding to  $11^\circ$  in water. The peaks are separated by  $0.80 \pm 0.28$  ns and the widths at half maximum differ by  $1.80 \pm 0.40$  ns. Such a dependence of timing on angle is expected for step-index fibres without complete mode-mixing. In order to achieve the calibration goal of approximately 0.5 ns precision on the PMT timing, this effect will have to be corrected for in the calibration procedure. The measurement of the angular dependence of the fibre timing will be carried out in-situ, by comparing the timing offsets measured for the same PMTs with different fibres, and by comparing the offsets measured with TELLIE and the laserball.

A wide two-dimensional intensity scan was also performed. The 2D map of coincidences between PMT and LED driver is corrected for accidental coincidences, the geometry of the setup, and the refraction in and reflection on the filter. It is then converted into an angular intensity map in water, shown in Figure 6.7. The fraction of the total light emitted within a cone of  $14.5^\circ$ (in air) from the centre is found to be 80%<sup>1</sup>. The visible asymmetry about the central point in Figure 6.7, likely due to the way the fibre is mounted in the duplex termination point; a metal band is used to clamp the fibre just before this point, effectively flattening it a little.

The bulk attenuation of the full length fibre is of the order of 10, but the effective dynamic

<sup>1</sup>given the refractive index of air and water, and the numerical aperture of the fibre,  $14.5^\circ$  in air corresponds to  $11^\circ$  in water

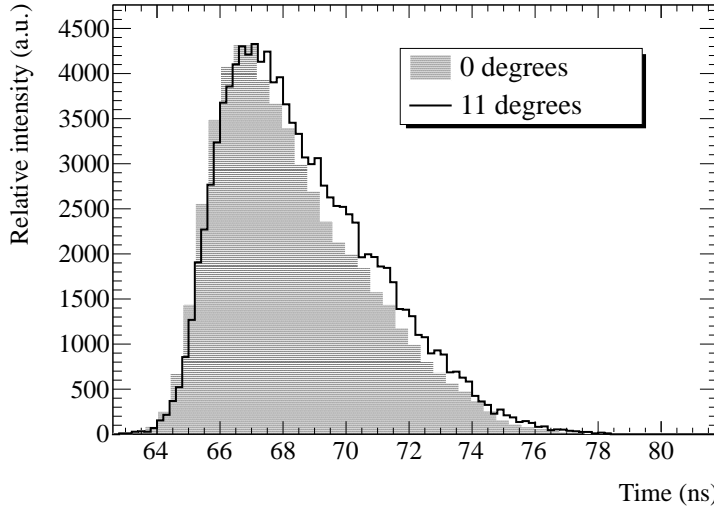


Figure 6.6: *Time distribution of the light pulses emitted by the LED driver after going through the full length optical fibre, at the central position (filled area) and at an angle corresponding to 11° in water (solid line). The time offset is common to both histograms, and both are normalised to their integrals.*

range of the driver allows it to make up for small differences that can arise.

### Fibre-to-Fibre Variation

All the 110 duplex fibres were checked under the same conditions for timing, angular aperture and transmission. For the timing measurements, the PMT [109] was connected to a 1 GHz oscilloscope in order to record the rise and fall times of the signal and its total width, the driver used was the aforementioned prototype. Constant LED light sources at the same wavelength were used to measure the total light output for each fibre, first with a portable power-meter for a faster measurement to be repeated to check for possible damage during the installation, and then with a more precise measurement with a dedicated set-up for optical fibre characterisation.

The base automated test-bench described in [123] was adapted to check the light output at different angles in a transverse scan, in order to cross-check the variation of the angular opening between fibres. The peak value and the integration of the angular scan also gives the variability in terms of light transmission. The set-up consists of a X-Y table in which one of the motors (X) was unused, while the other (Y) positioned the fibre at a given transverse position. The end of the fibre was 51 mm from the detector, a PMT connected to a light guide with a Y-Z slit of  $2.8 \times 15 \text{ mm}^2$ . The Y-movement, in steps of 1 mm,

## Angular Distribution in Water

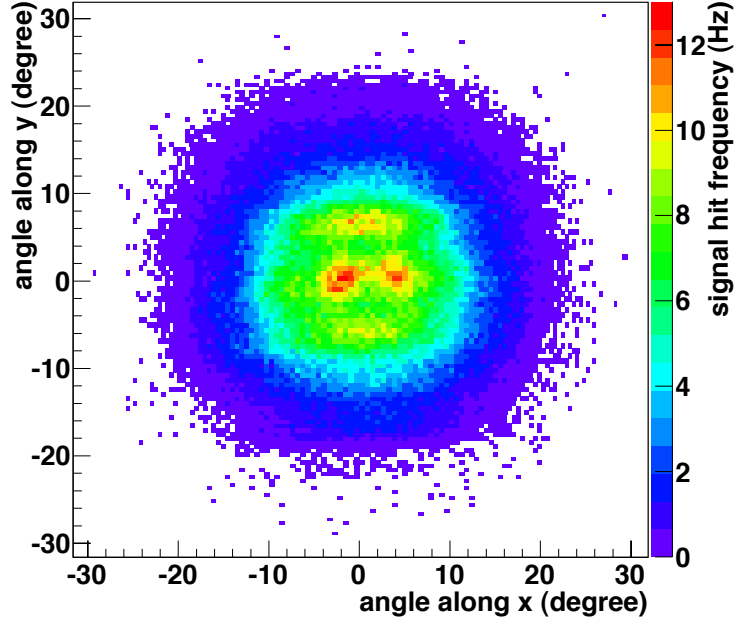


Figure 6.7: Two dimensional angular emission profile of a fibre. The white area corresponds to zero intensity. The steps in  $x$  and  $y$  are fixed during the measurement, hence the variable angular resolution, ranging from  $0.6^\circ$  at the centre to  $0.26^\circ$  at the edges.

and the corresponding measurement of PMT current by a pico-ammeter, were computer controlled and fully automated.

Figure 6.8 shows the interior of the dark box, adapted for this test. Three duplex fibres can be mounted simultaneously in the XY-table. Since they are illuminated independently from outside the dark-box, they could all be checked in sequence without turning the PMT high voltage off, allowing for a reasonably fast check of all the 220 fibres. The light intensity was set to be above the system background which was measured and subtracted independently for each HV cycle. The edges of some of the angular distributions were cut for some of the fibres and showed some distortions, but the central part was consistent for all the six tested positions. The variations between the 220 fibres are shown in Figure 6.9, compared with the higher resolution measurement of a single fibre in the two-dimensional scan.

The shapes of the angular distribution and time signals were quite uniform, and consistent with the previous detailed studies. The maximum intensity measured in the scan is well correlated with the power-meter measurements, even if it includes extra variation from the angular distribution shape. At installation, big drops in intensity will be used to identify

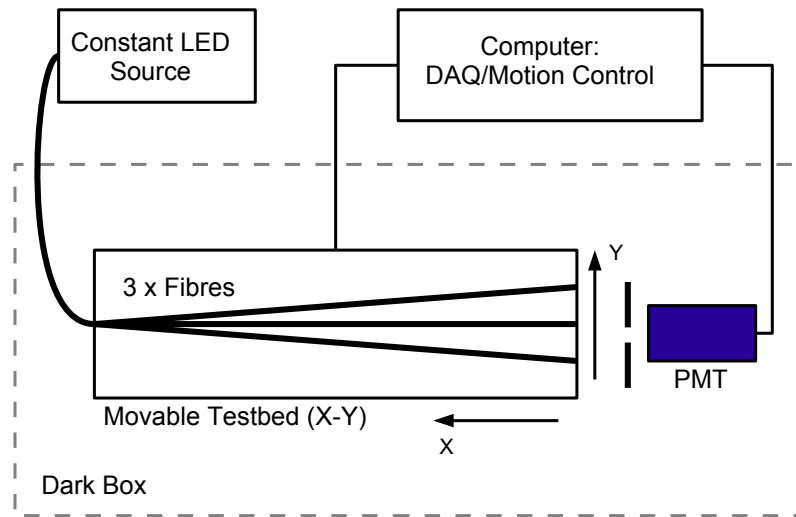


Figure 6.8: *The interior of the dark box, showing the mounting of three 45 m fibres in front of the PMT and light guide with associated slit.*

damaged fibres so that they can be replaced. The figure-of-merit used to characterise the angular distribution is the half width at 20% intensity, after a correction to convert angles measured in air to angles measured in water (as will be the case in SNO+).

The selection of fibres was done in terms of the maximum intensity in the transverse scan, the angular opening (converted to water) at 20% intensity, and the signal rise time, with values shown in Table 6.3.1. Any significant damage to the fibre would have lead to increased mode mixing, which presents as an increase in rise time and the FWHM, with the set-up used for these measurements rise time was an easier parameter to extract quickly, hence its use. No fibre failed the angular criterion, although two were classified as preferably spares; in practice, even if the angular profile is slightly narrower than required, a larger intensity may allow the recovery of light at wider angle positions. Only one of the double fibre cables that had one fibre with lower transmission and the other with values close to the limit was excluded. In addition, four single fibres had timing or transmission values close to the established limits (some above, some below). Since their parameters were not far off from the requirements, and the other fibres in the same cable were well within the limits, these fibres were installed as well, but as spares.

Two of the duplex fibres (both with good parameters) were kept back for ageing studies and future tests.

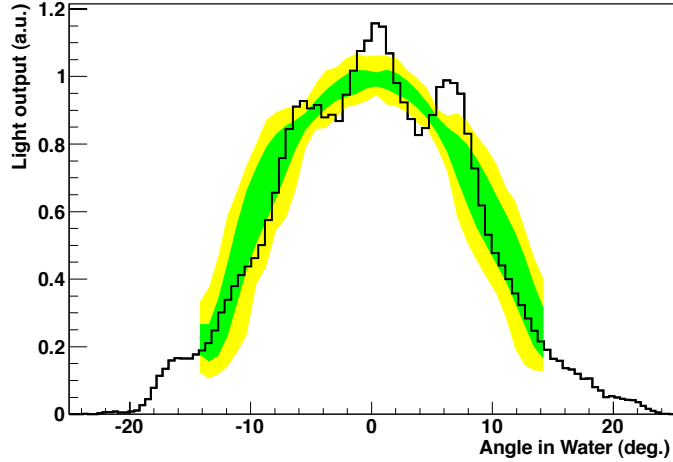


Figure 6.9: Comparison of independent measurements of the intensity profile of the fibre with respect to the angle in water: the black histogram is the profile of the detailed measurement with one fibre, from Figure 6.7; the coloured bands summarise the measurements of the full set of fibre cables. The yellow band shows the full spread and the green band represents the RMS, both over the total 220 fibres.

Characteristic	Mean and RMS	selection
$I_{max}$ (nA)	$120.2 \pm 21.9$	$>60.0$
20% Angle (deg.)	$14.5 \pm 0.2$	$>13.5$
Rise Time (ns)	$1.9 \pm 0.1$	$<2.25$

Table 6.1: Fibre quality checking and selection was based on three parameters connected to transmission, numerical aperture and timing profile. The LED driver used was a prototype of the final version.

## 6.4 Mechanical Structure

The design of the mechanical structure of the PMT calibration fibres system is determined by the requirement of providing a coverage of the PMTs as uniform as possible, and by the access constraints to the existing detector structure.

The 9500 PMTs are mounted with light reflectors within hexagon-shaped boxes called “hex cells”, made of Acrylonitrile Butadiene Styrene (ABS), see Figure 6.10. These are assembled in flat panels, supported by the PSUP. Most PMTs are mounted in triangular panels that follow the faces of the geodesic shape. Close to the nodes, 91 extra panels of hexagonal shape are mounted.



Figure 6.10: *Illustration of a SNO+ PMT casing (hex cell) with a mount fitted for TELLIE fibres. The face hex cell is a little over 30 cm across.*

The location of the hardware to support the fibre termination points must not cause any shadowing on neighbouring PMTs nor suffer from light blocking by them. The sides of the hex cells themselves provide a convenient mount point. The hex cell panels in the geodesic nodes of the PSUP were chosen for the location of the mount points, since they have a slightly wider gap with respect to the neighbouring panels, facilitating installation. In addition, their distribution in the detector guarantees in a simple way a uniform coverage of all the PMTs, when all 91 nodes and the neck aperture are used.

The number of LED-driver channels is 96, chosen to be slightly higher than the required 92 in order to ensure some redundancy in case of channel failure. The number of fibres installed is also higher, 110 double cables, in order to have enough spares in case of breakage during installation. In addition to the 110 TELLIE fibres, there are an additional 25 single quartz fibres for AMELLIE and SMELLIE [84].

#### 6.4.1 Fibre Termination Points at the Detector

The fibre ends are mounted in plates made from Polyethylene Terephthalate Glycol (PETG) and designed to be attached to the hex cells. Since the available space between hex cells can be as small as 4-5 cm, and their inner edge is not accessible, the fibre mount plates, shown in Figure 6.10, are secured to pre-existing holes in the outer edge of the hex cells with nylon push-in rivets.

The fibre mount is designed for the latching fibre connector to simply clip in, for ease of

installation. The two smaller holes visible in the centre of the plate are used to secure cable ties that hold the fibre straight. The remaining holes are used to fix the plate with the rivets, and the four holes aligned in the lower edge also serve to secure a black plastic sheet held between the PMT panels, that serves as a light barrier between the inner and outer water volumes.

## 6.5 Radioactivity

To determine the appropriate acceptance limits for contamination by natural radioactive isotopes from the  $^{238}\text{U}$ ,  $^{235}\text{U}$  and  $^{232}\text{Th}$  chains, and from  $^{40}\text{K}$  in components to be installed in SNO+, the known amounts of contamination of the main components of SNO were used as a benchmark. The structure of SNO+ is one of concentric shells of increasing radiopurity, each layer acting as a barrier for gamma radiation and neutrons originating from decays in outer shells. Therefore, the requirements on TELLIE components in terms of contamination by these isotopes depend on their location. Since TELLIE will be installed in the PSUP, close to the PMT array, with the fibre bundles coming out of the detector as the PMT cables do, the comparison is made with the contamination of the PMTs and associated cabling.

Simulations of the backgrounds induced by the PMTs in the SNO+ analysis windows for its main physics goals –  $^{130}\text{Te}$  neutrinoless double-beta decay and solar neutrinos – were carried out by the SNO+ collaboration [124]. These show that, while external backgrounds are responsible for limiting the FV for the planned measurements, the contribution from the PMTs is subdominant with respect to that of other components located closer to the scintillator volume. Based on these considerations, the acceptance limit is set at a total amount of radioactive isotopes equivalent to 10% of the PMTs and cables.

The materials used in each of the PMTs include approximately 100  $\mu\text{g}$  of  $^{238}\text{U}$  and  $^{232}\text{Th}$  [57]. The total number of PMTs in SNO+ was assumed to be 9500 (installation and repairs are still ongoing), giving a total amount of each radioactive isotope of 0.95 g, as shown in Table 6.2. The levels of  $^{235}\text{U}$  and  $^{40}\text{K}$  in the PMTs are not included in this study.

The contamination measurements were done by low-background gamma counting with a HPGe detector at SNOLAB [125]. The results are available for reference [126] and the values shown in Table 6.2 are for 110 full-length fibres. As seen, the total amount

Item	$^{238}\text{U}$ (g)	$^{235}\text{U}$ (g)	$^{232}\text{Th}$ (g)	$^{40}\text{K}$ (g)
Fibre cables	$3.83 \times 10^{-4}$	$< 1.33 \times 10^{-7}$	$6.81 \times 10^{-6}$	$6.13 \times 10^{-1}$
Mounting plate	$4.61 \times 10^{-5}$	$2.12 \times 10^{-7}$	$3.67 \times 10^{-6}$	$1.10 \times 10^{-2}$
Mounting parts	$3.79 \times 10^{-4}$	$2.44 \times 10^{-7}$	$2.36 \times 10^{-5}$	$6.61 \times 10^{-2}$
Total	$7.36 \times 10^{-4}$	$5.38 \times 10^{-7}$	$3.10 \times 10^{-5}$	$6.28 \times 10^{-1}$
<i>PMTs</i>	$9.50 \times 10^{-1}$	-	$9.50 \times 10^{-1}$	-
<i>PMT Cables</i>	$2.72 \times 10^{-1}$	$2.72 \times 10^{-1}$	$2.72 \times 10^{-1}$	$3.6 \times 10^3$

Table 6.2: *Full installation values for the amount of each isotope included in the calibration systems. The amount shown corresponds to 110 fibre cables and 9500 PMTs and PMT cables.*

of radioactivity introduced by TELLIE is well below the limit of 10% of the PMTs and cables.

### 6.5.1 Radon Emanation

Emanation of  $^{222}\text{Rn}$  from material surfaces has to be checked independently from the bulk radioactivity due to the mobility of the Radon gas. The guidelines for acceptable levels were established by the SNO Collaboration [127] at  $14 \text{ mBq/m}^3$  for the outer UPW region, where the fibres will be located. The actual measured value of Radon contamination in that region was  $4.3 \text{ mBq/m}^3$ . This value is taken as a guideline, similarly to the bulk radioactivity, it is required the additional activity be less than 10% of the guideline value.

A sample of fibre was measured at Queen’s University. The measurement setup is described in [128] and the results are shown in Table 6.3. The equilibrium level is the number of counts in the detector that is asymptotically approached after a period of deployment, hence higher than the counted rate for a day. In addition to presenting the raw emanation rate as obtained, the equilibrium number of radon atoms is also included. This is calculated using the half life of  $^{222}\text{Rn}$  to determine at what number of counts the balance between production and decay will be reached. The results are presented first on a ‘per fibre’ basis and then adjusted to account for the total 110 fibres. The value in the last column is calculated considering that the emanated Radon atoms are fully dispersed in the total outer water volume ( $5.3 \times 10^6$  litres).

The mounting plates and associated parts were not tested for Radon emanation, so a worst-case scenario is considered, in which all the Radon atoms produced in decays of

Material	Counted Rate (atoms/day/fibre)	Equilibrium Level (atoms/fibre)	Rate per Volume (mBq/m <sup>3</sup> )
fibres	53±33	290.6±181.0	(1.21±0.75)×10 <sup>-2</sup>
	<sup>238</sup> U Rate (mBq/kg)	Rate (mBq)	
Plates (PETG)	6.22±4.83	82.10±63.75	(1.55±1.20)×10 <sup>-2</sup>
Add. parts	67.28±28.95	333.04±143.30	(6.28±2.70)×10 <sup>-2</sup>
<b>Total</b>			<b>(9.04±4.65)×10<sup>-2</sup></b>

Table 6.3: *Radon emanation budget for the PMT calibration system. The fibre results come from measurements of <sup>222</sup>Rn emanation. The values for the other parts of the system come from a worst-case scenario estimate based on the bulk radioactivity results (Table 6.2). The total mass considered for the plates and additional materials was 16.0 kg and 6.0 kg, respectively, corresponding to 110 units.*

the bulk <sup>238</sup>U radioactivity are assumed to disperse freely in the water volume. From the results shown in Table 6.3, the conservative estimate yields a total rate per volume at equilibrium equivalent to 2% of the guideline.

## 6.6 Water Compatibility

TELLIE components are located within both water volumes, the mount plates internally and the fibres and externally. The internal volume comprises the water between the acrylic vessel and the PMTs. The external volume is also instrumented with OWL PMTs and serves as a water Cherenkov veto detector for muons. It is therefore important to prevent the installation of any materials that could leach optical impurities into the water. For this reason, all TELLIE components: fibres, connectors, plates and auxiliary parts were screened for water leaching at the Brookhaven National Laboratory. After thorough cleaning, they were immersed in UPW, and the absorbance of the UPW measured with an UV spectrometer. The first candidate material for the fibre mounts, black polyoxymethylene (POM), had clearly leached since the absorbance increased with immersion time, so white PETG was selected instead. For all the other tested materials the absorbance was found to be very low (below 0.002 for 10 cm cells) in the wavelength region of the PMT sensitivity and very stable over periods up to several months.

Evaluation of the fibre ageing in the water is made both in laboratory measurements and in-situ. The chemical effects include a possible residual polymerisation that would modify

the optical properties of the fibres, but as initial tests showed no degradation this is not expected to be an issue. Accelerated ageing tests of the performance of the optical fibres in water over time are under way at Sussex, using a heated UPW bath.

The other measure of ageing comes from the installed monitoring channel, consisting of a fibre looped through the UPW shielding back onto the deck. One end of the fibre is inserted into an LED whose intensity is measured by a PIN diode, as all other channels. Instead of terminating at the PSUP, the detector-side end is fed back into a coupler, see Figure 6.1, with a PIN diode allowing the transmitted intensity to be measured. Regular runs of this fibre will provide the actual control of the ageing of fibres. The absence of the detector-side end connector in the water is the only change with respect to other channels.

## 6.7 SNO+ Trigger Interface

As mentioned in Chapter 3, the SNO trigger and data acquisition systems, described in [57], have been upgraded to handle the expected higher rates in SNO+. TELLIE will be connected into this existing setup so that it receives and acknowledges the detector trigger signals, allowing the calibration to be synchronised with the SNO+ central clock avoiding additional digital time jitter.

The integration of the TELLIE control into the trigger system must let it retain its designed flexibility, i.e. the possibility to run various calibration sequences, while remaining synchronised with the main trigger. Timing delays, from light emission at the LEDs to the propagation down the fibres, PMT cables, until the trigger board's signal generation, must all be accounted for. The sum of these delays is approximately 620 ns, see Figure 6.11; the control board compensates for this through an adjustable delay of between 0 and 1275 ns in 5 ns increments. In addition, each channel is equipped with a fine adjustment of between 0 and 63.75 ns, in 0.25 ns increments.

TELLIE electronics takes up one rack, located on the deck close to where the fibres are routed into the cavity. As mentioned the electronics comprises twelve boxes of LED drivers and one control box, see Figure 6.2. To monitor the calibration stability, each motherboard is equipped with five temperature sensors and each channel LED outputs light into cone, illuminating both fibre and PIN diode. The control box handles communications with the SNO+ digital master trigger board, sets signal amplitudes and delays for individual

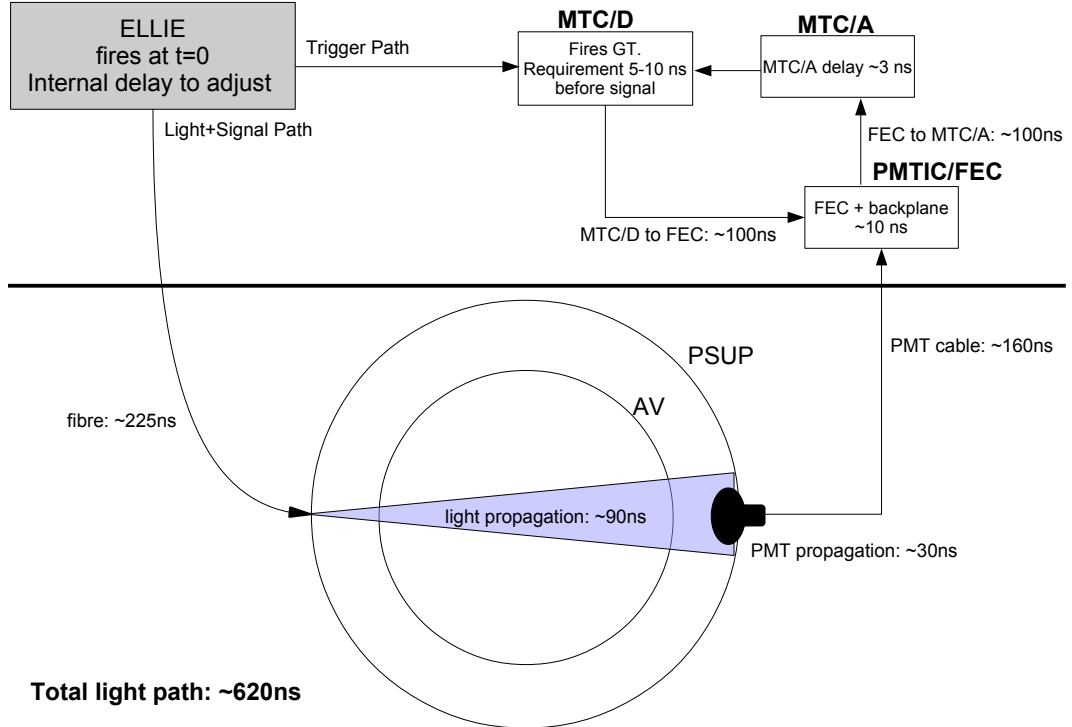


Figure 6.11: Delays in a light calibration run. The control board must send out a light pulse and a trigger signal delayed by a predetermined time, to account for both the light propagation time in the fibre and in the detector on one hand, and in the PMTs and electronics on the other. The total light and signal time, from the emission to the acquisition of the data, is about 620 ns.

channels along with system-wide pulse rates and both signal and trigger delays, as well as extracting monitoring information from the PIN diodes and temperature sensors.

The available signal frequency from a single channel ranges from 3.9 Hz to 10.0 kHz. Various calibration sequences are defined that include dedicated calibration runs at high frequency and calibration as part of standard physics runs at Hz level. Standard runs consist of generating a defined number of pulses from each LED in turn, with similar intensities, and the detector being forced to trigger on each pulse. During calibration runs the temperature of the driver board is read and recorded at appropriate intervals. Once a given calibration sequence has been completed for a channel, the average pulse height measurement from the PIN diode is recorded.

## 6.8 Performance

The goal of the performance study is to confirm TELLIE had met the requirements needed to characterise the time and charge response of each PMT. The relevant parameters that need to be validated are the intensity and coverage of the pulses, as well as their timing spread. This validation was carried out by performing realistic simulations of the beams from all positions, and by taking data with a partial set of the installed system, during air-filled commissioning runs. This section gives an overview of simulations performed and the comparisons of simulation results and commissioning data. The simulations and the PMT calibration code are the results of the Berkeley group efforts reported in [59].

### 6.8.1 Simulation of TELLIE Pulses

The simulation and analysis tool RAT, has been verified to accurately model the detector using the well-calibrated simulation of SNO. This framework provides a complete simulation of particle generation and transit within the detector, and the production, propagation and detection of optical photons. Optical processes in the different detector media are included, such as absorption, scattering, reflection and refraction using a detailed detector geometry, as well as the simulation of the PMT-response including the single photon charge spectra and the full DAQ-chain.

An LED/fibre beam event generator was developed and included in the simulation, allowing the generation of light pulses for each selected fibre mounting position, and the individual setting of the beam intensity, spectrum and angular emission profile. The simulations presented in this section were produced using the ex-situ measurements of wavelength, angular distribution and time spread described above as input. In this way, the performance of the light injection calibration system can be investigated and the calibration analysis code that will perform the hit-level time and charge PMT calibration can be tested.

Figure 6.12 shows a representation of a simulated high-intensity TELLIE event inside the SNO+ detector. The time histogram (right) shows the early hits in purple. This is light that is reflected off the acrylic vessel and detected by the PMTs that are located around the LED position. The forward light, in blue, has a larger distance to travel to the PMTs located opposite the injection point. Light that is reflected back from those PMTs makes up the yellow population of hits. Scattered light will arrive still later and is shown in

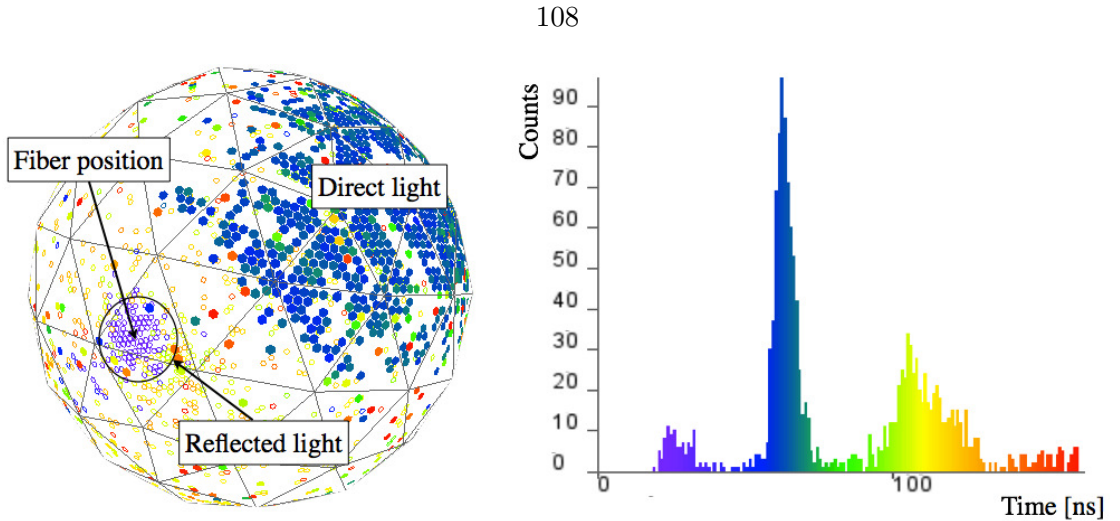


Figure 6.12: *Left:* 3D viewer display for a simulated high intensity light injection event inside the SNO+ detector. Each dot represents a PMT, and open circles represent PMTs on the far side of the detector as viewed. *Right:* The colour indicates the time at which the PMT triggered, according to the time histogram.

orange.

### 6.8.2 Expected Performance of Complete System

As mentioned, the intensity of each channel can be independently adjusted. The dynamic intensity range of each channel must obey the following requirements: If the intensity is too low, the time taken to accumulate the necessary statistics for the PMT calibration becomes prohibitively long, especially in the high charge tail region. However, too many photons in a single pulse translates into a higher percentage of multi-photon hits at the target PMTs and therefore a contaminated single-photon charge spectra. The goal of the simulations is to determine the optimal intensity in order to meet these requirements.

A check of the number of multi-photon hits as a function of intensity was performed for different phases of the SNO+ experiment. In a first phase, the AV will be filled with UPW. The UPW will then be replaced by the liquid scintillator. Finally,  $^{130}\text{Te}$  will be added to the scintillator for the  $0\nu\beta\beta$  phase. The optical properties of water, loaded and unloaded scintillator are different, therefore the transmission of light through the AV volume changes between these phases.

The dynamic range of the pulses must be such that enough light gets through to the PMTs, while also keeping the multi-photoelectron hit contamination below 1%. Using the Poisson distribution, that corresponds to a maximum hit probability of around 5%.

The LED pulse intensity can be set for the different SNO+ phases, so that hit probability will be close to the maximum of 5% for the PMTs receiving the highest intensity from the fibre, the ones within the central region,  $14.5^\circ$  around the injection direction, see Figure 5.4. From simulations, the required intensity for the single-photon charge calibration is between  $10^2$  and  $10^4$  photons per pulse at the injection point for the water phase and the loaded scintillator phase, respectively. Fortunately the drivers have been demonstrated at intensities of  $10^3$  photons per pulse without a fibre, the attenuation of the fibre means that pulses of  $10^3$  are reduced to almost  $10^2$  at injection point. So, we have to tolerate only slightly more multiple photon hits during the water phase.

With this setting, the expected hit probability in the border region, between  $14.5^\circ$  and  $29^\circ$  around the injection direction, has a mean of about 1%. This value is then used to calculate the expected total time needed to collect a complete calibration data-set, that depends as well on the desired time resolution and the frequency at which the pulses are fired, as described in Chapter 5.

Assuming a required time precision of 0.5 ns, a pulse width of 5.2 ns and a 10 Hz operating frequency, this gives a total required run duration of approximately 5 hours to accumulate enough data for the border region. This is the duration required when running at low rate within a physics run. Dedicated calibration runs can be taken at least at 1 kHz and will thus require only a few minutes. With this performance a flexible calibration program, with fast dedicated runs and low rate continuous running will be possible in SNO+.

For charge spectrum studies and calibration, it is enough that each PMT is hit by light from at least one fibre. However, for the PMT time calibration, a more redundant data-set is required, where PMTs detect light from more than one fibre. This redundancy will allow for the time offsets between the different fibres to be extracted and corrected for.

In terms of PMT coverage, the first level of redundancy in the system is ensured by having two fibres in each node. The fibre positions at the 91 PSUP nodes have been chosen in such a way that all PMTs see direct light from at least one fibre, and in most cases two. The two-node redundancy requirement faces two difficulties. The aperture in the PSUP to accommodate the AV neck effectively removes its 92<sup>nd</sup> node, reducing the coverage of the PMTs in the lower hemisphere. To overcome this, an extra duplex fibre is positioned close to the AV neck. In addition, the hold-down and hold-up ropes surround the AV, casting shadows in the injected beams. In several cases, these shadows are large enough to block or significantly reduce the intensity seen at opposite PMTs.

Simulations including a detailed model of the rope system, show that even with those shadows, most PMTs receive light from more than five different fibres. Considering 10% of the central region intensity as the acceptance limit for worse illuminated PMTs, the simulations show that all PMTs see at least one fibre, with 20 seeing only one fibre. If that acceptance is relaxed to 2% of the central region intensity, then all PMTs are illuminated by at least two fibres. This means that, in the unlikely event of failure of the two fibres illuminating those 20 PMTs, they can still be calibrated, with dedicated runs of neighbouring fibres, at higher intensities.

It is equally important that all fibres have enough overlap so that any relative time offset can be measured. This is verified by the PMT calibration code, which extracts time offsets between individual fibre pairs by combining the data from the overlapping PMTs. A minimum of 20 PMTs need to see hits from the same fibre pair before a time offset can be extracted. Simulations also show that the number of PMTs that see each adjacent fibre pair<sup>1</sup> is always above 30, normally around 80 for most pairs.

The main goal of the PMT timing calibration algorithm is to provide hit-time corrections to account for each channel's offset and for the time walk effect, see Figure 6.13 (left). Several million light injection events were simulated and used to extract timing calibration constants which were then applied to calibrate simulated data of uniform light pulses emitted in the detector centre. For the simulated detector, the calibration performed with the light injection system has been shown to effectively correct for the time walk, see Figure 6.13(right).

### 6.8.3 Commissioning with Partial System

Commissioning air-filled runs took place in October 2012, March 2013 and February 2014. During these runs, 36 of the 110 light injection fibres were installed in the lower hemisphere of the PSUP<sup>2</sup>. For the first and the last run, all the SNO+ electronic crates were powered on and the majority of the PMTs were at high voltage. Seven of the nineteen crates were on for the second run. The light injection event intensity was high at around  $10^5$  photons per pulse, for the first run. The second and third run had a flexible intensity, between  $10^3$  and  $10^5$  photons per pulse. Using the commissioning data, two verifications

---

<sup>1</sup>fibres for which the injection point is within 4.5 m of each other, or 30° measured from the detector centre.

<sup>2</sup>due to the PSUP geometry, remaining fibres in the upper hemisphere need to be initialised during water-fill

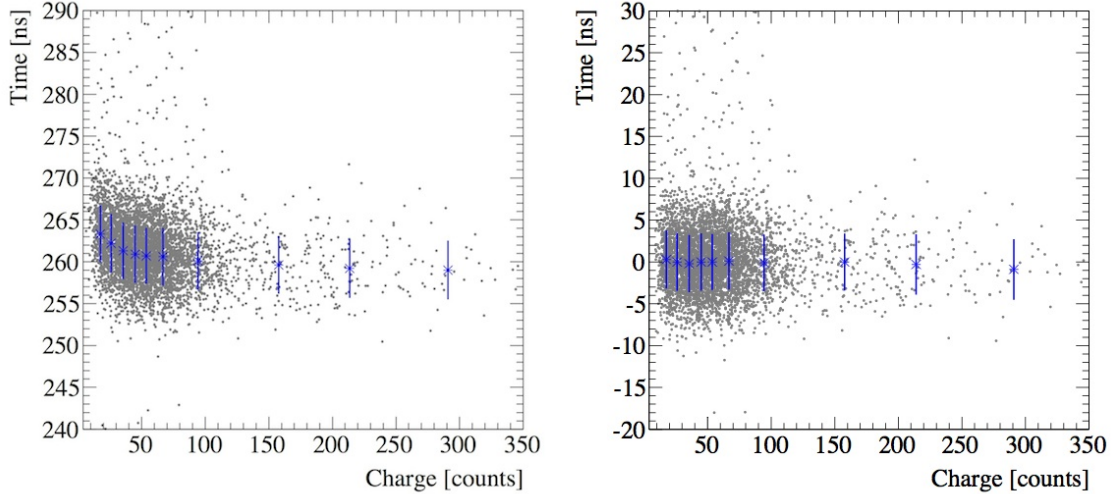


Figure 6.13: *Left:* An example of the discriminator walk effect in simulated light injection data. The data points with error bars correspond to an average evaluated in a given charge bin and used to interpolate the time-charge dependence. *Right:* simulated light injection data after applying the extracted time corrections. For a comparison with SNO data, see Fig. 3.2 of reference [83].

for the light injection system were performed: coverage and charge response.

First, all installed fibres were tested and their positions and directions were compared to the values inserted in the database after their installation. All fibres were found to be undamaged and with matching positions and directions. Figure 6.14 shows the number of hit PMTs per event versus the cosine of the angle between PMT and fibre with respect to the detector centre, for data and two simulations of the same fibre, with different angular distributions.

Since the intensity is quite high, the comparison of the measured number of detected hits at the PMTs with simulations is expected to be distorted by MPE effects in the forward region. From Figure 6.7, an opening angle of  $14.5^\circ$  is expected in air. The data at high intensity had between  $9 \times 10^4$  and  $1.1 \times 10^5$  photons per event. From this, a minimum and maximum hit probability was simulated, represented by the light grey area in Figure 6.14, showing a good agreement with data.

Second, the PMT charge calibration code used the low-intensity commissioning data to verify that the single-photon-electron level was achieved. To characterise the charge spectrum, the PMT calibration analysis extracts three parameters for each PMT: the threshold, peak and high-half point (the lines visible in Figure 6.15). The latter is used in simulations to scale the charge spectrum for each individual PMT. Figure 6.15 shows the charge

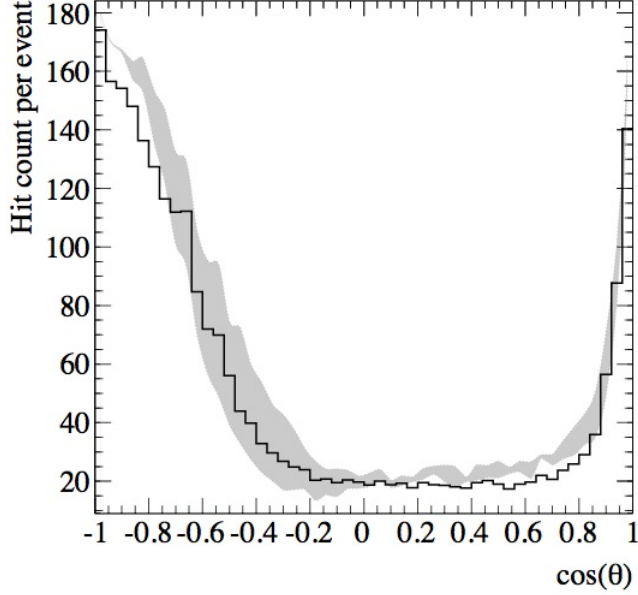


Figure 6.14: Number of hits per event versus the cosine of the angle between PMT and fibre position for commissioning data (black, thick solid). The light grey band represents the region between minimum (simulation with  $11^\circ$  opening angle and  $9 \times 10^4$  photons per pulse) and maximum ( $13^\circ$  opening angle and  $1.1 \times 10^5$  photons per pulse) hit probability. The direct and reflected light are detected around  $\cos \theta = -1$  and  $1$  respectively.

spectrum for a single PMT with the extracted values for the three spectrum parameters, compared to the values that were extracted in SNO using the LB. The small differences seen between SNO and SNO+ are likely caused by a difference in the electronics calibration. Since the light attenuation is expected to increase when the detector is filled, the data taken during the commissioning of the SNO+ light injection system shows that the pulse intensity can be lowered to a level where the multi-photon hit contamination is minimal. This means that the light injection system will be able to produce events low enough in intensity to be used for the PMT charge calibration.

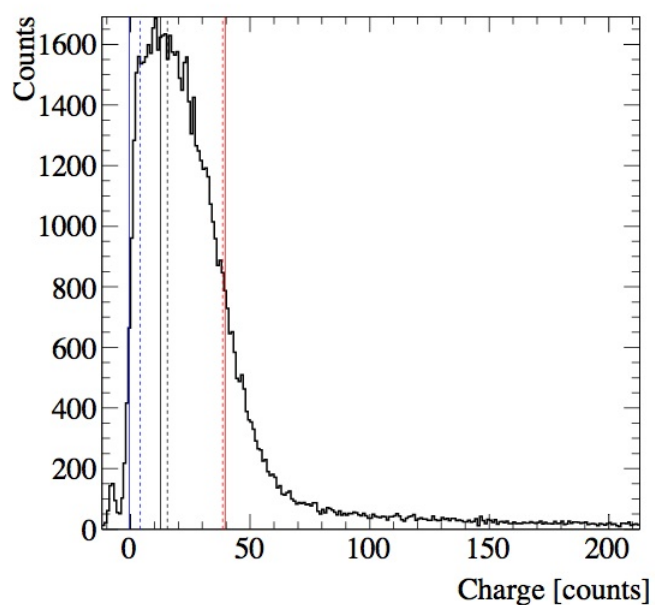


Figure 6.15: *An example of the PMT charge calibration constant extraction using low-intensity light injection data. The dashed (solid) lines show the position of the threshold, peak and high-half point from left to right for SNO (SNO+) data.*

## Chapter 7

# The Laserball

This chapter will describe the design and construction of the scintillator-phase LaserBall (LB), a deployed optical source. It will begin with a summary of the LB used in SNO, using the SNO calibration results to motivate the design of the scintillator phase LB - namely the shadowing in the upper hemisphere of the PSUP. The components and a construction procedure for the scintillator phase LB will be outlined and its expected performance presented.

### 7.1 Requirements

The LB is a triggered, multi-wavelength and virtually isotropic laser source, used for both the PMT and the optical calibration. It was and is to be used to measure the relative PMT efficiencies and timing as well as detector optical properties such as the media attenuation lengths, the PMT angular response and the detector suspense as a function of source position.

The SNO LB will be reused during the initial water-fill phase of SNO+, when radiopurity is less of an issue given the reduced sensitivity. However, the increased sensitivity intrinsic to the scintillator-phase introduces more stringent radiopurity constraints. There are two main points motivating the redesign of the LB for the scintillator-phase: radio cleanliness and improving the asymmetry in shadowing to the upper hemisphere of the PSUP.

The radiopurity constraint is set by the level of backgrounds already present in the LAB.

As mentioned in Chapter 3,  $^{222}\text{Rn}$  is a background of particular concern.  $^{222}\text{Rn}$  is part of the decay chain of  $^{238}\text{U}$ , shown in Figure 3.3. Its daughter nucleus  $^{214}\text{Bi}$  contributes a direct background for neutrinoless double-beta decay, and the longer lived daughter nucleus  $^{210}\text{Pb}$  decays to  $^{210}\text{Bi}$  which has a similar energy spectrum to the CNO neutrino spectrum [61]. As yet SNO+ has no direct measurement of the levels of  $^{222}\text{Rn}$  present in LAB, though it is expected that Borexino levels will be achieved. Borexino measured  $^{238}\text{U}$  at  $1.6 \times 10^{-17} \text{ g/g}$  [62] which at a decay rate of  $1.55 \times 10^{-4} \text{ Hz}$  corresponds to 6278 events/year/ktonne. So for 780 ktonnes of LAB at this level of  $^{238}\text{U}$ , 4897  $^{222}\text{Rn}$  events/year are expected. This corresponds to 13.4 counts per day, which defines the upper limit of  $^{222}\text{Rn}$  emanation for deployed sources.

The shadowing will be discussed later, once the geometry of the LB has been introduced.

## 7.2 The SNO Laserball

The LB, a light diffusing sphere, consists of a quartz flask containing small silica beads suspended in clear silicone gel [87]. A quartz optical fibre terminates at the centre of the flask; this fibre forms part of the umbilical connecting the LB and N<sub>2</sub> laser on deck. Figure 7.1 shows drawing of the LB and its umbilical connection.

The scattering length of light inside the source is of order of 1 cm, which is a good compromise between having a good isotropy (requiring short scattering length) and reducing the intensity losses due to dispersion and absorption (requiring a large scattering length) [129]. The neck of the LB is encased in a stainless steel shroud preventing light refracted upward reaching the PMTs. This shroud and the umbilical connection considerably reduced the intensity of the source in the upward direction; the SNO LB mounting hardware casts a 30° shadow from the vertical axis at the centre of the LB flask. The light pulses are generated by an external short pulse-length N<sub>2</sub> laser at 337.1 nm. The laser was coupled to a series of dyes to produce pulses of longer wavelengths [130]. The layout of the laser and its dye system is shown in Figure 7.2.

To cover most of the Cherenkov spectrum of interest to SNO, there were five dyes enabling a total of six different wavelengths. The laser had a pulse width of 0.6 ns, with the dyes adding between 0.3 and 0.5 ns to the width [129]. Figure 7.3 shows the spectra of the various dyes. The system allowed for the selection of neutral density filters from two

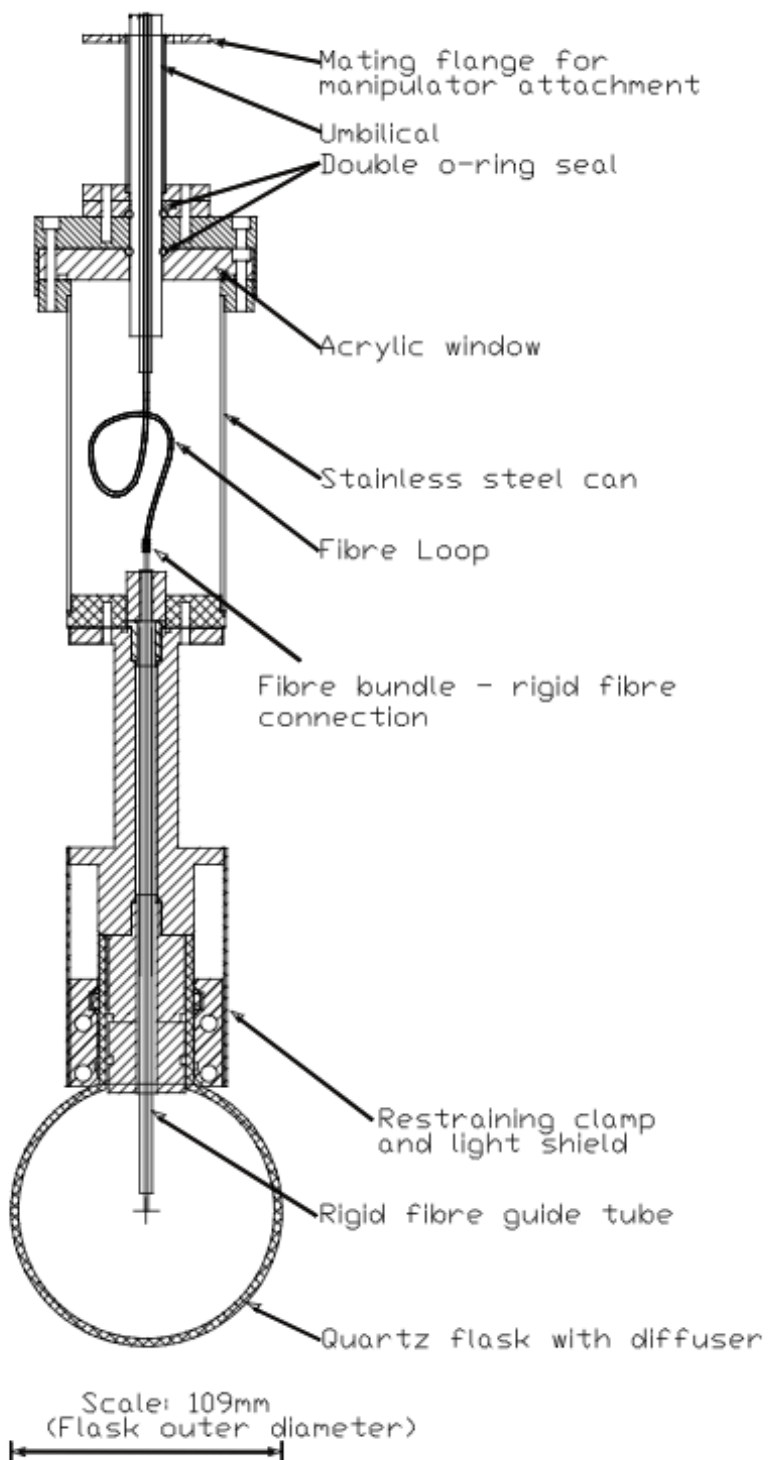


Figure 7.1: The SNO laserball and umbilical connection [87].

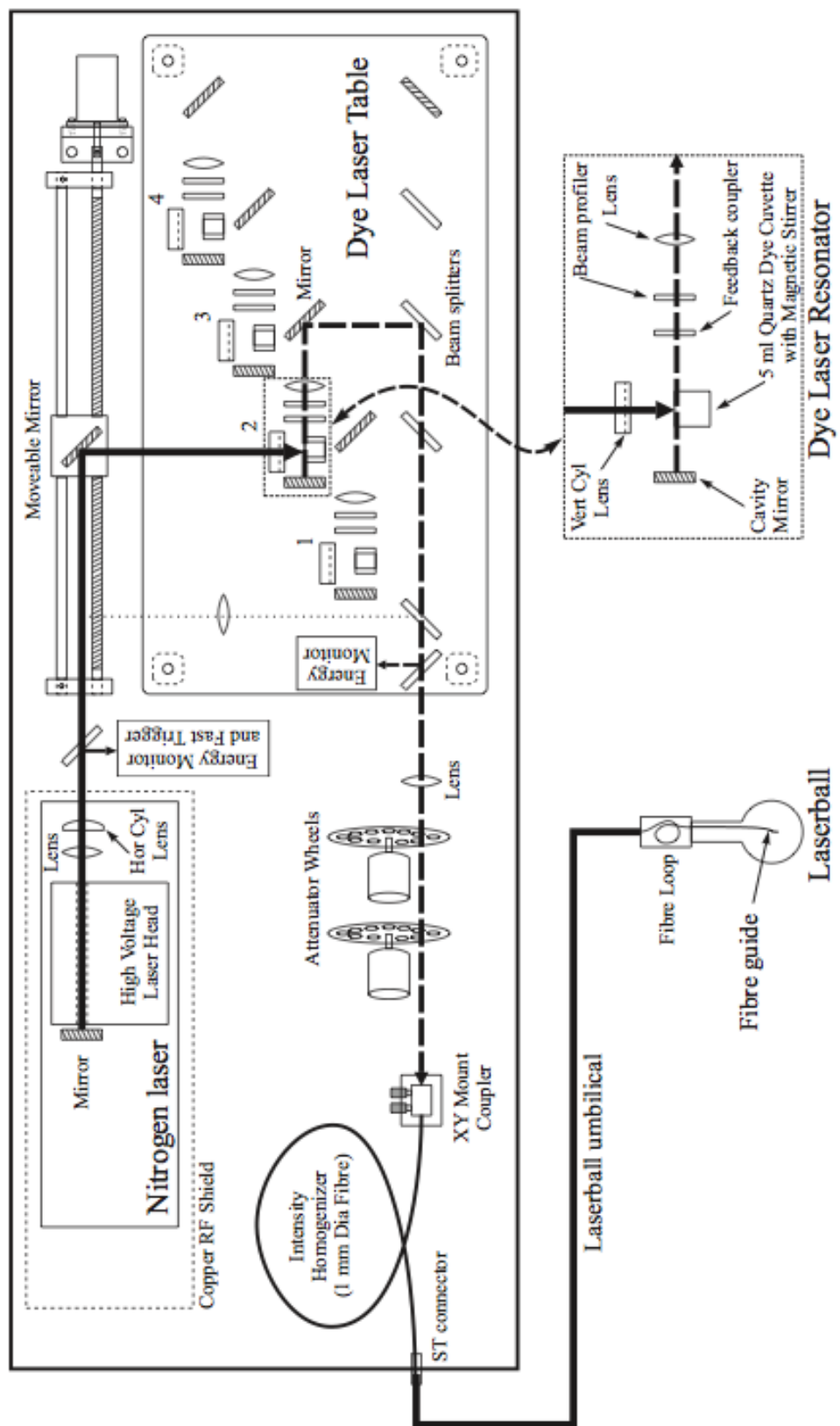


Figure 7.2: *Schematic of the SNO laserball system [129].*

wheels, shown in Figure 7.2, to reduce the intensity of the laser. This is particularly important for optical calibrations, where the intensity of the light is adjusted to very low values so that each hit PMT sees essentially a single photo electron, corresponding to between 300 and 400 hit PMTs per event [87].

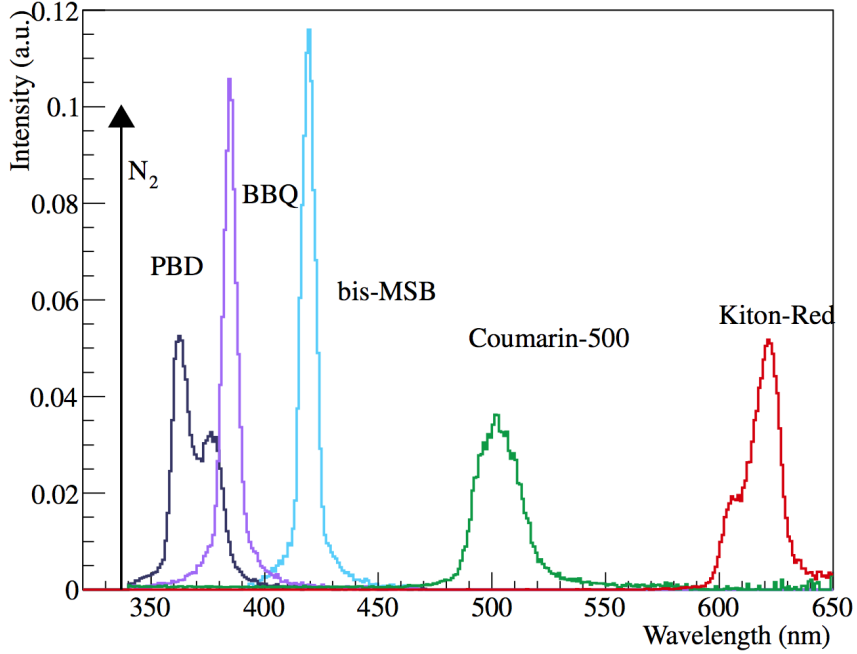


Figure 7.3: Spectra of  $N_2$  laser and dyes used in SNO [129].

### 7.3 The SNO+ Scintillator Phase Laserball

As mentioned above, the intensity of the source in the upward direction is considerably reduced by its design. This is causing a systematic error in the measurement of the PMT angular response. Therefore, as well as building a LB that is sufficiently radioactively pure to be deployed within scintillator, it has also been redesigned to maximise its intensity in the upward direction.

Another problem highlighted in the SNO LB was the consistent positioning of the fibre at the centre of the flask. This misalignment is believed to have caused a drop in intensity at larger transmission angles relative to the neck.

#### 7.3.1 Design

Much like the original SNO LB, the scintillator phase LB is a deployed source that can be manipulated into various positions within the AV. It consists of quartz flask filled with

silica beads suspended in silicon gel, forming a light diffusing sphere. The flask is connected via stainless steel mounting hardware to an umbilical containing an optical fibre, which guides laser pulses generated on the deck into the centre of the flask. The neck of the flask and the stainless steel connector are as narrow as possible to minimise shadowing to the upper hemisphere, yet maintain sufficient material to support the flask.

### 7.3.2 Mechanical Design

The overall diameter of the flask remains the same as the SNO LB at 109 mm, with a 3 mm wall thickness, the neck is considerably narrower, reduced from 38 mm to 19 mm. More detailed information on the various components can be found in [131]. The following is a summary of the components and their function.

The issue of misaligning the light guide has been eliminated with the design of the new plug and light guide, a prototype of which is shown in Figure 7.4, Figure 7.5 shows how the components fit together. The plug's lower section slots into neck of the flask, sealing on the inside of the flasks' neck. The mid section is the same diameter as the lip of the flask, the lower edge seals against the top of the flask, there are two bolt holes in the top edge to hold the clamps in place, the top section is narrower and extends beyond the clamps. The plug is hollow, in the lower and mid sections the bore is honed to the same diameter as the light guide, the upper section has a larger diameter bore: the lower portion of this bore is threaded to hold the light guide in place, the upper portion is honed to provide another sealing edge.

The clamps are cylindrical with a conical base, they are split lengthways with the each half machined hollow to slot over the flask neck and mid section of the plug. The hollow has to be precisely machined to each flask, to ensure minimal compression of the seal between the plug and the top edge of the flask. There are holes in the top of each clamp to accommodate locating bolts that thread into the corresponding holes on the plug. The lower inner edge of the clamps have a recess machined into them to accommodate the shrouds.

The shrouds cover the neck of the flask below the the clamps. They are a cylinder split length ways, with an internal bore to match the external diameter of the flask neck. The splits are staggered, to prevent light leaking. The shrouds are held together by the recess in the clamps. The need for a shroud to cover the neck is well illustrated in Figure 7.6(a).

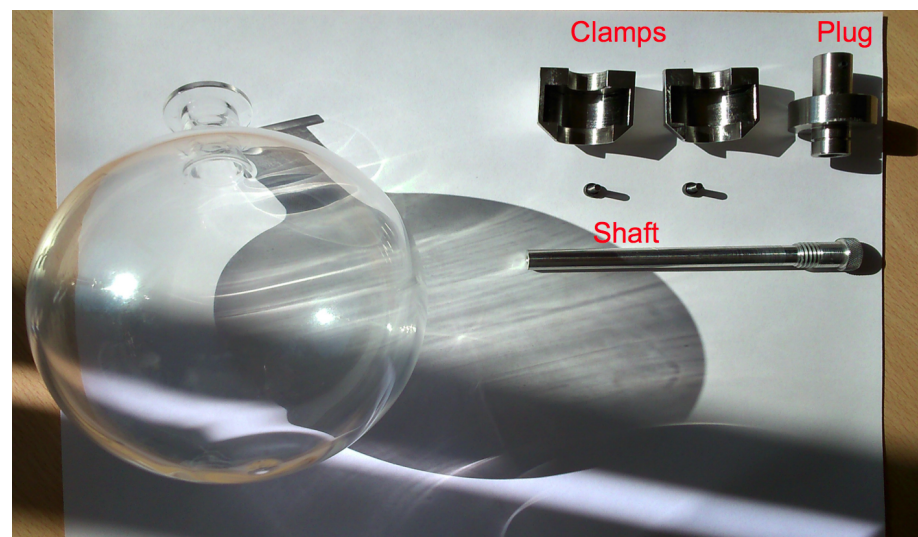


Figure 7.4: A prototype of the scintillator phase laserball, showing the main components without seals or shrouds.

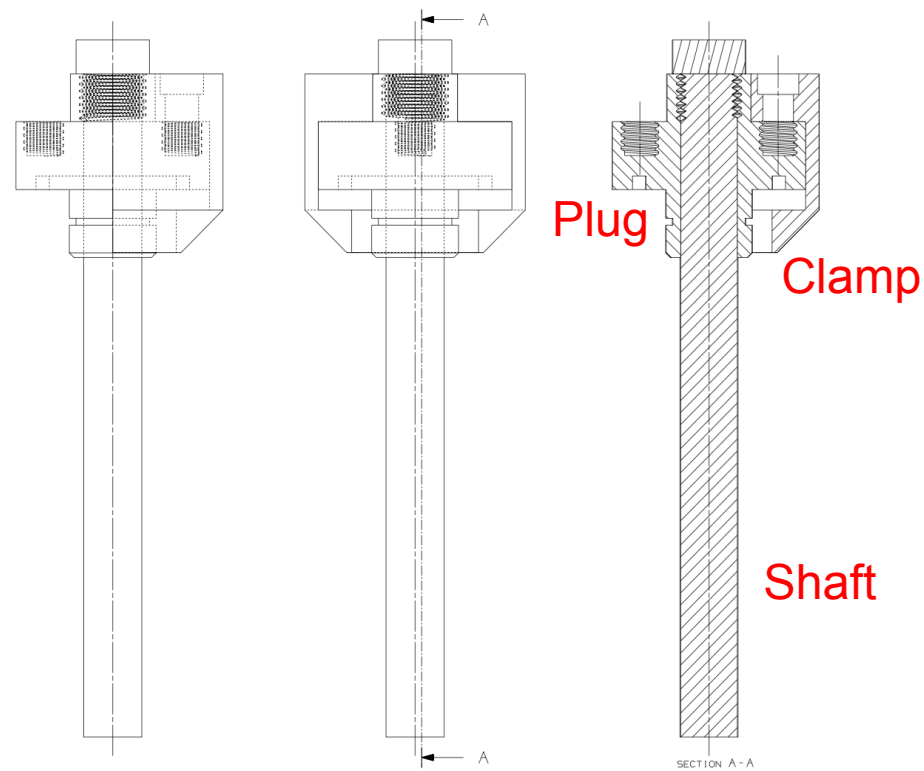


Figure 7.5: A drawing of the scintillator phase laserball connection, showing how the main components of the connection fit together.

The light guide consists of a hollow steel shaft, with an acrylic or quartz rod mounted within the bore. The lower section of the shaft fits the bore of the lower section to the plug. The upper section houses two seals to seal below the threads in the plug, above these are the threads to fix the guide into the plug, and above the threads are a shoulder that stops against the top of the plug. So the guide can only be inserted a set depth into the plug. The rod protrudes beyond the shaft, terminating just above the centre of the flask. The location of the termination point will need optimising for each flask, to ensure isotropic emission.

The method of coupling to the umbilical is yet to be confirmed, therefore no components beyond the light guide have been developed, though the shaft of the light guide can easily be modified to accommodate further fittings, Figure 7.6(b) shows a filled LB with the fittings for the DEAP-3600 dark matter experiment.

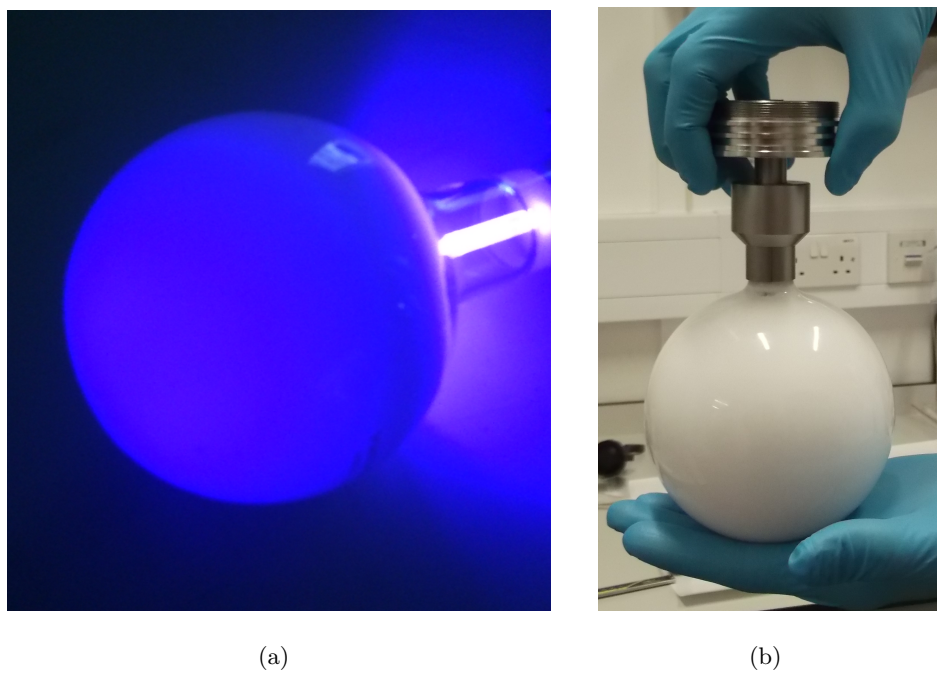


Figure 7.6: *Left:* A prototype LB illuminated with a laser diode, using an acrylic light guide. *Right:* A filled LB, for the DEAP-3600 dark matter experiment.

Technical drawings of all individual components are provided in Appendix B. The scintillator phase LB mounting hardware casts only an  $8^\circ$  shadow from the vertical axis at the centre of the LB flask.

The flask was made by Technical Glass Products of Painesville Ohio<sup>1</sup>, from domestically sourced fully synthetic fused quartz. The gel used to fill the flask is ACC Silicones'

---

<sup>1</sup>[www.technicalglass.com](http://www.technicalglass.com)

Egel3005, 2 component low viscosity silicone gel<sup>1</sup>. The silica beads suspended within the gel are 3M's S32 Glass Bubbles density: 0.32 g/cc, size: 80 microns<sup>2</sup>. All mounting components are made from certified as 316L low carbon stainless steel, which is electro polished and washed with citric acid. All O-rings used are Viton, Du Pont's brand name for fluoroelastomers also known as FKM or FPM depending on naming standards, supplied by Polymax<sup>3</sup>.

Detailed step-by-step instructions on how to assemble the LB are provided in Appendix A.

### 7.3.3 Radioactivity and Scintillator Compatibility

The LAB compatibility test of the Viton o-rings [132] showed significant peaks of absorbance in UV and visible light scans, as well as no indication of any change in flexibility or swelling after 41 days of exposure to LAB. A sample of Viton was sent to Queen's University, Kingston, and measured in their radon emanation counter. The sample was 6.15 m long and 3.5 mm in diameter, in a counter with a background of  $45 \pm 10$  atoms per day the sample emitted  $94 \pm 22$   $^{222}\text{Rn}$  atoms per metre per day. The LB design has only one o-ring partially in contact with LAB, the circumference of that o-ring is only 75 mm. Despite Viton being a relatively hot material, its compatibility with LAB makes it an ideal seal, and the LB design means that the levels of  $^{222}\text{Rn}$  are kept below the required 13.4 counts per day.

316L stainless steel was also shown to be compatible with LAB after 41 days exposure [132]. Radon emanation is less of an issue for stainless steel, as any radon plated out on the surface can be removed and surface roughness reduced through electrolytic polishing. In addition stainless steel tends not to emanate  $^{222}\text{Rn}$ , even if it has uranium or thorium contamination - emanation from metals is much smaller than from plastics or rubbers [133].

The quartz flask was cleaned with alcohol then placed in the radon emanation counter at Queen's and found to be cleaner than the counter [134]. The background of the counter is 30 atoms per day. The first measurement showed 50 atoms per day, the two subsequent measurements both showed only 30 atoms per day. This measurement counted atoms from both the inner and outer surfaces of the flask, in normal operation only the outside of the flask will be in contact with LAB, so the number of  $^{222}\text{Rn}$  atoms emitted per day

---

<sup>1</sup>[www.acc-silicones.com](http://www.acc-silicones.com)

<sup>2</sup><http://www.3mdirect.co.uk/engineering-additives-sample-products.html>

<sup>3</sup>[www.polymax.co.uk](http://www.polymax.co.uk)

will be less than 30. It is possible to reduce this number further, by scorching the surface of the flask effectively melting it smooth - reducing surface roughness and therefore the emanating surface area.

## 7.4 Expected Performance

Since the SNO LB will not be deployed within the scintillator, we cannot directly compare the performance of the scintillator phase LB with the SNO LB. It is possible to compare the two in MC at least. What follows is a summary of work carried out at Sussex [135].

### 7.4.1 The Mask Function

As an approximation in RAT, rather than simulating the precise geometry of the LB mounting hardware a mask function is used. The mask function is as a sixth order polynomial to account for any anisotropies due to manufacturing flaws such as inhomogeneities within the gel or a misaligned light guide:

$$f(x) = 1 + ax + bx^2 + cx^3 + dx^4 + ex^5 + fx^6 \quad (7.1)$$

where

$$x = 1 + \cos(\theta), \quad (7.2)$$

and  $\theta$  is the angle between the direction of the emitted photon and the vertical axis. There is no  $\phi$  dependence as the LB is assumed symmetrical about the vertical axis.

Von Neumann accept-reject sampling is used to determine if a photon passes the mounting hardware. For a given value of  $\theta$  a random number is generated between 0 and 1, if the number is less than  $\frac{f(x)}{f_{max}(x)}$  at the given  $\theta$  it is accepted as passing. If it is larger, then it is considered to have struck the mounting hardware. At small angles a large number of photons will strike the mounting hardware, although there remains a small probability of them not as the flask's diameter extends beyond the mounting hardware. At large angles, when  $x \approx 1$ , only a small number photons strike.

### 7.4.2 Obtaining the Mask Functions

Although there is extensive data for the SNO LB mask functions [129], it is unrealistic to compare directly with a MC generated mask function for the scintillator phase LB, as any anisotropies in the new design will not be understood well enough to be included in the simulation. Therefore, mask functions for both designs were generated using MC. The internal structure of the LBs were not modelled, rather they were treated as ideal isotropic sources, with Lambert's cosine law describing the emission of photons from the surface; the likelihood of a photon being emitted from a diffuse surface at a certain angle is proportional to the cosine of that angle:

$$P(\Theta)d\Theta = \cos(\Theta)d\Theta \quad (7.3)$$

where

$$-\frac{\pi}{2} \leq \Theta \leq \frac{\pi}{2}. \quad (7.4)$$

First a position on the LB surface was generated, modelling it only in 2D as symmetry is again assumed about the vertical. The emission angle for a photon at this position was generated with Equation 7.3. This angle was then converted to a 2D vector, with the y-axis normal to the LB surface. A direction vector with respect to the LB neck rather than surface was then calculated, and a ray representing the photon emitted at this position is then generated. The vertices of the mounting hardware were modelled as a set of vectors, with lines between them representing its surface. If the ray crossed this surface it was discarded, if it did not it was binned in a histogram of  $1 + \cos(\theta)$ . For both LB designs the MC ran for  $10^8$  events. The histograms were then normalised to have an intercept of 1, and then fitted with a sixth order polynomial to obtain the two mask functions.

The fitted MC generated mask functions are shown along with data [87] for the SNO LB in Figure 7.7. The MC produced mask function for the SNO LB agrees well with data at small angles when  $1 + \cos(\theta) \approx 2$ , both show the expected increased gradient due to the  $30^\circ$  shadow at roughly 1.8. At larger angles there is a greater difference between the fit and data, this is due to neglecting any internal anisotropies and treating the LB as an ideal isotropic source in the MC. As expected the scintillator phase LB mask function is higher at small angles, due to the small shadow cast by the mounting hardware,  $8^\circ$ , and a greater portion of the flask extends beyond the width of the mounting hardware. There is some oscillation in the mask function at larger angles for the scintillator phase LB, this

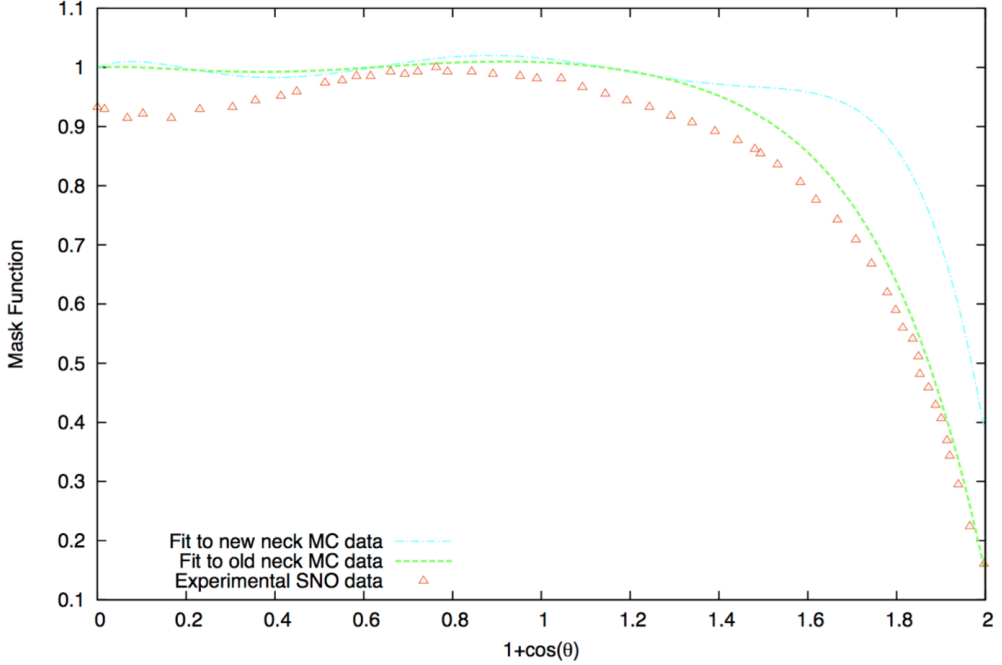


Figure 7.7: The fitted mask functions for the Monte Carlo generated SNO (green) and scintillator phase (blue) laserball designs, experimental data from SNO is also shown (red).

could be reduced by fitting a lower order polynomial.

#### 7.4.3 PMT Angular Response

It is possible to determine what angle of incidence the PMTs are most sensitive to. During SNO an investigation was performed into the distribution of angles of photons causing successful PMT hits [136]. Photons were generated uniformly and isotropically within the AV and the angle of incidence for photons causing successful hits was recorded, Figure 7.8 shows the distribution of successful hits. The peak of the distribution is between 20-40°, which is close to the peak in the PMT response of around 40° [129]. The peak is not at zero, since fewer photons strike at lower angles of incidence, due to the geodesic structure of the detector.

Simulations were carried out to investigate how the scintillator phase LB design improves the emission of photons within this angular range for PMTs within the upper hemisphere of the PSUP [135]. The LB was moved symmetrically in the  $x, y$  plane, as well as up and down in  $z$  whilst keeping  $x = y = 0$ . Figure 7.9 show a histogram of the angle of incidence for photons striking PMTs at least 6.5 m above the equator, for all LB positions. The peaks at 10° and 35° are due to the limits of range of motion in  $z$ . The peak at 4° is

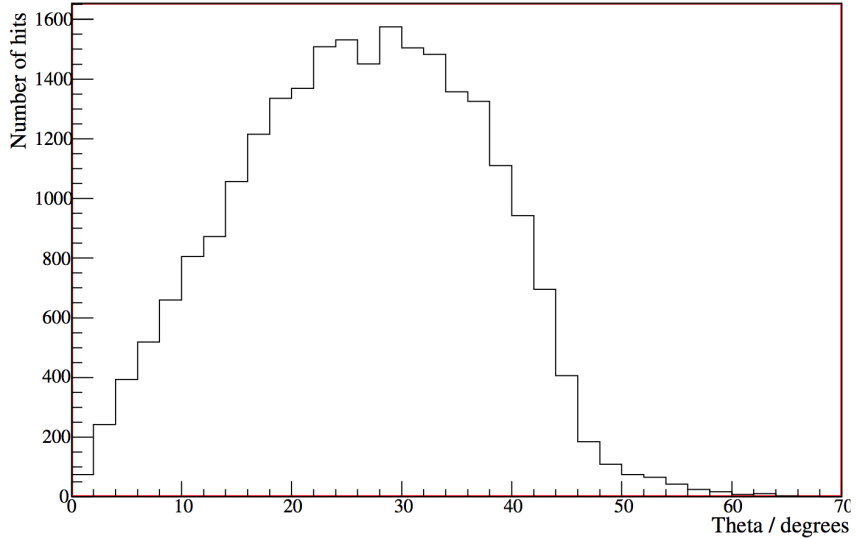


Figure 7.8: *Monte Carlo simulation of the angular distribution of photons incident on the PMT photocathode that cause a successful hit [136].*

due to the laserball being positioned at the centre of the detector, it is non-zero because the PSUP is geodesic rather than a perfect sphere, which means that only a very small number of PMTs are actually inline with and perpendicular to the LB position.

The scintillator phase LB shows more photons hitting the PMT at small angles, and the total number of photons hitting the PMTs is higher. This indicates the scintillator phase LB will be able to probe the angular response of the upper most PMTs more accurately than SNO LB.

## 7.5 Conclusions

The original SNO LB was successfully used for both the PMT and the optical calibration, and will be used again during water-fill. However, the design of the mounting hardware for the SNO LB casts a  $30^\circ$  shadow - limiting its intensity in the upward direction. The stringent radiopurity requirements of the scintillator phase require that if a calibration source is to be deployed it must be no more radioactive than the scintillator. To meet this requirement a scintillator phase LB has been designed and built at Sussex; the new LB has been designed with a narrower neck, the mounting hardware cast only an  $8^\circ$  shadow. Simulations have shown that the scintillator phase LB has a greater intensity in the upward direction - minimising any systematic uncertainty in the calculation of angular response for PMTs within the upper hemisphere. Furthermore, the increase in the number of photons

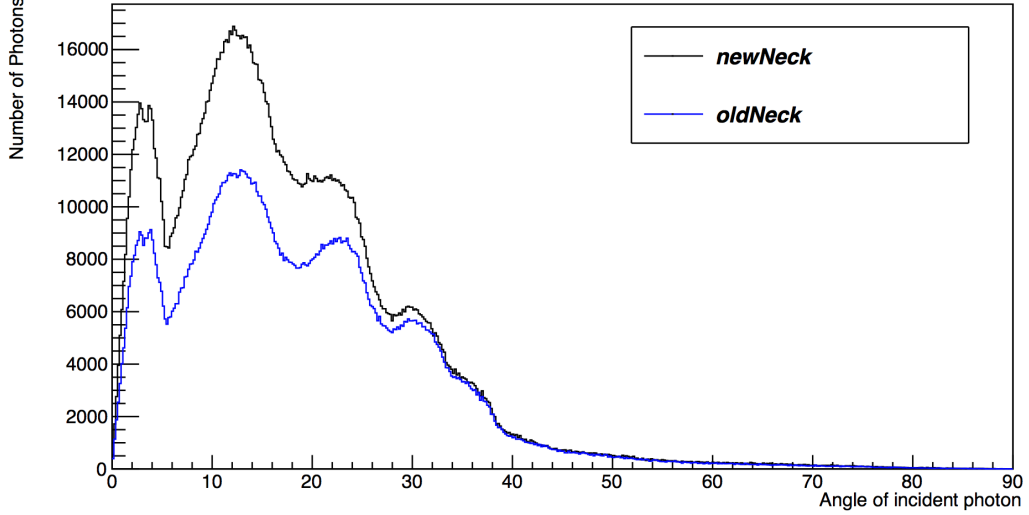


Figure 7.9: *Angular distribution of photons incident on the PMT photocathode that cause a successful hit, showing only PMTs at least 6.5m above the equator [135]. The Monte Carlo generated mask functions for the scintillator phase (black) and SNO (blue) laserball designed were used [135]. This is for all LB positions. The peaks at  $10^\circ$  and  $35^\circ$  are due to the limits of range of motion in  $z$ . The peak at  $4^\circ$  is due to the laserball being positioned at the centre of the detector, it is non-zero because the PSUP is geodesic rather than a perfect sphere, which means that only a very small number of PMTs are actually inline with and perpendicular to the LB position.*

emitted within the angular range that is most likely to cause a successful PMT hit, improves the physics sensitivity for PMTs within the upper hemisphere of the PSUP.

## Chapter 8

# Acrylic Vessel Monitoring with TELLIE

It was shown in Chapter 4 that ropes supporting the AV have already stretched and will continue to do so. If the temperature in the cavity is maintained at 10°C, the AV is expected to move by 50 mm over the next 10 years. In the worst case scenario, it could potentially move by as much as 90 mm. The AV has been positioned to accommodate the expected movement. However, drawbacks to the current systems used to monitor the position of the AV were also highlighted; such as corrosion effecting equator monitors and the inability to accurately measure deformation of the AV with the current system. As will be seen in the following chapter, accurately knowing the position of the AV is vital if external backgrounds are to be successfully minimised through the definition of a FV.

This chapter will describe how the TELLIE system can be used to monitor the position of the AV by measuring the time of flight for photons injected at the PSUP and reflected from the surface of the AV. The principle of the fitting the position will be discussed, highlighting all of the properties of the detector and simulation software that need to be understood before such a fit is possible. The expected resolution will then be presented.

Unfortunately the full PMT timing calibration has yet to be completed, due to the delays with filling the detector with water. This means that, although the tools are ready, there is no useable data.

Medium	Group Velocity (m/ns)	Effective Refractive Index
Ultra-pure water	0.219	1.34
Acrylic	0.195	1.50
Liquid scintillator	0.200	1.49

Table 8.1: *Group velocity and refractive indices as stored in RAT, for a wavelength of 507 nm. The refractive indices for ultra-pure water and scintillator agree with [138, 139] respectively.*

## 8.1 Principals of Fitting the AV Position

TELLIE has been shown to be a functioning timing calibration system, capable of injecting light pulses with well defined time profiles and intensities from every node of the PSUP. It will be shown here that TELLIE can be used to continually monitor the position of the AV, by measuring the time of flight for light pulses injected at the PSUP and reflected from the surface of the AV. The multiple injection points provide ample coverage to precisely triangulate the AV within the PSUP: any shift in position or even shape deformation would be detected as a change in the time of flight for reflected photons.

There are a number of issues that need to be understood in detail before it is possible to begin fitting the location of the AV, such as: the optical properties of all media the pulses propagate through, the types of reflection intrinsic to the detector's structure, the PMT geometry, the light path and the various delays within the trigger system.

## 8.2 Refractive Indices and Group Velocities

To understand the time of flight for TELLIE pulses in the different media the group velocities are needed. The group velocities of various media are stored in the RAT database as  $\text{mm s}^{-1}$  as a function of energy in MeV. To find the effective mean group velocity, first the LED spectrum was scaled by the PMT QE, both shown in Figure 5.1. After extracting the weighted mean for the LED energy spectrum, the corresponding velocity could be extracted from the RAT database. The wavelength from the weighted mean is 507 nm, the group velocities are shown along with corresponding refractive indices for this wavelength in Table 8.1. The refractive indices are also stored in the RAT database, and can be extracted using the same technique. Figure 8.1 shows the indices as stored in RAT, notice there is little variation around 500 nm.

It is important to determine whether there is a greater probability for light to be reflected

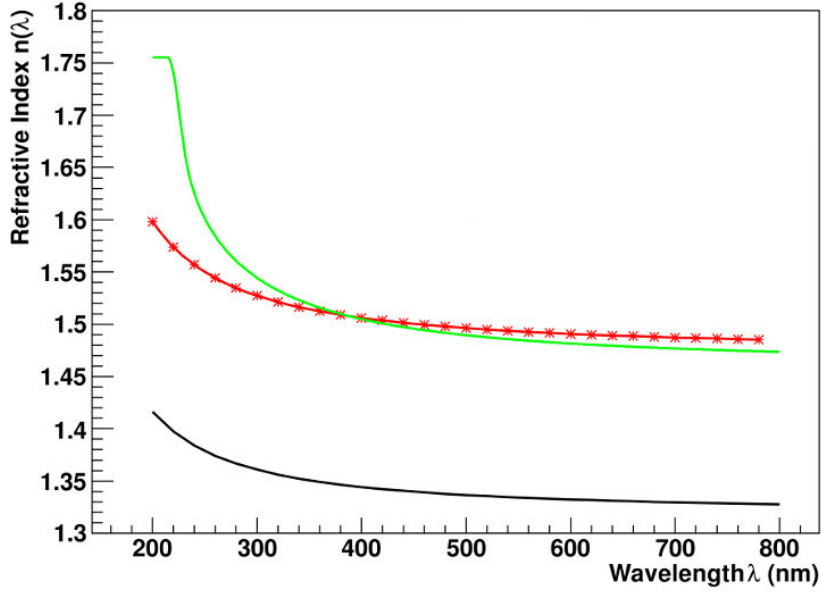


Figure 8.1: The refractive indices for water (black), acrylic (red) and scintillator (green) as stored in RAT. Adapted from [137].

from the inner or outer surface of the AV, this can be calculated using the refractive indices. Using the Fresnel equations and assuming incident light to be normal to the surface, which is to a good approximation the case for the TELLIE fibres, the reflection probability is calculated as:

$$R = \left( \frac{n_1 - n_2}{n_1 + n_2} \right)^2, \quad (8.1)$$

where  $R$  is the reflection coefficient, and  $n_i$  is the refractive index of a given medium. For the interface between UPW and acrylic the reflection coefficient is  $3.2 \times 10^{-3}$ , for the interface between acrylic and scintillator the probability of reflection is  $5.5 \times 10^{-6}$ : three orders of magnitude smaller. Therefore, for a scintillator filled detector, the light in the reflection from the near side of the AV is reflected from its outer surface.

### 8.3 Time of Flight Calculations

Given the group velocity of light, all that is needed to calculate time of flight is the path length. As shown in Figure 8.2, by defining vectors from the centre of the coordinate system to the injection ( $\vec{I}$ ) and detection ( $\vec{D}$ ) points, a vector to the reflection ( $\vec{R}$ ) point

can then be calculated. The light path ( $P$ ) can then be calculated using these three vectors, as described below.

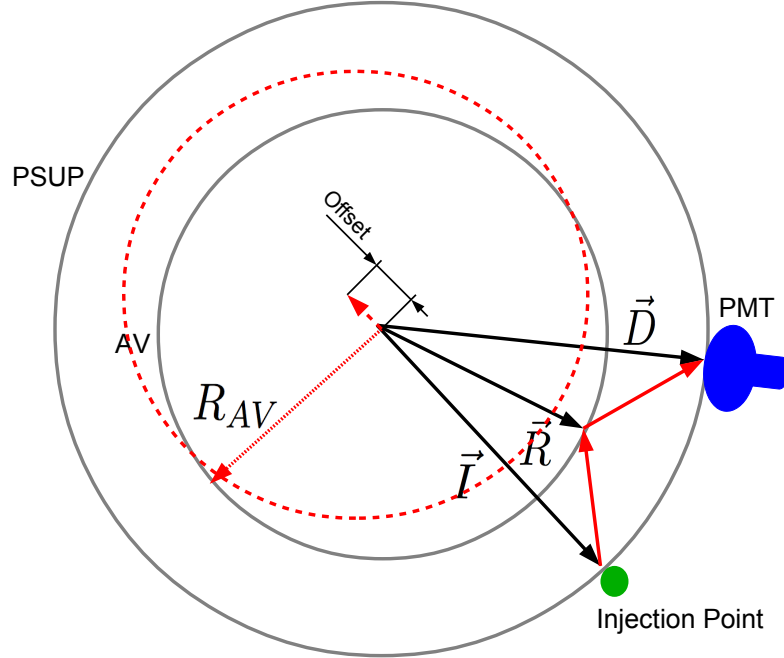


Figure 8.2: *Vector diagram used to calculate the light path between the injection and detection points, and subsequently, the time of flight.*

$$\vec{R} = \frac{\vec{I} + \vec{D}}{|\vec{I} + \vec{D}|} R_{AV}, \quad (8.2)$$

where  $R_{AV}$  is the radius of the AV. From here the path is simply:

$$P = |\vec{R} - \vec{I}| + |\vec{D} - \vec{R}|. \quad (8.3)$$

However, we are interested in any variation in the distance between the AV and the injection point as there is the least amount of uncertainty in the location of the injection, and all measurements from PMTs detecting reflected light are (nearly) symmetrical around this point, so we include an offset vector ( $\vec{O}$ ) defined as:

$$\vec{O} = \frac{-\vec{I}}{|\vec{I}|} S, \quad (8.4)$$

where  $S$  is the parameter to be minimised. For an offset AV position:

$$\vec{I} \rightarrow \vec{I}' = \vec{I} - \vec{O}, \quad (8.5)$$

$$\vec{D} \rightarrow \vec{D}' = \vec{D} - \vec{O}, \quad (8.6)$$

$$\vec{R} \rightarrow \vec{R}' = R_{AV} \left( \frac{\vec{I} + \vec{D} - 2\vec{O}}{|\vec{I} + \vec{D} - 2\vec{O}|} \right). \quad (8.7)$$

Using these vectors and the group velocity, the time of flight can be calculated and compared to the measured hit time. In reality, the AV is not a perfect sphere as there are ropes, belly-plates and pipes. Therefore, the RAT class LightPath [137] is used to calculate the time-of-flight, which uses an iterative method to take these effects into account. Benchmark tests have shown LightPath to give results in good agreement with the brute force vector calculation of the path length.

## 8.4 Data Selection

The first cuts to be applied are to select the PMTs based on operational status. These cuts remove faulty PMTs and PMTs connected to faulty electronics as well as those with special purpose. For example, SNO+ has a number of PMTs with a lower gain setting to analyse high light events: These are all excluded from this analysis; only standard PMTs in good working order are accepted. In addition to this default cut, there are two other cuts made for this fit based on PMT location and hit time. These cuts will be explained below.

There are a number of distinct reflections from different parts of the detector's structure that cause well defined peaks in PMT hit times, see Figure 8.3. Other, less distinct, features are due to diffuse reflections caused by imperfections of the acrylic vessel or light that has been reflected multiple times. The six different paths shown are defined as follows: 1 - is the reflection from near AV surface, the light of interest when fitting the AV position. 2 - is the direct transmission, as used for the PMT calibration. 3 - is the reflection from the far AV surface, 4 - is the reflection around AV from PSUP. 5 - is the reflection of the direct transmission, 6 - 35° reflection from the PMT concentrator [140].

Given the PSUP radius of 8.89 m and the AV radius of 6.05 m, the expected path length for light reflected from the near surface of the AV is 5.68 m, the mean group velocity gives a time of flight close to 26 ns. The reflections and direct light can be seen in Figure 8.4, where the hit time is plotted as a function of PMT distance from injection point. Notice

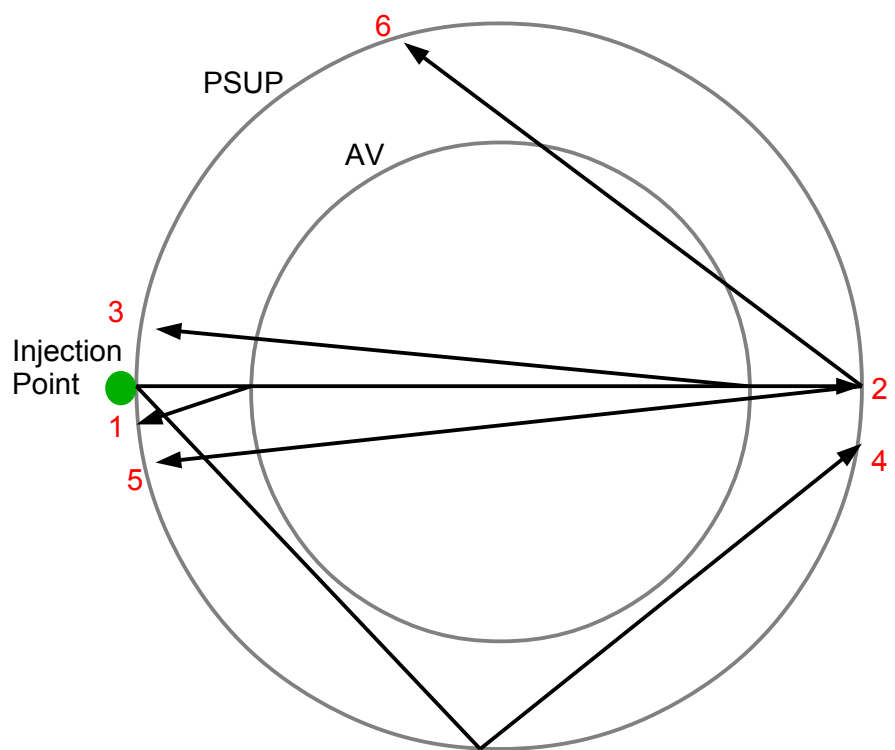


Figure 8.3: The types of reflection for light injected from the PSUP: 1 - reflection from near AV surface, 2 - direct transmission, 3 - reflection from far AV surface, 4 - reflection around AV from PSUP, 5 - reflection of direct transmission, 6 -  $35^\circ$  reflection form PMT concentrator.

that the hit time for light reflected from the near surface of the AV is not around the expected 26 ns but rather 276 ns. This offset is due to the trigger delays, which will be explained below.

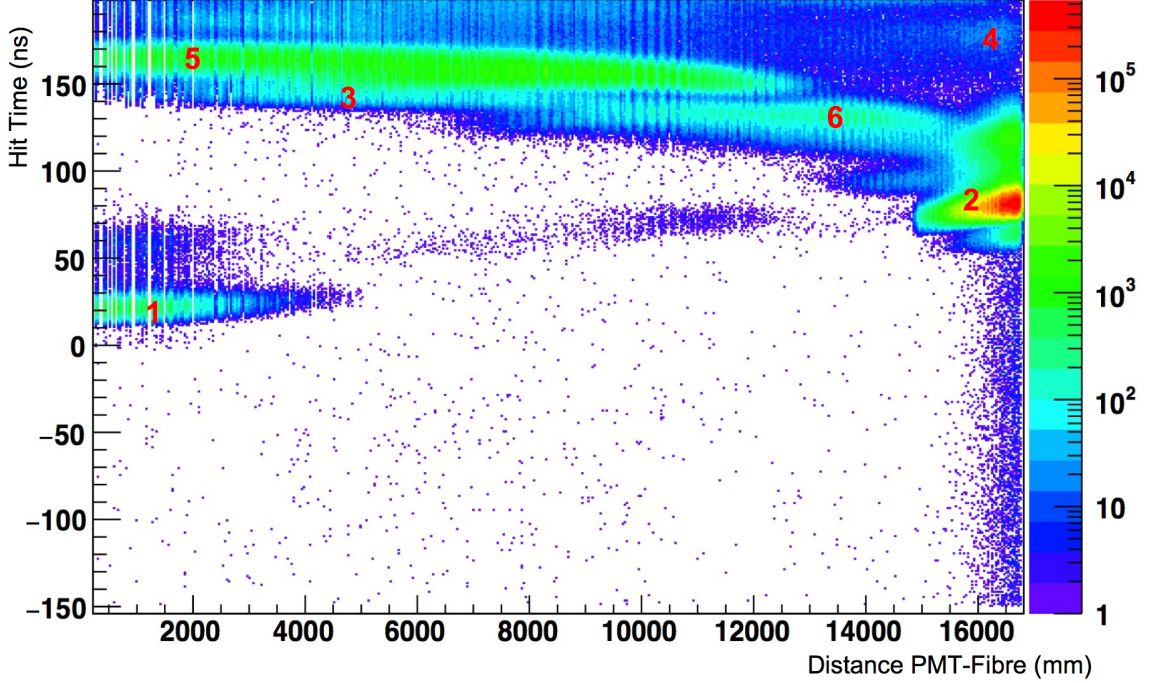


Figure 8.4: *Time of detection for light injected at node 79, as a function of distance from the injection point. The types of reflection are highlighted with reference to the numbering system used in Figure 8.3. The earlier diagonal band between 5000 and 13000 mm is due to scattering from the AV. Prepulseing can be seen just before the direct transmission (2).*

The effect of light from the other reflections is limited by selecting PMTs close to the injection point and setting a time window for each PMT based on the expected time of flight. From Figure 8.4 it is clear that the intensity of light reflected from the near surface of the AV drops after 3 m, a cut of 2.5 m is therefore applied in order to maintain sufficient statistics.

#### 8.4.1 Trigger Delays

As mentioned above, there is a delay applied to the PMT hit time due to the trigger system. The various components of the trigger system and their various delays were introduced in Section 3.4, here a worked example will be provided in greater detail for a TELLIE pulse reflected from the near surface of the AV. The following timing information for delays in the trigger system as set in RAT is taken from [141].

The TELLIE pulse is injected at  $t = 0$  ns. The light reflected directly back from the AV takes approximately 26 ns to reach a PMT within 2.5 m of the injection point. A photoelectron is generated at  $t = 26$  ns (+ TTS). The TAC starts to ramp, as a trigger pulse is generated. The pulse is summed by the master trigger with propagation delay of 110 ns,  $t = 26 + 110 = 136$  ns. An external trigger is generated at  $t = 140$  ns to catch TELLIE light. A GT is sent to the stop the TAC with a propagation delay of 110 ns, arriving at  $t = 140 + 110 = 250$  ns.

The voltage read from the TAC contains the information of when the hit occurred, with a larger voltage meaning the hit occurred earlier in time. This is stored as the uncalibrated PMT hit time as ADC counts, which are backwards, with larger values occurring earlier in time. To calibrate those hit times, electronics calibration data is used to convert backward ADC counts to forward ns. The problem is that ADC counts only tells you how long before GT the hit occurred, but the time since some start point is needed. This is found using a fixed offset of 500 ns<sup>1</sup>

The TAC has been ramping for  $250 - 26 = 224$  ns. In the absence of an electronics calibration for this example, let's say a time of 224 ns is 2200 ADC counts, an uncalibrated PMT hit time of hit time 2200 is stored. Using our electronics calibration a hit time of 2200 ADC counts corresponds to hit time of 224 ns. The ADC is backwards to correct the time it has to be removed from the fixed offset  $500 - 224 = 276$  and a calibrated PMT time is created with hit time of 26 ns.

## 8.5 Uncertainties

There are a number of uncertainties affecting the accuracy of the AV position fit, such as the PMT geometry, group velocities, spread in the time profiles of injected pulses and the TTS. These are described below in detail.

### 8.5.1 PMT Geometry

There is an uncertainty in the PMT location, the parameter used as the detection point. As in the experiment, it is not possible to determine where on the photocathode the photon

---

<sup>1</sup>The event window has a maximum aperture of 400 ns. the additional 100 ns prevents negative hit times, provides some information about activity in the PMT array before the event and allows some dead time for the trigger to reset between events.

struck the PMT and whether it was reflected from the concentrator, so the detection point is stored as the PMT location. The location is a single point, while the actual PMT has a physical shape. The PMT location is 5.67 cm away from the photocathode in the centre of the outer face of the concentrator, as shown in Figure 8.5.

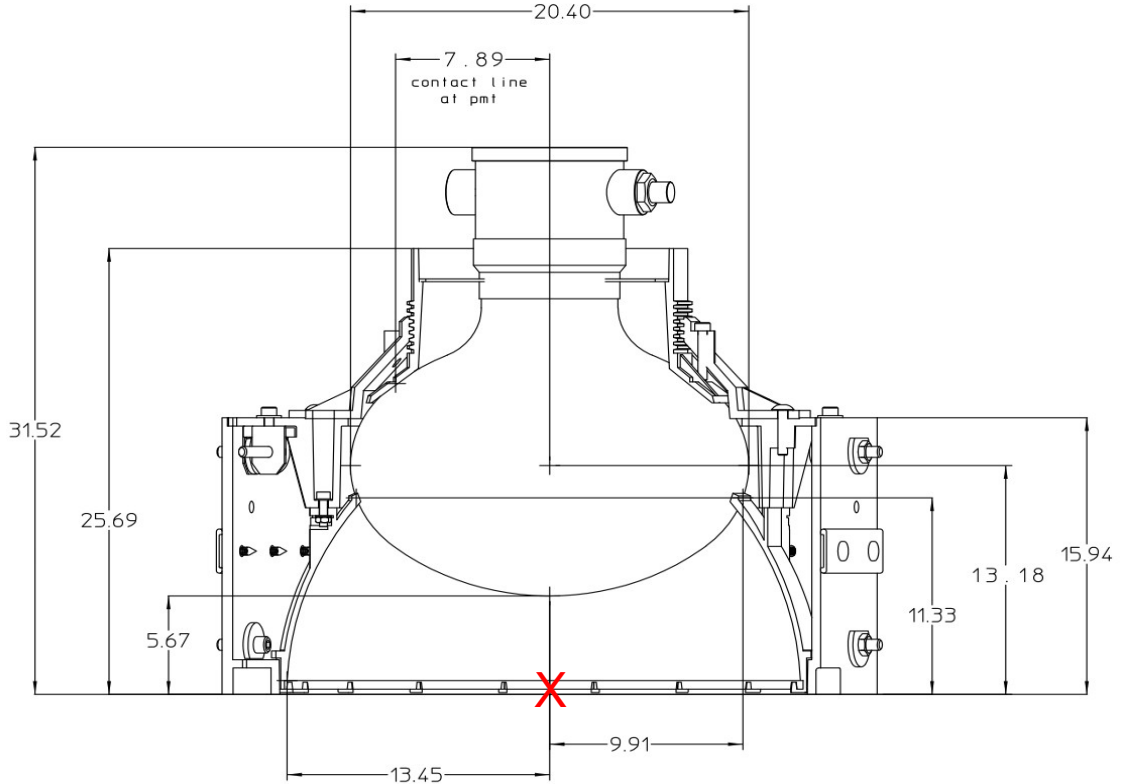


Figure 8.5: Dimensions (in cm) of the PMT and light concentrator housing. The PMT location as stored in RAT is marked in red: the centre of the front of the concentrator. Adapted from [57]

This discrepancy between the position at which photon strikes the photocathode and the PMT location adds an unavoidable uncertainty to the time of flight; using the given speed of light in water the minimum offset is 0.258 ns (for 5.67 cm). This offset is reduced by the position cut mentioned above: by selecting PMTs close to the injection point, for which light enters the PMT at an angle closer to its normal. For PMTs further from the injection point, reflected light will strike the PMT at a shallower angle and therefore have a larger propagation time in the concentrator. The distribution of observed arrival times, as observed by looking at many SPE events, will include this geometrical effect and lead to a slightly larger mean arrival time.

As mentioned, a cut of PMTs within 2.5 m of the injection point is applied to reduce the effects of other reflections and keep statistics high compared to the PMT dark current. The path length for light entering the centre of the concentrator for a PMT with a location

at 2.5 m from the injection point is 6.10 m. However, for light entering the far edge of the same concentrator, the path length increases to 6.23 m, assuming only one reflection from the concentrator. There is also an increase in path length if light enters the near edge of the concentrator, to 6.13 m, assuming no reflections. This uncertainty is illustrated in Figure 8.8, as the error in the time of flight increases with distance from injection point. This uncertainty is reducible through increased statistics, assuming it to be proportioned to  $\frac{\sigma}{\sqrt{N}}$ , where  $\sigma$  is that of the pulse time profile. The effect of a reduction in intensity as distance from the injection point increases is reduced by the 2.5 m cut.

However, as the observed pulse shape will be distorted due to the geometrical effect described here, there will be a small shift. This uncertainty could be reduced by a detailed MC of light propagation through the concentrator, however, this is beyond the scope of this thesis.

### 8.5.2 Time

In the absence of a complete PMT calibration, which will have used the laserball to determine the group velocities of light in the various media, the uncertainty due to group velocity spread is minimised by selecting the weighted mean of the LED spectrum augmented by the PMT QE. To provide a measure of the spread in time of flight due to the group velocity spectrum of the LED, the time of flight was calculated using the upper and lower limits of the spectrum for a path of 5.68 m. The mean group velocity gave a time of 26 ns, while the lowest gave 25 ns and the highest 30 ns.

The trigger jitter and PMT TTS can be combined with the spread in the TELLIE time profile, by adding the RMS of the time profile and the TTS in quadrature. This yields an uncertainty of 3 ns, corresponding to 60 cm. Fortunately, the mean of the distribution is measured and the uncertainty on this is inversely proportional to  $\sqrt{N}$ , where  $N$  is the number of hits. With only 1000 hits, this statistical uncertainty can be less than two centimetres. During normal TELLIE operation, the number of hits will be sufficiently high that statistics will minimise this uncertainty.

As mentioned in Chapter 3, multi-photon hits always skew the detected time profile in favour of the first photon detected. This will cause the AV to appear closer to the injection point. Despite being beneficial in counteracting the effect of late light and increased path lengths due to the PMT geometry, this systematic skewing of the time profile in favour of early light is shared by the PMT calibration and will drop out. This is something that

needs to be kept in check by keeping the probability of two or more photoelectrons low, below 5% would make this effect negligible [142]. It is a strong function of hit probability though, which is different between near and far PMTs.

### 8.5.3 Minimising Uncertainties

To summarise, the uncertainties due to the PMT geometry, TTS and the spread in the TELLIE time profile can be minimised through increased statistics. While the uncertainties from the group velocity and the skewing of the time profile by early light will be reduced by the PMT calibration, all of these uncertainties are accounted for within the MC, presenting themselves as a spread in the observed hit time, see Figure 8.6.

There are additional uncertainties that are not taken into account in the MC, such as: the flatness of the AV surface and the movement and rigidity of the PSUP. The surface of the AV is not perfectly flat, during its construction material had to be removed at the joints of the various sections, to remove any bubble that formed within the bond and alleviate tensions, resulting in undulations at the joints. The PSUP is an extremely rigid structure and was expected to deform by no more than 0.08 mm [143] during the running time of SNO, although any deformation has yet to be reassessed for SNO+. There is however an uncertainty in the position of the PSUP due to movements in the ropes supporting it when filling the cavity or working on the structure, of between 1.9 and 3.8 cm [143].

## 8.6 Fitting The AV Position

With the details of fitting the AV position introduced, the fit itself can now be described.

For light injected at a given fibre, the fit searches all events looking for trigger events. It checks if the event registered as a PMT hit and whether the hit PMT is within 2.5 m of the injection. If the PMT is within the cut, a histogram of hit times is created for each PMT, the size of the histogram is restricted to cut hits from other reflections. For each hit PMT within the cut, the path between the injection point and PMT is then calculated using  $\vec{I}'$ ,  $\vec{R}'$  and  $\vec{D}'$  as parameters for the LightPath class. Using this path, the the time of flight is then calculated and the expected trigger offset is added to the calculated time.

For each histogram of hit times, the mean hit time is extracted. The mean hit time is

compared to the calculated hit time for each PMT and the magnitude of  $S$  is varied in the calculation until  $\chi^2$  is minimised.

This process can be repeated for all injection points to construct the shape and location of the AV with respect to the PSUP. Although, it should be made clear that the work in this chapter is only a proof of principle to demonstrate the achievable resolution to the problem identified in Chapter 4; reconstructing the shape of the AV requires a separate larger analysis.

The following results are for simulations of light injected at the lower most PSUP node, 79. This node is the most sensitive to any shifts in the AV position along the z-axis. As described Chapter 4, assuming the AV does not deform it is only expected to move in the z-axis with the buoyant force as the ropes stretch.

The hit time for a single PMT within 2.5 m of the injection point, with a time cut applied around the expected time of flight for that PMT is shown in Figure 8.6. The spread in time is due to the aforementioned uncertainties due to the pulse shape, convoluted with the TTS, the finite width of the wavelengths and the geometrical shape of the PMTs. The mean of this distribution is taken to be the measured time of flight for that PMT, and the precision on the mean is used as the uncertainty for the  $\chi^2$  minimisation.

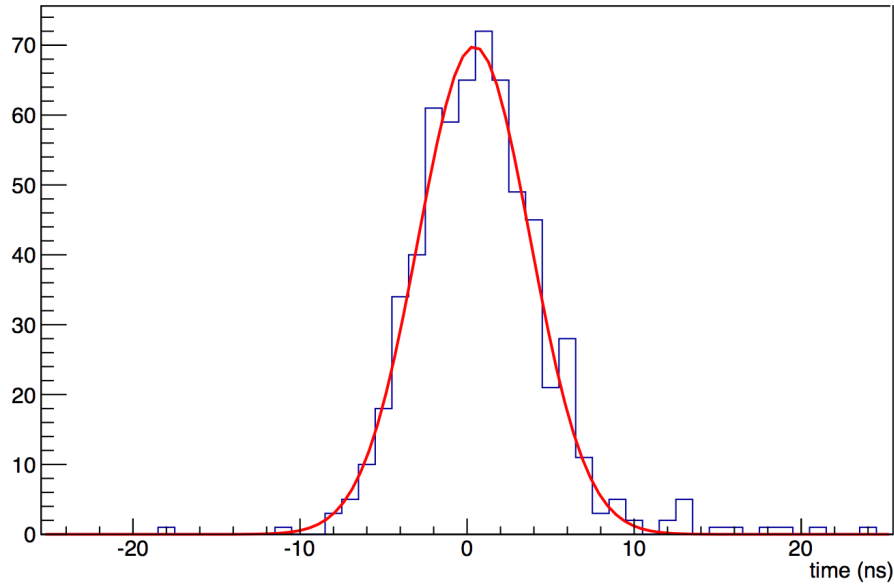


Figure 8.6: *The hit times for a single PMT within the cut of distance from the injection point and the time window surrounding the expected time of flight. The spread is due to uncertainties described in Section 8.5.*

The hit times for PMTs within the 2.5 m cut are shown in Figure 8.7, the expected increase in time of flight with distance from the injection point is clear as well as an increase in uncertainty due to the concentrator geometry.

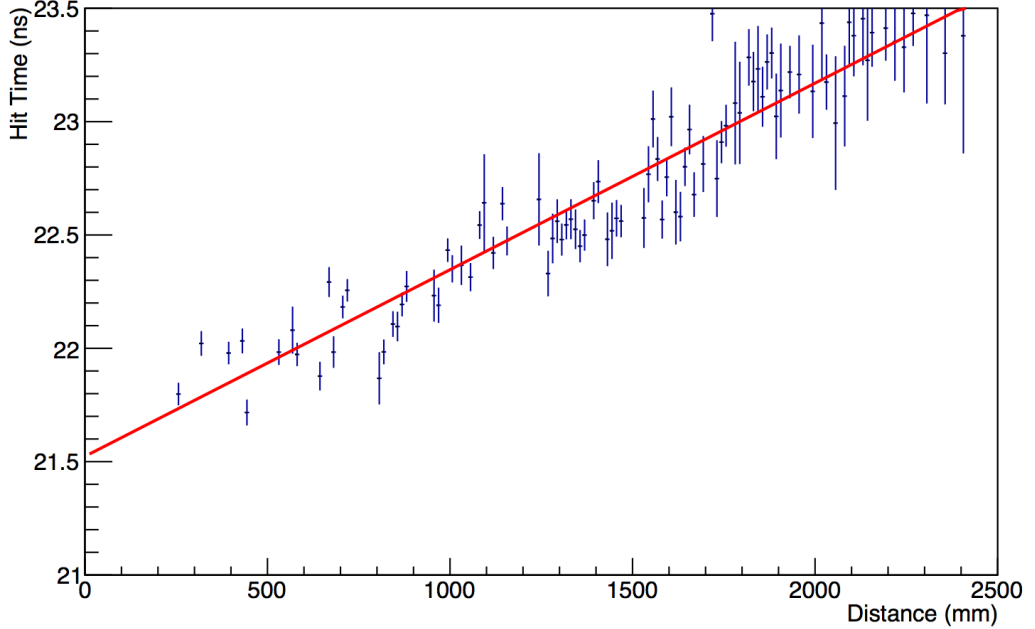


Figure 8.7: *Hit times for all PMTs within the 2.5 m distance cut from the injection point, The grouping of data is due to the structure of the PMT panels within the PSUP.*

The residual of hit times ( $t_{\text{measured}} - t_{\text{calculated}}$ ) for all PMTs within the 2.5 m cut are shown as a function of distance from injection point in Figure 8.8; notice uncertainty increasing with distance from injection point. The grouping of data points is due to the grouping of PMTs within the structure of the PSUP.

The spread in the residuals is shown in Figure 8.9 and 8.10, it is this time that can be converted to a distance using the group velocity of the injected light and used to show the offset of the AV.

However, Minuit is used to minimise the AV offset with the mean hit times and precisions. With the AV centred about (0,0,0) in truth, the fit found the AV to be off set by  $0.45 \pm 2.73$  cm. With the AV shifted along the z-axis by -10 cm in the Monte Carlo, the offset was found to be  $-8.25 \pm 2.82$  cm. For the AV shifted by the expected extension of the ropes, 5 cm, the offset was found to be  $4.91 \pm 2.70$  cm. A study has shown that the most dominant contribution to the error is the PMT geometry, by an order of magnitude [144].

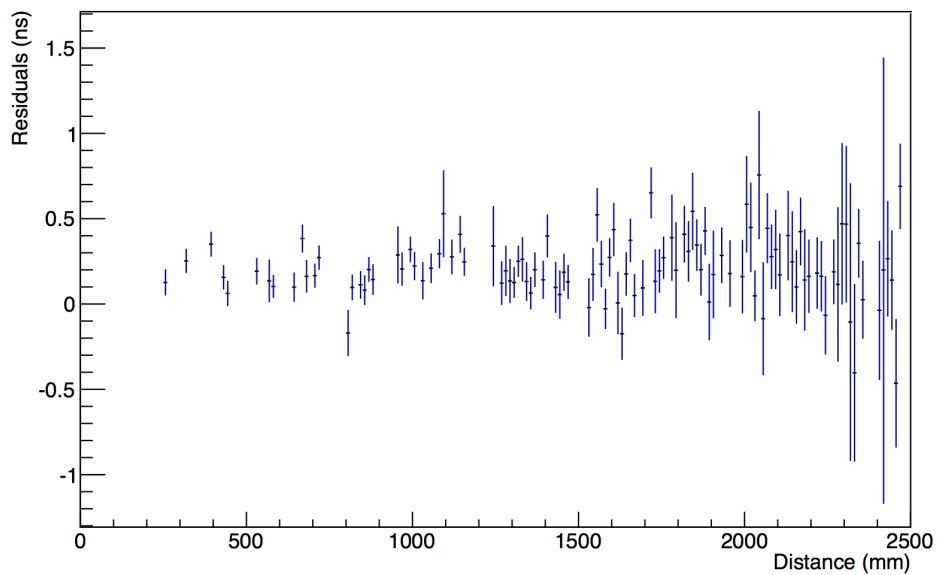


Figure 8.8: The residual of hit times ( $t_{\text{measured}} - t_{\text{calculated}}$ ) for all PMTs within the 2.5 m.

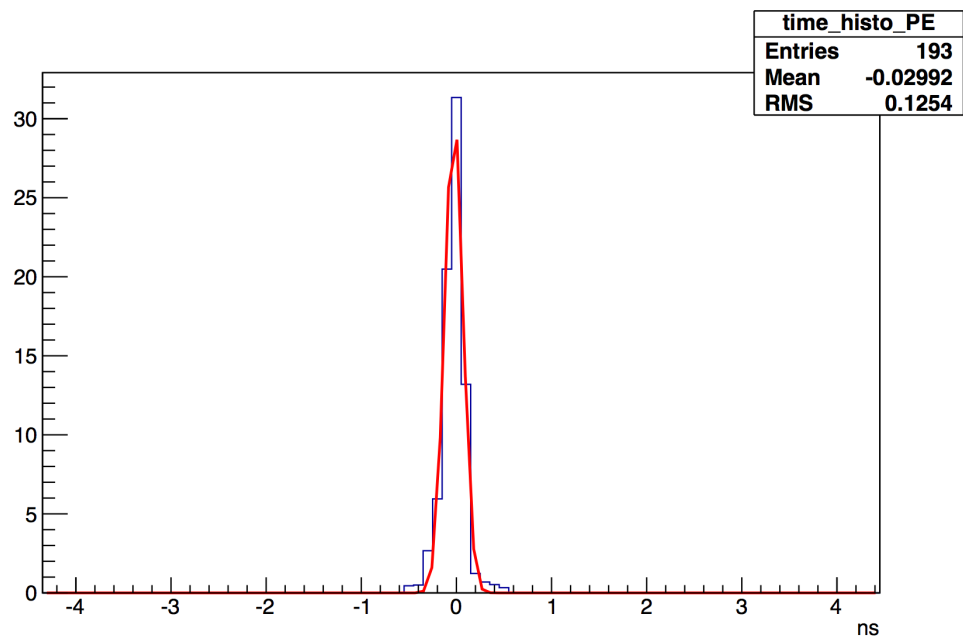


Figure 8.9: The spread in residuals for the times of flight, centred at -0.03 ns with the AV at  $(0,0,0)$ .

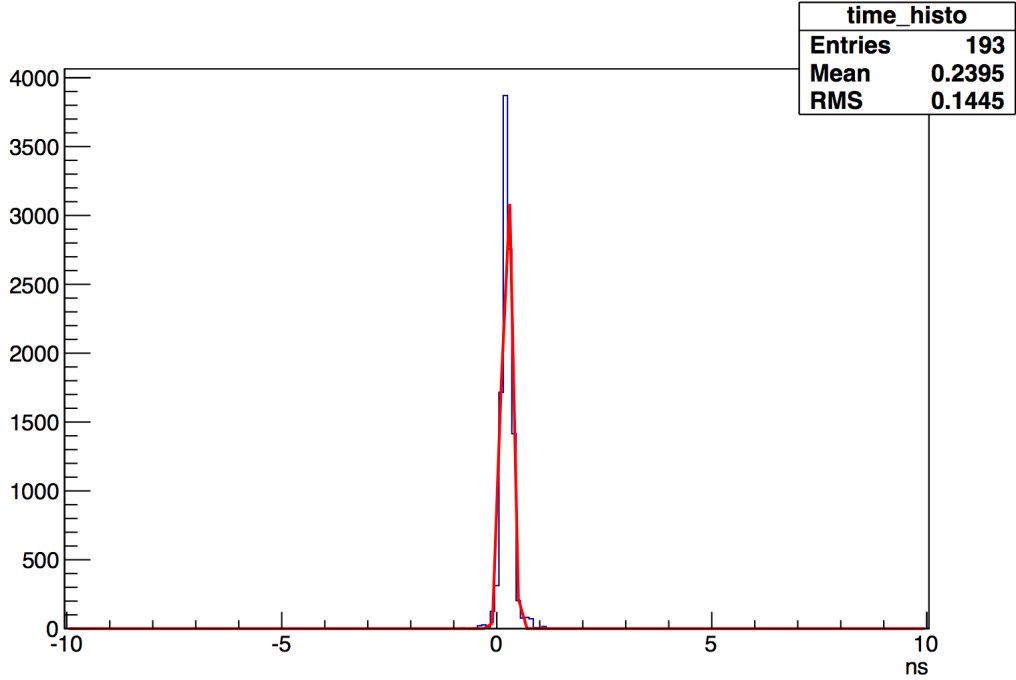


Figure 8.10: *The spread in residuals for the times of flight, centred at 0.24 ns with the AV at (0,0,50) (mm).*

## 8.7 Conclusions

The fit is capable of resolving an offset in the AV position to within three centimetres. The uncertainty is approaching the uncertainty in the PSUP position and is less than half that of the expected reconstruction resolution within scintillator, 10 cm [88].

As this is only simulated data this uncertainty is due to fitting the mean PMT hit time, the largest contribution to spread in hit time being due to the propagation of light within the PMT concentrator. To model light propagating in the concentrator correctly a detailed Monte Carlo of the PMT geometry would be required, and the mean deterioration of the concentrator reflector petals would have to be known.

For experimental data it is likely that the systematic uncertainty will be increased due movement of the PSUP and non uniformity in the surface of the AV, as well as degradation in the concentrators.

TELLIE is a valuable addition to the system used to monitor the performance of the ropes. It is sensitive to shifts in the position of the AV, of the magnitude predicted: if the ropes stretch as expected the AV will rise by 5 cm over the next 10 years; with the AV shifted 5 cm in z, the fit found the offset to be  $4.9 \pm 2.7$  cm . It is capable of providing a

measure of the location of the surface relative to all PSUP nodes accurate to within a few centimetres, which leads to a measurement of the actual shape of the AV, something that is not possible with any current monitoring system.

In reality the degree of data processing and analysis time required would make integrating TELLIE with DeltaV pointless in terms of real time detector monitoring. However, this fit allows for the AV to be located to within a few centimetres and can therefore be used to provide the best definition of the FV currently available. This is extremely valuable for any physics analysis, as will be demonstrated in the following chapter.

## Chapter 9

# Influence of TELLIE on the Neutrinoless Double-Beta Decay Sensitivity of SNO+

This chapter presents the effect of an uncertainty in the AV position and the accuracy of the timing calibration on the sensitivity to the neutrinoless double-beta decay signal. The expected sensitivity of SNO+ will be shown, highlighting the dominant backgrounds (BG) and the assumptions made to achieve this sensitivity. A study of the number of BG events in the FV as a function of the AV position will be shown. The effect of timing calibration accuracy will be presented as a function of the uncertainty in the reconstructed radius of events. This uncertainty in reconstructed radius can be compared in a similar manner to the uncertainty of the AV position, both having an effect on the number of BG events reconstructed within the FV. Ultimately, the sensitivity to neutrinoless double-beta decay will be presented as a function of the number of BG events within the FV.

### 9.1 Expected Sensitivity

In Chapter 2 it was shown that the sensitivity of SNO+ to the half-life of neutrinoless double-beta decay can be described as:

$$T_{1/2}^{0\nu} \propto \frac{M\sqrt{t}}{\sqrt{\Delta E}}, \quad (9.1)$$

where  $M$  is the isotope mass,  $t$  is the live-time and  $\Delta E$  is the energy resolution. The importance of energy resolution in distinguishing signal from BG can be clearly seen in Figure 9.1.

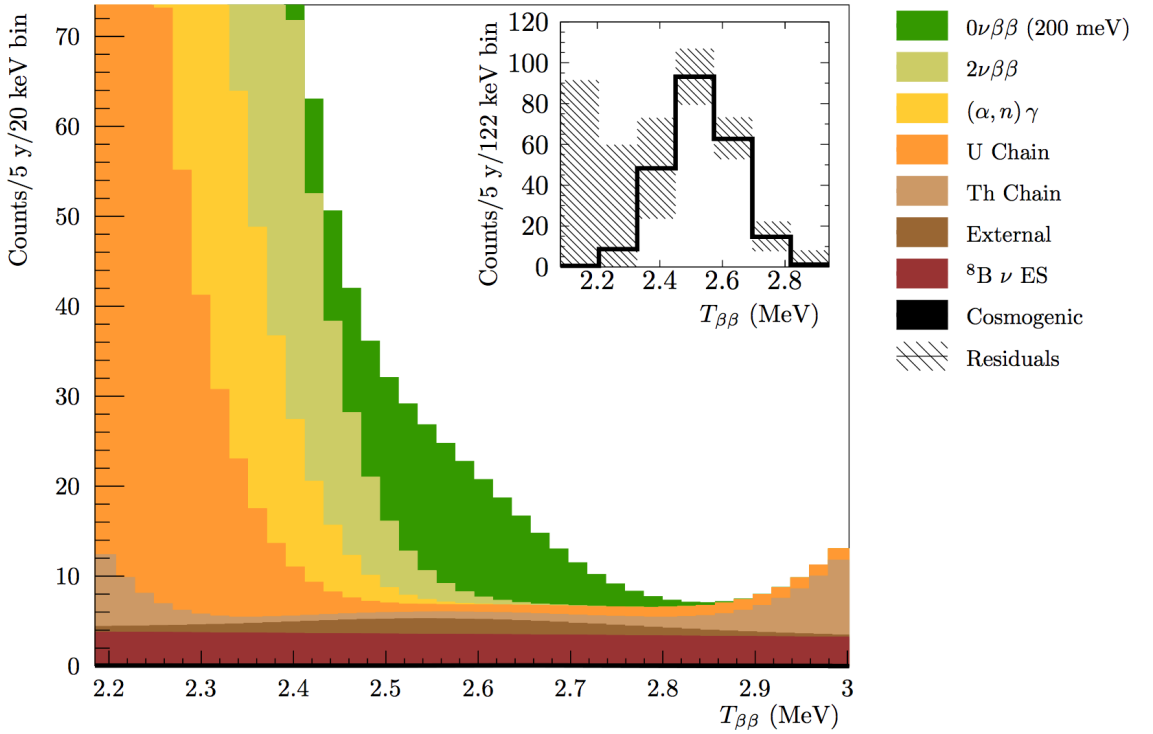


Figure 9.1: *The expected signal and BG for neutrinoless double-beta decay in SNO+ assuming 0.3% loading of tellurium, after five years of data taking. Taken from [56].*

Figure 9.1 shows the expected reconstructed energy spectrum of signal and BG in SNO+ at 0.3% loading of tellurium. This plot assumes a Majorana neutrino with  $m_{\beta\beta} = 200$  meV, using the nuclear matrix element of  $M^{0\nu} = 4.03$  [36] and the phase space factor of  $G^{0\nu} = 3.69 \times 10^{-14}$  yr $^{-1}$  from [145]. It also assumes purification to such an extent that cosmogenically induced BG can be neglected. It uses coincidence tagging to reduce the  $^{212}\text{Bi}$ - $^{212}\text{Po}$  and  $^{214}\text{Bi}$ - $^{214}\text{Po}$  by a factor of 50 [56]. A likelihood method for rejecting  $^{208}\text{Tl}$  from the AV [88], was applied to all external BG in order to find the optimal FV cut, which was found to be 3.5 m [146]. Perhaps most important is the assumed 100% efficiency of detection and analysis, including reconstruction.

The raw radial distributions of the external BG used in the definition of the FV cut are shown Figures 9.2(a) and 9.2(b). In the absence of an energy cut, it can be seen that the dominant external BG penetrating deepest into the scintillation volume are the  $^{208}\text{Tl}$  from the hold-down ropes, UPW shielding and AV and the  $^{214}\text{Bi}$  from the AV and the UPW shielding.

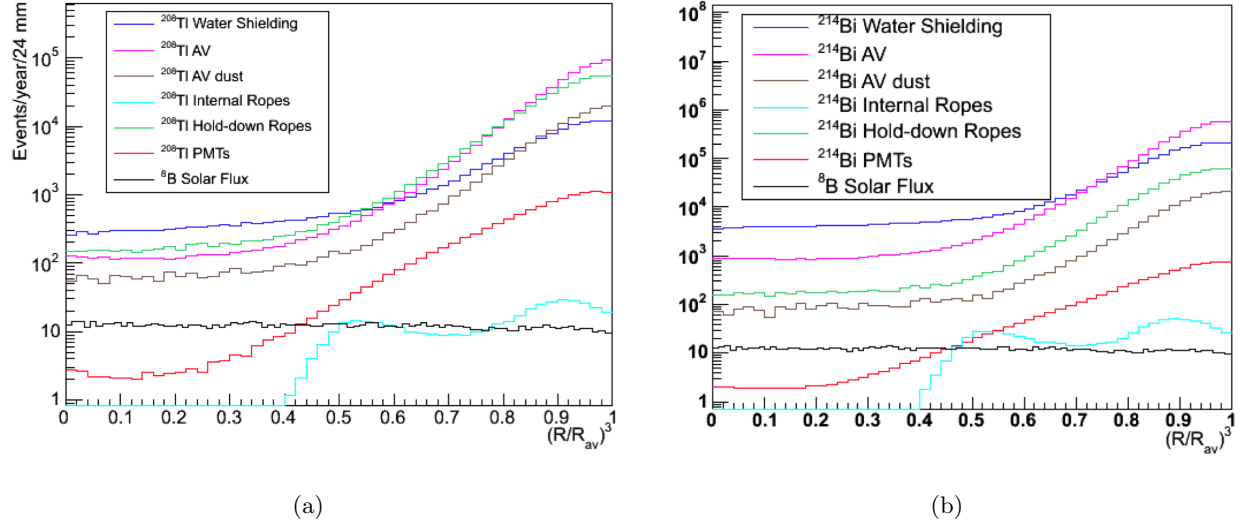


Figure 9.2: The reduced radial (defined as  $R_{reduced} = (R/R_{AV})^3$ ) distributions for the external BG in the signal range for neutrinoless double beta decay from  $^{130}\text{Te}$ . The energy range is defined from 2.4 to 2.64 MeV. The distributions for  $^{208}\text{Tl}$  (left) and  $^{214}\text{Bi}$  (Right). The  $^8\text{B}$  solar flux is also shown for comparison. Taken from [146].

If there was any uncertainty in the AV position relative to the PSUP, due to deformation or creep in the ropes, there would be a corresponding uncertainty in the definition of the FV. For example: If the AV were to move, as expected, upward without a correction to the FV, then more BG events from the AV, UPW and the hold-down ropes would be reconstructed within the FV. This effect will be quantified below.

An uncertainty in the timing calibration would have the same effect as an uncertainty in the location of the AV, as the uncertainty would effect the reconstructed position resolution leading to more external BG events being reconstructed with the FV. This is quantified below.

## 9.2 AV Location

### 9.2.1 Shift in AV Position

As shown, the dominant external BG are  $^{208}\text{Tl}$  from the hold-down ropes, UPW and AV and the  $^{214}\text{Bi}$  from the AV and the UPW. Excluding the neck of the AV, most of these BG are symmetric around the AV, that is to say a movement of the AV in any direction would result in the same increase in the penetration of FV by external back grounds. This is not the case for the hold-down ropes, which are only in contact with the upper

hemisphere of the AV. Therefore, it is not possible to simply take the spectra shown in Figures 9.2(a) and 9.2(b) and apply a shift in radius then calculate the corresponding number of BG events within the FV. Instead, the dominant BG were simulated in RAT using the expected rates from [66], with the AV shifted in 20 mm increments from -100 to 100 mm (twice its expected movement in both directions) along z. The number of BG events reconstructed within the FV were then calculated for each 20 mm increment.

Figure 9.3 shows the number of  $^{208}\text{Tl}$  events from the hold-down ropes reconstructed within the FV as a function of AV position along the z-axis. As expected the number of events within the FV is reduced as the AV rises, and the hold-down ropes move away from the FV.

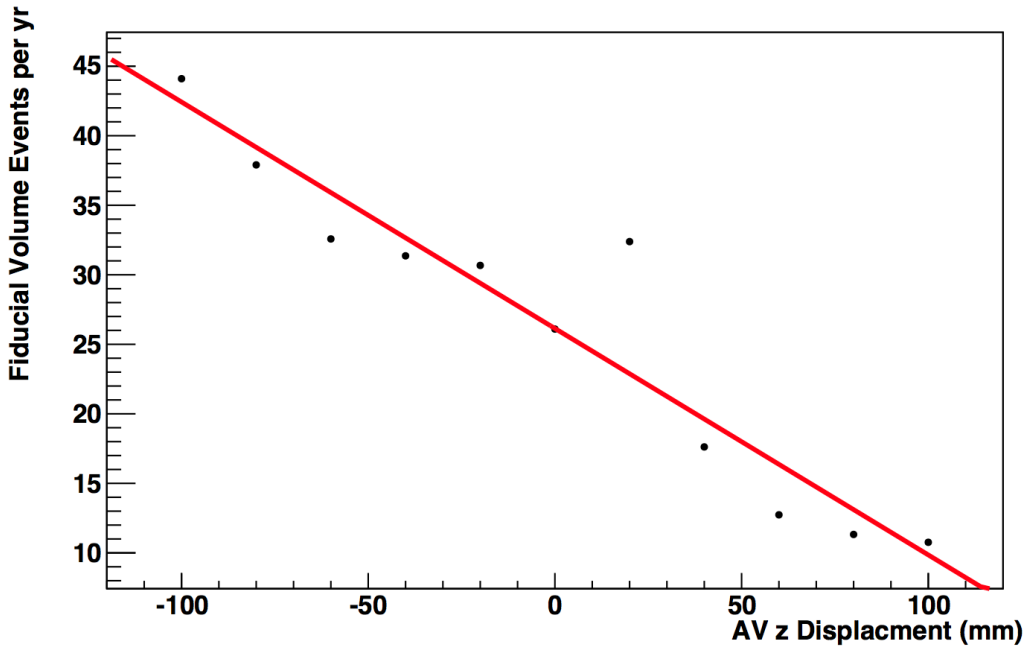


Figure 9.3: The number of  $^{208}\text{Tl}$  events from the hold-down ropes reconstructed within the FV as a function of AV position along the z-axis. The linear fit produced a gradient of -0.16 events/mm

The number of BG events reconstructed in the FV for  $^{208}\text{Tl}$  and  $^{214}\text{Bi}$  from the AV is shown as a function of AV position along the z-axis in Figure 9.4.

The number of BG events reconstructed in the FV for  $^{208}\text{Tl}$  and  $^{214}\text{Bi}$  from the UPW is shown as a function of AV position along the z-axis in Figure 9.5. These BG also show an asymmetry about  $z = 0$ , although the number of events reduce by only 0.3%. This two orders of magnitude less than that of the hold-down ropes and close to statistical fluctuation.

The number of BG events reconstructed in the FV for all the dominant BG are shown as a

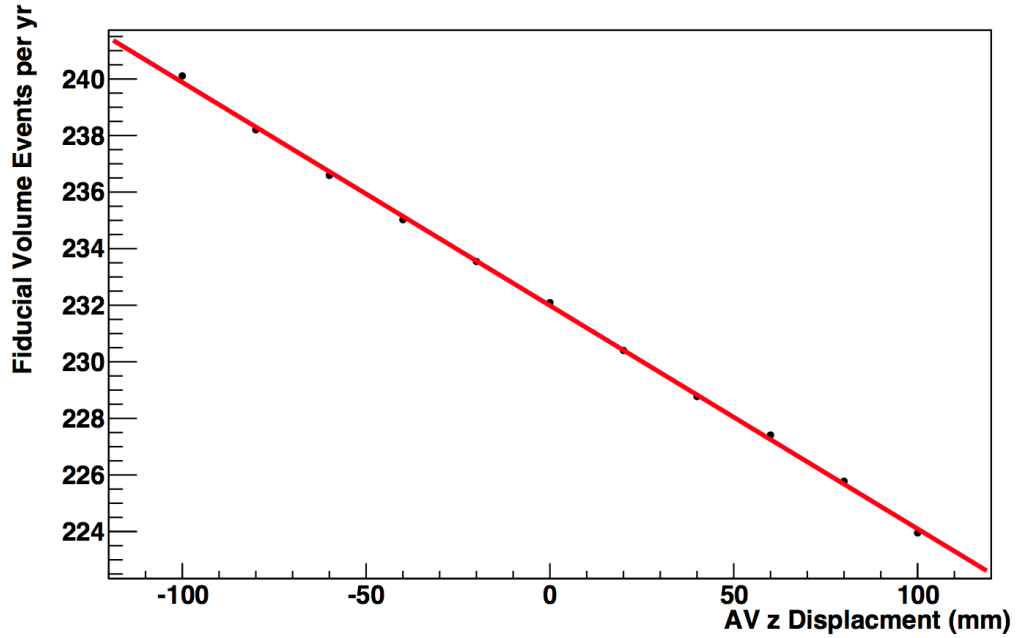


Figure 9.4: The number  $BG$  events reconstructed in the  $FV$ , caused by  $^{208}\text{Tl}$  and  $^{214}\text{Bi}$  from the  $AV$ , as a function of  $AV$  position along the  $z$ -axis. The linear fit produced a gradient of  $-7.9 \times 10^{-2}$  events/mm.

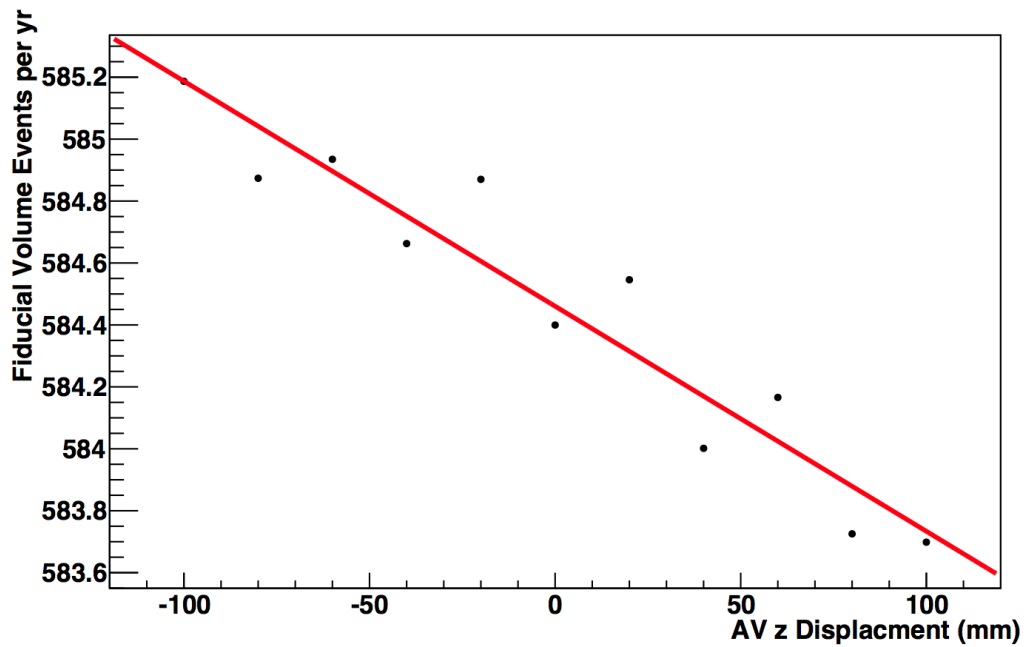


Figure 9.5: The number  $BG$  events reconstructed in the  $FV$ , caused by  $^{208}\text{Tl}$  and  $^{214}\text{Bi}$  from the  $UPW$ , as a function of  $AV$  position along the  $z$ -axis. The linear fit produced a gradient of  $-7.8 \times 10^{-3}$  events/mm.

function of AV position along the z-axis in Figure 9.6. These BG also show an asymmetry about  $z = 0$ , although as the fitted gradients show, the AV and UPW have gradients one and two orders of magnitude less than the hold down ropes, respectively. The asymmetry in BG events from the hold-ropes and AV is expected over this range of movement: It is obvious that the ropes are only in contact with the upper hemisphere so the number of BG events will fall as the ropes move further from the FV. The AV is less obvious, one would expect it to be symmetric about (0,0,0) since as the top of the AV is moved away from the FV, the base is moved towards it. However, the construction of the AV neck means there is considerably more acrylic in the upper hemisphere. At ranges greater than the maximum expected movement of the AV, the number of BG events from the AV will increase as its base nears the FV.

Lower counts at increased  $z$ , suggest the optimal centring of the FV to be below (0,0,0), to minimise the effect of external BG. An asymmetric FV could also be considered, with a larger volume in its lower hemisphere.

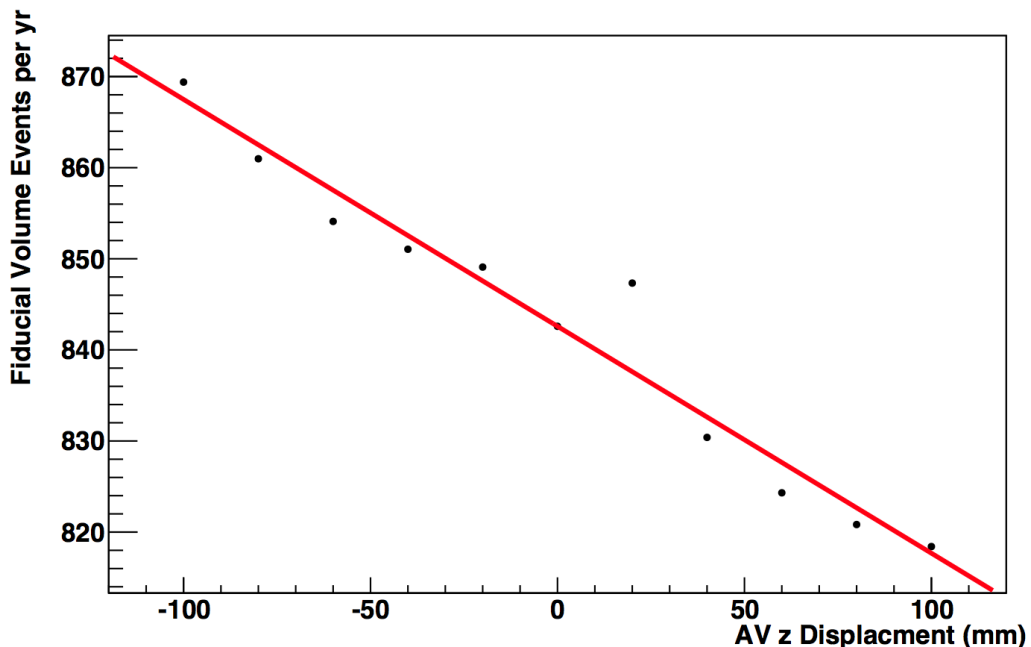


Figure 9.6: The number BG events reconstructed in the FV, caused by  $^{208}\text{Tl}$  from the hold-down ropes, UPW and AV as well as the  $^{214}\text{Bi}$  from the AV and the UPW, as a function of AV position along the z-axis. The linear fit produced a gradient of -0.25 events/mm.

### 9.2.2 Uncertainty in AV Position

To understand the effect of an uncertainty in the radius of the AV rather than a movement, the AV is assumed to be centred and the spectra of the dominant BG were used with the reconstructed event radius smeared. The event radius was smeared with a  $\sigma_R$  varying between 0 and 100 mm. Figure 9.7 shows the number of BG events reconstructed in the FV, caused by  $^{208}\text{Tl}$  from the hold-down ropes, UPW and the AV along with  $^{214}\text{Bi}$  from the AV and the UPW, as a function of the smearing of the event radius.

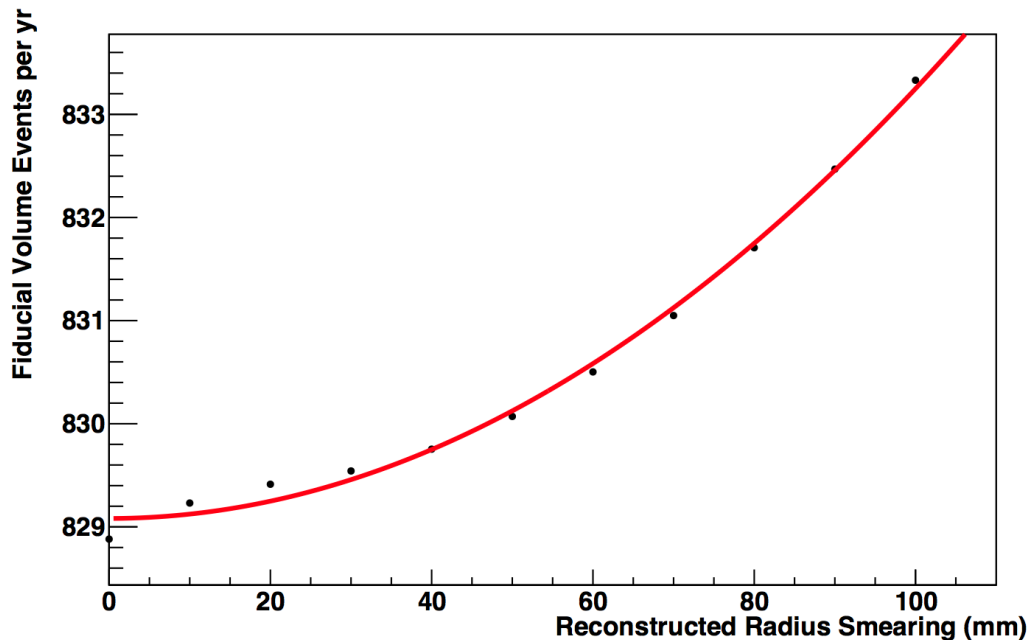


Figure 9.7: The number BG events reconstructed in the FV, caused by  $^{208}\text{Tl}$  from the hold-down ropes, UPW shielding and AV and the  $^{214}\text{Bi}$  from the AV and the UPW, as a function of the smearing of the reconstructed event radius. The plot has been fitted with a second order polynomial; the parameters were minimised to:  $P_0 = 829.1$ ,  $P_1 = 6.4 \times 10^{-5}$  and  $P_2 = 4.2 \times 10^{-4}$ .

As expected, as the uncertainty on the event ratios increases, more events are reconstructed within the FV. However, the spread is not particularly large with an increase of only four BG events for an additional 100 mm uncertainty in the radius. It was shown in Chapter 8, that by using reflections from TELLIE pulses, an uncertainty of approximately 30 mm on the radius of the AV is achievable.

### 9.3 Timing Calibration

As the timing calibration inaccuracy increases, the uncertainty in the locally measured radius of the AV will also increase. To quantify this, 3 MeV electrons were simulated at the radius of the FV, for each event an offset was applied to each PMT hit time. The individual PMT offsets were selected randomly from a Gaussian distribution with  $\sigma_{offset}$  varied between 0 and 5 ns to increase the spread of the distribution. The events were then reconstructed, the fitted radius of each event was binned in a histogram and then fitted with a Gaussian to find the mean reconstructed radius and uncertainty for each value of  $\sigma_{offset}$ . The reconstructed radii for  $\sigma_{offset} = 0.5$  ns are shown in Figure 9.8.

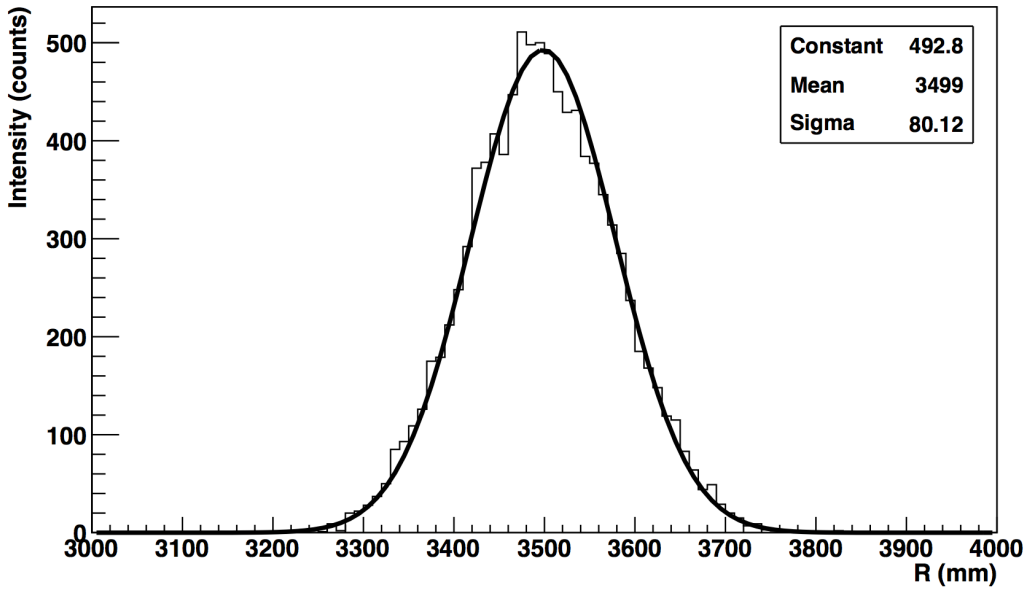


Figure 9.8: *The reconstructed radius for 3 MeV electrons generated at the radius of the FV (3500 mm), with the PMT hit time spread by 0.5 ns. The mean of the fit is taken to be the reconstructed radius with  $\sigma$  describing the uncertainty.*

Reconstructed radius is shown as a function of  $\sigma_{offset}$  in Figure 9.9. As the accuracy of the timing calibration is reduced, the reconstructed radius for electrons generated at the edge of the FV increases, as does the uncertainty on the radius. The increase in radius is most likely due to events being given greater weighting at larger radius, because of the larger volume being included as the uncertainty on radius increases.

This uncertainty in radius can be compared with Figure 9.7 to obtain the number of BG events within the FV for a given accuracy of the timing calibration. If TELLIE is able to achieve the designed timing calibration accuracy of 0.5 ns then the uncertainty in the reconstructed radius will be  $\pm 80$  mm; there will only be an additional 3 external BG

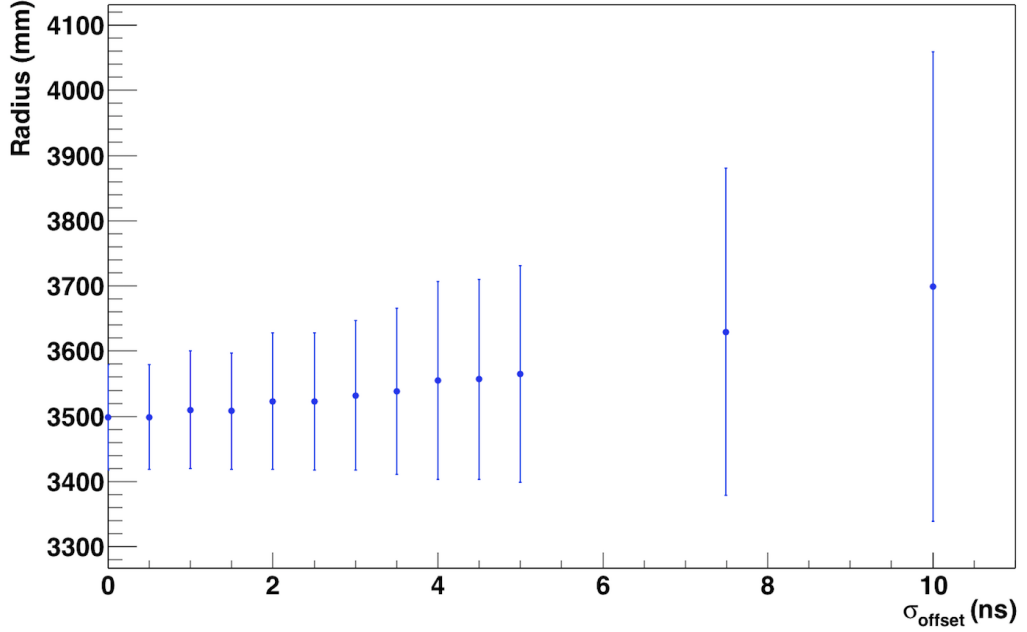


Figure 9.9: The reconstructed radius of 3 MeV electrons simulated at the radius of the FV as function of the magnitude of an offset applied to PMT hit time, demonstrating the effect of an inaccurate timing calibration.

events per year, compared with a completely accurate timing calibration.

## 9.4 Sensitivity to Neutrinoless Double-Beta Decay

To relate the above uncertainties to the sensitivity to a neutrinoless double-beta decay signal, the sensitivity can be plotted as a function of the displacement of the AV and the uncertainty in radius, as shown in Figures 9.10 and 9.11, respectively.

For this analysis the software used to find these sensitivities combines the generated spectra for the dominant external backgrounds with the MC truth spectra for the  ${}^8\text{B}$ , two-neutrino and neutrinoless double-beta decays, from RAT. These spectra are then smeared to approximate reconstructions, with  $\sigma = \sqrt{E/N_{\text{hits}}}$ , where  $E$  is the energy deposited in the scintillator and  $N_{\text{hits}}$  is assumed to be 200 per MeV. The Baker-Cousins method [147] is then used to extract a likelihood, from which a general chi-squared can be constructed. By defining the likelihood function for a Poisson distributed histogram as:

$$L_p(y : n) = \prod_i e^{(-y_i)} \frac{y_i^{n_i}}{n_i!}, \quad (9.2)$$

where  $y_i$  is the number of events predicted to be in the  $i$  th bin and  $n_i$  is the number of

events in the  $n$  th bin. The likelihood ratio test can then be used to construct a general chi-squared. The likelihood ratio is defined as:

$$\lambda = \frac{L(y : n)}{L(m : n)}, \quad (9.3)$$

where  $m$  is the true values of  $n$  obtained without errors, for a Poisson distributed histogram  $m$  can be replaced with its maximum likelihood estimation, which is just  $n$ . The likelihood ratio theorem states that the likelihood chi-squared is defined as:

$$\chi^2_\lambda = -2\ln\lambda = 2 \sum_i y_i - n_i + n_i \ln \left( \frac{n_i}{y_i} \right). \quad (9.4)$$

A 90% confidence level is achieved by taking the expected and observed spectra at zero signal, then iteratively increased until chi-squared exceeds 2.712 [24]. The region of interest is defined as:  $-1/2\sigma_{0\nu} \rightarrow +3/2\sigma_{0\nu}$ , where  $\sigma_{0\nu}$  is the width of the neutrinoless spectrum. In terms of energy, the selection window is 2.46 → 2.68 MeV.

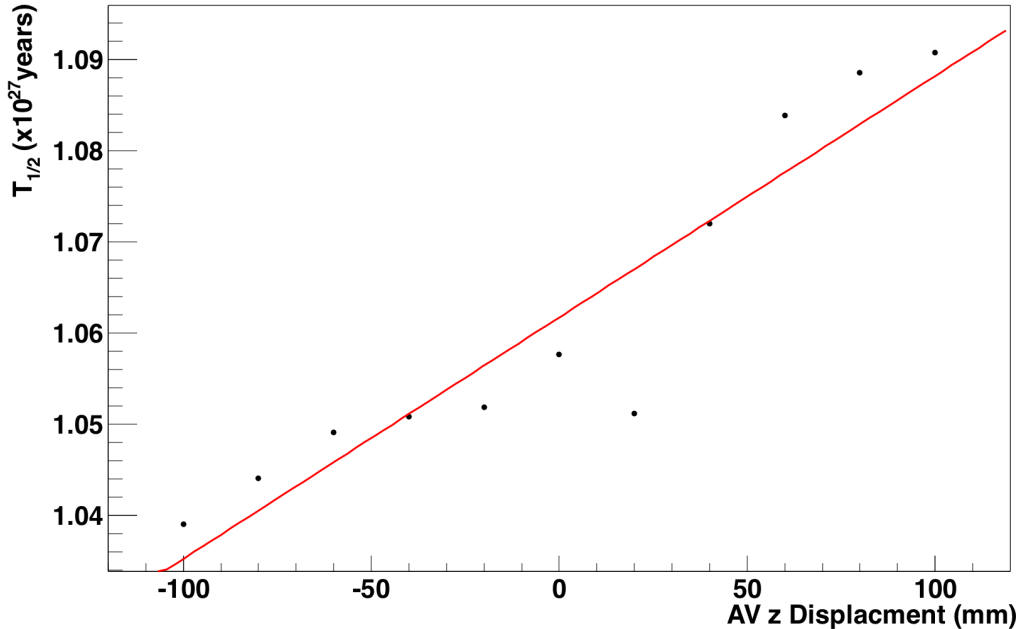


Figure 9.10: The limit on the neutrinoless double-beta decay life time as a function of the AV displacement along the  $z$ -axis. The linear fit produced a gradient of  $2.7 \times 10^{23}$  years/mm.

Low statistics have been accounted for by scaling the 0-shift spectra at each shift by the number of events in the FV at each shift. This therefore assumes that number of events in the region of interest is directly proportional to number of events in the FV. The point

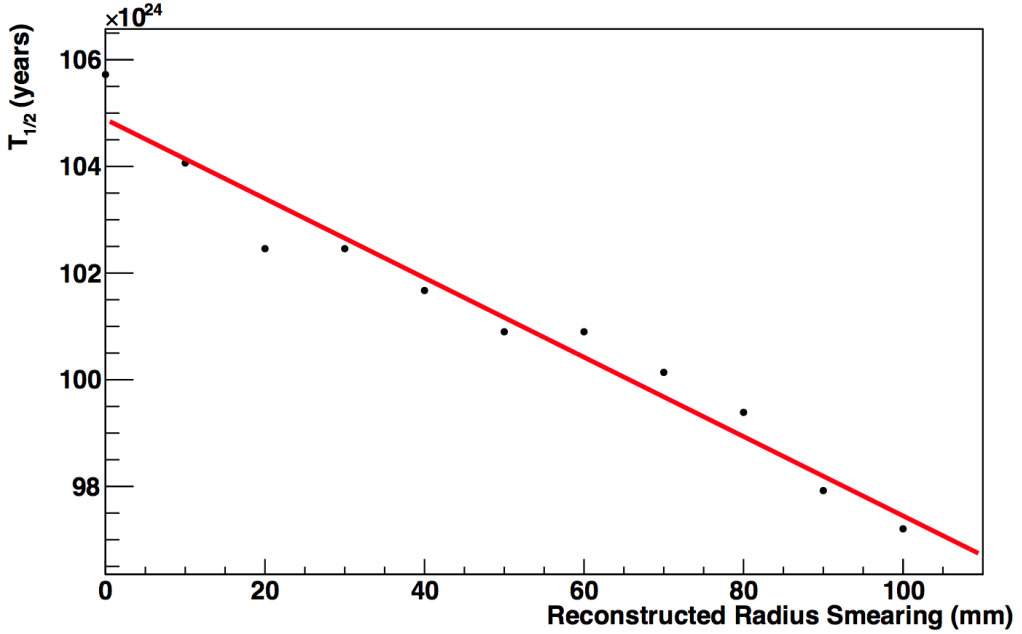


Figure 9.11: *The limit on the neutrinoless double-beta decay life time as a function of the uncertainty in radius. The linear fit produced a gradient of  $-7.4 \times 10^{22}$  years/mm.*

at +20 mm is due to fluctuations in the  ${}^{208}\text{Tl}$  hold-down ropes, see Figure 9.3, increasing statistics when generating this background should remove this.

At zero shift in the z-axis and with no smearing applied to the radius, these results are comparable to the expected SNO+ sensitivity [56].

## 9.5 Conclusions

Despite the relatively low statistics, the fits clearly show a trend in the sensitivity to the neutrinoless double-beta decay half-life as a function of the smearing applied to the reconstructed radius and an AV shift along the z-axis. More detailed simulations will be required to precisely determine these relationships.

As shown, an inaccurate timing calibration reduces the position reconstruction resolution, and can therefore be compared to the effect of smearing the reconstructed radius. Quantifying the improved sensitivity through the use of TELLIE is not trivial, since the same calibration accuracy can be achieved with the LB. The problem with the LB is that, as mentioned, it can not be regularly deployed due to risk of introducing further backgrounds. TELLIE will be used continually, and fortunately it has been shown that the expected uncertainty in the timing calibration will have less than a 2% effect on the sensitivity, in

comparison to a completely accurate timing calibration.

A higher order effect of an inaccurate timing calibration is its effect on the energy reconstruction, which would in turn effect the ability to reduce BG through tagging. U and Th chain daughter BG are reduced through  $\alpha$  coincidence tagging.  $\alpha$  tagging is based on the ability to distinguish between the daughter electrons which travel only a few  $\mu\text{m}$ , and photons that scatter. This technique relies on a completely accurate timing calibration [148]. A reduction in energy resolution would also make it harder to distinguish the two neutrino peak from the neutrinoless peak in Figure 9.1.

Shifting the AV along the z-axis has an order of magnitude larger effect on the sensitivity than an uncertainty in timing. It was shown in Chapter 8 that TELLIE can locate the AV to within 30 mm. So given the worst case scenario; if the AV were to move by 90 mm, TELLIE would be necessary for accurately defining the FV and maximising the sensitivity.

The results of the sensitivity study also suggest that the FV should be centred lower than the centre of the AV, or an asymmetrical FV be defined, to minimise the number of external BG events reconstructed within the FV.

The presented analysis will be extended by the Sussex group, fully assessing the effect on energy resolution and the efficiency of coincidence tagging. A study is already underway to identify the ideal location of the FV relative to AV, based on these results.

## Chapter 10

# Discussion and Conclusions

SNO is being upgraded to SNO+, a multipurpose neutrino detector with the primary goal of observing neutrinoless double-beta decay. To meet requirements imposed by the physics on the detector a new calibration system was required.

This thesis has described the development and implementation of the calibration system. A study has been presented of the potential for using part of the system to monitor the detector's structure enabling a better definition of the fiducial volume.

### 10.1 SNO+

The upgrades to SNO+ are nearing completion, the detector should be fully operational in 2016. The main purpose of the upgrade is the search for neutrinoless double-beta decay in  $^{130}\text{Te}$ , which, if observed, would confirm neutrinos to be Majorana particles. This would explain the relative lightness of neutrinos in comparison to other fermions, and provide a process that meets the Sakharov conditions for explaining the observed matter-antimatter asymmetry in the universe. As the decay rate for neutrinoless double-beta decay is proportional to effective Majorana neutrino mass, the observation would also help determine the neutrino mass hierarchy and further constrain neutrino oscillation parameters.

SNO+ is expected to be sensitive to a decay rate of  $10^{26}$  years after five years running at a 0.3% loading of Te. Te loading will eventually be increased to percent level, further improving sensitivity.

## 10.2 Optical Calibration Systems

The upgrade to SNO+ is characterised by changing the target mass from heavy water to scintillator. Scintillator allows for the lowering of the energy threshold, but this increases sensitivity to backgrounds. Due to increased background sensitivity, a new external LED-based calibration system has been developed and the existing laser calibration system has been modified to meet radiopurity requirements.

### 10.2.1 Scintillator Phase Laserball

The laserball was successfully used in SNO for both the PMT and the optical calibration, and will be used again during the water-fill. However, the design of the mounting hardware for the SNO laserball casts a large shadow on the upper hemisphere of the PSUP, introducing a systematic uncertainty in the calibration of PMTs within this region.

The stringent radiopurity requirements dictate that if a calibration source is to be deployed it must be no more radioactive than the scintillator. To meet this requirement, a scintillator phase LB has been designed and built at Sussex; Rn emanation tests have shown the components of the new laserball to have less than the upper limit of 13.4 counts per day of  $^{222}\text{Rn}$ .

The new laserball has been designed with a narrower neck, the mounting hardware casting a significantly smaller shadow. Simulations have shown that the scintillator phase LB has a greater intensity in the upward direction - minimising any systematic uncertainty in the calculation of angular response for PMTs within the upper hemisphere. Furthermore, there is an increase in the number of photons emitted within the angular range most likely to cause a successful PMT hit, this will improve the physics sensitivity for PMTs within the upper hemisphere of the PSUP.

### 10.2.2 TELLIE

To reduce the need to deploy sources within the scintillator a new LED-based external calibration system has been developed. The timing component of the external calibration system, TELLIE, has been successfully installed and tested. The system uses optical fibres to inject light produced by LEDs and their dedicated drivers.

The use of such a system, external to the target mass is crucial for low background

experiments, as it allows continual calibration with no risk of introducing backgrounds. Using multiple injected beams to illuminate PMTs opposite the injection point allows for a simple system, with a small number of calibration channels. About 100 PMTs can be calibrated with each fibre. This requires overlapping in the data analysis for different injection points.

The design and quality control tests for this system were presented. The wavelength distribution was found to be very uniform, with a spread on the peak measurement of only 2.6 nm (sigma) across all the selected 96 LEDs. The product of fibre transmission and LED intensity at constant current has a large spread, of a factor of more than ten. This spread can be compensated for by intensity adjustments at each driver. All channels are able to cover the whole range of required intensities from  $10^3$  to  $10^5$  photons per pulse. The timing performance of the LED/fibre combination was also found to match the requirements, with a FWHM of 4.4 to 5.2 ns over the necessary intensity range. The spread of rise time measured over all fibres during quality control, was approximately 0.1 ns, showing good uniformity.

For the angular distribution, three measurements were carried out: a detailed two dimensional scan of a single fibre, a semi-automated one dimensional measurement for all 220 fibres, and a measurement in the detector during the air commissioning phase. All three tests gave comparable results, and showed that the beam profile is wide enough to ensure sufficient PMT coverage. Commissioning results were combined with extensive Monte Carlo simulations to demonstrate that the system is capable of calibrating all SNO+ PMTs to the required accuracy.

The accuracy of the event reconstruction resolution is directly proportional to the accuracy of the timing calibration. If TELLIE achieves the designed accuracy in timing calibration of 0.5 ns, the uncertainty in the reconstructed resolution is comparable to within less than  $\pm 1$  mm of that for a completely accurate timing calibration.

To demonstrate the effect of an uncertainty in the accuracy of the timing calibration, simulations of dominant external backgrounds were carried out and their reconstructed radius was smeared. If the timing calibration achieves its accuracy there will only be a 2% reduction on sensitivity to neutrinoless double-beta decay life-time, in comparison to a completely accurate timing calibration.

An alternative design LED driver was developed for TELLIE. The driver has been demonstrated to have equal performance as the one selected for TELLIE, but is more stable,

robust and reliable. Being made from inexpensive readily available components it is both cheaper and easier to repair. All of these attributes make this driver a viable option for any LED based timing calibration system.

### 10.2.3 AV Location

Filling the AV with liquid scintillator makes it buoyant in the UPW shielding, which necessitated a rope-net to hold the AV in place. Due to the radiopurity constraints, the rope-net had to be made from a cleaner material than the existing SNO hold up ropes, and the existing ropes had to be replaced. The new ropes will stretch over time. Based on the performance of the ropes thus far, the AV expected to move 50 mm after 10 years if the ropes are maintained at 10°C. In the worst case scenario this movement may be as much as 90 mm.

As the AV moves relative to the fiducial volume, the number of external events in the fiducial volume will change. It has been shown that by measuring the time of flight for TELLIE pulses reflected from the surface of the AV, the distance between the injection point and the surface of the AV can be determined to an accuracy of  $\pm 30$  mm. The 91 injection points of the TELLIE system provide ample coverage to locate the AV within the PSUP and better define the fiducial volume.

The uncertainty in the location of the AV using TELLIE,  $\pm 30$  mm, is less than the demonstrated event reconstruction resolution:  $\pm 80$  mm, assuming a completely accurate timing calibration.

A shift in the position of the AV, in the expected direction, along the z-axis has an order of magnitude larger effect on the sensitivity to neutrinoless double-beta decay life-time than smearing the event radius. This is due to the change in the number of background events reconstructed within the fiducial volume. Using TELLIE to monitor the AV position limits the change in systematics.

# Bibliography

- [1] Q. Ahmad and et al. Direct evidence for neutrino flavor transformation from neutral-current interactions in the Sudbury Neutrino Observatory. *Phys. Rev. Lett.*, 89(011301), 2002. Cited on 1, 5
- [2] W. Pauli. Letter, addressed to participants of the Tübingen conference on radioactivity. Available from the CERN Document server: <http://cdsweb.cern.ch/record/83282P>., Dec 1930. Cited on 4
- [3] J. Chadwick. Possible existence of a neutron. *Nature*, 129(312), 1932. Cited on 4
- [4] F. Perrin. Possibilité d'émission de particules neutres de masse intrinsèque nulle dans les radioactivités beta. *Comptes Rendus*, 197:1625, Dec 1933. Cited on 4
- [5] E. Fermi. Towards the theory of  $\beta$ -rays. *Z. Phys*, 88(161), 1934. Cited on 4
- [6] C. Cowan, F. Reines, F. Harrison, H. Kruse, and A. McGuire. Detection of the free neutrino: A confirmation. *Science*, 124, 1956. Cited on 4
- [7] M. Goldhaber, L. Grodzins, and A. W. Sunyar. Helicity of neutrinos. *Phys. Rev.*, 109(3):1015–1017, Feb 1958. Cited on 4
- [8] G. Danby, J. Gaillard, K. Goulianos, L. Lederman, N. Mistry, and M. Schwartz. Observation of high-energy neutrino reactions and the existence of two kinds of neutrinos. *Phys. Rev. Lett.*, 9(1), 1962. Cited on 5
- [9] R. Davis, D. Harmer, and K. Hoffman. Search for neutrinos from the sun. *Phys. Rev. Lett.*, 20:1205–1209, 1968. Cited on 5
- [10] M. Perl and et al. Evidence for anomalous lepton production in electron positron annihilation. *Phys. Rev. Lett.*, 35(22):1489–1492, Dec 1975. Cited on 5
- [11] R. Bionta and et al. Contained neutrino interactions in an underground water detector. *Phys. Rev. D*, 38:768–775, 1988. Cited on 5

- [12] K. Hirata and et al. Experimental study of the atmospheric neutrino flux. *Phys. Lett. B*, 205(416), 1988. Cited on 5
- [13] LEP Collaboration. Precision electroweak measurements on the z resonance. *Phys. Rept.*, 427:257–454, 2006. Cited on 5
- [14] Y. Fukuda and et al. Measurement of a small atmospheric  $\nu_\mu / \nu_e$  ratio. *Phys. Lett. B*, 433:9–18, 1998. Cited on 5
- [15] Y. Fukuda and et al. Study of the atmospheric neutrino flux in the multi-GeV energy range. *Phys. Lett. B*, 436:33–41, 1998. Cited on 5
- [16] K. Kodama and et al. Observation of tau neutrino interactions. *Phys. Lett. B*, 504:218–224, 2001. Cited on 5
- [17] K. Abe and et al. Indication of electron neutrino appearance from an accelerator-produced off-axis muon neutrino beam. *Phys. Rev. Lett.*, 107(041801), 2011. Cited on 5
- [18] P. Adamson and et al. Measurement of neutrino and antineutrino oscillations using beam and atmospheric data in MINOS. *Phys. Rev. Lett.*, 110(251801), June 2013. Cited on 5
- [19] Y. Abe and et al. Indication of reactor electron-antineutrino disappearance in the Double Chooz experiment. *Phys. Rev. Lett.*, 108(131801), March 2012. Cited on 5, 75
- [20] F. An and et al. Observation of electron-antineutrino disappearance at Daya Bay. *Phys. Rev. Lett.*, 108, April 2012. Cited on 5
- [21] J. Ahn and et al. Observation of reactor electron antineutrinos disappearance in the RENO experiment. *Phys. Rev. Lett.*, 108(191802), May 2012. Cited on 5
- [22] Y. Abe and et al. Reactor electron antineutrino disappearance in the Double Chooz experiment. *ArXiv e-prints*, (1207.6632), August 2012. Cited on 5
- [23] P. Di Bari. Some notes on neutrino physics and particle cosmology. Typeset for University of Southampton Neutrino Course, 2013. Cited on 6
- [24] K. Nakamura et al. Particle Data Group. *J. Phys. G*, 37, 2010. Cited on xiv, 8, 153
- [25] G. L. Fogli, E. Lisi, A. Marrone, and A. Palazzo. Global analysis of three-flavor neutrino masses and mixings. *ArXiv e-prints*, (0506083v2), 2005. Cited on 9

- [26] S. Bilenky and C. Giunti. Neutrinoless double-beta decay: a probe of physics beyond the Standard Model. *International Journal of Modern Physics A*, 30(1530001), Feb 2015. Cited on xiv, 9, 13, 14, 18, 19
- [27] F. Capozzi et al. Status of three-neutrino oscillation parameters, circa 2013. *Phys. Rev. D*, 89(093018), 2014. Cited on xii, 10
- [28] Mainz Collaboration. Final results from phase ii of the Mainz neutrino mass search in tritium beta decay. *Eur. Phys. C*, 40(4), 2004. Cited on 11
- [29] Troitsk Collaboration. An upper limit on electron antineutrino mass from Troitsk experiment. *Phys. Rev. D*, 84, 2011. Cited on 11
- [30] L. Bodine, D. S. Parno, and R. Robertson. Assessment of molecular efects on neutrino mass measurements from tritium beta decay. *ArXiv e-prints*, (1502.03497), Feb 2015. Cited on 11
- [31] P. Ade and et al. Planck 2013 results. XVI. cosmological parameters. *ArXiv e-prints*, (1303.5076v3), March 2014. Cited on 11
- [32] A. D. Sakharov. Violation of CP invariance, C asymmetry, and baryon asymmetry of the universe. *Sov. Phys. Usp.*, 34:392–393, May 1991. Cited on 12
- [33] Carlo Giunti and Chung W. Kim. *Fundamentals of Neutrino Physics and Astrophysics*. Oxford university press, 2007. Cited on 13
- [34] J. Menendez, A. Poves, E.Caurier, and F.Nowacki. Disassembling the nuclear matrix elements of neutrinoless double-beta decay. *arXiv*, 0801(3760v3), Dec 2008. Cited on 13
- [35] F. Simkovic, G. Pantis, J.D. Vergados, and A. Faessler. Additional nucleon current contributions to neutrinoless double beta decay. *arXiv*, (9905509v1), May 1999. Cited on 13
- [36] J. Barea, J. Kotila, and F. Iachello. Nuclear matrix elements for double-beta decay. *arXiv*, 1301(4203v1), Jan 2013. Cited on 13, 145
- [37] T. R. Rodriguez and G. Martinex-Pinedo. Energy density functional study of nuclear matrix elements for neutrinoless double beta decay. *arXiv*, 1008(5260v2), Nov 2010. Cited on 13

- [38] P. K. Rath, R. Chandra, K. Chaturvedi, P. K. Raina, and J. G. Hirsch. Uncertainties in nuclear transition matrix elements for neutrinoless double decay within the PHFB model. *arXiv*, 1104(3965v1), April 2011. Cited on 13
- [39] C. Vilela. Development of the tracking detector for SuperNEMO and analysis of double-beta decay in  $^{48}\text{Ca}$  using NEMO3 data. IOP HEP presentation, 2013. Cited on xiv, 14
- [40] K. Zuber. Status and perspectives of double beta decay searches. *Journal of Physics: Conference Series*, 578(012007), 2015. Cited on 14, 19
- [41] P. G. Jones. *Background Rejection for the Neutrinoless Double Beta Decay Experiment SNO+*. PhD thesis, University of Oxford, Lincon College, Oxford, 2011. Cited on xv, 15, 25
- [42] A.S. Barabash. Average and recommended half-life values for two-neutrino double beta decay. *Nuclear Physics A*, 935:52–64, March 2015. Cited on 16
- [43] R. Arnold and et al. Measurement of the double-beta decay half-life of  $^{130}\text{Te}$  with the NEMO-3 detector. *Phys. Rev. Lett.*, 107(062504), August 2011. Cited on 16
- [44] Richard B. Firestone, S.Y. Frank Chu, and Coral M. Baglin. *Table of Isotopes*. John Wiley and Sons, 1999. Cited on xiv, 17
- [45] Klapdor-Kleingrothaus and et al. Support of evidence for neutrinoless double beta decay. *Phys. Lett. B*, 578:54–62, 2004. Cited on 20
- [46] GERDA Collaboration. The GERDA experiment for the search of neutrinoless double-beta decay in  $^{76}\text{Ge}$ . *Eur. Phys. C*, 73(2330), 2013. Cited on 20
- [47] M. Agostini and et al. Results on neutrinoless double-beta decay of  $^{76}\text{Ge}$  from phase i of the GERDA experiment. *Phys. Rev. Lett.*, 111(122503), September 2013. Cited on 20
- [48] EXO-200 Collaboration. Search for majorana neutrinos with the first two years of EXO-200 data. *ArXiv e-prints*, (1402.6956), June 2014. Cited on 20
- [49] A. Gando and et al. Measurement of the double-beta decay half-life of  $^{136}\text{Xe}$  with the KamLAND-Zen experiment. *Phys. Rev. C*, 85(045504), April 2012. Cited on 20

- [50] S. Bolt, J. Mott, and C. Vilela. Latest results of NEMO-3: New limit on the neutrinoless double-beta decay half-life for  $^{100}\text{Mo}$ . *Journal of Physics: Conference Series*, 598(012015), 2015. Cited on 20
- [51] L. Simard. The NEMO-3 results after completion of data taking. *Journal of Physics: Conference Series*, 375(042011), 2012. Cited on 20
- [52] K. Lang. Latest results from the NEMO-3 experiment and status of SuperNEMO. *Proceedings of Science ICHEP*, (376), July 2012. Cited on 20
- [53] M. Sisti and et al. Status of the CUORE and results from the CUORE-0 neutrinoless double beta decay experiments. *ArXiv e-prints*, (1502.03653v1), Feb 2015. Cited on 20
- [54] CUORICINO Collaboration.  $^{130}\text{Te}$  neutrinoless double-beta decay with CUORICINO. *Astropart. Phys.*, 34, 2011. Cited on 20
- [55] K. Alfonso and et al. Search for neutrinoless double-beta decay in  $^{130}\text{Te}$  with CUORE-0. *arXiv*, 1504(02454v1), April 2015. Cited on 21
- [56] A. Matsbaum. Double-beta phase plots. *SNO+ DocDB*, (2593), Dec 2014. Cited on xiv, xxi, 21, 145, 154
- [57] J. Boger et al. The Sudbury Neutrino Observatory. *Nucl. Instr. and Meth A*, 449:172–207, 2000. Cited on xxi, 22, 43, 61, 87, 102, 105, 136
- [58] B. Aharim et al. Measurement of the cosmic ray and neutrino-induced muon flux at the Sudbury Neutrino Observatory. *Phys. Rev. B*, 80:012001, 2009. Cited on 22
- [59] R. Alves and et al. The calibration system for the photomultiplier array of the SNO+ experiment. *JINST*, 10(P03002), 2015. Cited on 24, 61, 64, 87, 107
- [60] SNOLAB. *SNOLAB User's Handbook*. SNOLAB, Sudbury, Ontario, Canada, second edition, June 2006. Cited on 24
- [61] H. O'Keeffe. Lead contamination from radon in the cover gas and calibration systems. *SNO+ DocDB*, (1121), August 2011. Cited on 24, 115
- [62] C. Arpesella et al. Direct measurement of the  $^7\text{Be}$  solar neutrino flux with 192 days of Borexino data. *Phys. Rev. Lett.*, 101:091302, Aug 2008. Cited on 24, 115
- [63] H. O'Keeffe. *Low Energy Backgrounds in the NCD Phase of The Sudbury Neutrino Observatory*. PhD thesis, University of Oxford, 2008. Cited on xv, 26

- [64] S. E. Quirk. Purification of liquid scintillator and monte carlo simulation of relevant backgrounds in the SNO+ detector. Master's thesis, Queen's University, Kingston, Canada, 2008. Cited on 26
- [65] M. Schumaker. Radon-reduced air system. *SNO+ DocDB*, (1359), 2012. Cited on 27
- [66] H. O'Keeffe, M. Chen, and V. Lozza. Expected radioactive backgrounds in the SNO+ experiment. *SNO+ DocDB*, (507v26), March 2015. Cited on 27, 147
- [67] P. G. Jones. RAT SNO+ geometry. *SNO+ DocDB*, (2192):9, April 2014. Cited on 28
- [68] A. Poon K. Lesko, C. Okada. Determination of true north for the Sudbury Neutrino Observatory detector. *SNO-STR*, (015):8, June 2000. Cited on xv, 29
- [69] J. Klien, M. Neubauer, F. Mitch Newcomer, and R. Van Berg. The SNO trigger system. *SNO+ DocDB*, (827):74, October 1997. Cited on 31, 33
- [70] Kuraray Co. Ltd. Kuraray Vectran. <http://www.kuraray.us.com/products/fibers/vectran/>. Cited on 34
- [71] Omega. *LCWD Series Load Cell, and DRC-4720 Bridge Signal Conditioner*, 2011. Cited on 35
- [72] Emerson Process Management. The DeltaV distributed control system. <http://www2.emersonprocess.com/en-US/brands/deltav/Pages/index.aspx>. Cited on 35
- [73] D. Earle. Vectran rope stretch. *SNO-STR*, (018a), August 2000. Cited on 35
- [74] International Atomic Energy Agency. Nuclear data services. Cited on 37
- [75] G. et al. Bellini. First evidence of *pep* solar neutrinos by direct detection in Borexino. *Phys. Rev. Lett.*, 108:051302, Feb 2012. Cited on 37
- [76] J. Benziger et al. The nylon scintillator containment vessels for the Borexino solar neutrino experiment. *Nuclear Instruments and Methods in Physics Research Section A: Accelerators, Spectrometers, Detectors and Associated Equipment*, 582(2):509 – 534, 2007. Cited on xii, 37, 38, 39
- [77] Jose Maneira. External background studies. *SNO+ DocDB*, (259), January 2009. Cited on xii, 37, 39

- [78] J. Heise. Rope status. *SNO+ DocDB*, (181), 2008. Cited on xii, 38, 39, 57
- [79] P. G. Jones. The SNO+ experiment, overview and status. *SNO+ DocDB*, (2793), 2014. Cited on xvi, 41
- [80] B. E. Berger et al. The KamLAND full-volume calibration system. *JINST*, 4:P04017, 2009. Cited on xvi, 42
- [81] B. Aharim et al. Measurement of the  $\nu_e$  and total  $^8\text{B}$  solar neutrino fluxes with the Sudbury Neutrino Observatory phase-iii data set. *Phys. Rev. C*, 87:015502, Jan 2013. Cited on 42
- [82] W. R. Leo. *Techniques for Nuclear and Particle Physics Experiments*. Springer-Verlag, La Tour de Peilz, Switzerland, second edition, 1994. Cited on 43
- [83] J.R.N. Cameron. *The Photomultiplier Tube Calibration of the Sudbury Neutrino Observatory*. PhD thesis, Oxford, 2001. Cited on xvi, xix, 43, 111
- [84] S. Peeters. Calibration overview. *SNO+ DocDB*, (1614), August 2012. Cited on 44, 101
- [85] Borexino collaboration. Borexino calibrations: Hardware, methods, and results. *ArXiv e-prints*, (1207.4816), July 2007. Cited on 44
- [86] K. Singh et al. Camera system for SNO+. *SNO+ DocDB*, (1680), March 2103. Cited on 44
- [87] B.A. Moffat et al. Optical calibration hardware for the sudbury neutrino observatory. *NIM A.*, 544:255–265, 2005. Cited on xvi, xx, 44, 45, 115, 116, 118, 124
- [88] I. Coulter. *Modelling and reconstruction of events in SNO+ related to future searches for lepton and baryon number violation*. PhD thesis, Oxford, Balliol College, Oxford, 2013. Cited on 47, 142, 145
- [89] S. Agostinelli and et al. Geant4-a simulation toolkit. *Nuclear Instruments and Methods in Physics Research Section A: Accelerators, Spectrometers, Detectors and Associated Equipment*, 506(3):250–303, July 2003. Cited on 47
- [90] I. Antcheva and et al. Root - a c++ framework for petabyte data storage, statistical analysis and visualization. *Computer Physics Communications*, 180(12):2499–2512, Dec 2009. Cited on 47

- [91] A. Hallin. Rope tensions after replacement. Communication, Feb 2012. Cited on xvi, 51
- [92] Gerd Schraner. *The Art of Wheelbuilding*. Number 0-9649835-3-2. Buopane Publications, Denver, CO 80204, 1999. Cited on 51
- [93] A. Hallin, M. Hedayatipour, J. Sinclair, and K. Singh. The expected performance and motion of the upward and downward ropes in the SNO+ rope net. *SNO+ DocDB*, (1872), Dec 2012. Cited on xvi, 53, 57, 58
- [94] American Society for Testing and Materials. *ASTM D4268: Standard Test Method for Testing Fibre Ropes*, 1993. Cited on 57
- [95] J Stachiw. Allowable stress levels in the design criteria for the SNO acrylic vessel. *SNO-STR*, 1991. Cited on 58
- [96] A. Hallin. Expected deformation of the AV. Private communication, March 2015. Cited on 58
- [97] A. Bialek and et al. A rope-net support system for the SNO+ liquid scintillator detector. *SNO+ DocDB*, (3074), 2015. Cited on xvi, 58
- [98] J.S. Kapustinsky et al. A fast timing light pulser for scintillation detectors. *NIM A*, 241:612–613, 1985. Cited on xvii, 60, 74
- [99] P. Adamson. *An LED Calibration System for the MINOS Long Baseline Neutrino Oscillation Experiment*. PhD thesis, University of Sussex, March 2001. Cited on 60
- [100] E. Fred Schubert. *Lighth-Emitting Diodes*. Cambridge university press, 2010. Cited on 61, 75, 93
- [101] S.D Biller et al. Measurements of photomultiplier single photon counting efficiency for the Sudbury Neutrino Observatory. *Nuclear Instruments and Methods in Physics Research Section A: Accelerators, Spectrometers, Detectors and Associated Equipment*, 432(2–3):364 – 373, 1999. Cited on xvi, 62, 63
- [102] T. Bromwich. LED Tests. *SNO+ DocDB*, (2884), September 2011. Cited on 63
- [103] Brite-LED Optoelectronics. *Ultra Brightness Cyan LED Lamp BL-LUCY5N15C*, July 2003. Cited on 63, 82
- [104] S. Peeters. TELLIE pulse fitting notes. *SNO+ DocDB*, (2880), 2014. Cited on 65

- [105] F. Descamps. TELLIE hit probabilites revisited. *SNO+ DocDB*, (1703v2), Feb 2015. Cited on xii, 65, 69
- [106] G. Lefevre. TELLIE fibre emission profile. *SNO+ DocDB*, (1226), 2011. Cited on 66
- [107] F. Descamps. TELLIE angle definitions. *SNO+ DocDB*, (2556), June 2014. Cited on xvii, 66
- [108] ESKA OPTICAL FIBER DIVISION. *Specification Sheet, SH 4002, Super ESKA Polyethylene Jacketed Optical Fibre Cord*. MITSUBISHI RAYON CO., LTD., 6-41 Kounan 1-Chome, Minato-ku, Tokyo, Japan, dpf1132-17 edition, July 2001. Cited on 70, 93
- [109] Hamamatsu. *Metal package PMT photosensor modules H10720/H10721 series*. Cited on 71, 73, 91, 94, 97
- [110] HAMAMATSU PHOTONICS K. K. *PHOTOMULTIPLIER TUBES: Basics and Applications*. HAMAMATSU PHOTONICS K. K., 3rd edition, 2007. Cited on 71, 91
- [111] L. Bollinger and G. Thomas. Measurement of the time dependence of scintillation intensity by a delayed coincidence method. *The Review of Scientific Instruments*, 32(9), September 1961. Cited on 71
- [112] G. Lefevre. Sussex optical scan setup. *SNO+ DocDB*, (2882), 2012. Cited on xvii, 71, 72, 73
- [113] B. K. Lubsandorzhiev and Y. E. Vyatchin. Studies of kapustinsky's light pulser timing characteristics. *JINST*, T06001, 2006. Cited on 74, 75
- [114] H.E.S.S. collaboration. H.E.S.S. contributions to the 28th international Cosmic Ray Conference. *arXiv*, (0307452v1), 2003. Cited on 75
- [115] P. Amram et al. The ANTARES optical module. *NIM A*, 484:369–383, 2002. Cited on 75
- [116] A. Avrorin et al. An experimental string of the NT1000 Baikal Neutrino Telescope. *Instruments and Experimental Techniques*, 54(5):649–659, 2011. Cited on 75
- [117] B.K. Lubsandorzhiev, R.V. Poleshuk, B.A.J. Shaibonov, and Y.E. Vyatchin. LED based powerful nanosecond light sources for calibration systems of deep underwater

- neutrino telescopes. *Nuclear Instruments and Methods in Physics Research Section A: Accelerators, Spectrometers, Detectors and Associated Equipment*, 602(1):220 – 223, 2009. Proceedings of the 3rd International Workshop on a Very Large Volume Neutrino Telescope for the Mediterranean Sea. Cited on 75
- [118] O. Veledar et al. Simple techniques for generating nanosecond blue light pulses from light emitting diodes. *Measurement Science and Technology*, 18(1):131–137, 2007. Cited on 75
- [119] Brite-LED Optoelectronics. *High Output Violet Blue LED Lamp BL-LUVB5N15C*. Florida, Dec 2006. Cited on 77
- [120] IXYS Colorado. *IXLD02SI Data Sheet*. IXYS Colorado, Colorado, second edition. Cited on 79, 80
- [121] J.Rose. Measurement of LED photons per pulse using the IXLD02 driver board and the Thorlabs PM100 USB power meter. *SNO+ DocDB*, (2837), January 2013. Cited on 80, 85
- [122] G. U. Agostinho. Aperture angle measurement in SNO+. *SNO+ DocDB*, (1210), October 2011. Cited on xviii, 95
- [123] A. Maio and et al. Ageing studies of wavelength shifter fibers for the TILECAL/ATLAS experiment. *Nuclear Instruments and Methods in Physics Research Section A: Accelerators, Spectrometers, Detectors and Associated Equipment*, 580(1):318–321, 2007. Cited on 97
- [124] M. Chen. The SNO liquid scintillator project. *Nuclear Physics B - Proceedings Supplements*, 145:65–68, August 2005. Cited on 102
- [125] I. Lawson and B. Cleveland. Low background counting at SNOLAB. *American Institute of Physics Conf. Proc.*, 1338(68), 2011. Cited on 102
- [126] B. Cleveland and I. Lawson. SNOLAB gamma assay results. [http://www.snolab.ca/users/services/gamma-assay/HPGe\\_samples\\_pub.html](http://www.snolab.ca/users/services/gamma-assay/HPGe_samples_pub.html). Cited on 102
- [127] I. Blevis and et al. Measurement of 222Rn dissolved in water at the Sudbury Neutrino Observatory. *Nuclear Instruments and Methods in Physics Research Section A: Accelerators, Spectrometers, Detectors and Associated Equipment*, 517:139–153, 2004. Cited on 103

- [128] M. Seddighin. Low energy 8B solar neutrinos in SNO+: Controlling and constraining radon backgrounds. Master's thesis, Queen's University, Kingston, Canada, 2013. Cited on 103
- [129] N. de Barros. *Precision measurements of the neutrino oscillation parameters: Combined three-phase results of the Sudbury Neutrino Observatory.* PhD thesis, Universidade de Lisboa, Lisbon, portugal, 2011. Cited on xx, 115, 117, 118, 124, 125
- [130] R. Ford. Nitrogen/dye laser system for the optical calibration of SNO. Master's thesis, Queen's University, Kingston, Canada, 1993. Cited on 115
- [131] J. Sinclair. Scintillator phase Laserball hardware status. *SNO+ DocDB*, (2901), October 2013. Cited on 119
- [132] H. O'Keeffe, M. Chen, and V. Lozza. Materials compatible with lab. *SNO+ DocDB*, (1291), April 2014. Cited on 122
- [133] D. Waters. Radon emanation from stainless steel. Private communication, May 2015. Cited on 122
- [134] N. Fatemi-Ghom. Emination results of cover gas bags and Laserball. *SNO+ DocDB*, (1791), March 2013. Cited on 122
- [135] M. Stringer. Monte carlo simulation of the effect of the new Laserball neck on the PMT angular response. *SNO+ DocDB*, January 2015. Cited on xx, 123, 125, 127
- [136] G. D. Orebi Gann. *An Improved Measurement of the 8B Solar Neutrino Energy Spectrum at the Sudbury Neutrino Observatory.* PhD thesis, Oxford, Merton College, Oxford, 2008. Cited on xx, 125, 126
- [137] R. Stainforth. Light paths in rat. *SNO+ DocDB*, (1700v8), Feb 2015. Cited on xxi, 130, 132
- [138] W. M. Haynes, editor. *CRC Handbook of Chemistry and Physics.* Number ISBN 9781482208672. CRC Press Taylor and Francis Group, 95 edition, June 2014. Cited on xiii, 129
- [139] I. Yeo and et al. Measurement of the refractive index of the lab-based liquid scintilator and acrylic at reno. *Phys. Scr.*, 82(065706), 2010. Cited on xiii, 129
- [140] B. Moffat. *The Optical Calibration of the Sudbury Neutrino Observatory.* PhD thesis, Queen's University, Kingston, Canada, July 2001. Cited on 132

- [141] G. D. Orebí Gann. Dealing with time in RAT. *SNO+ DocDB*, (481), April 2010. Cited on 134
- [142] S. Peeters. Discussion of PMT hit time distortion by multi-photon hits. Private communication, March 2015. Cited on 138
- [143] K. Lesko. PSUP question. Email regarding PSUP rigidity, July 2013. Cited on 138
- [144] M. Stringer, S. Peeters, and J. Sinclair. AVLOC theory and initial results. *SNO+ DocDB*, (3432), August 2015. Cited on 140
- [145] J. Kotila and F. Iachello. Phase space factors for double-beta decay. *arXiv*, 1209(5722v1), September 2012. Cited on 145
- [146] S. Asahi, S. Grullon, and J. Maneira. External background studies for NewNd. *SNO+ DocDB*, (1720), July 2013. Cited on xxi, 145, 146
- [147] S. Baker and R. Cousins. Clarification of the use of chi-square and likelihood functions in fits to histograms. *Nuclear Instruments and Methods in Physics Research*, 221:437–442, 1984. Cited on 152
- [148] K. Majumdar. Functional form energy reconstruction. *SNO+ DocDB*, (2945), March 2015. Cited on 155
- [149] ACC Silicones. Technical data sheet EGel3005 (ESP491) low viscosity silicone gel. Technical report, ACC Silicones Ltd, Bridgwater, Somerset, UK, Dec 2012. Cited on 172
- [150] 3M. 3M glass bubbles, types K and S saftey data sheet. 10-4852-9 122.03, 3M, August 2014. Cited on 172

## Appendix A

# Laserball Construction Instructions

This appendix will describe the filling procedure for the flask, a non-trivial task. The glass beads become airborne easily, so a respirator with sufficient particulate filter should also be worn, see [149] and [150] for necessary safety measures.

- To begin ensure the flask is cleaned thoroughly with alcohol.
- Pour 300 ml of component A of the gel into a 1 l beaker, pour 310 ml of component B into a 500 ml beaker. N.B. once exposed to air the gels must be mixed within 4 min, or they will not cure when mixed.
- On top of component A, pour an equal volume of beads. Do not mix the two yet.
- Pour component B on top of the beads in the 1 l beaker. This limits the amount of beads that become airborne during mixing.
- Mix thoroughly. It is important the two components are mixed in a 1:1 ratio, the extra 10 ml should allow for what remains in the 500 ml beaker. N.B. The curing time is 15 min at 25°C.
- Place the 1 l beaker in a vacuum chamber and pump down slowly, to degas the mixture.
- Pour the degassed mixture into the LB flask, fill the flask to the base of its neck. Do not discard the leftover.
- Place the flask in the vacuum chamber and pump down very slowly, to avoid ejecting

the mixture form the flask.

- The leftover mixture will provide an indication of when the silicone has cured.

Once the silicone has cured the LB can be assembled.

## Appendix B

# Laserball Technical Drawings

This appendix contains technical drawings for the individual components of the SNO+ scintillator phase and DEAP-3600 laserball.

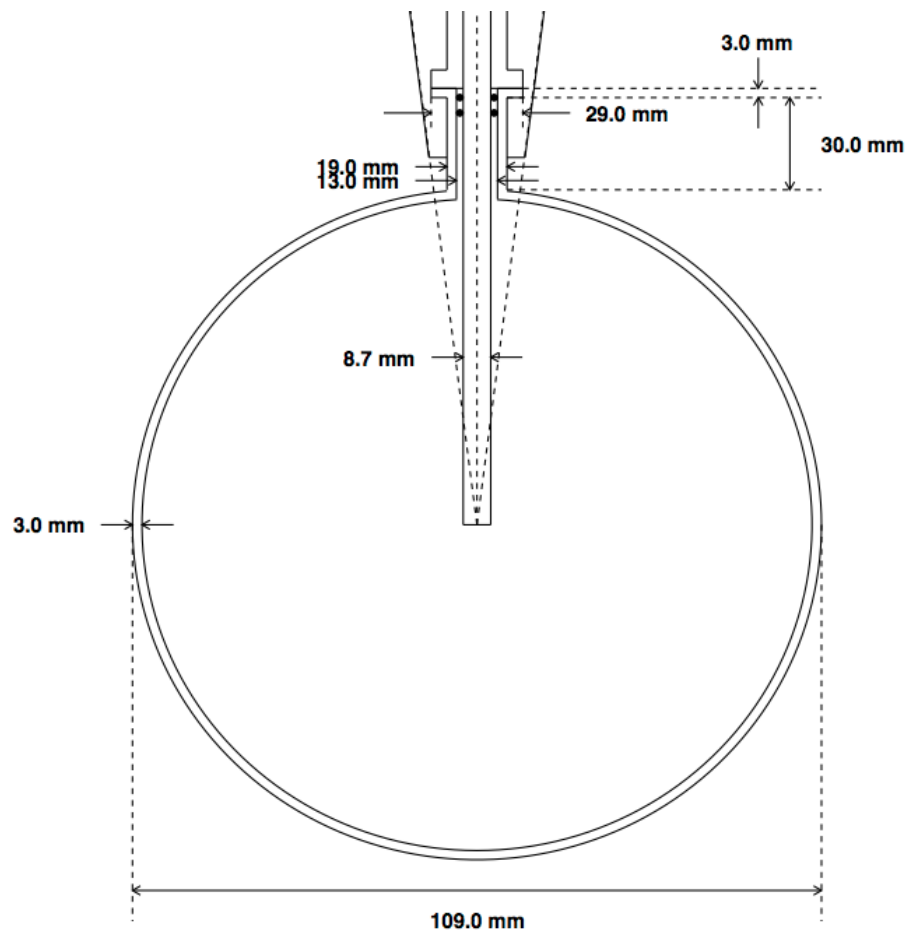


Figure B.1: *The dimensions of the SNO+ scintillator phase laserball flask.*

## Part 1

## Flask neck Shield

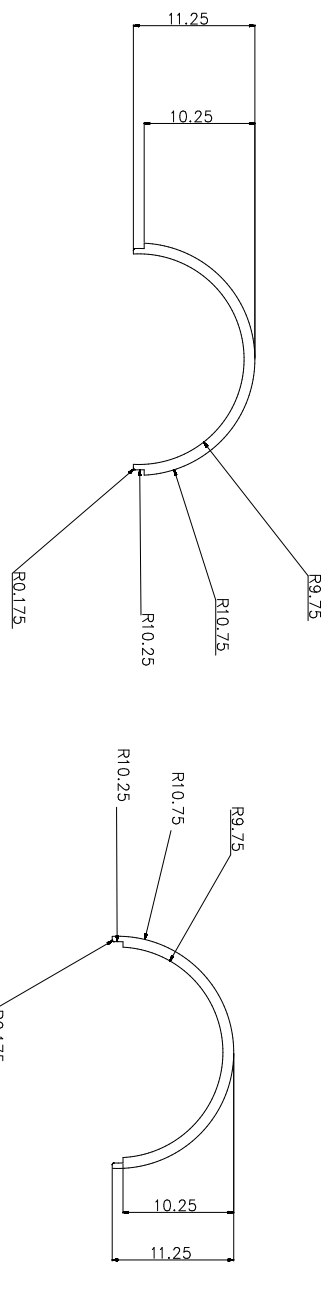


Figure B.2: Technical drawing of shroud for SNO+ scintillator phase laserball.

Material: 316L Stainless Steel  
Side 1

Scale 10:1

Material: 316L Stainless Steel  
Side 2

Scale 10:1

Do not scale  
Remove all sharp edges  
All Dimensions in mm

# Part 2

## F|ask neck Clamp

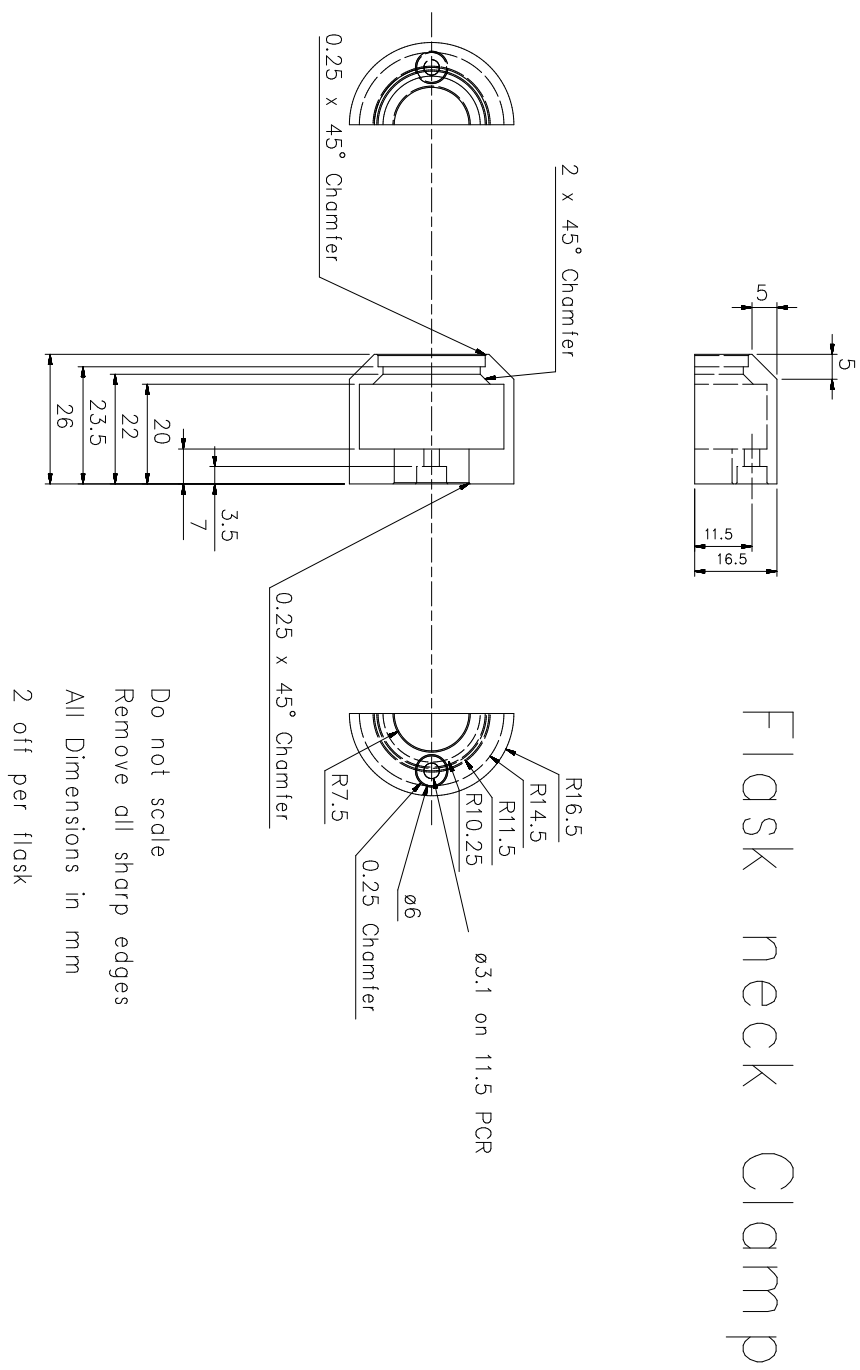


Figure B.3: Technical drawing of clamps for SNO+ scintillator phase laserball.

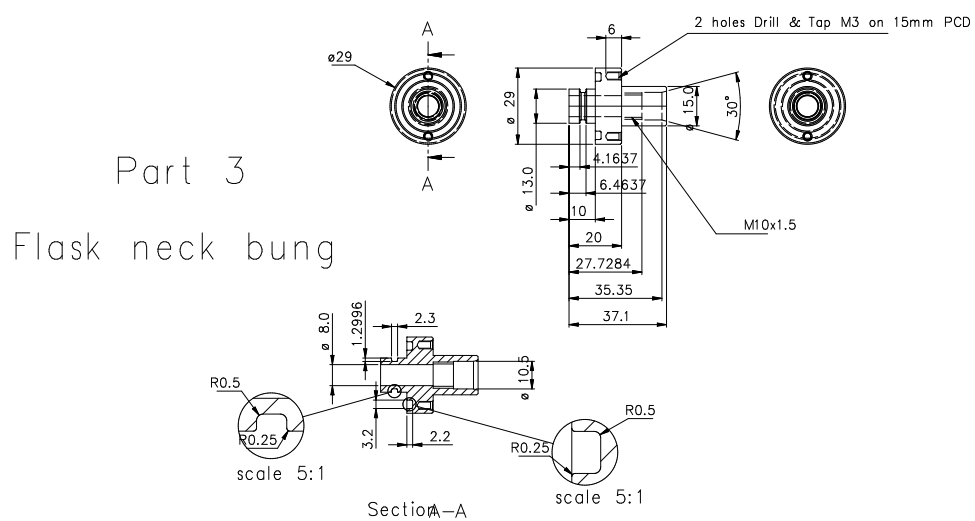


Figure B.4: Technical drawing of plug for SNO+ scintillator phase laserball.

## Part 4

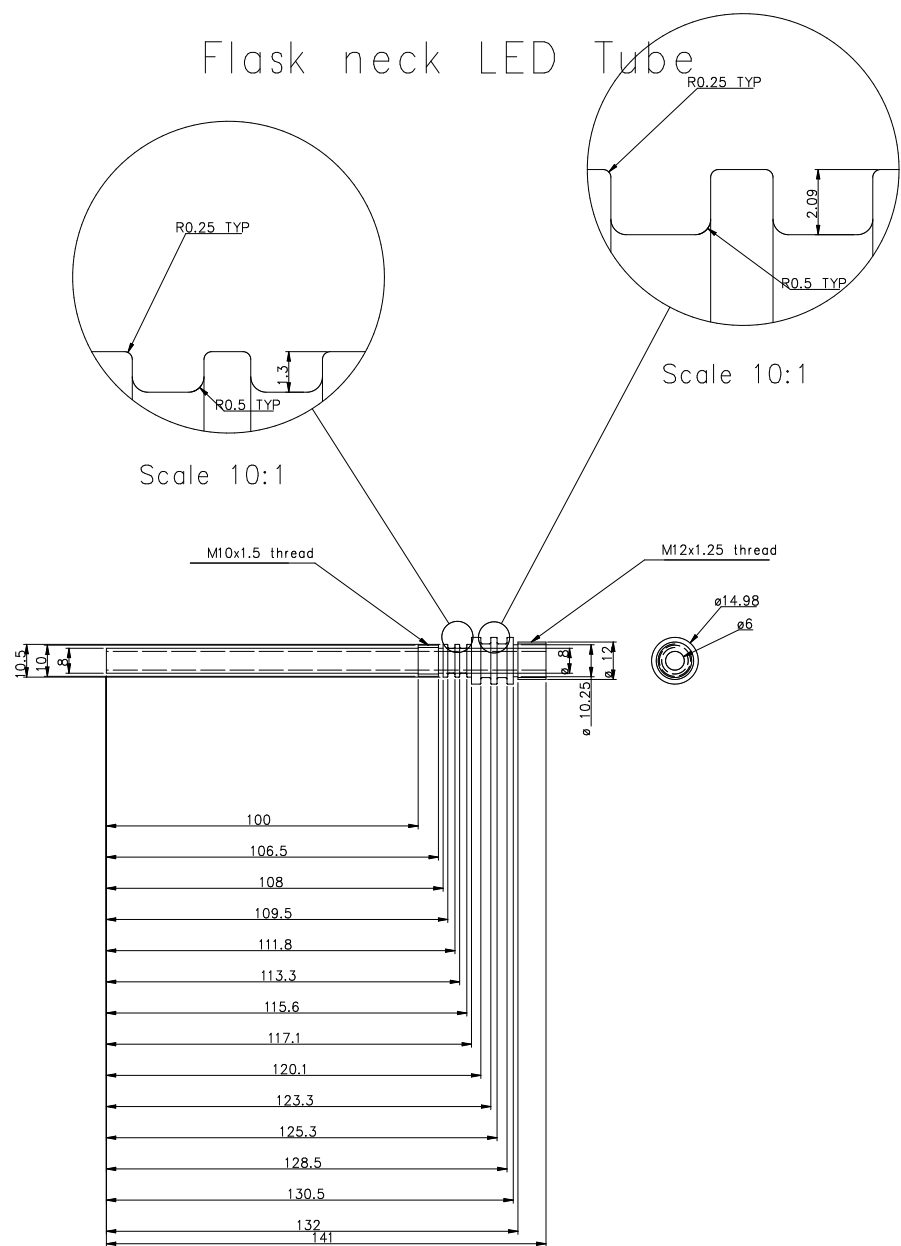


Figure B.5: Technical drawing of light guide shaft for SNO+ scintillator phase laserball.

## Part 5 LED tube attachment cap

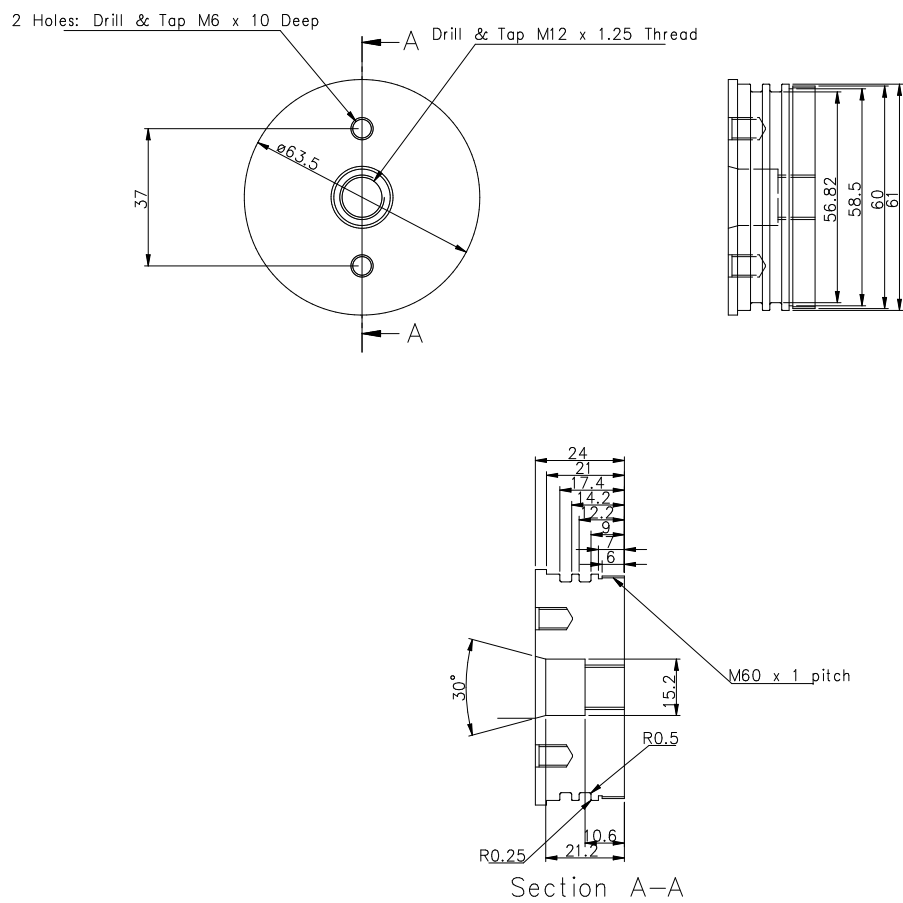


Figure B.6: Technical drawing of driver housing base for DEAP-3600 laserball.

## Part 6

## LED COAX Tube

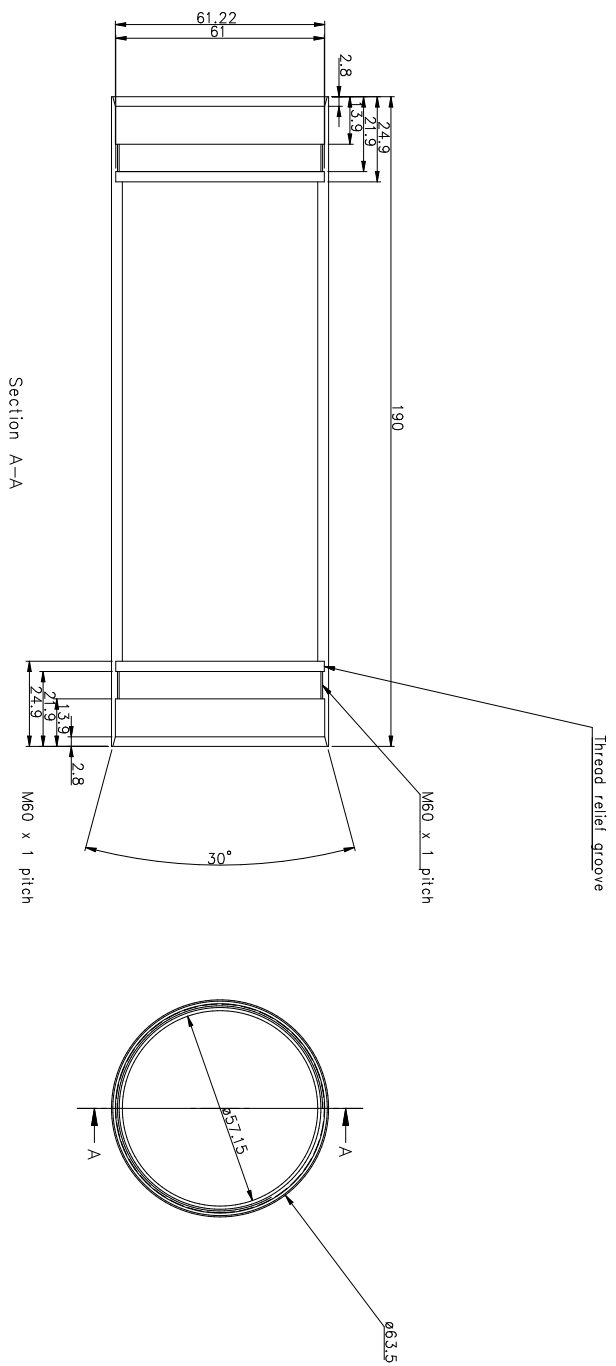


Figure B.7: Technical drawing of driver housing for DEAP-3600 laserball.

Part 7  
COAX attachment cap

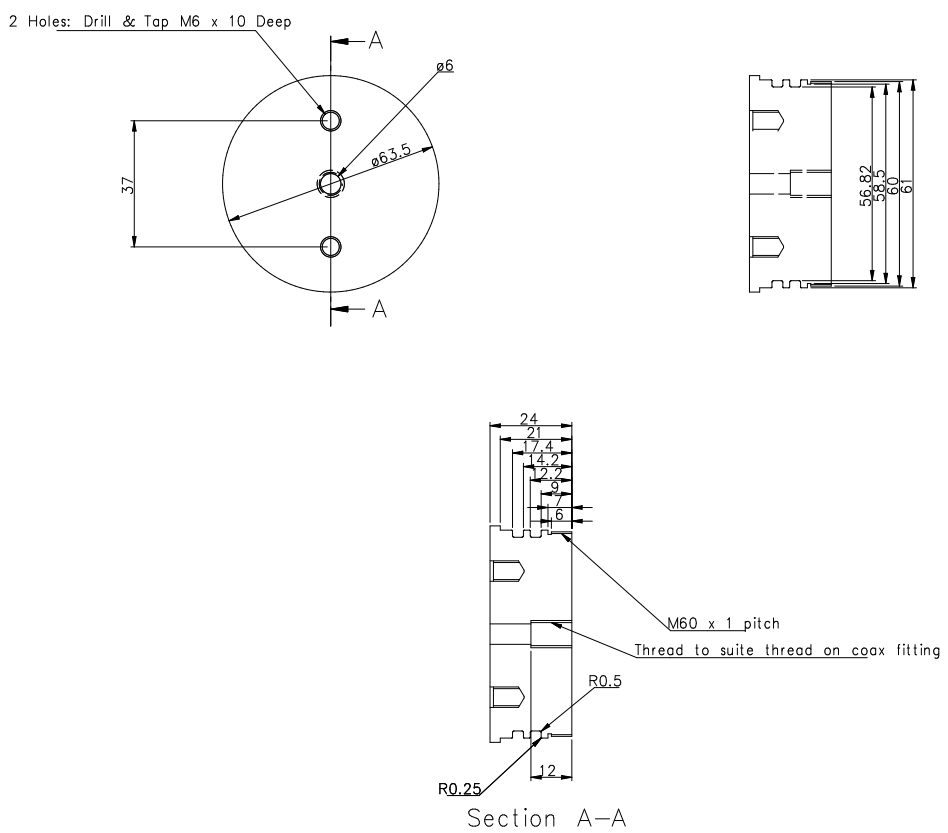


Figure B.8: Technical drawing of driver housing cap for DEAP-3600 laserball.

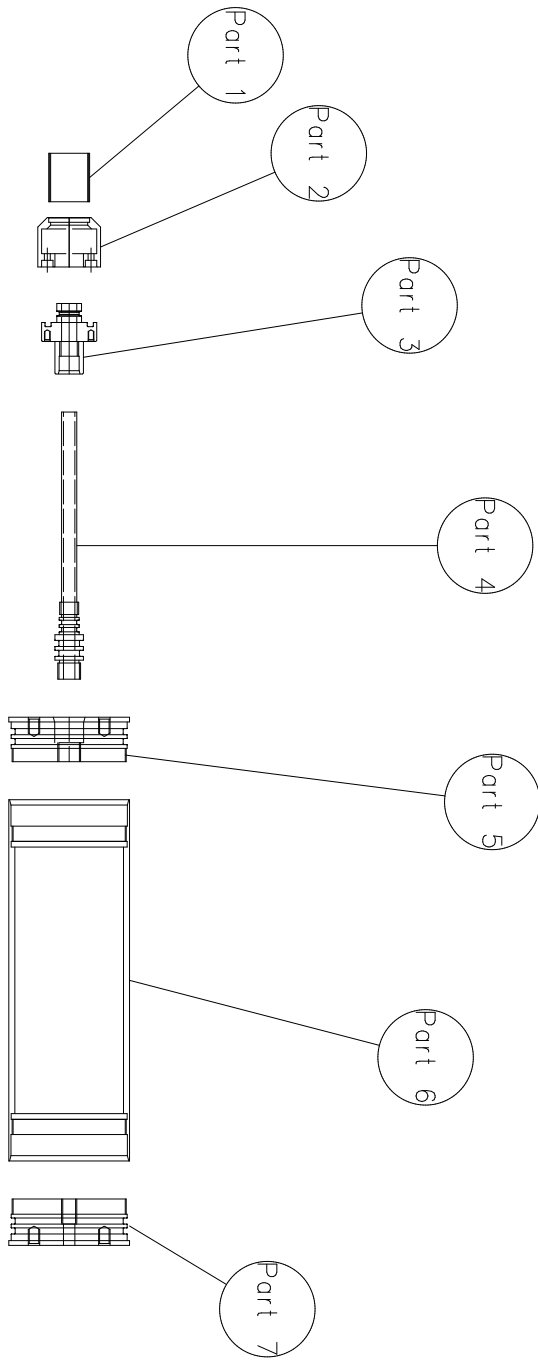


Figure B.9: *Technical drawing of DEAP-3600 laserball assembly.*